MOLECULAR DOPING OF ORGANIC SEMICONDUCTORS – CONTRIBUTIONS TO ITS BASIC UNDERSTANDING AND APPLICATION

D i s s e r t a t i o n

zur Erlangung des akademischen Grades
d o c t o r r e r u m n a t u r a l i u m
(Dr. rer. nat.)
im Fach Physik
Spezialisierung: Experimentalphysik
eingereicht an der

Mathematisch-Naturwissenschaftlichen Fakultät
der Humboldt-Universität zu Berlin
von

Herrn Berthold Wegner, M. Sc.

Präsidentin der Humboldt-Universität zu Berlin
Prof. Dr.-Ing. Dr. Sabine Kunst

Dekan der Mathematisch-Naturwissenschaftlichen Fakultät
Prof. Dr. Elmar Kulke

Gutachter/innen:

1. Prof. Dr. Norbert Koch
2. Prof. Dr. Thuc-Quyen Nguyen
3. Prof. Dr. Christoph T. Koch

Tag der mündlichen Prüfung: 1. März 2019

ABSTRACT

Doping is a key technological procedure to control the charge carrier density and Fermi level position in semiconductors. For organic semiconductors, the use of strong molecular electron acceptors and donors as p-type and n-type dopants, respectively, has emerged as the most reliable approach. In the present thesis, a variety of topics related to the molecular doping of organic semiconductors will be investigated.

First, the suitability of two different material parameters to predict ion pair formation in molecular doping will be explored: i) redox-potentials measured by cyclic voltammetry (CV) in solution and ii) ionization energy (IE) / electron affinity (EA) measured on individual films by (inverse) photo-electron spectroscopy (PES/IPES). Optical absorption spectroscopy measurements reveal redox-potentials to be better suited to identify matching material pairs than IE/EA values. This is ascribed to the strong dependence of IE/EA values of molecular assemblies upon film structure on and above the meso-scale, while CV measurements capture the energy levels on the molecular scale, which is more relevant for doping.

Secondly, the n-type doping of a prototypical p-type co-polymer by an organometallic dimer is studied. Combined PES/IPES, optical absorption and conductivity measurements show that the p-type polymer can be rendered n-type upon doping. However, it will be demonstrated that the n-doping is not stable over time and the doping-induced n-type conductivity is decreasing again over two orders of magnitude within a few days stored under ideal inert conditions.

Thirdly, the p-type doping of the polymer P3HT by a boron based organic salt is investigated. Combined optical absorption, electron paramagnetic resonance (EPR) spectroscopy and conductivity measurements will show the formation of polarons at low and bipolarons at high dopant concentrations above ten percent. Mono-chromatized PES measurements show a strong depletion of the delocalized valence π-band near the Fermi level, indicating a significant increase in hole density. In addition, PES detail measurements of the sulfur core levels reveal the emergence of polaronic and bipolaronic components upon doping. Furthermore, it will be shown that air-exposure leads to a back-transition of bipolarons to polarons. Conductivity measurements on air-exposed samples indicate bipolaronic charge carriers to be less mobile than polaronic ones.

Finally, the modification of electron-selective contacts in organic-inorganic metal halide perovskite solar cells (PSCs) is studied in order to minimize electron collection losses. Here, an interlayer of organometallic dimers will be introduced between electrode and organic electron transport layer (ETL) in order to form an Ohmic contact. PES measurements reveal that the introduction of such an interlayer significantly reduces the work function of the electrode leading to Fermi level pinning of the ETL. In addition, the interlayer induces interfacial doping of the ETL. Optical absorption measurements show that annealing enhances the interfacial doping and leads to a moderate diffusion of the dimers into the ETL. PSCs employing such modified electron-selective contacts show increased power conversion efficiencies.

KURZFASSUNG

Dotierung ist ein technologisches Schlüsselverfahren zur Kontrolle der Ladungsträgerdichte und der Position des Fermi-Levels in Halbleitern. Für organische Halbleiter hat sich die Verwendung von starken molekularen Elektronenakzeptoren und -donatoren als p- bzw. n-Dotanten als zuverlässigster Ansatz erwiesen. In der vorliegenden Arbeit wird eine Reihe von Themen im Zusammenhang mit der molekularen Dotierung von organischen Halbleitern untersucht.

Zuerst wird die Eignung zweier verschiedener Materialparameter zur Vorhersage der Ionenpaarbildung bei der molekularen Dotierung untersucht: i) Redox-Potentiale, gemessen durch Cyclovoltammetrie (CV) in Lösung, und ii) Ionisationsenergie (IE) / Elektronenaffinität (EA), gemessen an dünnen Filmen mittels (inverser) Photoelektronenspektroskopie (PES/IPES). Optische Absorptionsmessungen zeigen, dass Redox-Potentiale besser geeignet sind passende Materialpaare zu identifizieren als IE/EA-Werte. Dies wird auf die starke Abhängigkeit der IE/EA-Werte von molekularen Anordnungen der Filmstruktur auf und über der Meso-Ebene zurückgeführt, während CV-Messungen die Energieniveaus auf der für Dotierung relevanten molekularen Ebene erfassen.

Zweitens wird die n-Dotierung eines prototypischen, p-artigen Co-Polymers durch metallorganische Dimere untersucht. Die Kombination von PES/IPES, optischen Absorptions- und Leitfähigkeitsmessungen wird zeigen, dass das p-Polymer durch Dotierung zu einem n-Polymer transformiert werden kann. Es wird jedoch auch demonstriert, dass die n-Dotierung nicht langzeit-stabil ist und die dotierungsinduzierte n-Leitfähigkeit in inerter Atmosphäre innerhalb von wenigen Tagen wieder über zwei Größenordnungen abnimmt.

Drittens wird die p-Dotierung des Polymers P3HT durch ein bor-basiertes organisches Salz untersucht. Durch die Kombination von optischer Absorptions- und Elektronenparamagnetresonanzspektroskopie (EPR) sowie Leitfähigkeitsmessungen wird die Bildung von Polaronen bei niedrigen und von Bipolaronen bei hohen Dotanten-Konzentrationen von über zehn Prozent gezeigt. Monochromatisierte PES-Messungen zeigen eine starke Abnahme des delokalisierten π-Bandes im Valenzband in der Nähe des Fermi-Levels, was auf eine signifikante Erhöhung der Lochdichte hinweist. Darüber hinaus zeigen PES-Detailmessungen der Schwefel-Kernniveaus die Entstehung von polaronischen und bipolaronischen Komponenten bei der Dotierung. Weiterhin wird gezeigt, dass Exposition an Luft zu einer Rücktransformation von Bipolaronen zu Polaronen führt. Leitfähigkeitsmessungen an luftexponierten Proben zeigen deutlich, dass bipolaronische Ladungsträger weniger mobil sind als polaronische.

Zuletzt wird die Modifikation von elektronenselektiven Kontakten in organisch-anorganischen Metallhalogenid-Perowskit-Solarzellen (PSCs) untersucht, um Elektronensammel-Verluste zu minimieren. Hierzu wird eine Zwischenschicht aus metallorganischen Dimeren zwischen Elektrode und org. Elektronentransportschicht (ETL) eingebracht, um einen ohmschen Kontakt herzustellen. PES-Messungen zeigen, dass das Einfügen einer solchen Zwischenschicht die Austrittsarbeit der Elektrode stark reduziert, was zum Fermi-Level-Pinning der ETL führt. Zudem wird dabei Grenzflächendotierung der ETL induziert. Optische Absorptionsmessungen zeigen, dass Heizen die Grenzflächendotierung verbessert und zu einer moderaten Diffusion der Dimere in die ETL führt. PSCs, die aus derart modifizierten elektronenselektiven Kontakte bestehen, weisen erhöhte Wirkungsgrade auf.

CONTENTS

Abstract ... **ii**

Kurzfassung ... **iii**

List of Abbreviations and Symbols ... **vi**

1 Introduction ... **1**

2 Fundamentals ... **5**

2.1 Organic Semiconductors ... 5

2.1.1 Electronic Structure ... 5

2.1.2 Optical Properties ... 18

2.1.3 Charge Transport ... 24

2.1.4 Energy Level Alignment ... 28

2.1.5 Film Formation ... 33

2.1.6 Organic Electronic Devices ... 35

2.2 Doping of Organic Semiconductors ... 41

2.2.1 Mechanisms of Doping ... 41

2.2.2 p-Type Doping ... 46

2.2.3 n-Type Doping ... 48

3 Theory of Experimental Methods ... **53**

3.1 Photoelectron Spectroscopy ... 53

3.1.1 Process of Photoemission ... 54

3.1.2 Ultraviolet Photoelectron Spectroscopy ... 59

3.1.3 X-Ray Photoelectron Spectroscopy ... 61

3.1.4 Inverse Photoelectron Spectroscopy ... 64

3.2 Optical Absorption Spectroscopy ... 65

3.3 Cyclic Voltammetry ... 68

3.4 Electrical Conductivity Measurements ... 71

3.5 Scanning Force Microscopy ... 72

4 Materials and Experimental Setups ... **75**

4.1 Materials ... 75

4.2 Sample Preparation ... 78

4.3 Experimental Setups ... 80

4.4 Data Analysis Methods ... 82

5 Predicting Ion Pair Formation Yield in Molecular Doping ... **85**

5.1 Comparison of Frontier Orbital Energy Levels ... 86

5.2 Material Set I 88
5.3 Material Set II 92
5.4 Material Set III 96
5.5 Summary 100

6 N-Doping of a P-Type Polymer 102
6.1 Doping Capability and Activation by Light Irradiation 103
6.2 Electronic Structure and Electrical Properties of Doped Films 110
6.3 Application in Organic Field Effect Transistors 114
6.4 Summary 117

7 Bipolaron Formation in P3HT 118
7.1 Doping Process 119
7.2 Polaron to Bipolaron Transition 122
7.3 Conductivity and Influence of Thermal Annealing 127
7.4 Electronic Structure and Core Level Analysis 130
7.5 Influence of Air-Exposure 138
7.6 Summary 141

8 Electrode Modification for Use in Perovskite Solar Cells 143
8.1 Modification of FTO 143
8.2 The Interface between Modified FTO and Organic ETMs 150
8.3 Diffusion of Dimers into the Organic Layers 155
8.4 Application in Perovskite Solar Cells 159
8.5 Summary 160

9 Conclusion and Outlook 162

Appendix 168

Record of Publications 173

References 174

Acknowledgements 193

Selbstständigkeitserklärung 195

A_i	absorbance of species i
Al	aluminum
ARUPS	angle resolved UPS
ARXPS	angle resolved XPS
ASF	atomic sensitivity factor
Au	gold
BCF3	tris(pentafluorophenyl) borane
BCF4	tetrakis(pentafluorophenyl) borate
BE	binding energy
C_{60}	fullerene
c_i	concentration of species i
CB	conduction band
CB	chlorobenzene
$CoCp_2$	cobaltocene
CPX	charge transfer complex
CT	charge transfer
CV	cyclic voltammetry
d	thickness
D_a	1,3,6,8-tetra[bis(p-anisyl)-amino]-4,5,9,10-tetra-methoxypyrene
D_b	1,3,6,8-tetra[bis(p-anisyl)-amino]pyrene
DCB	dichlorobenzene
DCM	dichloromethane
DH6T	α,ω-dihexylsexithiophene
DOS	density of states
EA	electron affinity
e	elementary charge
ε	extinction coefficient
E_B	binding energy
E_F	Fermi level
E_g	energy gap
E_{kin}	kinetic energy
E_{red}	reduction potential
EIB	electron injection barrier
EPR	electron paramagnetic resonance
ETL	electron transport layer
ETM	electron transport material
E_{vac}	vacuum level
F	Faraday's constant
F_1TCNQ	2-fluoro-7,7,8,8-tetracyanoquinodimethane
F_2TCNQ	2,5-difluoro-7,7,8,8-tetracyanoquinodimethane
F_4TCNQ	2,3,5,6-tetrafluoro-7,7,8,8-tetracyanoquinodimethane
Fc	ferrocene
FF	fill factor
FTIR	fourier-transform infrared spectroscopy
FTO	fluorine-doped tin oxide
FWHM	full width at half maximum
η_{MPP}	stabilized power conversion efficiency
HIB	hole injection barrier
HOMO	highest occupied molecular orbital
HV	high vacuum
IDT-BT	indacenodithiophene-co-benzothiadiazole
IE	ionization energy
IPES	inverse photoelectron spectroscopy
IR	infrared
IRAV	infrared active vibrations
ISC	inorganic semiconductor
I_{SC}	short-circuit current
IV	current-voltage

E_{ox}	oxidation potential
K	equilibrium constant
k_B	Boltzmann constant
KE	kinetic energy
LCAO	linear combination of atomic orbitals
LED	light emitting diode
LUMO	lowest unoccupied molecular orbital
μ	mobility
Mes_2B^+	dimesitylboronium
Mg	magnesium
Mono-UPS	monochromatized ultraviolet photoelectron spectroscopy
Mono-XPS	monochromatized X-ray photoelectron spectroscopy
N_i	molar number of species i
NIR	near infrared
MPP	maximum power point
OFET	organic field-effect transitor
OLED	organic light emitting diode
OPVC	organic photovoltaic cell
OSC	Organic semiconductor
P	probability of charge transfer
P3HT	poly(3-hexylthiophene-2,5-diyl)
PCE	power conversion efficiency
PDI	perylene diimide
PES	photoelectron spectroscopy
PFP	perfluoropentacene
PSC	perovskite solar cell
PTCBI	perylene-3,4:9,10-tetracarboxylic bis(benzimidazole)
PTCDA	perylene-3,4,9,10-tetracarboxylic
J_{SC}	short-circuit current density
QCM	quartz crystal microbalance
R	gas constant
RMS	root mean square
σ	conductivity
SAM	self-assembled monolayer
SCLC	space-charge-limited-current
SECO	secondary electron cutoff
SFM	scanning force microscopy
SNR	signal-to-noise ratio
T	temperature
TBABH	tetrabutylammonium borohydride
TCNQ	7,7,8,8-tetracyanoquino-dimethane
THF	tetrahydrofuran
UHV	ultrahigh vacuum
UPS	ultraviolet photoelectron spectroscopy
UV	ultraviolet
VB	valence band
Vis	visible
V_{OC}	open-circuit voltage
w	full width at half maximum
ϕ	work function
XPS	X-ray photoelectron spectroscopy
z_e	number of moles of transferred electrons
6T	sexithiophene
$[RhCp^*Cp]_2$	(pentamethylcyclopentad-enyl)(cyclopentadienyl) rhodium dimer
$[RuCp^*Mes]_2$	(pentamethylcyclopenta-dienyl)(1,3,5-trimethylben-zene) ruthenium dimer

1 INTRODUCTION

In today's world, semiconductors govern our daily lives as they are the fundamental building blocks of modern electronics. Although most electronic devices like processors in computers or smartphones, light-emitting diodes (LEDs) in displays, or photovoltaic cells are still mainly composed of inorganic semiconductors (ISCs) such as silicon, the field of organic semiconductors (OSCs) has gained increasing attention in the past decades leading to the development of many devices based on organic electronics. While the term organic semiconductors was first coined in the 1950s by Inokuchi in his work on polycyclic aromatic compounds, work on organic semiconductors already began in the early 1920s.[1,2] However, only with the work of Inokuchi it started to gain more attention and then became a boost in the late 1970s with the pioneering work of Heeger, MacDiarmid and Shirakawa on electrically conductive polymers.[3] In 2000, Heeger, MacDiarmid and Shirakawa were awarded the Nobel Prize in Chemistry for their pioneering work, which gave the research field an additional major boost.[4–6]

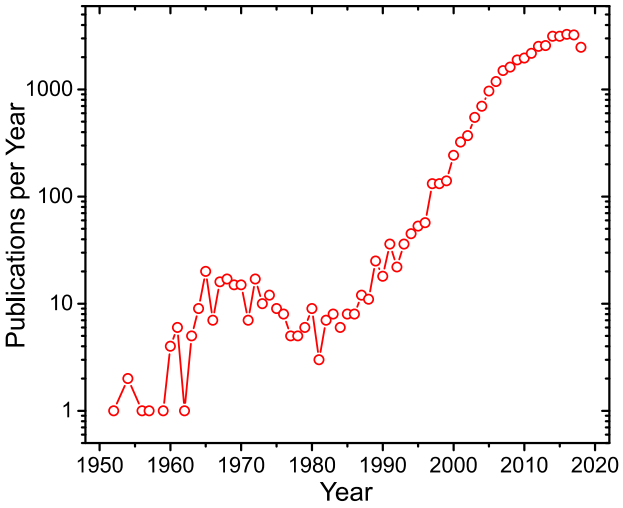

Figure 1.1 Development of the field of organic semiconductor research indicated by the number of annually publications related to relevant keywords based on the web of science database (Clarivate Analytics).[1]

The discovery and development of electrically conductive polymers has led to the development of organic electronic devices like organic light emitting diodes (OLEDs), organic field effect transistors (OFETs) and organic photovoltaic cells (OPVCs). Today, OLED technology has already become a multibillion euro business, where OLEDs are mainly employed in smartphone displays or TV screens.[7,8] OFETs, on the other hand, have so far not reached the performance required for broad application in daily-use devices. However, current research shows promising developments in this field and OFETs are expected to soon enter the market, for example in the form of printed electronics such as radio-frequency identification (RFID) chips in intelligent labels for consumer goods.[9–11] In the case of OPVCs, their research field has recently undergone dramatic changes with the

[1] The data was chosen to representatively show the development of the research field and most likely does not comprise all relevant publications. Related keywords included: "organic semiconductors", "organic electronics", "organic devices", "organic doping", "organic transistor", OFET, "organic light emitting diode", OLED, "organic photovoltaics", OPVC (data accessed on 2018-10-31).

development of a new generation of solar cells, the organic inorganic metal halide perovskite solar cells (PSCs). With this new kind of solar cells, power conversion efficiencies over 20% can be reached easily.[12] While the attention has shifted from organic semiconductors to perovskites as active materials, OSCs are still being employed in PSCs, e.g. as hole or electron transport layers.[13]

The success of OSCs stems from their many advantages over ISCs. Their mechanical flexibility and light weight make them attractive for mobile and wearable applications,[14,15] while easy-to-use solution based preparation methods like ink-jet or roll-to-roll printing offer low cost and large scale production possibilities.[10,16] Furthermore, the electronic and optical properties of OSCs can easily be tuned due to the high flexibility of chemical synthesis in developing derivatives of organic molecules and polymers. These properties make them suitable for mass production and a wide range of applications. Nonetheless, OSCs also show some disadvantages compared to ISCs. For example, organic electronic devices currently still exhibit lower efficiencies, device performances and also shorter lifetimes due to lower device stability compared to their inorganic counterparts. The main disadvantage, though, remains the very low charge carrier mobility due to the low orbital overlap between the weakly interacting molecules, and the generally low density of intrinsic charge carriers of OSCs, which leads to low conductivities of organic layers.[17] For this reason, OSCs (at least with current technologies) can never replace inorganic ones in regard to fast electronics like processors, but they are more than able to compete with their inorganic counterparts regarding the slow electronics mentioned above.

A strategy to overcome these deficiencies is the concept of doping. Here, impurities are purposely introduced into the semiconductor matrix enabling the control of type and density of charge carriers as well as the position of the Fermi level. For inorganic semiconductors, the concept of doping was a breakthrough allowing precise control of the transport properties and the creation of p-n-junctions, both of which led to improvement of the existing semiconductor technology as well as the development of new device concepts like the bipolar transistor. In a similar fashion, the concept of doping can also be applied to OSCs, which was investigated by researchers since the early days of organic electronics. At this time, known methods from doping ISCs were transferred to OSCs, which involved strongly oxidizing gases like iodine or bromine as well as small atoms like lithium or cesium and led to high conductivities of the doped organic materials.[3,18,19] However, due to the tendency of these small dopants to diffuse, both approaches suffer from devices instabilities.[20] In the past two decades, a more efficient and stable way to dope organic semiconductors was developed by the use of molecular dopants.[21–24] Here, doping is achieved by admixture of suitable molecules with a high electron affinity (or low ionization energy) to the host OSCs, which act as electron acceptors (or donors) with respect to the host. The use of molecular dopants was shown to lead to stable and efficient doping and

has been successfully employed to enhance the performance of OLEDs,[25,26] OPVCs,[27,28] and OFETs.[29–32]

Although the intensive research efforts during the past two decades have yielded a broad and profound understanding of the mechanisms involved in the molecular doping of OSCs, there are still many open questions remaining. In this thesis, a variety of topics related to the molecular doping of organic semiconductors is investigated ranging from i) the question which experimentally determined energy level values should be used to guide host-dopant selection, over ii) the n-doping of a p-type polymer, iii) the first indication of bipolaron formation in the polymer P3HT employing molecular dopants, and last but not least, iv) the application of with organometallic n-dopants modified electrode contacts in perovskite solar cells.

Topic i) compares the suitability of solid state ionization energies / electron affinities measured by (inverse) photoelectron spectroscopy (UPS/IPES) versus redox-potentials measured by cyclic voltammetry (CV) to predict ion pair formation yield for different sets of host/dopant material pairs. Since efficient doping of OSCs relies on identifying appropriate molecular dopants capable of ionizing the host molecules with a high yield, many researchers rely on comparing energy values measured by UPS/IPES to select matching host/dopant pairs.[33–39] Alternatively, energy values measured by CV can serve to guide the material selection, which, however, has only been done in comparably few studies.[40] Since both experimental approaches have their shortcomings in accounting for the actual physical environment of host/dopant ion pairs, it will be investigated which data-set is more practical to properly predict ion pair formation yield.

In topic ii), the n-type doping of a prototypical p-type co-polymer is investigated. Although organic semiconductors should in principal exhibit equal transport of p- and n-type charge carriers, there is usually a high asymmetry between electron and hole mobilities, where the hole mobility exceeds the electron mobility by several orders of magnitude.[41] This asymmetry was recently related to a universally present trap level due to oxygen/water complexes.[42] For this reason, suitable n-type polymers with high electron mobilities usually have electron affinities higher than the found trap level.[43–45] Here, it will be investigated if n-doping of a predominantly p-type co-polymer with a low electron affinity by using organometallic, dimeric n-dopants can effectively render the polymer n-type.

Topic iii) deals with the formation of bipolarons in the polymer P3HT, which thus far has never been achieved by molecular doping. The polaronic or bipolaronic character of charge carriers formed upon doping of conjugated polymers with a degenerate ground state has been a widely discussed topic throughout the past decades.[46–51] Today, it is commonly accepted that molecular doping of such polymers in general leads to the formation of polarons as charge carriers.[21,22,52,53] Furthermore, no direct evidence has been reported

so far for bipolaron formation to also occur during the molecular doping of the polymer P3HT. Here, the p-type doping of P3HT with a recently developed boron based organic salt is investigated, the strength of which is believed to exceed the ones of other typical molecular p-dopants. Strong evidence for bipolaron formation at high dopant concentrations above 10% will be presented.

In topic iv), the modification of electron-selective contacts in PSCs by insertion of a dopant interlayer between electrode and electron-transporting layer (ETL) is investigated. While organic transport layers have been used early on in the development of PSCs,[13] they are currently mostly employed in hole transport layers. In ETLs, commonly metal oxides such as TiO_2 are employed,[12,54,55] which, however, were shown to be unstable under UV irradiation and, thus, lead to short device lifetimes.[56,57] An alternative approach is to use organic ETLs like fullerene or perylene diimide (PDI) derivatives, which has been shown to reduce hysteresis in the current-voltage characteristics, leading to higher stabilized power outputs and thus increased lifetimes of the devices.[58–62] The goal of this study is to further minimize electron-collection losses at the interface of organic ETLs and the electron selective contact in PSCs. For this reason, an interlayer of an organometallic, dimeric n-dopant is introduced between electrode and ETL in order to form an Ohmic contact. Furthermore, a fullerene and a PDI derivative are compared for their efficient use as ETLs in PSCs.

This thesis is structured as follows. First, the fundamental principles of organic semiconductors as well as the doping of OSCs required to understand the body of this work will be introduced in chapter 2. This chapter will focus on the electronic and optical properties going from single molecules to molecular and polymeric solids, as well as charge transport in organic solids and the energy level alignment at interfaces. Furthermore, the basic models of molecular doping and different concepts of p- and n-type doping will be presented. This is followed by a description of the theory of the used experimental methods in chapter 3, which mainly focuses on the primarily used techniques of (inverse) photoelectron spectroscopy as well as optical absorption spectroscopy. In chapter 4, the organic materials used in this work will be introduced as well as the details of the sample preparation methods, the used experimental setups, and data analysis methods. The results of the above described topics i)-iv) will be presented and discussed each for itself in chapters 5-8, respectively. Finally, the work will close with a conclusion and outlook.

2 FUNDAMENTALS

In this chapter the fundamental principles of organic semiconductors and doping of such are introduced. In recent years, a number of textbooks and multi-author volumes were published, describing very well the various aspects of organic semiconductors and their application in devices.[17,63–67] Based on this textbook literature and also more recent experimental and theoretical studies, I want to introduce the most important aspects necessary to understand the work presented in this thesis. Therefore, first an overview of the electronic and optical properties of organic semiconductors is given, followed by a description of the processes happening during charge transport and energy level alignment at interfaces, and brief sketch of the theory of film formation. Finally, a short description of organic electronic devices will be provided. In the second part, the principles and models of doping of organic semiconductors with molecular dopants will be discussed.

2.1 ORGANIC SEMICONDUCTORS

Organic semiconductors are hydrocarbon based compounds with semiconducting properties. They are sub-grouped into two classes: small molecules with a low molecular weight (typically thermally evaporated in vacuum) and polymers (only processable from solution). While organic semiconductors are mainly comprised by carbon, they usually also contain heteroatoms like oxygen, sulfur, nitrogen, phosphorus, or fluorine. Still, the main characteristic of organic semiconductors is their conjugated π-electron system stemming from sp^2-hybridized carbon atoms. This conjugated π-system is responsible for the characteristic electronic and optical behavior, which renders them of high interest for opto-electronic applications. Since small molecules and polymers show in principal the same behavior, this section will focus mainly on molecules, whereas polymers will be explained separately, if specific differences exist.

2.1.1 Electronic Structure

Molecular Orbitals

The electronic structure of organic semiconductors is dominated by their conjugated π-system formed by sp^2-hybridized carbon atoms. The electron configuration of atomic carbon in its ground state is $(1s)^2(2s)^2(2p)^2$. For covalent bonds, however, it is energetically favorable, if the involved atomic orbitals of the valence electrons are hybridized. In this context, hybridization refers to a linear combination of the 2s- with the 2p-orbitals, where the 2s-orbital can be combined with one, two or all three of the 2p-oribtals, accordingly referred to as sp-, sp^2- and sp^3-hybridization. Out of these three, the sp^2-hybridization is

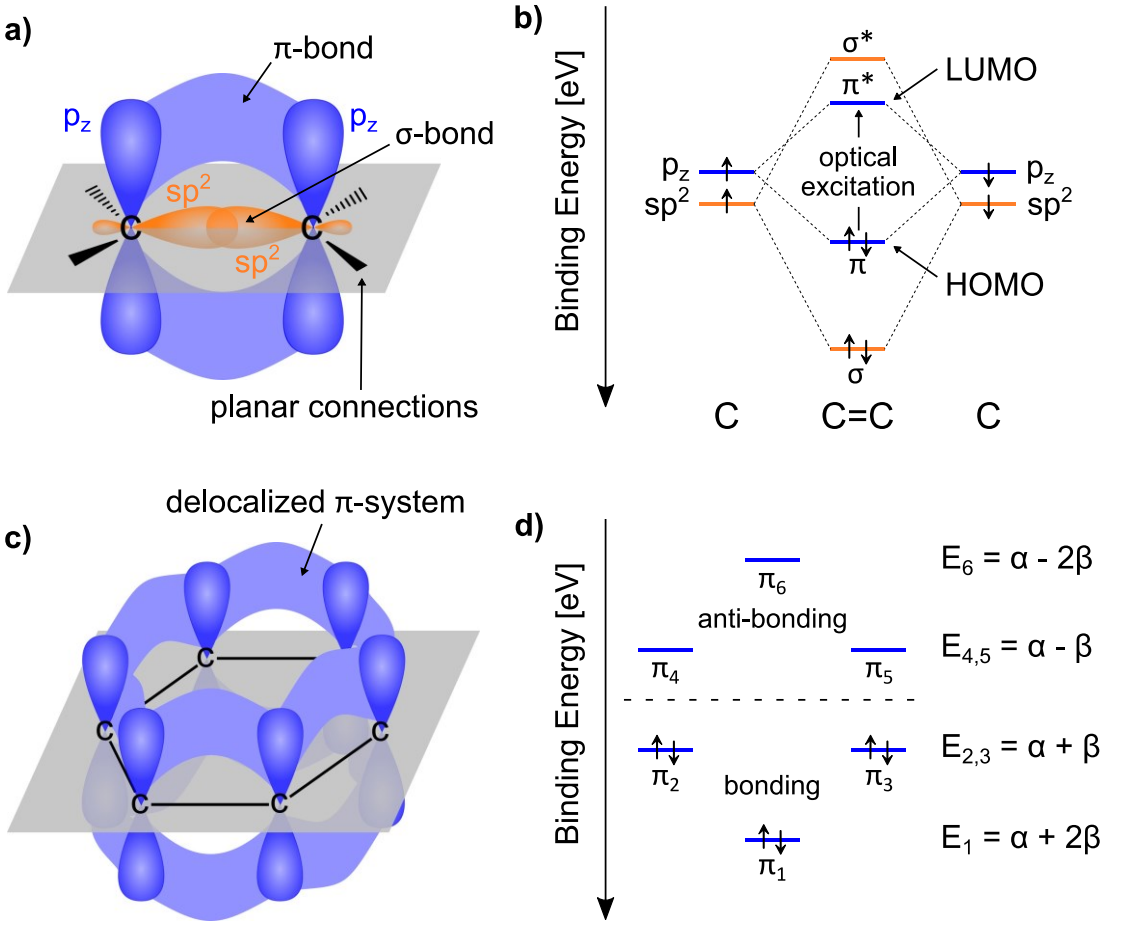

Figure 2.1 a) Scheme of a covalent double bond between two sp^2-hybridized carbon atoms. The sp^2-orbitals are lying in a plane (grey) and a covalent bond, the σ-bond, is formed between one of the sp^2-orbitals of each carbon. The p_z-orbitals are standing perpendicular to the plane and overlap above and below it, forming the π-bond. To maximize overlap, the p_z-orbitals are aligned in parallel, which forces all sp^2-orbitals to lie in a plane. Further covalent bonds to other atoms occur via planar connection to the free sp^2-orbitals. **b)** Formed energy levels of the double bond (here for ethene). Due to the different overlap of the sp^2- and p_z-orbitals, the energy splitting between the bonding σ-orbital and anti-boding σ*-orbital is much stronger than the splitting between the bonding π-orbital and anti-bonding π*-orbital. The π-orbital denotes the highest occupied molecular orbital (HOMO) and the π*-orbital the lowest unoccupied molecular orbital (LUMO). Optical transitions between HOMO and LUMO are possible without breaking the molecule. **c)** Scheme of molecular bonding in benzene. Here, again all the σ-bonds lie in a plane (grey), while the perpendicular p_z-orbitals are overlapping above and below the plane and form a π-system completely delocalized over the whole ring. **d)** Energy levels of benzene as calculated by the Hückel-method. Here, HOMO and LUMO are two-fold degenerate states.

crucial for the formation of conjugated π-systems. In the sp^2-hybridization, the 2s-orbital is mixed with two of the p-orbitals (usually referred to as p_x and p_y) forming three degenerate sp^2-orbitals with one p-orbital (p_z) remaining, schematically shown in Figure 2.1. The three sp^2-orbitals are oriented in-plane at 120° relative to each other with the remaining p-orbital standing perpendicular to the plane. In a double bond formed by two sp^2-hybridized carbon atoms, a covalent bond is formed in the sp^2-hybrid's plane by one of the sp^2-orbitals of each atom, which is called the σ-bond. In addition, the two perpendicular standing p-orbitals

overlap above and below the plane forming another covalent bond, the so-called π-bond. The π-orbital is delocalized across the σ-bond above and below the sp^2-plane, which is a nodal plane for the π-bond. Thus the contribution of the π-electrons to the bonding of the molecule is small.

This description of σ- and π-bonds is based on the LCAO method (linear combination of atomic orbitals), where the molecular orbitals are approximated by a linear combination of the involved atomic orbitals. The main assumption of LCAO is that the number of molecular orbitals and the sum of all involved atomic orbitals are the same. Thus, the wavefunctions of the molecular orbitals ψ_j can be constructed from the wavefunctions of the atomic orbitals ϕ_i by linear combination

$$\psi_j = \sum c_{ij}\phi_i \,. \tag{2.1}$$

The corresponding coefficients c_{ij} are determined by minimizing the total energy of the system (e.g. by the Hartree-Fock method)[68] and using the wavefunctions ψ_j, the energy levels E_j of the molecule can be calculated by

$$E_j = \frac{\langle \psi_j | \hat{\boldsymbol{H}} | \psi_j \rangle}{\langle \psi_j | \psi_j \rangle}, \tag{2.2}$$

where $\hat{\boldsymbol{H}}$ denotes the Hamiltonian of the system. The energy levels of the σ- and π-orbitals in Ethen are qualitatively sketched in Figure 2.1 b). Here, the energy levels of the sp^2-orbitals (p_z-orbitals) split up into the bonding and antibonding σ- and σ*-levels (π and π*), respectively. Here, the π-orbital constitutes the highest occupied molecular orbital (HOMO), and the π*-orbital the lowest unoccupied molecular orbital (LUMO).

In compounds with alternating single and double bonds, the p_z-orbitals of the involved σ-bonded carbon atoms are overlapping and can therefore form a conjugated system, where the π-electrons are delocalized throughout the whole system. The classic example for a conjugated π-system is benzene depicted in Figure 2.1 c). Here, each p-orbital contributes one electron, thus leading to six π-electrons, which are delocalized throughout the whole ring. Many organic semiconductors contain benzene rings as well as five-membered rings.

An analytical approach to calculate the energy levels of the π-system of benzene (and other organic molecules, where the valence electrons stem from the π-system) is the Hückel method, which is based on the LCAO approach.[69] Following the variation principle (Rayleigh-Ritz method), minimization of the total energy of the system can be performed by minimizing the energy eigenvalues (equation (2.2)) with respect to the coefficients c_{ij},

$$\frac{\partial}{\partial c_{ij}} \langle \psi_j | \hat{\boldsymbol{H}} | \psi_j \rangle = 0 \,. \tag{2.3}$$

By inserting equation (2.1) in (2.3), one obtains a set of linear equations, which only have a non-trivial solution, if

$$\left|H_{\mathrm{ij}} - ES_{\mathrm{ij}}\right| = 0\,, \tag{2.4}$$

where $H_{\mathrm{ii}} = \langle\phi_{\mathrm{i}}|\widehat{\boldsymbol{H}}|\phi_{\mathrm{i}}\rangle$ is the Coulomb integral, $H_{\mathrm{ij}} = \langle\phi_{\mathrm{i}}|\widehat{\boldsymbol{H}}|\phi_{\mathrm{j}}\rangle$ is the resonance integral (for $\mathrm{i} \neq \mathrm{j}$), and $S_{\mathrm{ij}} = \langle\phi_{\mathrm{i}}|\phi_{\mathrm{j}}\rangle$ is the overlap integral. In the Hückel method, the problem is simplified by treating the π-orbitals separately from the σ-orbitals and by only considering interactions between the p_z-orbitals of neighboring Carbon atoms of the π-system. Here, the Coulomb integrals are set to be equal, hence $H_{\mathrm{ii}} = \alpha$, resonance integrals are only considered from neighboring atoms, $H_{\mathrm{ij}} = \beta$, and overlap of the wavefunctions of different atoms is neglected, $S_{\mathrm{ij}} = \delta_{\mathrm{ij}}$. With these approximations, equation (2.4) can be expressed as a polynomial equation on the order of the number of involved Carbon atoms, which can be analytically solved. Figure 2.1 d) shows the calculated energy levels of benzene, where the HOMO and LUMO levels are degenerate states.

Frontier Orbitals

HOMO and LUMO of a π-system are the so-called frontier orbitals and play a critical role in optical and electronic processes. The energy difference between them is called the energy gap, in analogy to inorganic semiconductors. However, here, the energy gap is an intrinsic property of the molecule itself, unlike the band gap in an inorganic semiconductor, which is a property of the crystal. Due to the weak bonding of the π-electrons the energy gap of typical organic semiconductors lies in the visible or near ultraviolet spectral region (ca. 1.5 eV to 3.0 eV), rendering organic semiconductors suitable for optoelectronic devices. As can be seen from the energy level diagram in Figure 2.1 b), optical excitations from the bonding π- to the antibonding π*-orbital are possible without breaking up the molecule.

The position of HOMO and LUMO as well as the size of the energy gap depend on both the length of the conjugated system and the influence of functional side groups. For this reason, organic chemistry has the possibility to tailor the optical and electronic properties of organic semiconductors to specific needs. By increasing the size of the π-system, the energy gap of the molecule gets lowered. This is nicely illustrated by the acene series (benzene to pentacene) depicted in Figure 2.2 a), where each additionally attached benzene ring lowers the energy gap.[70] Electron-donating (phenyl-, amine-groups, etc.) or electron-withdrawing substituents (halides, nitro-groups, etc.) can raise or lower the energies of HOMO and LUMO relative to the unsubstituted system, respectively.[71] This is illustrated in Figure 2.2 b) for the fully fluorinated pentacene. Here, HOMO and LUMO of perfluoropentacene are energetically lowered by more than 1 eV with respect to

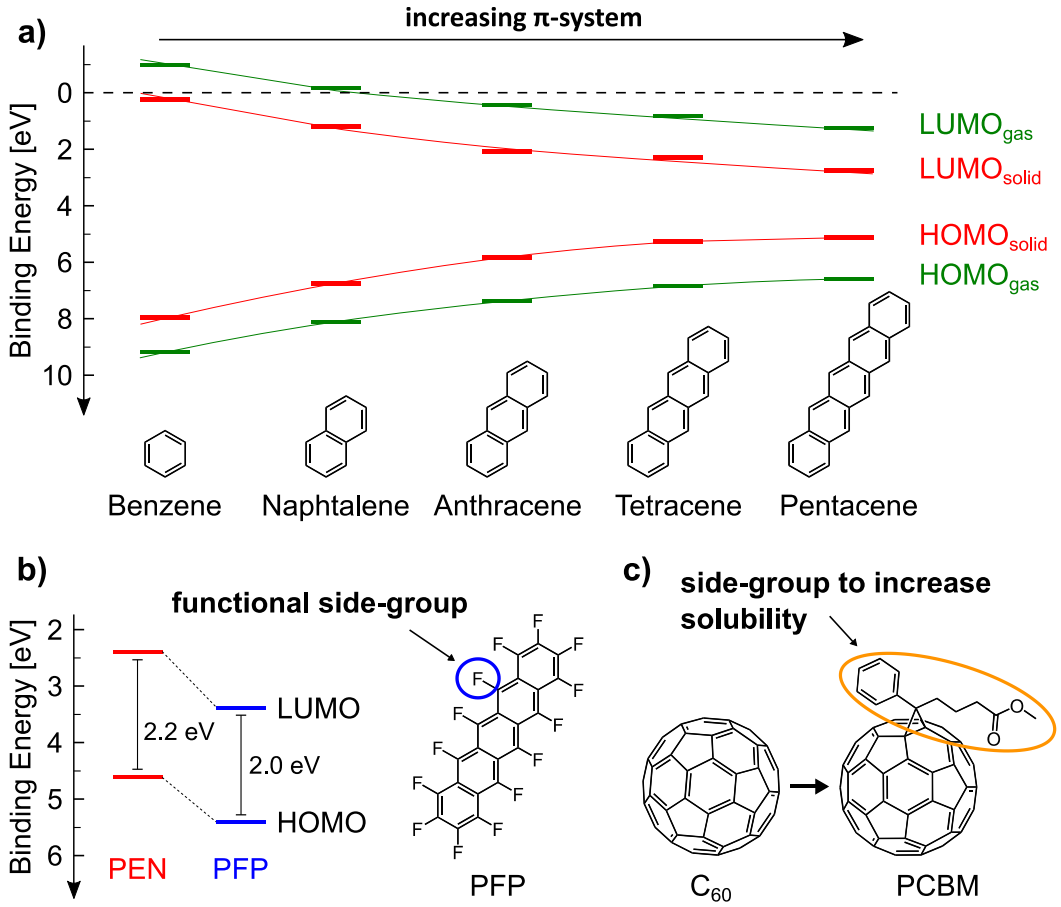

Figure 2.2 a) HOMO – LUMO energy levels of the acene series benzene to pentacene. Increasing the π-system leads to a narrowing of the energy gap and accordingly a red-shift of the optical absorption. Additionally, due to polarizations in thin films, the energy gap of molecules in a solid (red) decreases compared to the one of the molecules in gas phase (green). **b)** Energy levels of pentacene (PEN) and perfluoropentacene (PFP). Substitution of functional side-groups (here fluorination) leads to shift of HOMO and LUMO, while the energy gap is nearly retained. **c)** Additional side-groups can be added to increase parameters like packing or solubility. In the case of PCBM, the substituted side-group leads to a higher solubility, while simultaneously retaining the electron accepting character of fullerene. Data for a) was taken from ref. [70] and b) from ref. [72].

pentacene, while the energy gap and its optical properties[2] are nearly fully retained.[72] Additionally, side-groups (alkyl chains, etc.) can be used to change properties like solubility or the packing structure in solids, while leaving the electronic and optical properties nearly unchanged. For example, such a side-group is used for the fullerene derivative PCBM[3] [depicted in Figure 2.2 c)] to highly increase its solubility compared to unmodified fullerene while preserving its electron accepting character.[73] Due to this high flexibility in synthesis, organic semiconductors combine the mechanical and chemical benefits of organic compounds with the electronic advantages of semiconductors.

[2] The optical gap is lowered by ca. 200 meV, while the vibronic structure is nearly the same as evidenced by optical absorption spectroscopy (see also section 5.3).
[3] [6,6]-phenyl-C_{61}-butyric acid methyl ester.

Conjugated Polymers

Conjugated polymers represent quasi one dimensional systems, where the overlap of p_z-orbitals along the backbone of the chain leads to a formation of a one dimensional band structure along the chain. Here, in accordance with inorganic semiconductors, the highest filled band is called the valence band (VB) and the lowest unfilled band the conduction band (CB). There is a difference, however, between polymers with a degenerate and polymers with a non-degenerate ground state. In polymers with a degenerate ground-state like trans-polyacetylene, there exist two energetically and structurally equal lattice relaxations [as depicted in Figure 2.3 a)], since an interchange of single and double bonds reproduces the same geometry. As a consequence, the formed π-band would only be half-filled and such polymers would thus be one dimensional metals. However, due to an instability of the system against lattice vibrations, the structure becomes distorted, which is named Peierls' distortion, and now has alternating longer and smaller bonds. The Peierls' distortion leads to a splitting of the π-band into two sub-bands, one completely occupied (VB) and one completely unoccupied (CB) with an energy gap between them. In the case of polymers with a non-degenerate ground state like polythiophene, a change of single and double bonds does not reproduce the same geometry [as depicted in Figure 2.3 b)], but rather a

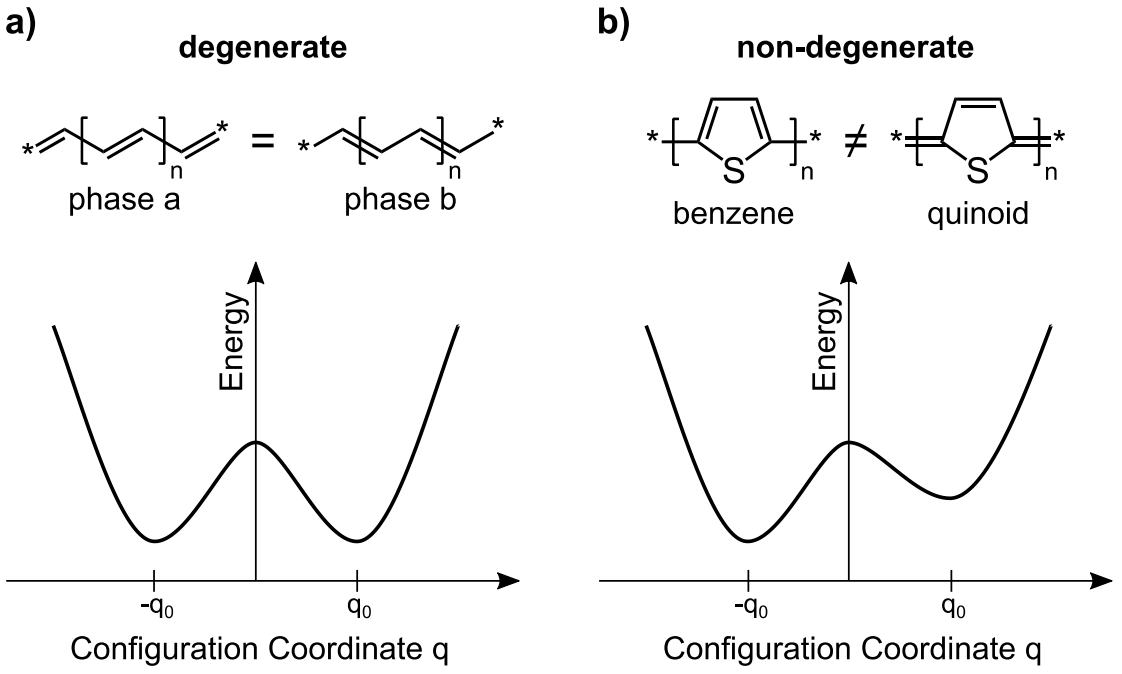

Figure 2.3 a) Polymers like trans-polyacetylene have a degenerate ground-state, since the exchange of single and double bonds yields the same energy geometry. This is shown by the adiabatic potential as function of a dimensionless lattice distortion (configuration coordinate). Here, phase a and phase b (representing the resonance structures) are having the same energetic minimum. **b)** In contrast, polymers like polythiophene have a non-degenerate ground-state, since an exchange of single and double bonds does not yield the same geometry. In this case, it rather yields a higher energetic structure, called quinoid structure. The adiabatic potential shows the quinoid structure to have a higher energetic minimum than the benzene ground-state. Thus, the quinoid structure represents the first excited state. Inspired by ref. [47] and ref. [74].

structure with a higher-energy geometry. The structure of the ground-state in Figure 2.3 b) is termed aromatic, while the structure of the excited state is termed quinoid. The electronic structure of conjugated polymers can be described by the Su-Schrieffer-Heeger (SSH) model.[66,74] However, due to several short-comings of this model – the main one being the underestimation of Coulomb interactions – the model will not be discussed further at this point and the reader is referred to the respective literature.

From Molecule to Solid

In organic molecular or polymeric solids, molecules or polymer chains are bound by weak van-der-Waals forces in contrast to inorganic materials, where atoms form strong covalent or metallic bonds.[4] Van-der-Waals forces are attractive forces between neutral molecules, which arise from weak electrical dipoles induced by fluctuating dipole moments due to temporal fluctuations in the charge distribution of the (neutral) molecules. These forces are very short range and thus comparably weak. In addition to the attractive van-der-Waals forces, there are also repulsive forces due to Coulomb repulsion and the Pauli exclusion principle of electrons, which prevent a collapse of the molecules. The potential in molecular solids can be described by the empirical Lennard-Jones potential $V(r)$ in dependence of the distance between the molecules r,

$$V(r) = V_0 \left[\left(\frac{r_0}{r} \right)^{12} - 2 \left(\frac{r_0}{r} \right)^{6} \right], \tag{2.5}$$

where r_0 is the distance at which the potential has its minimum and V_0 is the minimum potential. The first term in this equation describes the Pauli and Coulomb repulsion, while the second one accounts for the attractive van-der-Waals forces. Consequently, there is normally no formation of electronic bands in solids consisting of organic semiconductors (apart from organic single crystals), but rather narrow localized molecular energy levels.

The transition from isolated molecules to a molecular solid is illustrated in Figure 2.4, represented by potential wells for the electrons.[5] Figure 2.4 a) shows the effective potential well of a polyatomic molecule. The potential wells of the atom nuclei and electrons are merged in the upper part, forming the delocalized molecular orbitals described previously. The deep atomic levels stay localized in the atomic potential wells. The top of the potential well is the vacuum level E_{vac} beyond which the electron can escape the molecule.[6] In a molecular solid, the potential wells of the isolated molecules are joint [Figure 2.4 b)], but the highest occupied states (valence states or bands) and lowest unoccupied states

[4] In covalent bonds, electrons are shared between neighboring atoms, while in metals, the conducting electrons are delocalized throughout the lattice of positively charged metal ions, holding the crystal together.
[5] The same model similarly applies for single polymer chains and polymeric solids, where the energy levels just have to be replaced by bands, thus HOMO → VB and LUMO → CB.
[6] A more detailed definition of the vacuum level can be found in refs. [75,218].

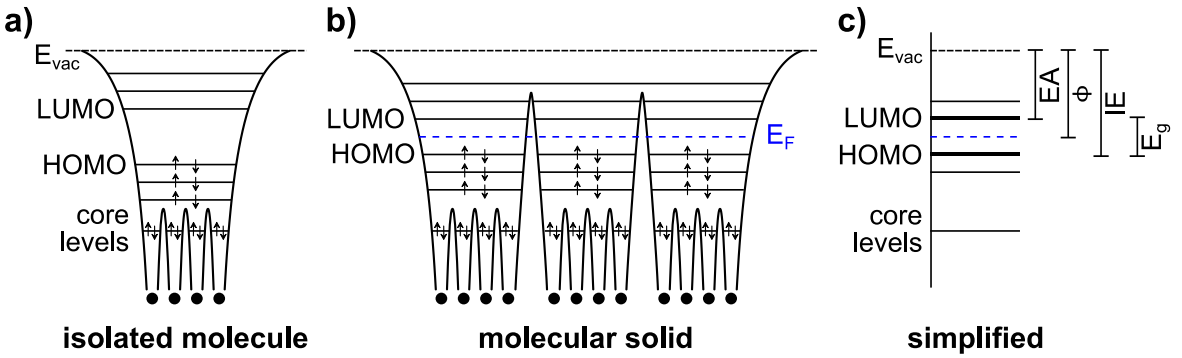

Figure 2.4 a) Electronic structure of an isolated molecule. While the deep atomic levels stay localized in the atomic potential wells, the ones in the upper part are merged forming the delocalized molecular orbitals. The top of the potential well is represented by the vacuum level E_{vac}. **b)** In a molecular solid (here shown for a non-crystalline solid, i.e. without band formation), the potential wells of the isolated molecules join. However, the highest occupied states and lowest unoccupied states (HOMO and LUMO) are usually still localized on each molecule. HOMO and LUMO are shifted upwards and downwards, respectively, compared to the levels in gas phase due to electronic polarizations. **c)** Simplified energy level diagram, where the electron affinity (EA), work function (Φ), ionization energy (IE), and energy gap (E_g) are defined as energetic distances between the respective levels. Inspired by ref. [75].

(conduction states or bands) are usually localized on each molecule.[7] The highest valence states and the lowest conduction states are also denoted as HOMO and LUMO, respectively, reflecting that the electronic structure of the molecular solid mainly preserves the one of the isolated molecule. Due to electronic polarizations in the molecules surrounding the ionized molecule (explained later in detail), the ionization energy of a molecular solid is lowered and its electron affinity raised compared to the molecules in the gas phase. This difference between gas and condensed phase is depicted in Figure 2.2 a) for the acene series. Here, it can be seen that although the polarizations are in the order of a few eV, the electronic structure of the isolated molecule is mainly preserved in the solid.

Figure 2.4 c) shows the energy level diagram, which is usually drawn for the electronic structure of a molecular solid. Here, also the ionization energy (IE), electron affinity (EA), Fermi level (E_F) and work function (Φ) are depicted, which will be defined in the following.[8] IE is the energy needed to remove an electron from the HOMO of the molecule (creating a cation) and EA is the energy gained, when adding an electron (creating an anion). According to Koopman's theorem, IE can be defined as the energy difference between HOMO and E_{vac}, while EA as the energy difference between the LUMO and E_{vac}. However, this is formally not correct, since HOMO and LUMO are defined for the neutral ground state of the molecule, whereas IE and EA are the difference in total energy of a molecule between the N-electron ground state and the (N±1)-electron ionized state and thus describe the

[7] The exceptions are perfect single crystals, where the overlap of the frontier orbitals of neighboring molecules results in orbital-derived electronic bands similar to inorganic semiconductors.
[8] It has to be noted here, that, strictly speaking, the ionization energy, electron affinity and work function are only defined at the surface of a solid.

single particle levels. Nonetheless, due to a compensation of errors, this approximation holds for most cases and is widely used in literature.[76,77] The Fermi level of the system is defined by the Fermi-Dirac distribution $f(E)$, which determines the occupation probability of electronic states by electrons in a solid,

$$f(E) = \left(e^{\frac{E-\mu(T)}{k_B T}} + 1 \right)^{-1}, \tag{2.6}$$

where E is the energy of the electron, k_B is the Boltzmann constant, T the absolute temperature, and $\mu(T)$ the temperature-dependent chemical potential of the system. In solid-state physics, the chemical potential is referred to as Fermi level, $\mu(T) = E_F$, independent whether the material is a metal or semiconductor.[9] In a non-degenerate semiconductor, the Fermi level takes on a statistical value in the energy gap between the HOMO and LUMO, as there are generally no states, and therefore no electrons at the Fermi level. The work function of a material is defined as the energy difference between E_F and E_{vac} and, thus, can basically be seen as an energy barrier preventing an electron at the Fermi level from escaping the solid.

Structural and Energetic Disorder

In amorphous (and polycrystalline) molecular films, the structural disorder leads to an energetic disorder.[10] The commonly used Bässler model assumes the distribution of these localized electronic states – the density of states (DOS) – to be a Gaussian distribution, schematically depicted in Figure 2.5. Here, the HOMO level region of an amorphous film is shown, which consists of a collection of energetically distributed localized states. The transport of holes occurs via hopping between these states (see further discussion in section 2.1.3). A practical and widely used method to determine the onset of the occupied states (and with it also the IE) is to extrapolate the tangent of the HOMO feature to the zero-background line, as used for example when analyzing photoelectron spectroscopy data (see section 3.1). Some of the HOMO states, the so-called gap states, are also extending beyond the HOMO onset into

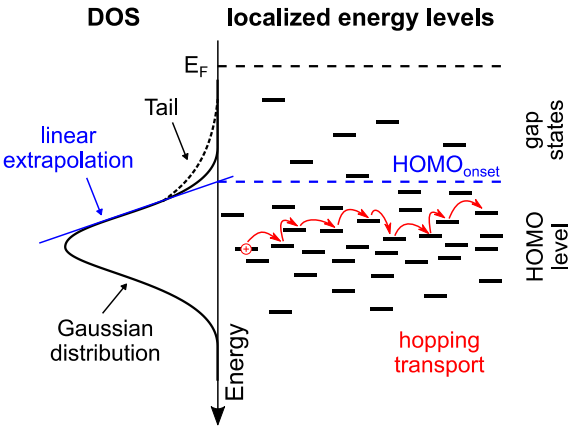

Figure 2.5 Schematic representation of energetic disorder in an amorphous film. The HOMO level consists of a collection of physically separated and energetically disordered localized states, which can be described by a Gaussian distribution. The transport of holes occurs via hopping between these states. Inspired by ref. [78].

[9] Care must be taken, not to confuse the terms "Fermi energy" and "Fermi level", as the Fermi energy is defined as the highest state occupied by electrons at absolute zero temperature.

[10] Energetic disorder can, however, also be induced by other effects like e.g. the occurrence of isomers.

the energy gap of the molecular solid. These gap states are crucial for charge transport (see subsection 2.1.3) and energy level alignment (see subsection 2.1.4). There are many physical origins for gap states like energetic disorder (as shown here), defects, or impurities. However, in most cases, it is sufficient to know that a finite density of states exists within the gap without regard to their physical origin.

In “real” polymers, chemical (e.g. side-groups at the wrong position) and morphological defects (e.g. twists and kinks) lead to an effective conjugation length of monomer units, with, in the best case, 10 to 20 conjugated monomer units. Since the effective conjugation length is a statistical quantity, the different lengths of the unperturbed segments in an amorphous polymer film also contribute to broadening of the bands. Thus, it is common practice to also model the VB and CB by a Gaussian envelope function.

Polarization Effects

A charge carrier localized on a molecule has several effects on its electronic structure, each causing different shifts of the energy levels (polarizations). When a molecule embedded in a solid film becomes ionized, it will introduce an electronic polarization in the surrounding molecules, which screen the charge and therefore stabilize the system. This is associated with an energy in the order of 1.0-1.5 eV.[79–81] Furthermore, it will lead to a reorganization of the nuclear core of the ionized molecule (ca. 100 meV) and a lattice relaxation of the neighborhood due to intermolecular phonon-coupling (ca. 10 meV).[81] The IE and EA of a molecular solid is thus related to the IE and EA of the molecule in the gas phase via

$$IE_{\mathrm{film}} = IE_{\mathrm{gas}} - P_{+} \quad \text{and} \quad EA_{\mathrm{film}} = EA_{\mathrm{gas}} + P_{-} \ , \tag{2.7}$$

where $P_{\pm}$ are polarization energies, which always have a positive value (in general $P_{+} = P_{-}$).

These relaxation processes are schematically visualized in Figure 2.6 and occurr on different timescales. Since electrons move fast compared to the atoms nuclei due to their large difference in mass, the electronic polarization is believed to set in rapidly on the order of 10^{-17}-10^{-16} s, whereas the nuclear reorganization is slower, in the order of 10^{-14} s, and the relaxation of the surrounding lattice matrix occurs on a time scale of ca. 10^{-12} s.[78] The relaxation times of the electronic, intramolecular and lattice polarizations are much faster than the hopping time (see subsection 2.1.3). A as a result of this, charges traveling through the material must be described as structurally and energetically relaxed positive (hole) or negative (electron) polarons rather than free charge carriers. Since the electronic polarization of the neighborhood follows the charge nearly instantaneously, it is also spatially limited to the near environment of each ionized molecule.

In ultraviolet photoelectron spectroscopy (UPS, see subsection 3.1.2), the emitted electron leaves the vicinity of the ionized molecule within 10^{-16}-10^{-15} s for typical used electron and

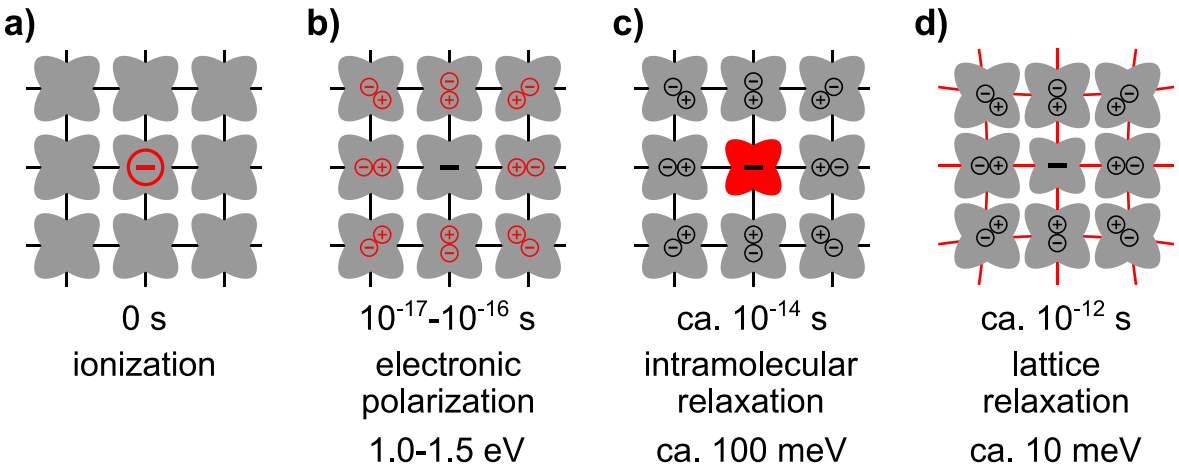

Figure 2.6 Schematic representation of polarization (relaxation) effects with associated energies and timescales. The highlighted parts in red illustrate each effect. **a)** A molecule embedded in a solid gets ionized. **b)** After 10^{-17}-10^{-16} s, the charge density in the adjacent molecules adapt to the ion, effectively screening the charge. **c)** The core of the ionized molecule relaxes in a timescale of ca. 10^{-14} s. **d)** Finally, after ca. 10^{-12} s, the lattice around the ionized molecule relaxes due to intermolecular phonon-coupling. Redrawn after ref. [82].

photon energies.[78] Considering the timescales of the polarization processes, the measured IE thus contains only the electronic polarization energy, but not the intramolecular and lattice relaxation energies. Similar considerations apply for the measurement of EA by inverse photoelectrons spectroscopy (IPES, see subsection 3.1.4). Thus, the measured IE (EA) in UPS (IPES) corresponds to that of a nearly fully relaxed positive (negative) polaron and the IE (EA) is accordingly over- (under-) estimated by around 100 meV. Organic semiconductors aretherefore often characterized in literature by a transport gap which overestimates the actual transport gap by a few 100 meV.

Additionally, since IE and EA are measured at the surface of a molecular solid, the polarization may differ from inside the bulk and surface dipoles (e.g., originating from intramolecular dipoles) contribute to the measured values.[83] Moreover, for molecular and polymeric solids, which are not perfectly amorphous, values of IE and EA depend strongly on the orientation of molecules with respect to the surface and inside the bulk. Collective electrostatic effects of the charge density distribution, including charge-permanent quadrupole interactions, are substantially modifying the energetic landscape, from molecular to macroscopic length scales.[84–87] In turn, values of IE and EA can differ for one material by more than 500 meV depending on sample structure. Including these solid-state effects, the solid-state IE/EA of a molecular thin film expressed in equation (2.7) has to be expanded to

$$IE_{\mathrm{film}} = IE_{\mathrm{gas}} - P_{+} - W_{+} \quad \text{and} \quad EA_{\mathrm{film}} = EA_{\mathrm{gas}} + P_{-} + W_{-}\,, \tag{2.8}$$

where $W_{\pm}$ includes orientation-dependent electrostatic effects as well as HOMO/LUMO

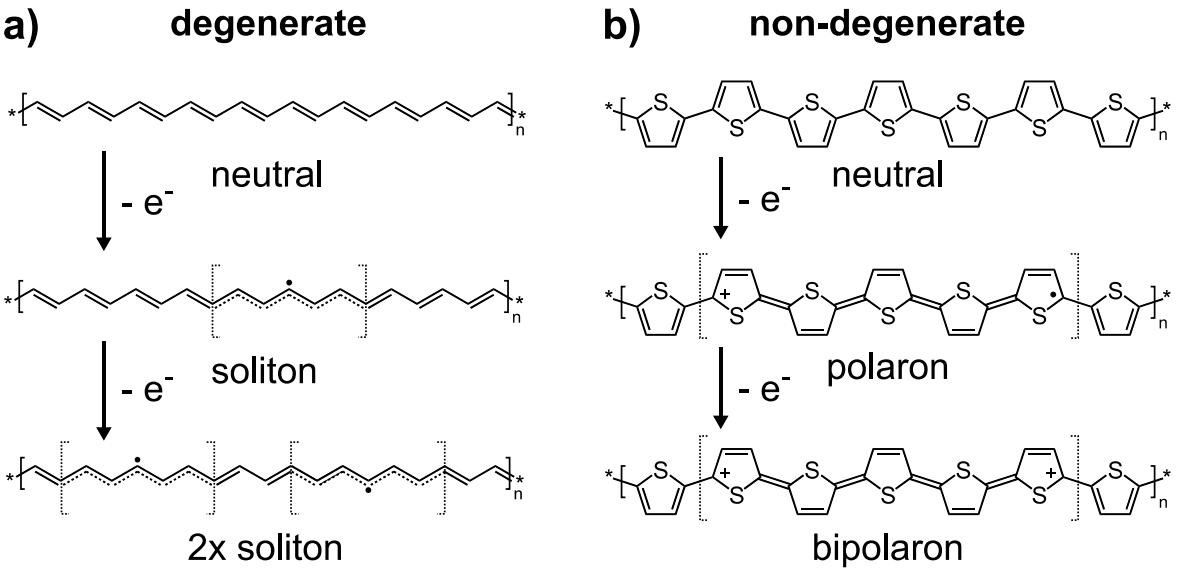

Figure 2.7 a) Soliton formation in a polymer with a degenerate ground-state. Upon extraction of an electron a neutral (or positively charged) soliton forms, which induces a structural relaxation on a segment of the polymer chain. Upon extraction of another electron, two solitons form, which can coexist in the vicinity of each other. **b)** Bi-/polaron formation in a polymer with a non-degenerate ground-state. Upon extraction of an electron, a positive polaron form, which induces a change from benzene to quinoid structure in a segment of usually 4-6 monomer units. Upon extraction of another electron, it is energetically more favorable to form a bipolaron, than to have two neighboring polarons. Note: the charge distribution is just drawn for illustrative purposes and does not actually reflect the real charge distribution of bi-/polarons.

band dispersion energies in case of crystalline materials and can accordingly have a positive or negative sign.[87]

In conjugated polymers, the introduction of charge carriers leads to different mechanisms than in molecules. Here, the added charge carrier is neither delocalized over the whole chain nor localized on a single monomer unit, but rather localized on a segment of the chain leading to structural distortions (relaxations) of that segment. There is again a difference between polymers with a degenerate and a non-degenerate ground state. In the case of trans- polyacetylene (degenerate ground state), introduction of a charge leads to the formation of a quasi-particle called soliton [see Figure 2.7 a)]. This soliton can be neutral as well as positively or negatively charged, and displays an unusual charge-spin relationship in the sense that the neutral soliton is a radical with an unpaired spin, whereas a charged soliton is spinless.[11] In the case of polymers with a non-degenerate ground-state like polythiophene, adding a charge leads to the formation of a polaron, which is also localized within a segment of the chain (usually around 4-6 units)[47] and leads to a change from aromatic to quinoid structure in this segment, as displayed in Figure 2.7 b). In contrast to solitons, where the addition of more charges leads to neighboring solitons, here, it is

[11] Since solitons are not relevant for this thesis, the reader is referred to the respective literature.[47,74]

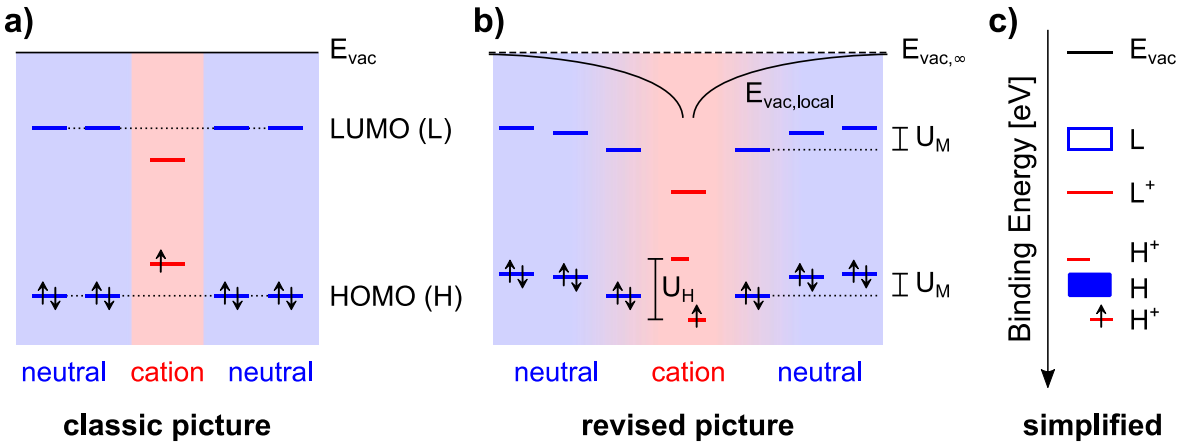

Figure 2.8 a) Classic representation of the electronic structure of a cation. Here, the half-filled HOMO is shifted upwards in the energy gap and the LUMO is parallel shifted downwards. **b)** Revised picture including Coulomb interactions. Due to Hubbard interactions (U_H) the HOMO level of the cation ion is split into a singly unoccupied level residing in the energy gap and a singly occupied level below the neutral HOMO level. Due to Mandelung interactions (U_M), the (neutral) levels of the molecules in the vicinity of the cation are shifted downwards. **c)** Revised, simplified energy level diagram of a cation and its surrounding neutral neighborhood. Redrawn after ref. [88].

energetically unfavorable to have neighboring polarons. Thus, at a certain concentration of added charges, the formation of doubly charged polarons – bipolarons – becomes energetically favorable. Since polarons are radicals, they have an unpaired spin, while bipolarons are spinless. For this reason, polarons can be detected by electron paramagnetic resonance (EPR) spectroscopy, while bipolarons cannot.[89–91]

Electronic Structure of Polarons

Following the concept of polarizations, the electronic structure of polarons[12] embedded in a neutral molecular (or polymeric) solid is commonly drawn in a classic picture[13] like depicted in Figure 2.8 a), which is also widely used to date.[47,92–95] The following description is based on a positive polaron, bearing in mind that completely analog shifts are occurring for a negative polaron. In the classical picture, polarization leads to a half occupied HOMO of the positively ionized molecule within the neutral matrix shifting the half occupied level upwards compared to the neutral level. In addition, the fully unoccupied LUMO is symmetrically shifted downwards with respect to the neutral level. However, recent experimental and theoretical studies have shown that Coulomb interactions of the polaron have to be considered, which changes the picture of energy levels drastically.[88,96,97] Here, on-site Coulomb interactions (Hubbard interactions) lead to a splitting of the HOMO into a singly occupied sublevel lying below and a singly unoccupied sublevel lying above the

[12] Which are induced by for example doping (see section 2.2) or by charge transfer from the substrate (see subsection 2.1.4).

[13] The classic picture was originally developed to explain the optical absorption spectra of polarons and bipolarons.[47,93]

neutral HOMO in energy, as shown in Figure 2.8 b). Furthermore, inter-site Coulomb interactions (Mandelung interactions) cause a distance dependent downward shift of the HOMO / LUMO levels of neutral molecules in the vicinity of the cation. The same argumentation applies for polarons in polymers, where local Coulomb repulsions lead to a local relaxation of the molecular geometry and with it to localized energy levels shifted into the energy gap of the polymer. At the same time, the VB and CB are locally bulging downwards (upwards) around the localized positively (negatively) charged level.[97] The widely established picture of polarons has thus to be replaced with one which involves Hubbard and Mandelung interactions and therefore more accurately models the electronic structure of ionized species.

2.1.2 Optical Properties

Electronic and Vibrational Structure

The optical properties of organic semiconductors are closely linked to their electronic structure. In addition to the electronic structure, molecules have a vibrational structure and rotational (and translational) fine structure, which stem from the movement of the atom nuclei with respect to each other (vibrations) and the rotation (and translation) of the nuclei, respectively. The total wavefunction ψ_{tot} of a molecular state can thus be described in the Born-Oppenheimer approximation[14] by the product of the single contributions,

$$\psi_{\mathrm{tot}} = \psi_{\mathrm{el}} \cdot \psi_{\mathrm{spin}} \cdot \psi_{\mathrm{vib}} \cdot \psi_{\mathrm{rot}} \ , \tag{2.9}$$

where ψ_{el} is the electronic, ψ_{spin} the spin, ψ_{vib} the vibrational, and ψ_{rot} the rotational wavefunction. The total energy E_{tot} of a molecular state is accordingly expressed as

$$E_{\mathrm{tot}} = \underset{\text{(1-5 eV)}}{E_{\mathrm{el}}} + \underset{\text{(10^{-1} eV)}}{E_{\mathrm{vib}}} + \underset{\text{(10^{-3} eV)}}{E_{\mathrm{rot}}} \ , \tag{2.10}$$

where the difference between the electronic states E_{el} is typically in the order of 1 to 5 eV, the difference between vibrational states E_{vib} in the order of 10^{-1} eV, and the difference between rotational states E_{rot} in the order of 10^{-3} eV.[15] Since the energetic difference in rotational states is very small compared to the one of the electronic and vibrational states and can also usually not be resolved with the experimental methods used in this thesis, it will be neglected in the following discussions.

[14] In the Born-Oppenheimer approximation, the wave-functions of the electrons and the nuclei can be described separately, since electrons move fast compared to the atoms nuclei due to their large difference in mass. Thus, electronic transitions occur with a fixed position of the nuclei.
[15] The spin energy is so small that it is usually omitted.

For low vibrational energies, the vibrations of the nuclei around their equilibrium position is approximated by a harmonic oscillator model with vibrational frequency ω. The vibrational energy is thus expressed as $E_{\mathrm{vib}} = \left(\nu + \frac{1}{2}\right)\hbar\omega$, where ν is the number of excited quanta and $\hbar$ the reduced Planck's constant. Since the difference in energy of the electronic states is an order of magnitude larger than the vibrational energies, each electronic state carries a manifold of vibrational sub-states. The potential energy curve of a molecule in its ground state and first excited state is shown in Figure 2.9 a) for a normal mode coordinate Q (with Q_0 being the equilibrium position of the ground state). The potential of the electronic states is of a similar form as the Morse potential (developed for a diatomic molecule), where, similarly to the Lennard-Jones potential, the potential for $Q < Q_0$ is governed by the Pauli exclusion principle. For $Q \approx Q_0$, the potential can be approximated by a harmonic oscillator, and for $Q > Q_0$, the potential converges to a constant energy (dissociation energy), since the molecule dissociates for $Q >> Q_0$. The energies, of the vibrational states can be drawn as straight lines within the potential of the electronic states.

Optical Transitions

Optical transitions take place between the ground and excited potential curve and, due to the Born-Oppenheimer approximation, occur always straight vertical between the potential curves, meaning at fixed nuclei positions (also called the Franck-Condon principle). Transitions due to absorption of photons with the respective energy occur from the vibrational ground state of the electronic ground state to the different excited vibrational states of the first excited electronic state, where there is an overlap of the wavefunctions. Since the excited vibrational states usually radiation-free relax very fast to their ground state, emission of a photon occurs by transition from the lowest vibrational state to the excited vibrational states of the electronic ground state (rule of Kasha). The resulting energetic shift between the maxima in the absorption and emission spectra is called the Stokes-shift.

According to Fermi's golden rule, the rate of a transition k_{if}, which is the number of transitions per second and thus proportional to the intensity of the transition, between an initial state ψ_i and a final state ψ_f depends only on the perturbing Hamiltonian $\widehat{\boldsymbol{H}}'$. For optical transitions, the perturbing Hamiltonian is the optical dipole moment operator $e\hat{\boldsymbol{r}}$ and the rate of the transition can thus be expressed as

$$k_{\mathrm{if}} = \frac{2\pi}{\hbar}\rho\left|\left\langle \psi_{\mathrm{el,f}} \cdot \psi_{\mathrm{spin,f}} \cdot \psi_{\mathrm{vib,f}} \middle| e\hat{\boldsymbol{r}} \middle| \psi_{\mathrm{el,i}} \cdot \psi_{\mathrm{spin,i}} \cdot \psi_{\mathrm{vib,i}} \right\rangle\right|^2, \tag{2.11}$$

where ρ is the density of the final states. Since the (electronic) dipole operator $e\hat{\boldsymbol{r}}$ only acts on the electronic wavefunction (ψ_{vib} is only a function of the position of the nuclei, not the electrons), equation (2.11) can also be written as

$$k_{\mathrm{if}} = \frac{2\pi}{\hbar}\rho\left|\langle\psi_{\mathrm{el,f}}|e\hat{\boldsymbol{r}}|\psi_{\mathrm{el,i}}\rangle\right|^2 \cdot \left|\langle\psi_{\mathrm{spin,f}}|\psi_{\mathrm{spin,i}}\rangle\right|^2 \cdot \left|\langle\psi_{\mathrm{vib,f}}|\psi_{\mathrm{vib,i}}\rangle\right|^2 . \qquad (2.12)$$

From this equation, it can be seen that an optical transition between two electronic states has a higher intensity, if there is a larger overlap between the vibronic wavefunctions. Additionally, a flip of the spin during the transition is forbidden. Thus, only transitions in between singlet states (total spin equals 0) or triplet states (total spin equals 1) are spin-allowed, whereas transitions between singlet and triplet states are spin-forbidden.[16]

Environmental Effects

The environment of a molecule (now called chromophore) has several effects on its photon absorption (and emission) spectrum. Figure 2.9 b) (top) schematically shows the line positions of a molecule in the gas phase (without interaction with other molecules) as obtained from the transitions between the potential curves in Figure 2.9 a). In (dilute) solutions, the interaction between the chromophore with the solvent molecules leads to an energetic shift of the spectrum as depicted in Figure 2.9 b) (middle), which is called solvatochromism, and an energetic broadening of each transition.[17] Here, the solvent molecules rearrange around the chromophore maximizing interaction (and interaction energy) in order to minimize the overall energy. This leads to bathochromic (red) or hypsochromic (blue) shifts of the absorption spectrum, which increase with increasing polarity of the solvent. Bathochromic shifts occur when the ground state of the chromophore is mostly non-polar, while the excited state ismore polar. Thus, the electric dipole moment for the excited state is larger than for the ground state, and the (polar) solvent molecules interact more strongly with the excited state than with the ground state. Following, the reduction of the potential energy of the excited is larger than the one of the ground state and, accordingly, the transition energy for absorption (and emission) is reduced. Vice versa, hypsochromic shifts occur for chromophores, where the ground state is more polar than the excited state. Since the excited states of organic molecules are usually more polar than the ground states, bathochromic shifts are usually observed for π-π* transitions.

In solids, the interaction between the chromophores (van-der-Waals forces) leads to a further, usually bathochromic shift of the absorption spectrum as shown in Figure 2.9 b) (bottom). This shift is stronger for stronger molecule-molecule interactions, thus organic crystals show a larger red-shift than amorphous films. While the spectra of highly ordered

[16] This is true for optical absorption. However, for compounds which include heavier atoms, there is the possibility of intersystem crossing between an excited singlet and triplet state, which can be followed by an emissive transition between the excited triplet state to the singlet ground state, known as phosphorescence. However, since emissive processes are not a part of this thesis, it will not be further discussed here, and the reader is referred to the respective literature.

[17] For sufficiently diluted solutions, chromophore-chromophore interactions can normally be neglected.

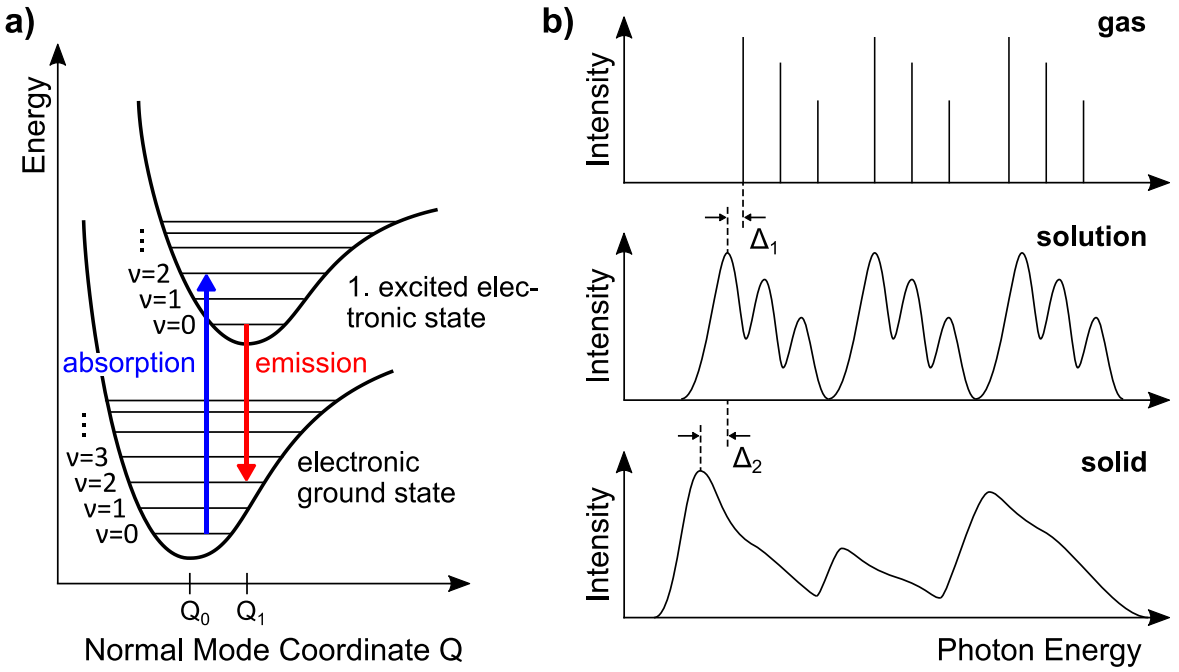

Figure 2.9 a) Electronic and vibronic structure of a molecule. Each electronic level carries a main-fold of vibronic sub-levels, which are represented by horizontal lines. The potential of the electronic levels can be represented by a Morse-like potential. Optical transitions between electronic states, always start at the lowest vibronic states and are represented by vertical arrows due to the Born-Oppenheimer approximation. Electrons in excited vibronic states relax to the respective ground-state radiation-free. **b)** Environmental effects on the absorption spectrum. The optical transitions of an isolated molecule in gas phase (top) are shifted (here to red) and broadened, once the molecule is dissolved due to solvation effects (middle). In a molecular solid (bottom), the positions of the transitions are further shifted, where the shift is stronger with larger molecule-molecule interaction. Additionally, the transitions are further broadened and due to possible structural orientation of the molecules in the solid, the relative intensities of the transitions are changed. Fig. b) inspired by ref. [17].

organic crystals (at low temperature) are usually less broad than the spectra of solutions, the spectra of structurally disordered solids become broader due to a distribution of the chromophore distances. Thus, at room temperature, the spectra of not perfectly crystalline solids are usually much broader than of solutions and are nearly (vibrational-) structure less.[18] As additional effect, the relative intensity of different transitions can change drastically compared to solution. While, in solution, the orientations of the chromophores (and thus the orientation of their optical dipole moments) are dispersed isotropically, they are (at least partially) oriented in a solid (except perfectly amorphous solids) and the intensity of some transitions increases, while others decrease.

In “real” polymers, the length of a chromophore is not identical with the chain length. As discussed in the previous subsection, the chromophore rather consists of an unperturbed segment of the chain with an effective conjugation length. This effective conjugation length of polymers can be determined by comparing the optical gap of the polymer with the

[18] Obviously, the broadening is a function of temperature and decreases with lower temperature.

optical gaps of oligomers with a different number of monomer units, where the optical gap becomes smaller with increasing oligomer size [compare Figure 2.2 a)].[98]

Excitons

Absorption of photons in organic semiconductors leads to the formation of quasiparticles called Frenkel excitons. In general, an exciton is a neutral quasiparticle consisting of an electron-hole pair bound by electrostatic Coulomb forces. Most relevant for semiconductors are Mott-Wannier excitons, Frenkel excitons, and charge transfer excitons, all schematically depicted in Figure 2.10 a). The excitons in inorganic semiconductors, which typically have large dielectric constants (in the order of 10), are called Mott-Wannier excitons. Here, the high dielectric constant leads to a screening of both charge carriers and therefore reduces the Coulomb interaction. For this reason, Mott-Wannier excitons are characterized by a low binding energy in the order of 10 meV and a radius much larger than the lattice spacing of the inorganic crystal. Organic semiconductors, on the other hand, have low dielectric constants (around 3) and, thus, an exciton in an organic semiconductors, the so-called Frenkel exciton, is located on one molecule and has a high binding energy in the order of 0.1-1 eV.[99,100] Due to their high binding energy, Frenkel excitons cannot be dissociated by thermal energy (approx. 25 meV at room temperature of around 300 K) and therefore a driving force is needed to generate free charge carriers. This is in contrast to inorganic semiconductors, where nearly every absorbed photon immediately generates free charge carriers. Additionally, the optical gap in organic semiconductors is unequal to the transport gap, which is again in contrast to inorganic semiconductors. There, this

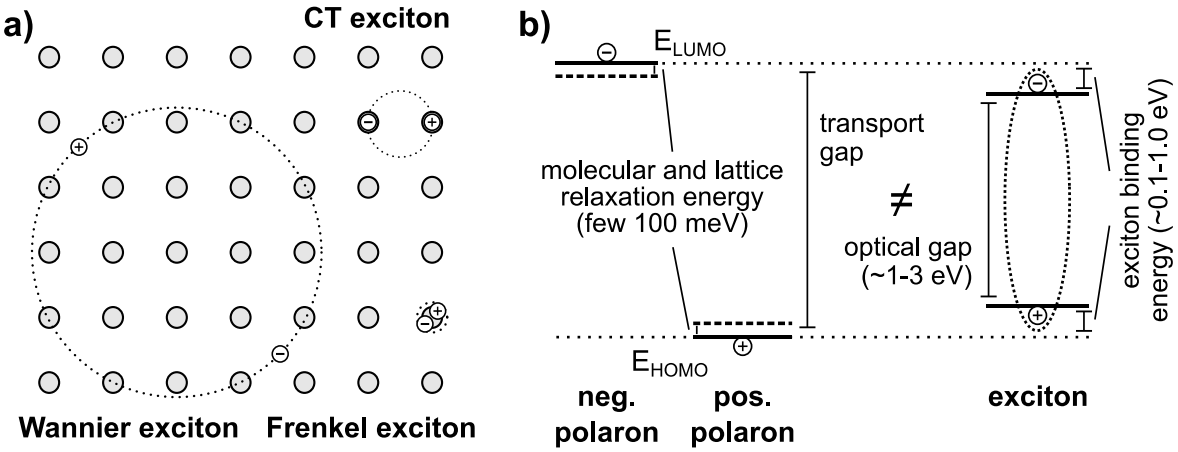

Figure 2.10 a) Schematic representation of different kinds of excitons. While Mott-Wannier excitons (inorganic semiconductors) have a low binding energy and thus a high radius, Frenkel excitons (organic semiconductors) are localized on one molecule and have a high binding energy. A second kind of excitons occurring in organic semiconductors, are charge transfer (CT) excitons, where the charges are localized on adjacent molecules. **b)** Level representation of the exciton binding energy. The transport gap is defined as the total energetic difference between two oppositely charged polarons (experimentally molecular and lattice relaxation energies are not included). The exciton binding energy is now defined as the energetic difference between the transport gap and the optical gap measured by optical absorption spectroscopy.

difference is much smaller and the optical gap can be considered equal to the transport gap for most purposes. The difference between optical gap and transport gap, which is defined as the difference in total energy between two polarons of opposite sign, is called the exciton binding energy, see Figure 2.10 b).[19] A second kind of exciton occuring in organic semiconductors, is the so-called charge transfer (CT) exciton, where the charges are located on adjacent molecules. Its binding energy and spatial extension lie in between the ones of the Mott-Wannier and Frenkel excitons. In contrast to those two, CT excitons have a static electric dipole moment. CT excitons are usually hard to observe due to their very weak absorption, but they play an important role in the photoconductivity of organic single crystals like for example anthracene.[101] The migration of excitons through the organic solid is dispersive and occurs via hopping. The mean free path of a Frenkel exciton, called the exciton diffusion length, is in the order of 3 nm to 30 nm.[102]

Optical Properties of Polarons

In the previous subsection, it was discussed how the electronic structure of a molecule (or polymer) is changed, once it becomes ionized (see Figure 2.8). Obviously, this also leads to changes in the optical transitions, which allows the identification of neutral and charged species by optical absorption spectroscopy (see section 3.2). In general, ionization leads to the emergence of new optical transitions in the optical gap of the neutral molecule. In the classic picture, the emergence of those sub-gap transitions of charged molecules and polymers was explained for polarons [Figure 2.11 a) – cation] by the upward shift of the singly occupied HOMO (in the case of a positive polaron) and the symmetrical downward shift of the LUMO. In the case of polymers, the localized levels of the distorted (relaxed) lattice around the charge are shifted in a similar manner. If a second electron is removed from (added to) the positive (negative) polaronic species, bipolarons form. Since the lattice relaxation around two charges is stronger than around simply one, the electronic states of bipolaron [Figure 2.11 b) – dication] are localized further away from the neutral levels. In this picture, there are four new transitions possible for polarons and two new transitions for bipolarons as depicted in Figure 2.11 a) and b), respectively. However, usually there are only two strong sub-gap transitions observed for polarons in molecules and polymers, and one sub-gap transition for bipolarons in molecules (which is usually energetically located in between the two sub-gap transitions of the polaron).[24,93,103–107] The fact, that nearly half of the in the classic picture theoretical possible transitions is usually not observed, has often been explained by those transitions having a very weak oscillator strength and thus to be commonly not observable.[105–107] The revised picture of the electronic structure of polarons in molecules, explained in detail in the last subsection, offers other possibilities for optical transitions in charged molecules.[88] However, no attempt has been made in this

[19] Note that, as explained earlier, the experimentally determined transport gap usually stated in literature is overestimated by a few 100 meV.

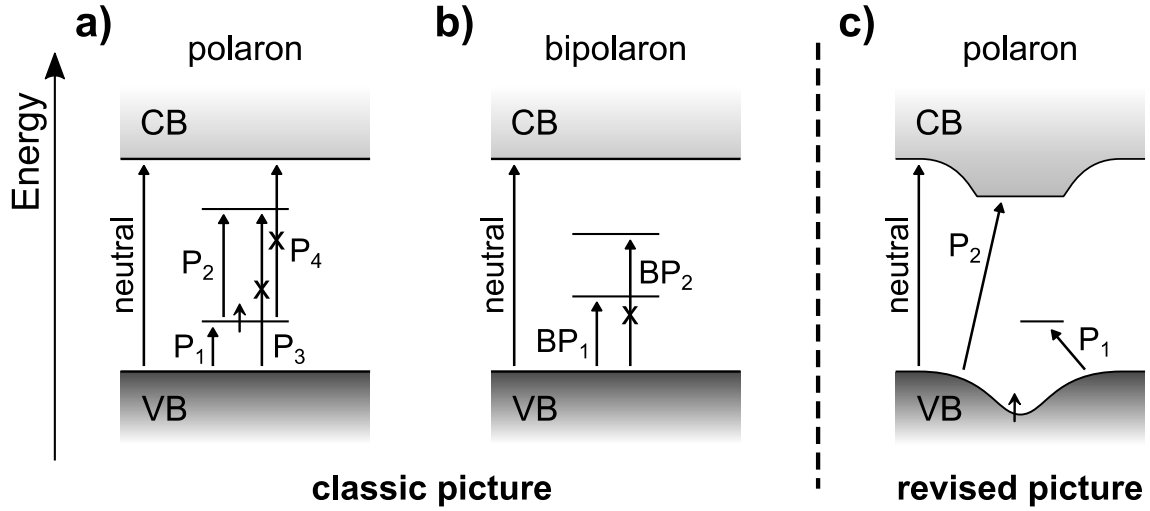

Figure 2.11 Classic and revised picture of optical transitions of bi-/polarons in polymers. **a)** For a polaron, two localized levels, one half occupied and one fully unoccupied, are created in the energy gap. Optical transitions P_1 to P_4 between the electronic states are possible. However, P_3 and P_4 were never experimentally observed and are expected to be symmetry forbidden. **b)** For a bipolaron, the former half-occupied level is now emptied and both unoccupied levels are shifted deeper into the gap. From the two possible optical transitions BP_1 and BP_2, only BP_1 is experimentally observed and the second one is again thought to be symmetry-forbidden. **c)** Revised picture including Coulomb interactions. The Coulomb interactions lead to a downward bulging of the VB and CB, with one electron residing at the bottom of the bulged down VB. Additionally, a singly local unoccupied level is created within the gap. The two transitions are both starting from the VB edge, with one ending in the localized gap-level, and the other in the locally bulged down CB. Redrawn from ref. [97].

study to assess the compatibility of the revised picture with the optical transitions measured by optical absorption spectroscopy. In the theoretical work of Heimel, optical transitions of polarons in polymers were investigated.[97] Here, it was shown that (for the case of a positive polaron) the two sub-gap transitions usually observed are both starting from the valence band edge and ending in the singly unoccupied intra-gap state for the lower energy transition P_1, and in the locally bulged down conduction band for the higher energy transition P_2, as depicted in Figure 2.11 c). Unfortunately, bipolarons were found to be not stable in the used theoretical model and thus no predictions could be made about optical transitions of bipolarons. These studies demonstrate that there is still more experimental and theoretical work needed to better understand the fundamental properties and behavior of polarons and bipolarons in organic molecules and polymers.

2.1.3 Charge Transport

Pure organic solids consisting of one kind of molecule or polymer chain are insulators at room temperature (and below), since the intrinsic density of thermally excited charge carriers in organic semiconductors at room temperature is typically very low compared to inorganic semiconductors. The intrinsic charge carrier density n of a semiconductor in general can be estimated using Boltzmann statistics by

$$n(T) = N_{\mathrm{eff}}\, e^{-\frac{E_{\mathrm{g}}}{2k_{\mathrm{B}}T}} \ , \tag{2.13}$$

where N_{eff} is the effective density of states, E_{g} the energy gap of the semiconductor, k_{B} the Boltzmann's constant and T the absolute temperature. Using the typical molecular density of 10^{21} cm^{-3} as N_{eff} and a typical energy gap for organic semiconductors of 2 eV to 3 eV, the intrinsic charge carrier density at room temperature ($k_{\mathrm{B}}T$ is ca. 25 meV) can be estimated to be in the range of 10^{-5} cm^{-3} to 10^{3} cm^{-3}. This is much lower than for inorganic semiconductors like silicon or germanium, where its value lies at 10^{10} cm^{-3} to 10^{13} cm^{-3}.[66] The conductivity of organic semiconductors is therefore extrinsic, which means that the charge carrier density has to be increased by either injecting charges from electrodes, dissociation of photo-induced excitons, or (unintentional) doping (see section 2.2).

Charge Injection

Charge injection occurs at electrode interfaces, where the energy levels of the electrode and the organic semiconductor align (for further discussion see next sub-section). Electrodes usually consist of metals, metal oxides or degenerate semiconductors.[20] The energetic difference between the Fermi level E_F of the electrode and the HOMO onset is called the hole injection barrier (HIB), while the difference between E_F and the LUMO onset is called the electron injection barrier (EIB), as schematically shown in Figure 2.13 a). When the injection barriers are low and thus the flow of current is limited the organic semiconductor itself and not by the contacts, this contact is called Ohmic.[108],[21] As can be easily seen from Figure 2.13 a), an Ohmic contact can either be hole or electron selective. In contrast, when the injection barriers are high, thus providing additional electric resistance, the current is mainly limited by the contacts and not the organic semiconductor, which is referred to as contact- or injection-limited current.

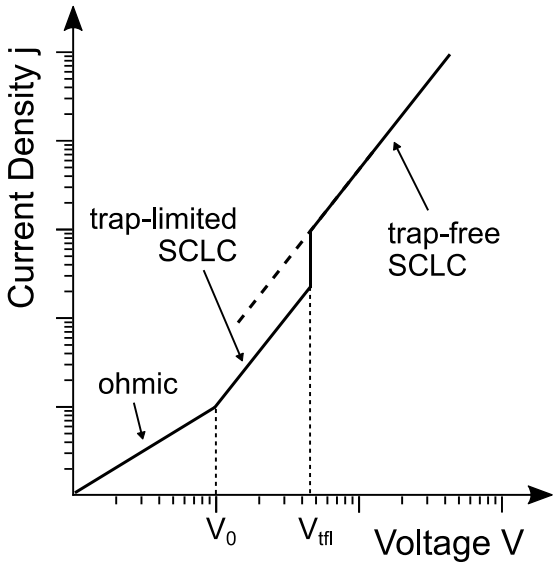

Figure 2.12 Current-voltage characteristics of an organic semiconductor. For low voltages, the current shows an Ohmic behavior, while for high voltages, there is a stationary space charge region formed at the electrodes and the current thus shows a quadratic behavior. The region of the space-charge-limited-current (SCLC) is divided in two regions. One where the transport is governed by traps and the other at high voltages, where all traps are filled and the transport can thus be viewed as trap-free.

[20] A degenerate semiconductor is highly doped, so that its behavior can be described as metallic.

[21] In general, a contact is considered Ohmic, when the density of charge carriers at the contact and in its vicinity is much higher than in the bulk of the semiconductor, thus providing a sufficient reservoir of charge carriers.

For non-Ohmic contacts, there are two main processes of charge injection with which the energetic barriers are overcome, when an electric field is applied. In the first process, an electron at the Fermi level of the electrode tunnels through the barrier, which is tilted due to externally applied electric field (field emission). This effect is called the Fowler-Nordheim tunneling and is dominant for large barriers and/or at low temperatures. The second process is called thermionic injection, where a thermally activated electron can overcome the tilted barrier. In both cases, the barrier is lowered by an image charge induced by the electron at equal distance to the interface, which is called the Schottky-effect.

Current-Voltage Characteristics

In the case of a trap-free organic semiconductor with Ohmic contacts, its current-voltage (IV) characteristics can be divided into two regions, as schematically shown in Figure 2.12. In the first region, the applied voltage is low, so that fewer charge carriers per volume are injected than initially present in the bulk due to thermal activation. Here, the current is determined by the motion of the free charge carriers present in the bulk and shows a linear behavior between the current density j_{Ohm} and the externally applied voltage V. It can be described by Ohm's law,

$$j_{\mathrm{Ohm}} = en\mu\frac{V}{L}\ , \tag{2.14}$$

where e the elementary charge, n the density of intrinsic charge carriers, μ the charge carrier mobility and L the length of the sample. The product of elementary charge, density of charge carriers, and mobility is the conductivity σ of the sample,

$$\sigma = en\mu\,. \tag{2.15}$$

In the second region at higher applied external voltages, the injected charge carriers begin to outnumber the ones initially present in the bulk. Thus, the semiconductor gets charged and has a stationary space charge, which leads to the IV characteristics to become nonlinear. The current now flowing through the semiconductor is called space-charge-limited-current (SCLC) and can be described by the Mott-Gurney law,

$$j_{\mathrm{SCLC}} = \frac{9}{8}\epsilon_{\mathrm{r}}\epsilon_0\mu\frac{V^2}{L^3}\ , \tag{2.16}$$

where $\epsilon_{\mathrm{r}}\epsilon_0$ is the dielectric constant of the sample. Here, the mobility is generally assumed to be independent of the electric field. As can be easily seen from equations (2.14) and (2.16), the Ohmic and SCLC region can be used to either determine the conductivity σ or the mobility μ of the sample, respectively.

However, in a realistic case, traps are present in the energy gap of the semiconductor, which suppress the current flow by localizing (trapping) charge carriers. Here, the mobility μ in equation (2.16) has to be replaced by an effective mobility (2.16) $\mu_{\mathrm{eff}} = \Theta\mu$, where

$\Theta \ll 1$ is a parameter accounting for the density and depth of the traps and can be assumed to be constant for small current densities. However, at a certain critical voltage V_{tfl}, the injected charges are sufficient to fill all traps, the current abruptly increases and is practically the same as without traps. This is called the trap-filled limit (TFL). The trap-limited SCLC current represents the middle region between the Ohmic and trap-free SCLC region displayed in Figure 2.12. The mobility of a sample can only be directly determined from IV-characteristics, if the ideal case is realized or the external voltage is very high, whereas the conductivity can also be measured for non-ideal cases, since traps are not changing the Ohmic behavior.[22]

Charge Carrier Mobility

Charge transport in organic semiconductors is strongly dependent on the structural order of the molecular assemblies. In highly pure organic single crystals, band transport can be observed like in inorganic semiconductors with a temperature dependent mobility $\mu(T)$, which in general follows the power law

$$\mu(T) \propto T^{-\alpha} . \tag{2.17}$$

When the mobility is only limited by the scattering of the charge carriers with phonons (lattice vibrations) and usually $\alpha \approx 3/2$. Experimentally, though, α was found to vary between 0 and 3.[109] From the shown power law (2.17), it can be seen, that the mobility decreases with increasing temperature. In the case of more disordered systems of organic semiconductors, however, charge transport occurs via incoherent phonon-assisted tunneling or temperature-assisted hopping of charge carriers between sites, since charge carriers are mainly localized on molecular units due to the weak intermolecular overlap of orbital wave functions. In the framework of the already mentioned Bässler model (see Figure 2.5), the mobility for hopping transport at low electric fields can be expressed as

$$\mu(T) \propto e^{-c\left(\frac{\sigma}{k_{\mathrm{B}}T}\right)^2} , \tag{2.18}$$

where c is a constant and σ resembles the energetic disorder, i.e. the width of the DOS distribution. Here, the hopping rate depends on the wavefunction overlap between neighboring sites and itself follows a Gaussian distribution, since the overlap is dependent on the relative orientation of adjacent molecules. This Gaussian distribution of the DOS leads to the T^{-2} behavior of the exponential function, whereas an exponential DOS would lead to a T^{-1} behavior. Equation (2.19) describes the experimentally found temperature dependence of mobilities reasonably well. However, at high electric fields, the mobility also

[22] For this reason, the mobility is usually determined from OFET measurements and not from simple IV characteristics.

becomes field-dependent and is better described by a form similar to the Poole-Frenkel law,

$$\mu(T) \propto e^{-\frac{\Delta}{k_B T}} \cdot e^{\beta\sqrt{F}}, \tag{2.19}$$

where β and Δ are constants, and F is the applied electric field. Both equations show that hopping transport displays the inverse behavior of band transport, namely the mobility increases with increasing temperature. This demonstrates again that hopping transport is a thermally activated process.

In conjugated polymers, the molecular sites are resembled by the separate segments with an effective conjugation length. Along the delocalized part of the segment, the charge carrier can move barrier free, however, at the end of the segments, the break in conjugation marks an energetic barrier. Thus, also in polymeric solids charge transport occurs via hopping (or tunneling) between segments on the same chain or between segments of different chains. Due to the incoherent hopping transport, organic materials generally show much lower charge carrier mobilities, in the order of 10^{-5} cm^2/Vs to 10^{-2} cm^2/Vs, than inorganic semiconductors with band transport, where the mobility is in the order of 10^3 cm^2/Vs to 10^4 cm^2/Vs.

2.1.4 Energy Level Alignment

When layers of organic semiconducting materials are put in contact with metal surfaces or other (inorganic or organic) semiconducting material surfaces, several phenomena are occurring at the formed interface, which affect the electronic structure at this interface and are all summarized by the term energy level alignment. To understand the electronic structure of organic layers and the mechanisms of organic (opto-)electronic devices, it is important to understand all important phenomena associated with energy level alignment, i.e. vacuum level alignment, Fermi level pinning, formation of interface dipoles and the push-back effect. While they shall be discussed separately in this subsection, normally, there is a complex interplay of all phenomena occurring at the interface, which are affecting each other.

In general, the adsorption of molecules on surfaces can be divided into two modes, i.e. physisorption and chemisorption. During physisorption, the molecules interact only weakly with the surface and are bond via van-der-Waals forces, thus, the electronic structure of the molecules is only perturbed weakly. During chemisorption, however, the molecules interact strongly with the surface and, in the simplest case, are bond covalently. For most cases discussed here, molecules are adsorbed via physisorption.

Vacuum Level Alignment

The simplest case of energy level alignment of a metal-organic interface is vacuum level alignment (also called the Schottky-Mott limit), schematically shown in Figure 2.13 a). Here, the energy levels of the adsorbate (molecule) are simply aligned by alignment of the vacuum level of the absorbate (defined by its EA and IE) with respect to the work function Φ_{sub} of the substrate. As described earlier the difference between Φ_{sub} and the IE of the adsorbate is called the hole injection barrier (HIB – Δ_h) and the difference between Φ_{sub} and EA the electron injection barrier (EIB – Δ_e). Although, these energetic differences are usually called injection barriers, they are also likewise applicable for charge extraction. Here, however, they cannot be considered "extraction" barriers as they are rather

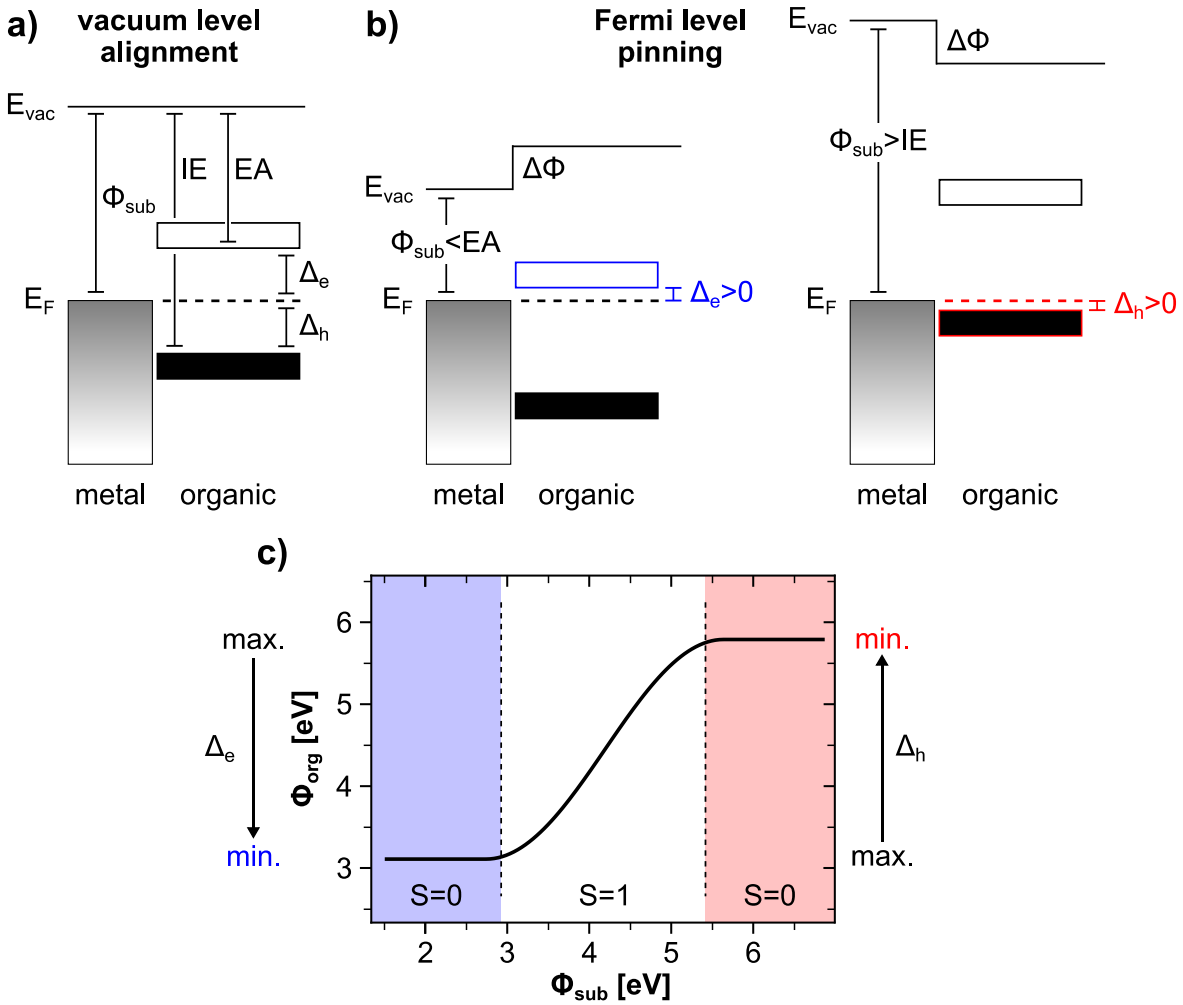

Figure 2.13 a) Schematic energy level diagram of a metal-organic interface in the Schottky-Mott limit. Here, the energy levels of the organic are aligned with respect to the vacuum level of the metal. **B)** Fermi-level pinning at the LUMO (left) and HOMO (right). Since the work function Φ_{sub} of the metal is lower (higher) than the EA (IE) of the organic, charges flow to (from) the organic to create an electronic equilibrium situation resulting in a jump of the vacuum level $\Delta\Phi$. The injection barriers (Δ_e and Δ_h) are found to not vanish completely, but rather to have a minimum value of a few 100 meV. **c)** Work function of a typical organic semiconductor with respect to the work function of the substrate Φ_{sub}. As can be seen, the curve can be divided into two regimes, called the Schottky-Mott limit (S=0) and Bardeen-limit (S=1).

potentials driving the charge transport. However, they contribute to the total resistance of the device and thus large HIB and EIB are also detrimental for charge extraction processes. Thus, minimizing those barriers is a key factor for improving device performance.

Similarly to the alignment at a metal-organic interface, the vacuum levels of two different organic layers can be aligned at an organic-organic interface. Here, the interface is usually characterized by the difference in the energy levels, i.e. EA and IE, and one material is described as donor-type and the other as acceptor type, i.e. $EA_{acceptor} > EA_{donor}$ and $IE_{acceptor} > IE_{donor}$.[23] Vacuum alignment often occurs at very weakly interacting interfaces, which are free of gap states. Its main advantage lies in the possibility of predicting the interfacial energy level alignment from the energy levels of the individual systems. While vacuum level alignment has been observed for many organic-organic interfaces,[75,110–112] it is rather the exception than the rule for metal-organic interfaces[75,81,113,114] and can highly underestimate the injection barriers.

Fermi Level Pinning

From Figure 2.13 a), it can already be seen that the vacuum level alignment is only possible for a limited range of the substrate work function Φ_{sub}, and is thus also semiconductor specific. Once Φ_{sub} approaches the IE or EA of the semiconductor, the Fermi level gets pinned near the HOMO or LUMO, respectively, and the vacuum level drops across the interface [as depicted in Figure 2.13 b)]. This behavior can be explained, when considering vacuum level alignment in a case where Φ_{sub} > IE (vice versa for Φ_{sub} < EA). Here, the substrate's Fermi level lies below the HOMO level of the semiconductor, which correspond to a non-equilibrium situation. As a response, charges are transferred across the interface, shifting Φ_{sub} by causing interface dipoles ($\Delta\Phi_{\mathrm{ID}}$) and / or band bending.[115,116] Charge transfer continues until E_{F} lies again above the HOMO and an equilibrium is established. This phenomenon is called Fermi level pinning and the energy at which the pinning occurs the pinning level.

A common parameter to describe the alignment between an organic semiconductor and a metal, i.e. the interplay between the work function of the substrate Φ_{sub} and the work function of the organic layer Φ_{org}, is the slope parameter

$$S = \frac{\mathrm{d}\Phi_{\mathrm{org}}}{\mathrm{d}\Phi_{\mathrm{sub}}} \ . \tag{2.20}$$

Figure 2.13 c) schematically shows the dependence of Φ_{org} on Φ_{sub} with the two limiting cases of S = 1, the Schottky-Mott limit, and S = 0, the so-called Bardeen limit. In the Bardeen

[23] In the case where $EA_1 > EA_2$ but $IE_2 > IE_1$, material 1 can be described as electron blocking (or hole transporting) material and material 2 as hole blocking (or electron transporting), depending on their use in the specific device.

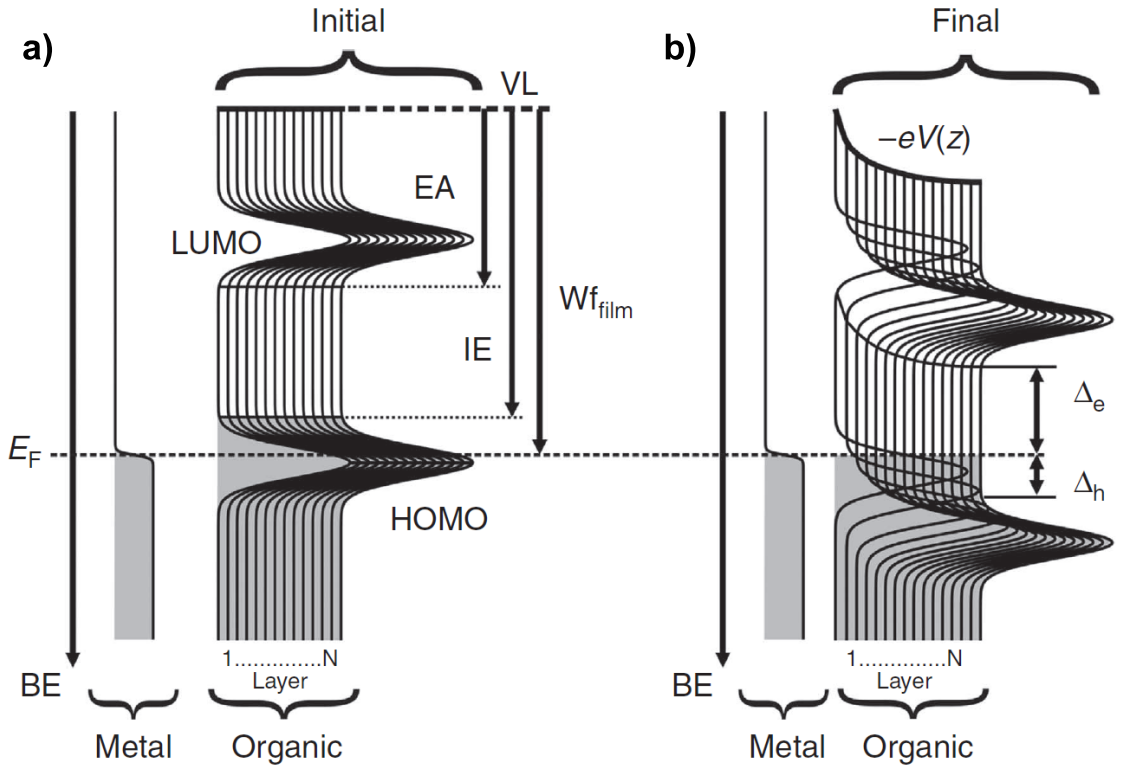

Figure 2.14 Electrostatic Model explaining the origin of Fermi level pinning. **a)** Possible initial situation, where the Fermi level of the metal is located within the HOMO of the organic, when assuming vacuum level alignment. **b)** Final situation after convergence of the iterative scheme. With increasing distance to the metal surface, the DOS of each organic layer increasingly shifts to higher binding energy (BE) due to the local electron potential. At a certain distance the energy levels converge to a final level with constant injection barriers. Reproduced with permission from Springer Nature ©2014.[117]

limit, the injection barriers are independent of Φ_{sub}, and reach their minimal/maximal values. However, it was experimentally found that the injection barriers never reach 0 eV (except in cases of monolayer formation for a few materials), but are always in the order of a few 100 eV.[75,81,118] Thus, the Fermi level is always pinned near the HOMO / LUMO levels but never directly at their onsets.

To explain this pinning behavior, several theoretical models have been proposed including induced density of interface states (IDIS)[119], integer charge transfer (ICT)[120] or gap states models.[121] All of these models implicitly assume the formation of interface dipoles by charge transfer from or to interface, polaronic or gap states. While these models can explain some parts of Fermi level pinning at metal-organic interfaces, they are only valid for certain applications/regimes[24] and mostly fail to explain the energy level alignment at organic-organic interfaces. Recently, an iterative electrostatic model based on a one dimensional Poisson equation has been developed with which the energy level alignment at metal-organic and organic-organic interfaces could be comprehensively simulated.[117,122]

[24] In some cases, they were intendedly developed only for certain applications.

In the case of a metal-organic interface, the model (Figure 2.14) assumes the metal to have a constant Fermi level with an infinite electron reservoir and a continuous DOS of HOMO and LUMO (here of Gaussian form) for each (closed) organic single layer. Electron occupation obeys Fermi-Dirac statistics and electron transfer can freely occur between the metal and the organic layers. Figure 2.14 a) shows a possible initial situation, where Φ_{sub} is located in the middle of the HOMO level and thus shows a classical Fermi level pinning situation. After convergence of the iterative process, the final situation [Figure 2.14 b)] shows that with increasing distance the DOS of each organic layer increasingly shifts to higher binding energies due to the local electron potential, until it converges to a final level. An additional introduction of gap states (of Gaussian or exponential form) can make S less than 1 in the Schottky-Mott regime and renders the transition between Schottky-Mott and Bardeen regime less steep. In conclusion, this model is not only able to accurately model the slope parameter S and explain the non-vanishing injection barriers, but it also demonstrates the dependence of Φ_{org} on the thickness of the organic layer.

Push-back Effect

Another important interface phenomenon which occurs at metal surfaces (and to a lesser extent also at metal oxide surfaces) is the pushback (or pillow) effect, where a deposition of organic molecules onto a clean metal surfaces leads to a reduction of the work function (even for very weakly interacting molecules).[123,124] In contrast to Fermi level pinning and interface dipoles, the pushback effect is a pure substrate-surface effect and does not affect the electronic structure of the organic layer. The work-function of a metal is composed of the chemical potential of the bulk and surface contributions, i.e. surface dipoles. Surface dipoles are due to a spill-out of electron density at the surface of the metal, since quantum-mechanically the electron density does not abruptly end at the surface, but rather decays

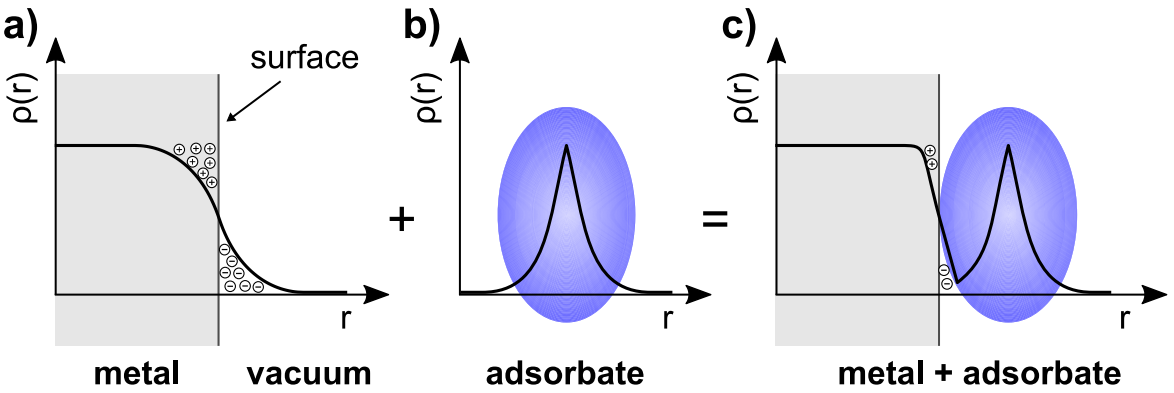

Figure 2.15 Illustration of the push-back effect. **a)** At a metal surface, the electron density does not end abruptly, but rather exponentially decays into the vacuum. Due to electrons are residing outside of the metal, which induces a surface dipole. **b)** Schematic electron density of a molecule. **c)** After adsorption of the molecule, the spilled out electron-density is pushed-back into the metal due to Coulomb repulsion of the adorbates electron density. This leads to a reduction of the surface dipole and thus a reduction of the substrates work function.

exponentially [schematically depicted in Figure 2.15 a)]. Additionally, a positive net charge exists at surface in the material due to the spilled out electrons. When a molecule is now adsorbed at the metal surface, the spilled out electron density gets pushed back into the metal by Coulomb repulsion of the adsorbate's electron density, as shown in Figure 2.15 b). This leads to a reduction of the surface dipole and hence a reduction of the work function. For clean metal surfaces the pushback effect can be in the range of 0.5 eV to 1 eV, while for metal oxide surfaces, it is usually approx. 0.3 eV.[81,125,126]

Electrode Modification

The surface of electrodes is often intentionally modified by the introduction of interlayers, which raise or lower the work function of the electrode in order to achieve Fermi level pinning of the organic adlayer and thus quasi-Ohmic contacts. One method is to insert an intrinsically conducting polymer layer like PEDOT:PSS[25] between the electrode and the organic layer, which was shown to yield high work function electrodes and has proven to be very efficient for hole injection.[127] Another method is to introduce interface dipoles at the surface of the electrode. This can be done by either self-assembled monolayers (SAMs),[128,129] polymers[130] or strong electron acceptor or donor molecules.[131,132] SAMs consist of two parts: an anchoring group (like thiols, silanes or phosphonates) and a functional group. Here, the anchoring group of the SAM attaches to the surface via e.g. the formation of covalent bonds or hydrogen bonds to surface hydroxyl groups. The functional group, on the other side, has a built-in dipole moment, which introduces the interface dipole, thus effectively lowering or raising the substrate's work function. The formation of SAMs occurs in a self-assembling process, where (in the simplest case) the substrate just has to be immersed in a solution containing the SAM molecules. This process was shown to form highly ordered and densely packed monolayers. Due to the many possibilities of using different functional groups, a large variety of SAMs has been developed, with which the work function of substrates can be tuned as desired, even allowing "fine"-tuning in the order of a few 100 meV. The use of strong acceptor or donor molecules leads to a charge transfer between the molecule and the electrode thus creating an interface dipole.

2.1.5 Film Formation

Film formation of organic thin films depends largely on the deposition process. While small molecules can be both processed from solution as well as by sublimation in vacuum, polymers are only processable from solution.[26] The most common depositing techniques are spin-coating from solution and molecular beam deposition in vacuum.

[25] Poly(3,4-ethylene-dioxythiophene):poly(styrenesulfonate.

[26] However, most organic small molecules are thus usually deposited via thermal evaporation in vacuum have often a very poor solubility compared to polymers and.

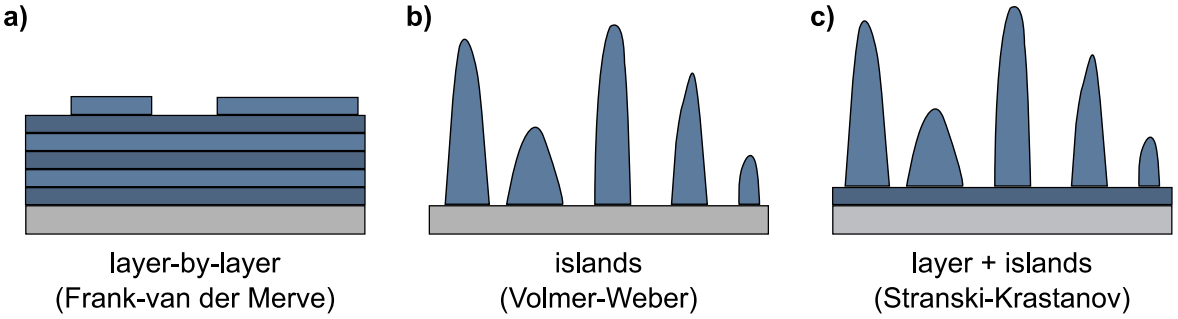

Figure 2.16 Growth modes occurring during molecular beam deposition. **a)** Frank-van der Merve mode, **b)** Volmer-Weber mode, and **c)** Stranski-Krastanov mode.

The simplicity and easy usability of spin-coating make it a widely used technique to achieve thin films with nanoscale thicknesses. The process of spin-coating can be described in four main steps. First, a small amount of solution containing the desired molecule/polymer is dispensed onto the surface of the substrate. Second, the sample is accelerated to high speed in order to spread the material across the sample and throw off excess amount of solution by centrifugal forces. Third, the film is thinned by spinning material off the edges of the sample. Simultaneously, the solvent evaporates, which increases the viscosity of the solution countering the centrifugal forces. Last, the sample is rotated until the desired film thickness is reached or until the viscosity of the solution becomes so high, that no more material can be spun off. Afterwards, the film is dried until only little residual solvent is left. The drying process is often enhanced by annealing it at a certain temperature. The final film thickness can be approximately described via

$$d \propto \frac{c_0}{(1-c_0)^{1/3}} \left(\frac{\eta_0}{\omega^2}\right)^{1/3}, \tag{2.21}$$

where c_0 is the initial concentration of the material in the solution, η_0 the initial viscosity of the solution, and ω the spin-speed.[133] This relation is very useful to determine relative thicknesses of films processed under similar conditions, where only c_0 and ω are changed.

Thermal evaporation (molecular beam deposition) in vacuum is a common technique to deposit thin organic films in the range of a few to hundreds of nm. For this purpose, the material (placed in a quartz glass crucible) is resistively heated in UHV via a constant current flow. The evaporation rate can be easily adjusted by varying the intensity of the current. When the evaporated molecules reach the substrate, which is placed above or in front of the molecular beam, they condense and therefore form a thin film, the thickness of which can be controlled on a sub Å scale. Evaporation rates are usually monitored by a quartz crystal microbalance (QCM). The QCM consists of a quartz crystal plate, which is driven to oscillate at its resonant frequency. When material is deposited on top of the plate, the change of the resonance frequency is proportional to the mass of the deposited material.

This change in frequency can be measured very accurately, therefore, small changes in mass and thus the evaporation rate can be measured.

The growth process during the molecular beam deposition is a non-equilibrium process, where several dynamic processes on the molecular are occurring simultaneously: nucleation of molecules leading to the formation of molecular assemblies, intra- and inter-layer diffusion of molecules, dissociation of molecular assemblies, and re-evaporation into vacuum.[133] Usually, the growth mode can be divided into three different modes as sketched in Figure 2.16, which depend largely on the substrate-molecule and molecule-molecule interactions. In the Frank-van der Merwe mode, substrate-molecule interactions are stronger than molecule-molecule interactions and the growth proceeds layer-by-layer, where each layer is closed. Thismode is typical for most amorphous materials. In the Volmer-Weber mode, the opposite is happening, where interactions between the molecules are much stronger than interactions to the substrates and consequently the molecules nucleate in clusters forming islands. This mode is typical for very crystalline materials which are grown on weakly interacting substrates like e.g. glass. The third mode, the Stranski-Krastanov mode, is an intermediate case between the other two modes, where the molecules first form a few closed layers on top of which islands-growth becomes dominant as the substrate-molecule interaction becomes weaker. This modes is typical for crystalline molecules which weakly interact with the substrate (e.g. metals). The knowledge of the growth mode is very important for the interpretation of experimental data, e.g. from photoelectron spectroscopy.

2.1.6 Organic Electronic Devices

In this work, also organic electronic devices were fabricated employing some of the investigated doped materials (OFETs – section 5.1 and OPVCs – 5.4). However, since they provide only a small contribution to the overall body of this thesis, OFETs and OPVCs as well as their operation mechanisms and characteristics shall be discussed rather briefly at this point.

Organic Field Effect Transistors

Organic field effect transistors (OFETs) are fundamental building blocks of organic electronics and are also frequently used to determine the mobility of organic semiconductors. They are three-terminal devices (source, drain, and gate), where the organic layer forms the charge transport channel between the source and drain contacts. There are four basic architectures in which an OFET can be built. In the bottom-contact, bottom-gate configuration [Figure 2.17 a)] the gate-insulator substrate is pre-patterned with the source and drain contacts and the organic layer is deposited on top, while in the top-contact, bottom-gate configuration [Figure 2.17 b)], the organic layer is first deposited

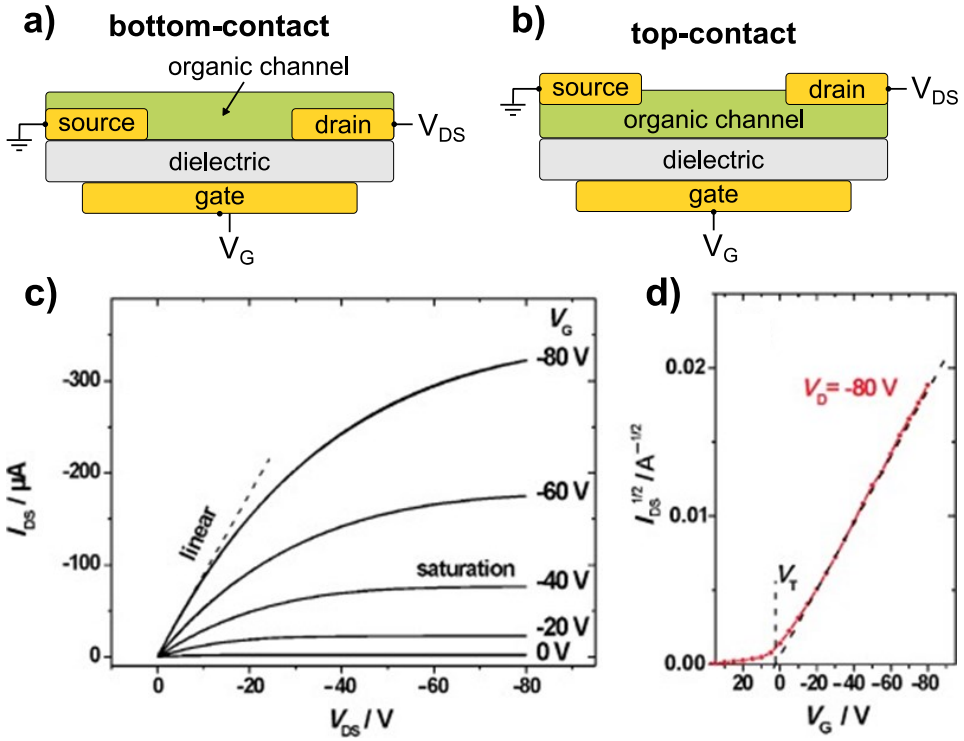

Figure 2.17 Basic architecture of an OFET in the **a)** bottom-contact bottom-gate and **b)** top- contact bottom-gate configuration. **c)** Typical output characteristics of an OFET showing the linear and saturation regimes for different gate voltages. **d)** Typical transfer characteristic of an OFET at constant source-gate voltage. Fig. c) and d) reproduced with permission from John Wiley and Sons ©2007.[134]

onto the gate-insulator substrate and the contacts are deposited subsequently. Alternatively (and less frequently used), both top-contact and bottom-contact configuration can be also fabricated with a top-gate, where the dielectric and gate contact are deposited last. The gate electrode is capacitively coupled to the organic channel via the dielectric layer. Depending on the device configuration and used electrode materials, p- or n-channel transistor can be realized.

Applying a bias at the gate leads to a large electric field at the organic/dielectric interface and consequently to band bending of the organic semiconductors energy levels. This induces an accumulation of charge carriers in the vicinity of the interface (field effect) and makes the organic channel highly conductive under an applied gate bias, leading to a significant current between source and drain I_{DS} when a voltage V_{DS} is applied between them. This mode is called the accumulation (or enhancement) mode and is the usual mode of operation for OFETs. Since the field-induced charge carriers are confined to the vicinity of the interface (typically only a few nm), charge transport occurs along the interface instead of bulk of the organic channel (like for IV measurements).[27]

[27] The description p- and n-channel refers to the type of the majority of accumulated carriers in the channel.

The electrical performance of OFETs is characterized by IV characteristics as exemplarily shown in Figure 2.17 c) and d). Figure 2.17 c) shows I_{DS} as a function of V_{DS} for constant gate voltages V_G (output characteristics) and Figure 2.17 d) as a function of V_{G} at constant V_{DS} (transfer characteristics). At low V_{DS}, the charge distribution is constant throughout channel and thus the output curve shows a linear behavior between I_{DS} and V_{DS}. Assuming Ohmic contacts, the source-drain current $I_{\mathrm{DS,lin}}$ in the linear regime is given by

$$I_{\mathrm{DS,lin}} = \frac{W}{L}\mu C_{\mathrm{i}} V_{\mathrm{DS}}\left(V_{\mathrm{G}} - V_{\mathrm{th}} - \frac{V_{\mathrm{DS}}}{2}\right) , \tag{2.22}$$

where W and L are the width and length of the channel, respectively, μ the charge carrier mobility, C_{i} the specific capacitance of the dielectric layer, and V_{th} the so-called threshold voltage. The threshold voltage is the minimum voltage that is needed to create a conducting path between the source and drain electrodes and is usually related to the filling of trap states or mismatches of the energy levels. An increase of V_{DS} leads to a carrier concentration gradient within the channel and thus to a deviation from linear characteristics. When V_{DS} is further increased, the charge carrier concentration density drops to zero at the drain contact (called pinch-off) and thus the total current does not increase anymore. This regime is called the saturation regime and its source-drain current $I_{\mathrm{DS,sat}}$ is given by

$$I_{\mathrm{DS,sat}} = \frac{W}{2L}\mu C_{\mathrm{i}}(V_{\mathrm{G}} - V_{\mathrm{th}})^2 \ . \tag{2.23}$$

In order to fabricate practical devices, i.e. OFETs which can be operated at low voltages, high charge carrier mobilities and high gate-insulator capacitances are needed as can be seen from equations (2.22) and (2.23). Another characteristic parameter of OFETs is the so called on-off ratio, which defines the ratio between the on state current and the off state (leakage) current and should be as high as possible to achieve good device performance.

In general, different mobilities are deduced from the linear and the saturation regime, with the ones from the saturation regime usually being higher, because the higher channel resistance in the saturation regime reduces the influence of contact resistance at the source/ drain electrodes. Thus, usually the mobilities of the linear regime are reported. However, care has to be taken when evaluating charge carrier mobilities, as kinks can occur in the linear regime leading to a misinterpretation of the data and an overestimation of more than one order of magnitude.[135]

In principle both n-channel and p-channel transport is possible for most organic semiconductors (ambipolar transport), however most materials show predominantly p-type behavior.[41] This is high asymmetry between electron and hole mobility is associated with a universally present electron trap due to oxygen/water, which is located at -3.6 eV below the vacuum level.[42] Since LUMO energies typically range in the region -2 eV to -3 eV

this trap level is present in nearly all organic semiconductors. For HOMO levels (usually in the range of -5 eV to -6 eV), however, trap states of filled orbitals above -5 eV are less frequent, which explains the apparent difference in susceptibility between holes and electrons to trapping. Additionally, surface hydroxyl groups at the interface between gate-insulator and organic provide additional electron traps.[136] Thus, passivating these traps is a key effort to improve the performance of n-channel OFETs, which can be achieved by bulk doping of the organic layer[35] (see next section) or passivation of the insulator surface by e.g. SAMs.[136]

Organic Photovoltaic Cells

In a simple heterojunction organic photovoltaic cell (OPVC), two organic semiconducting materials comprise the photoactive layer, which is sandwiched between two electrodes of different work functions as depicted in Figure 2.18 a). Here, one organic materials is acting as an electron donor and the other as an electron acceptor in order to create a driving force, which is needed to dissociate excitons (see subsection 2.1.3) and generate mobile charge carriers.[28] In order to get light to the active layer, one of the electrodes has to be optically transparent, which is usually the anode commonly consisting of transparent conductive oxides (TCOs) like indium tin oxide (ITO). The anode materials has to have a high work function in order to extract holes. Low work function metals like calcium, magnesium or aluminum are commonly used as cathode material. In order to increase the efficiency of the device, additional layers are introduced, e.g. hole and electron transport layers. The transport layers are placed between the active layer and the respective electrode in order to only allow the transport of the desired charge carrier and block the other one.

When the offset of the frontier energy levels of both materials is larger than the exciton binding energy, the exciton can dissociate at the donor/acceptor interface and mobile charge carriers are generated. The hole is transferred into the HOMO of the donor and the electron into the LUMO of the acceptor material. The process of charge generation can be described by a 4-step mechanism as shown in Figure 2.18 a):

1. Light is absorbed in either of the two materials of the active layer, leading to the formation of an exciton.
2. The exciton diffuses through the layer until it reaches the donor/acceptor interface.
3. It dissociates at the interface and mobile charge carriers are generated.
4. The mobile charge carriers are then transported to the collecting electrodes.

[28] In a solar cell containing only one organic material as photoactive layer (homojunction), charge separation can only occur at the interface of the organic material and an electrode. This process, however, is very inefficient.

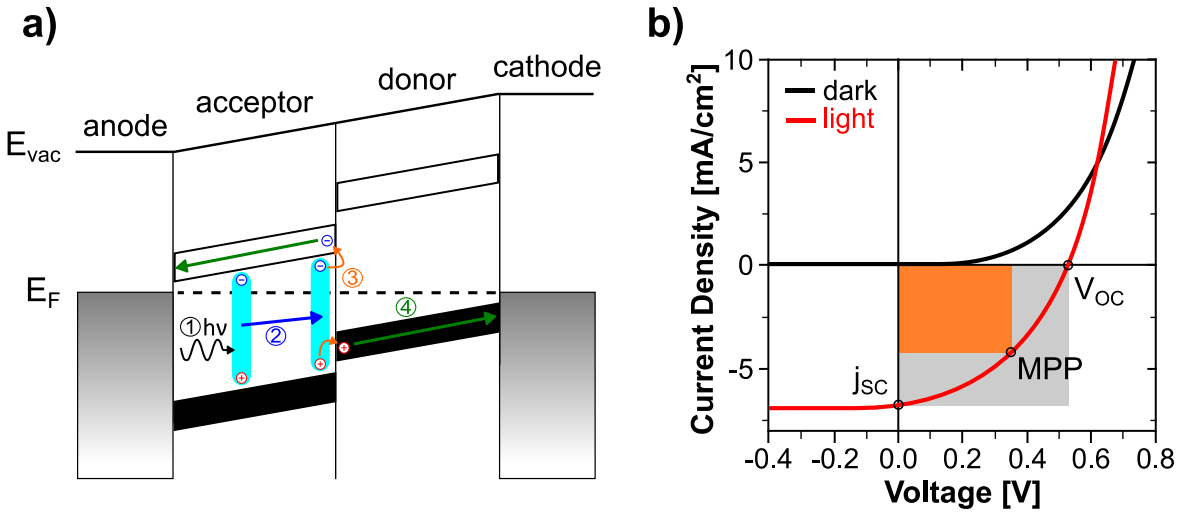

Figure 2.18 a) Electronic structure of a heterojunction solar cell. The 4-step operation mechanism is schematically depicted (for details see text). **b)** Typical IV characteristics of an OPVC, showing the short-circuit current density j_{SC} and the open-circuit voltage V_{OC}. The fill factor FF is defined as the ratio between the maximum power output at the maximum power point MPP (orange area) and the product $j_{SC} \cdot V_{OC}$ (grey area).

In general, photovoltaic cells are characterized by a few key parameters obtained from their current-voltage curves under illumination. The typical IV curves of an organic solar cell with and without illumination are shown in Figure 2.18 b). While the IV curve in dark shows a typical diode behavior, the IV curve under illumination is shifted towards the negative current regime due to the produced photocurrent. The current density measured in short-circuit conditions is called the short-circuit current density j_{SC}.[29] At the open-circuit voltage V_{OC} the photocurrent completely compensates the dark current and thus the net current reaches zero. The point where the product of current and voltage reaches its maximum is called the maximum-power-point (MPP) and defines the operating point of the solar cell. The ratio between the maximum power output [orange area in Figure 2.18 b)] and the product of the short-circuit current and the open-circuit voltage (grey area) is called the fill factor FF. The fill factor is an important parameter to characterize the performance of a solar cell, since it is directly affected by shunt and series resistances as well as diode losses and is therefore a measure of the quality of the solar cell.

The power conversion efficiency η_{PCE} is defined as the ratio between the electrical power output P_{max} and the power of the incident light P_{in} expressed as

$$\eta_{\mathrm{PCE}} = \frac{P_{\mathrm{max}}}{P_{\mathrm{in}}} = \frac{I_{\mathrm{MPP}} \cdot V_{\mathrm{MPP}}}{P_{\mathrm{in}}} = \frac{FF \cdot j_{\mathrm{SC}} \cdot V_{\mathrm{OC}}}{P_{\mathrm{in}}/A} \quad . \tag{2.24}$$

[29] To allow comparison between solar cells of different sizes, it is convenient to refer to the short-circuit current density $j_{\mathrm{SC}} = I_{\mathrm{SC}}/A$ rather than the short circuit current I_{SC}, since j_{SC} is independent of the size A of the cells.

The parameters fill factor, short-circuit current density and open-circuit voltage are thus the key parameters to describe the performance of a solar cell and have all to be maximized in order to increase the efficiency of the cell. The efficiency of organic solar cells is currently only in the order of 10%.[137]

Recently, a new generation of solar cells has been developed, where the active material consists of a perovskite compound.[138,139] In order to increase the performance and lifetime of these cells, organic interlayers (like electron / hole transport layers) have been employed in a way similarly to pure organic solar cells.[13] Such organic-inorganic metal halide perovskite solar cells currently reach efficiencies over 20%, although their performances are not stable yet and device lifetimes are rather short.[12]

2.2 DOPING OF ORGANIC SEMICONDUCTORS

The concept of doping was a breakthrough for inorganic semiconductors, since it allowed precise control of the transport properties and the creation of p-n-junctions, both of which lead to improvement of the existing semiconductor technology as well as the development of new device concepts like the bipolar transistor. With the development of organic semiconductors, the concept of doping was soon also applied to them by using the same methods, which were known for the doping of inorganic semiconductors. Thus, the first research studies on doping of organic molecules employed strongly oxidizing gases and later on small atoms or very small molecules, with which high conductivities could be achieved.[3,18,19] However, both methods suffer from device instabilities due to the tendency of these small dopants to diffuse in the organic layers.[20] At the beginning of this century, a more efficient and stable way to dope organic semiconductors was discovered through the development of molecular dopants, which work similarly, but, due to their larger size, they are not as prone to diffusion as atomic dopants.[33,140]

The fundamentals of molecular doping of organic semiconductors and its application in devices has been the topic of a series of reviews published in the last few years.[21–24,52,53,141–143] Based on these reviews, a brief introduction of doping of inorganic semiconductors will be given in this section, followed by a detailed description of the concepts of molecular doping of organic semiconductors and the hereby occurring mechanisms. Furthermore, existing concepts of p-type and n-type doping and different dopant classes will be introduced.

2.2.1 Mechanisms of Doping

Doping of inorganic semiconductors like silicon is achieved by incorporating impurity atoms into the crystalline structure of the semiconductor host material. Here, the incorporation of impurity atoms into the crystalline network occurs via the formation of covalent bonds. In the case of silicon, which has four valence electrons, the incorporation of pentavalent impurities such as phosphorous introduces one extra electron per impurity atom, which increases the density of mobile negative charge carriers and renders the semiconductor n-type (n for negative). Similarly, the incorporation of trivalent impurities like boron introduces one hole per impurity atom and thus increases the density of mobile positive charge carriers. The semiconductor is now called p-type (p for positive).

Following classical semiconductor theory, the density of negative n_0 and positive charge carriers p_0 in an intrinsic (un-doped) semiconductor can be calculated from Fermi-Dirac statistics (see also subsection 2.1.1) depending on the position of the conduction band E_C and valence band E_V to be

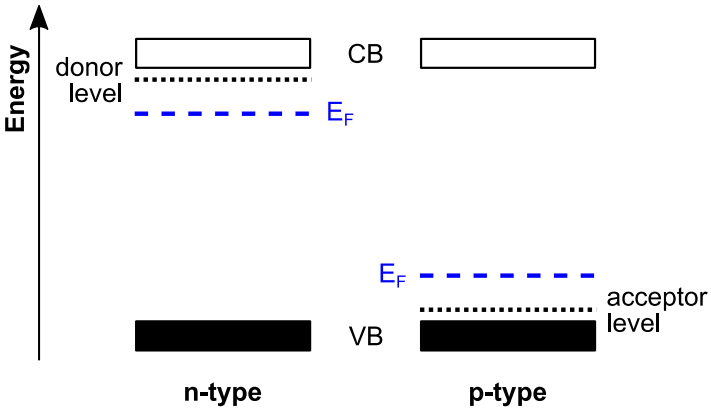

Figure 2.19 Shift of the Fermi level E_F in inorganic semiconductors due to the insertion of shallow impurity levels. In the case of n-type doping (left), shallow donor states located below the conduction band (CB) edge lead to a shift of E_F towards the CB. In the case of p-doping (right), the process is occurring vice versa. Here, the insertion of shallow acceptor states closely above the valence band (VB) leads to a shift of E_F towards VB. These shifts in E_F are associated with an increase in n-type or p-type conductivity, respectively.

$$n_0 = N_\mathrm{C} \cdot e^{\frac{E_\mathrm{F}-E_\mathrm{C}}{k_\mathrm{B}T}} \text{ and } p_0 = N_\mathrm{V} \cdot e^{\frac{E_\mathrm{V}-E_\mathrm{F}}{k_\mathrm{B}T}} , \tag{2.25}$$

where N_C and N_V is the effective density of states in the conduction and valence band, respectively.[144] For intrinsic semiconductors, where $n_0 \approx p_0$, the Fermi level is located close to the center of the gap with $E_\mathrm{g} = E_\mathrm{C} - E_\mathrm{V}$ and is consequently given by

$$E_\mathrm{F} = \frac{E_\mathrm{g}}{2} + \frac{k_\mathrm{B}T}{2} \ln\left(\frac{N_\mathrm{V}}{N_\mathrm{C}}\right) . \tag{2.26}$$

In the case of an n-type semiconductor, the introduction of the impurity (donor) atoms with density N_D leads to shallow donor states with E_D located below the conduction band edge, which leads to a shift of the Fermi level towards the conduction band as shown in Figure 2.19 (left). Similarly, shallow acceptor states with E_A are introduced above the valence band edge by the incorporation of acceptor atoms with density N_A in a p-type semiconductor leading to a shift of the Fermi level towards the valence band as shown in Figure 2.19 (right). These shallow states are positioned close to the respective band edges with

$$|E_\mathrm{C} - E_\mathrm{D}| < \left|k_\mathrm{B}T \ln\left(\frac{N_\mathrm{D}}{N_\mathrm{C}}\right)\right| \text{ and } |E_\mathrm{V} - E_\mathrm{A}| < \left|k_\mathrm{B}T \ln\left(\frac{N_\mathrm{A}}{N_\mathrm{V}}\right)\right| . \tag{2.27}$$

Consequently, their ionization only requires thermal energy and thus all dopant atoms are ionized even at temperatures below room temperature. As a result, the number of free mobile charge carriers is independent of the temperature and equals the number of dopant atoms. The Fermi level is thus given by

$$E_\mathrm{F} = E_\mathrm{C} - k_\mathrm{B}T \ln\left(\frac{N_\mathrm{C}}{N_\mathrm{D}}\right) \text{ and } E_\mathrm{F} = E_\mathrm{V} + k_\mathrm{B}T \ln\left(\frac{N_\mathrm{V}}{N_\mathrm{A}}\right) , \tag{2.28}$$

respectively.[145] These relation show that the number of charge carriers, hence the conductivity, and the position of the Fermi level can be precisely controlled by controlling the dopant concentrations N_D and N_A. For typical dopant concentrations in the range of

10^{-7} to 10^{-4} (atomic ratio), this leads to dramatic increases in conductivity, since at these concentrations the crystallinity of the semiconductor is largely undisturbed and thus the charge carrier mobility is retained.[144,146]

In contrast, doping of organic semiconductors follows different processes. Here, employing small atoms like halides or alkali metals as dopants was shown to lead to device instabilities.[20] The instabilities were linked to the tendency of these very small dopants to diffuse throughout the organic layer, since, in contrast to inorganic semiconductors, the dopants are not covalently bound to the organic semiconductors. This issue was resolved with the use of small donor or acceptor molecules as molecular dopants, which given their size have a smaller tendency to diffuse. Utilizing small molecules as dopants, the conductivity of organic semiconductors can indeed be increased by several orders of magnitude, enabling high performance devices.[23,52,141] Similar to the doping of inorganic semiconductors, doping of organic semiconductors leads to a shift of the Fermi level, which is increasingly moving towards the respective transport level (p-type to the HOMO, n-type to the LUMO) with increasing dopant concentration, as schematically shown in Figure 2.20. In contrast to the doping behavior in inorganic semiconductors,[31] both the increase in conductivity and the shift in Fermi level were found to saturate at dopant concentrations of few mole-percent (up to 10%). As indicated in Figure 2.20, the Fermi level gets pinned at the edge of the respective transport level (see also subsection 2.1.4) and thus the shift of the Fermi level comes to a stop at a certain dopant concentration. A possible reason for the saturation of the conductivity is discussed in section 7.3.

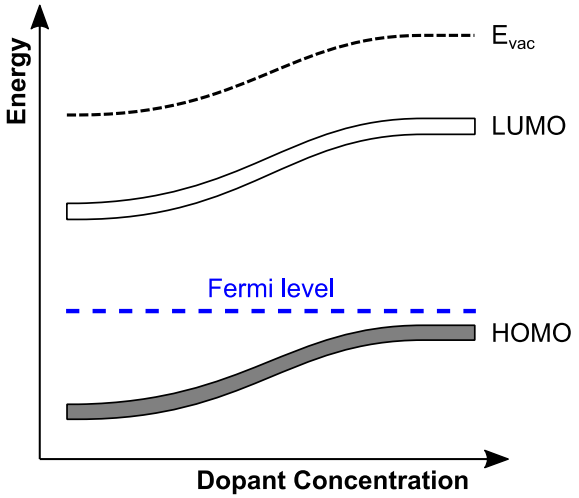

Figure 2.20 Idealized shift of the Fermi level in the case of molecular p-doping of organic semiconductors.[30] Upon increasing the dopant concentration the Fermi level E_F, intrinsically located in the middle of the energy gap, shifts towards the HOMO level. At a saturation concentration of a few percent the Fermi level is pinned. Redrawn after ref. [147].

However, the doping efficiency of molecular dopants is comparably low, which necessitates the use of dopant concentrations in the order of a few mole-percent.[141,148–150] The admixture of such an amount of dopant molecules to organic thin films has a great effect

[30] For low dopant concentrations in the order of a few mole-percent or below. For higher dopant concentrations, the ionization energy of the doped material can be increased due to a depletion of the HOMO states (see also subsection 7.4).

[31] Inorganic semiconductors can be degenerately doped, where at high dopant concentrations the Fermi level is located in the valance band (or conduction band) and thus the degeneratively doped semiconductors displays a metal like behavior (as e.g. indium tin oxide).

on the morphology and structure of the films. In the case of the pristine film being crystalline (or polycrystalline), the admixture of a typical concentration of a few mole-percent of dopants leads to an amorphous growth and, in turn, to a decrease in mobility. For crystalline materials at low dopant concentrations, the decrease in mobility can have a greater impact on the conductivity than the increase in charge carrier density due to the doping, leading to a drop in conductivity by a few orders of magnitude.[151] At some point, when the dopant concentration is further increased, the increase in charge carrier density can outweigh the decrease in mobility again leading to an increase in conductivity again. In contrast, for semi-crystalline molecules or polymers, a different behavior was observed.[152,153],[A2] Here, the decrease in order and hence the decrease in mobility is outweighed by the increase in charge carrier density at low dopant concentrations leading to a strong increase in conductivity. Only at high dopant concentrations in the order of 10%, where the doping efficiency decreases with increasing dopant concentration, the conductivity starts to decrease.

For molecular doping of organic semiconductors, there are two distinct mechanisms known describing the interaction between dopant and host: i) ion pair (IPA) formation and ii) ground state charge transfer (CPX) formation, both of which are schematically depicted in Figure 2.21. Both of these mechanisms can be spectroscopically evidenced by the observation of diagnostic absorption features of the molecular ions, both for electronic transitions (UV/Vis/NIR spectroscopy) and for vibrational transitions (FTIR spectroscopy).[52,140,150,154] The following description of the fundamental doping mechanisms is based on p-type doping while all mechanisms are also occurring vice versa for n-type doping.

In the case of IPA formation, an electron is transferred from the energetically higher lying HOMO level of the host to the LUMO level of the dopant resulting in the formation of an ion pair consisting of the host cation and dopant anion [see Figure 2.21 a)]. Therefore, host-dopant material pairs have to normally fulfill the condition

$$EA_{\mathrm{dopant}} > IE_{\mathrm{host}} \tag{2.29}$$

for this integer charge transfer to occur (at least when the transfer is desired to occur with a high efficiency). For IPA formation, it is generally assumed that the electron on the dopant is static, while the hole in the HOMO of the matrix molecule is mobile, contributing to an increase in mobile charge carriers and therefore an increase in conductivity.

In the case of CPX formation, the frontier molecular orbitals of the dopant (i.e. the admixed molecule) and the host molecule hybridize in a supramolecular complex forming a set of new HOMO/LUMO states [see Figure 2.21 b)]. Following Hückel's method (see subsection 2.1.1), the energy $E_{\mathrm{CPX}}^{\mathrm{H/L}}$ of the frontier levels of the formed complex can be derived via

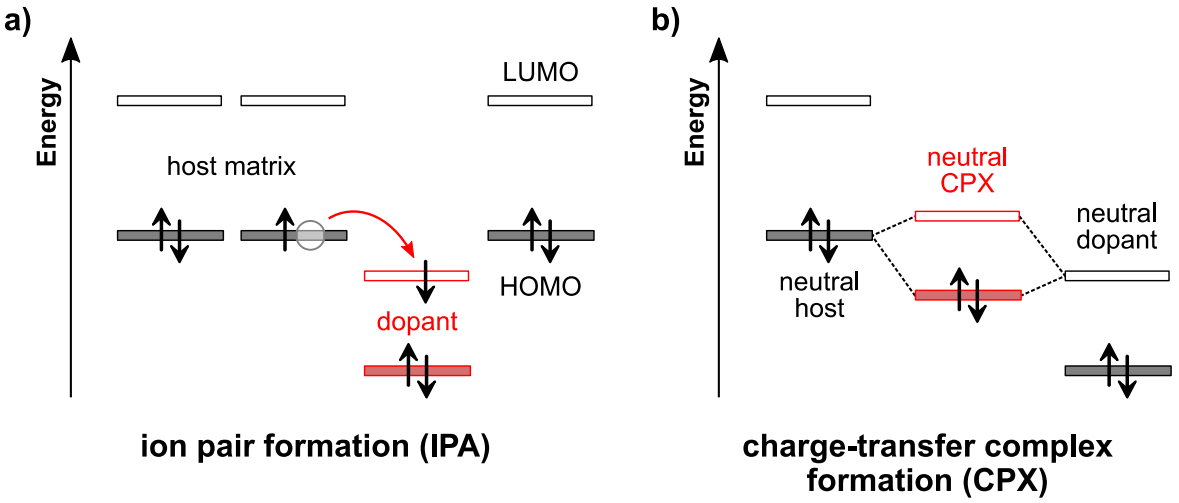

Figure 2.21 Distinct mechanisms occurring during molecular p-doping with organic semiconductors. **a)** In ion pair (IPA) formation, an electron is transferred from the HOMO of a host molecule to the LUMO of the dopant, thus creating a mobile hole charge carrier within the host matrix. **b)** Formation of a ground-state charge-transfer complex (CPX) due to overlap of the frontier orbitals of host and dopant. Here, a new set of states is created for the complex.

$$E_{\mathrm{CPX}}^{\mathrm{H/L}} = \frac{E_{\mathrm{host}}^{\mathrm{HOMO}} + E_{\mathrm{dop}}^{\mathrm{LUMO}}}{2} \pm \frac{1}{2}\sqrt{\left(E_{\mathrm{host}}^{\mathrm{HOMO}} - E_{\mathrm{dop}}^{\mathrm{LUMO}}\right)^2 + 4\beta^2}\,, \tag{2.30}$$

where $E_{\mathrm{host}}^{\mathrm{HOMO}}$ is the energy of the HOMO level of the host, $E_{\mathrm{dop}}^{\mathrm{LUMO}}$ the energy level of the LUMO of the dopant, and β the resonance integral describing the interaction.[155] This relation shows that for CPX formation to occur, condition (2.29) does not have to be fulfilled. Accordingly, the process of CPX formation can occur even in cases where IPA formation is not possible, which was indeed observed for different material combinations not fulfilling condition (2.29).[24,155,156],[A2] However, since the newly created empty level of the complex lies above and the filled level below the HOMO of the host, the CPX complex requires an additional energy to be ionized and allow the creation of a mobile hole in the host matrix. Consequently, CPX formation results in notoriously low doping efficiency, i.e., low yield of mobile charge carriers generated per dopant molecule, and is, therefore, not favorable for applications.[24] Since CPX formation requires a strong overlap of the frontier orbitals of both host and dopant, a strategy to avoid CPX formation (as deployed in this thesis) is to use bulky host or dopant molecules with side-groups, which lead to steric hindrances effectively prohibiting an overlap of the frontier orbitals.

Until recently, the doping mechanisms were observed to occur exclusively, in the sense that for given host-dopant material pair either only IPA or only CPX formation took place. However, lately, it was demonstrated that by employing special processing conditions, charge transfer complexes (CPXs) can also be achieved when doping P3HT with F_4TCNQ, which was evidenced by partial charge transfer measured via FTIR.[154] Hitherto, only IPA formation was observed for the doping of P3HT with F_4TCNQ.[50,150],[A2] This has been the

only study which was able to show the CPX and IPA formation to occur within the same material pair. Nonetheless, there is no general limitation known, due to which IPA and CPX formation cannot take place simultaneously for a given material pair.

2.2.2 p-Type Doping

In the early days of doping organic semiconductors, oxidizing gases like iodine (I_2), bromine (Br_2), chloride (Cl_2) or even oxygen[32] (O_2) were employed to p-dope organic semiconductors.[3,18,157,158] However, these atomic dopants lead to device instabilities due to their tendency to diffuse, as discussed above. The utilization of molecules with a quinone structures with unsatisfied aromatic rings as p-dopants marked the beginning of molecular p-dopants, a variety of which has been developed over the past two decades. The prototypical compound of this class is TCNQ, which was studied in great detail due to its ability to form charge-transfer salts with small donor molecules.[159,160] However, due to its low EA of 4.2 eV,[161] TCNQ is not able to dope most organic semiconductors employed in organic electronic devices, which usually display IEs in the range of 5-6 eV. For this reason, molecular dopants with higher EAs have been developed throughout the years, where the most commonly used synthetic strategy involves the development of an electron-poor core consisting of a π-system and the outside decoration with electron withdrawing substituents like esters, fluorine, -CF_3, or nitrile groups, further depleting the core and thus increasing the EA.[21]

The most prominent and well-studied molecular p-dopant is the fully fluorinated version of TCNQ, F_4TCNQ, which has an EA of 5.2 eV and is thus able to effectively dope a large number of organic semiconductors.[33,38,140,150,154,155,162,163] However, F_4TCNQ sublimes at around 80 °C in UHV and is known to contaminate the vacuum chamber in which it was deposited, leading to unwanted (partial) doping of samples subsequently transferred through or fabricated in this chamber.[164,165] Furthermore, F_4TCNQ was shown to diffuse in polymers such as P3HT when an electric field is applied to the doped film.[166,167] For this reason, larger molecular dopants like quinodimethane based TCNNQ and F_6TCNNQ[33] or fluorinated fullerenes like $C_{60}F_{36}$ have been developed, which display EAs of 4.7 eV, 5.6 eV and 5.4 eV, respectively.[161,165,168] These larger molecules have higher sublimation temperatures and thus can be reliably thermally evaporated, not causing contamination of other samples. Moreover, also due to their larger size they are less prone to thermal or electric field induced diffusion.[169]

[32] Doping by oxygen mainly occurred as a side product of incident exposure to air.[157]

[33] 11,11,12,12-tetracyanonaphtho-2,6-quinodimethane and hexafluoro-tetracyanonaphtho-2,6-quinodimethane, respectively.

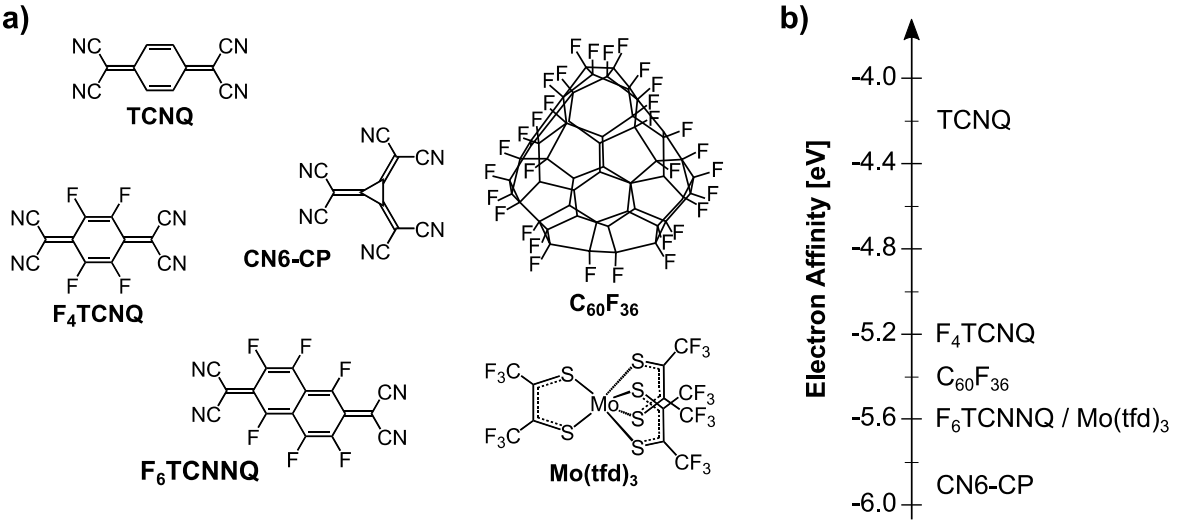

Figure 2.22 a) Chemical structures and **b)** electron affinities of typical p-type dopants.

The planarity of the F_xTCNQ and F_xTCNNQ compounds offers advantages, but also disadvantages. On the one hand, their planarity lets these molecules easily blend with the host molecules.[152,170] On the other hand, however, it increases their susceptibility to undergo CPX formation with also planar host molecules, leading to very low doping efficiencies as discussed above. To circumvent this issue, bulky molecules like the aforementioned $C_{60}F_{36}$ or the organometallic dopant $Mo(tfd)_3$ can be employed. The pinwheel like structured $Mo(tfd)_3$ was shown to be stable against diffusion and its EA of 5.6 eV is similar to F_6TCNNQ.[171] Recently, even a solution processable derivative of $Mo(tfd)_3$ was developed by replacing one $–CF_3$ on each side-group with an ester.[172] However, the tendency of F_4TCNQ to easily diffuse can be also utilized, by solution (sequential spin-coating) or vacuum depositing the dopant on top of already prepared host films, which was shown to lead to improved film qualities and conductivities in the same order or even exceeding the ones of co-processed samples.[59,173–175]

Nearly all of the presented molecular p-dopants can be processed both from solution and via thermal evaporation in vacuum, except $C_{60}F_{36}$, which can be only processed in vacuum. This fact makes molecular p-dopants suitable for a variety of applications in organic electronic devices.[22,141,142] The molecular p-dopant with the to-date highest EA is CN6-CP,[34] which was reported to have an EA of 5.9 eV.[40] Nonetheless, no molecular p-dopant is currently able to effectively dope large band gap materials with IEs exceeding 6 eV. This domain thus still remains the regime of metal oxides like WO_3, ReO_3 or MoO_3.[176–179] Metal oxides have been employed to realize efficient and long-term stable p-type doping of wide band gap organic materials.[180] However, their EA largely depends on the used processing

[34] Hexacyano-trimethylene-cyclopropane.

conditions, which is also known to decrease by up to 1 eV upon air exposure. Moreover, they need to be processed at higher temperatures than molecular dopants, although the most commonly used MoO_3 can be sublimed at temperatures around 400 °C in UHV and can thus be deposited from standard quartz crucibles like they are used for thermal evaporation of molecular dopants. However, since this section focuses primarily on molecular dopants, the reader is referred to the excellent review of ref. [180] for further information. Other used p-dopants for organic semiconductors are Lewis acids, the most common one being $FeCl_3$.[141] Lewis acids exhibit much larger solubilities than molecular p-dopants, which allows processing from higher concentrated stock solutions improving both film thickness and quality. Recently, the strong Lewis acid BCF3[35] has been shown to effectively dope P3HT leading to three times higher conductivities than similarly F_4TCNQ doped P3HT, which was related to the improved film quality.[181] However, its exact doping mechanism is not yet understood and only proposed to occur via an attack of the electrophilic borane center on the sulfur atom in the thiophene-moiety.

2.2.3 n-Type Doping

While a variety of stable molecular p-dopants has been developed and successfully deployed in devices during the past decade, molecular n-doping is generally more challenging. This is related to condition (2.29) that these molecules, if operated as one-electron reductants, must have an IE lower than the EA of the host material, which increases their susceptibility to oxidation. n-Doping is particularly challenging for organic semiconductors used as electron-transport materials (ETMs) in OLEDs, which generally have an EA lower than 3 eV, requiring dopants with comparably low IE.[182,183] For this reason, n-doping has been the domain of alkali metals like sodium (Na), potassium (K), lithium (Li), or cesium (Cs) for a long time, the use of which, however, leads to device instabilities as discussed before.[19,20,184,185]

The first molecular n-dopant used was BEDT-TTF,[36] which, although only semi-efficient, proved the general possibility of n-doping employing molecular dopants.[186] Later several other one electron reductants were explored like TTN,[37] organometallic compounds such as $[Ru(terpy)_2]^0$,[38] $W_2(hpp)_4$ or $Cr_2(hpp)_4$,[39] and organometallic sandwich compounds like cobaltocene or decamethylcobaltocene.[34,187–190] Although some of these dopants were found to be very efficient, e.g. doping of C_{60} with $W_2(hpp)_4$ and $Cr_2(hpp)_4$ lead to

[35] Tris(pentafluorophenyl)borane.
[36] Bis(ethylenedithio)-tetrathiafulvaene.
[37] Tetrathianaphthacene.
[38] Bis(terpyridine)ruthenium(II).
[39] Dimetal complexes formed by tungsten or chromium, respectively, and the anion 1,3,4,6,7,8-hexahydro-2H-pyrimido[1,2-a]pyrimidine (hpp).

conductivities of up to 4 S/cm,[190] they are not stable in air due to their low ionization energy, which complicates handeling the materials prior to processing.[40] In addition, cobaltocene and its derivative have a high vapor pressure and therefore can only be deposited in vacuum by creating a partial background pressure of dopants during the evaporation of the host molecules.[188,189]

A general approach to circumvent this issue involves the use of air-stable precursors, i.e. molecules with a relatively high IE, which are used both via solution and vacuum processing. These precursors a) liberate strongly reducing species during or subsequent to their insertion into the organic host or b) do not react via a simple one-electron transfer, but in a fashion where the electron transfer is accompanied by bond cleavage and/or formation. Approach a) was first exemplified by certain cationic dyes, such as pyronin B chloride,[191–194] and later benzoimidazole derivatives like *o*-MeO-DMBI-I.[41,195] Here, the corresponding neutral radicals (or other highly reducing species) sublime from the precursor material when heated in UHV. This approach has been used to efficiently dope materials with EA ≥ 4.0 eV.[193] It was also reported to dope materials with lower EAs, which, however, can be considered to be not very efficient as the conductivity was found to increase by only one order of magnitude.[196] A drawback of this method is that during deposition also impurities are released as side-products, which are uncontrolledly incorporated into the organic film.

For the second approach, several classes of materials have been employed including (i) hydride-reduction products of stable organic cations, (ii) tetraalkylammonium salts of inorganic ions such as halides, and (iii) dimers formed by certain 19-electron organometallic sandwich compounds. Class (i) consists of molecules such as leuco crystal violet[192] and DMBI[42] derivatives,[195,197–199] which react via a transfer of a hydrogen atom and an electron to the host, in some cases only following thermal or photochemical activation. These compounds have been shown to effectively n-dope fullerene derivatives (EA of 3.8 to 4.0 eV)[195,197,200,201] and the polymer P(NDIOD-T2)[43] (EA = 3.9 eV),[198] but have also been reported to doped TIPS-pentacene[44], which has an EA of around 3.0 eV.[30] However, in the latter case, it is likely that the observed change from p- to n-channel behavior can be attributed to trap-filling rather than generation of additional free carriers.[201] Class (ii) molecules have been reported to be effective solution-processible dopants for fullerenes.[202] Here, the reaction proceeds through a nucleophilic attack of the halide ion

[40] E.g. loading the material in vaccum chambers for molecular beam deposition.
[41] 2-(2-methoxyphenyl)-1,3-dimethyl-1*H*-benzoimidazol-3-ium.
[42] 2-aryl-1,3-dimethyl-2,3-dihydro-1*H*-benzoimidazole.
[43] Poly{[*N,N*´-bis(2-octyldodecyl)-napthalene-1,4,5,8-bis(dicarboximide)-2,6-diyl]-alt-5,5´-(2,2'-bithiophene)}.
[44] 6,13-bis(triisopropylsilylethynyl)pentacene.

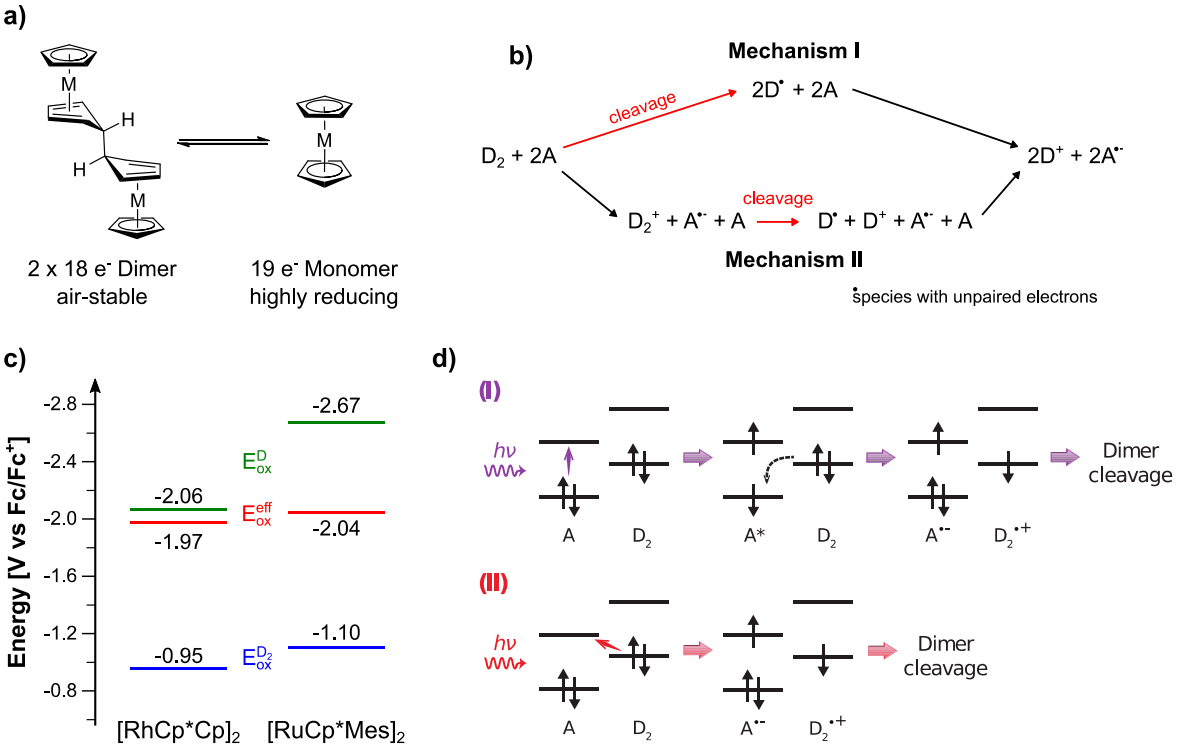

Figure 2.23 a) General chemical structure of organometallic dimers. The air-stable dimer can dissociate into two highly reducing monomers by cleavage of the central C-C bond. **b)** Main doping mechanisms of the dimer. In mechanism I, the dimer undergoes an endergonic cleavage, followed by a rapid exergonic electron transfer. In mechanism II, the dimer first undergoes an endergonic electron transfer followed by a rapid cleavage of the dimer cation and a second electron-transfer reaction. **c)** Electrochemical redox-potentials of the dimers. The oxidation potential of the dimers $E_{ox}^{D_2}$ and monomers E_{ox}^{D} as well as the calculated effective reducing strength E_{ox}^{eff} are shown for the organometallic dimers $[RhCp^*Cp]_2$ and $[RuCp^*Mes]_2$. Data taken from ref. [203]. d**)** Dominant pathways of photoactivation. Top: electron transfer from the dimer to the host excited state, followed by a cleavage of the dimer cation. Bottom: dimer-to-host electron transfer through an intermolecular charge-transfer absorption, followed by a cleavage of the dimer cation. Fig d) reproduced from ref. [A4].

on a fullerene. However, for both of these classes also side products, which might be incorporated as impurities, can be expected to occur during the doping process.

Recently, class (iii) consisting of organometallic dimers was introduced, which can dissociate into highly reducing monomers during or subsequent to deposition, as shown in Figure 2.23 a).[203,204] These dimers have been previously used via both solution and vacuum processing to dope several organic materials, both polymers and small molecules, with EAs ranging from 3.9 eV down to 2.8 eV,[205,206] including ultralow doping to increase conductivity by the filling of low lying trap states.[207,208] The dimers consist of two metallocene monomers, where a group 9 metal (e.g. rhodium or iridium) or a group 8 metal (e.g. ruthenium) is sandwiched between two cyclopentadiene groups or a cyclopentadiene and an arene group, respectively. These monomers have a 19 electron configuration and, thus, are highly reducing, but also highly oxygen and moisture sensitive. When the

monomers are formed by an one-electron reduction from their respective 18 electron cations, they tend to dimerize through the formation of a carbon-carbon bond resulting in moderately air-stable dimers with a stable 18 electron configuration.

The doping process of the dimers was found to occur via two distinct mechanisms, as depicted in Figure 2.23 b).[205] In mechanism I, the dimer in presence of acceptor molecules undergoes a reversible endergonic cleavage forming two highly reducing monomers, which is followed by a rapid exergonic electron transfer. In mechanism II, the dimer has to undergo a reversible endergonic electron transfer first, which is followed by an irreversible dissociation of the dimer into a monomer cation and a highly reducing monomer. The second monomer can then also undergo an exergonic electron transfer. While for $[RhCpCp^*]_2$ both mechanisms are possible, where the relative importance depends on the chosen acceptor molecules and specific experimental conditions, $[RuCp^*Mes]_2$ can only react via mechanism II.[204]

Cyclic voltammetry (CV) [see Figure 2.23 c)] revealed the oxidation potentials of the monomers $E(M^\bullet \rightleftharpoons M^+)$ to be 1-2 V higher than the oxidation potentials of the respective dimers $E(M_2 \rightleftharpoons M_2^{\bullet+})$, showing the high reducing strength of the dimers.[45,205] However, the dimer has to be cleaved at some point regardless of the underlying doping mechanism in order to dope host molecules, which is associated with a bond dissociation energy ΔG_{diss}. Therefore, its overall thermodynamic reducing ability is not equal to the oxidation potential of the monomer $E(M^\bullet \rightleftharpoons M^+)$, but rather the potential of the monomer cation / dimer couple $E(0.5M_2 \rightleftharpoons M^+)$. This quantity is very important for the dimers' use as a dopants, but cannot be accessed by CV measurements alone. For this reason, the dissociation energies $\Delta G_{\mathrm{diss}}(M_2)$ were estimated using DFT calculations, with which the effective reducing strength can be calculated via

$$E(0.5M_2 \rightleftharpoons M^+) = E(M^\bullet \rightleftharpoons M^+) + \frac{1}{2F}\,\Delta G_{\mathrm{diss}}(M_2)\ , \tag{31}$$

where F is the Faraday constant.[203] The effective reducing strengths for the dimers used in this work are also depicted in Figure 2.23 c). This effective reducing strength of around -2 V vs Fc/Fc^+ marks the overall thermodynamic reducing ability of the dimers and corresponds to the found EA limit of 2.8 eV, down to which the dimers can dope organic host materials.[205,206]

Nevertheless, in our recent study, we were able to break this thermodynamic limit by demonstrating that photo-activation of $[RuCp^*Mes]_2$ results in kinetically stable and efficient n-doping of low EA host semiconductors with EAs in the order of 2 eV.[A4] Here,

[45] The reduction potential of oxygen $E(O_2 \rightleftharpoons O_2^{\bullet-})$ is usually in the range of -1.2 to -1.4 V vs. Fc/Fc^+, which by comparison with the oxidation potentials of the dimers and their monomers explains the moderately air stability of the dimers and the high air sensitivity of the monomers.[203]

after co-evaporation of the low EA host and $[RuCp^*Mes]_2$, the conductivity was found to remain in the same order of magnitude as the one of the pristine host, whereas the Fermi level was already slightly shifted upwards in the gap. Upon UV irradiation, however, the conductivity increased over several orders of magnitude, while the Fermi level was further shifted upwards and pinned at the LUMO of the host. Activation by UV irradiation was found to proceed via an electron transfer from the dimer to the host excited state, followed by a cleavage of the cationic dimer, as depicted in the upper part of Figure 2.23 d). Surprisingly, the activation was also found to occur by irradiation with visible light (even lower energetic red light) although neither the host nor the dopant absorb in this region. Here, the activation proceeds via a dimer-to-host electron transfer through an intermolecular charge-transfer (CT) absorption as depicted in the lower part of Figure 2.23, which is also followed by a cleavage of the cationic dimer. Furthermore, OLEDs employing electron transport layers doped in this manner exhibit a significantly improved performance relative to un-doped devices. Our study proofed the combination of cleavable dimers with photo-activation to be a promising avenue for efficient n-doping of materials with very low EA, a range that so far was the domain of alkali metals.

3 THEORY OF EXPERIMENTAL METHODS

In this chapter, the theory behind the experimental methods is introduced. As the primary and most advanced technique used in this thesis, first, the basic principles of photoelectron spectroscopy (including inverse photoelectron spectroscopy) will be discussed. Next, optical absorption spectroscopy will be presented, which is a simple yet powerful technique. In the following, the basics of cyclic voltammetry will be introduced, which was, however, not conducted by myself, but plays a crucial role in the discussion in chapter 5. Furthermore, the measurement of electrical conductivity by current-voltage measurements will be presented, followed by a brief introduction of scanning force microscopy. The exact experimental setups and data analysis methods will be discussed in chapter 4.

3.1 PHOTOELECTRON SPECTROSCOPY

Photoelectron spectroscopy (PES) is a powerful and widely used technique to characterize the electronic properties and chemical composition of materials. The field of photoelectron spectroscopy was developed in the early 1960s by the pioneering works of the groups of Spicer,[209,210] Turner,[211] and Siegbahn.[212,213] Due to further development of the technique in the following decades, it has been established as one of the most important experimental methods to study the electronic structure of molecules, solids, and surfaces thereof.[214]

The basic principle of this technique exploits the external photoelectric effect, whereby a sample is irradiated with electro-magnetic radiation with a defined (monochromatic) photon energy $\hbar\omega$ leading to the emission of electrons, the so-called photoelectrons. The kinetic energy distribution of the emitted photoelectrons $I(E_{\mathrm{kin}})$ is then measured by an analyzer. The analysis of $I(E_{\mathrm{kin}})$ allows deep insights into the density of electronic states (DOS) of the sample, since in a first approximation the distribution of electronic states within the sample is pointwise proportional to the kinetic energy distribution, $I(E_{\mathrm{kin}}) \propto DOS(E_{\mathrm{B}})$. The measured kinetic energy of the emitted electrons is related to the binding energy E_{B} via the following equation,

$$E_{\mathrm{kin}} = \hbar\omega - \phi_{\mathrm{D}} - E_{\mathrm{B}} \ , \tag{3.1}$$

where E_{B} is the binding energy of the electron in its initial orbital with respect to the Fermi level E_{F} and ϕ_{D} is the work function of the detector. This equation, however, only applies to primary electrons, which have not undergone inelastic scattering within the sample and have thus not lost any kinetic energy. Electrons which have indeed undergone inelastic scattering before being able to escape the sample are called secondary electrons and

contribute to a background, which is increasing to lower kinetic energies. In point of fact, the inelastic mean free path (IMFP) of the electrons in a solid is very short and thus the probing depth of PES is only a few nm (see discussion in the next subsection), which makes PES a very surface sensitive technique. Also for this reason, PES is typically performed in ultrahigh vacuum (UHV) with pressures lower than 10^{-9} mbar in order for the escaped photoelectrons to reach the detector without scattering at residual gas molecules.

As photoelectrons are emitted, photoholes are continuously created within the sample, which have to be extracted to the substrate in order to keep charge neutrality. However, due to the notoriously low conductivity of organic molecules, the sample may get positively charged during the PES experiment with most of the charge residing at the sample surface. This positive potential built-up at the surface leads to a decrease in kinetic energy of the emitted photoelectrons and consequently, a shift of the spectra to higher binding energies is observed throughout the measurement. Thus, great care has to be taken in order to avoid this sample charging. A method to compensate for charging is to illuminate the sample with white light during the measurement in order to create excitons, which can dissociate and thus compensate the photoholes.[215],[46]

PES is commonly divided by the kinetic energy $\hbar\omega$ of the incident photons into ultraviolet photoelectron spectroscopy (UPS, $\hbar\omega$ = 5-100 eV) and X-ray photoelectron spectroscopy (XPS, $\hbar\omega$ > 1000 eV), both of which will be further addressed in subsections 3.1.2 and 3.1.3, respectively. The penetration depth of the incident photons is typically of the order of 1-10 µm, which is much larger than the actual probing depth in the order of a few nm and therefore leads to the backgrounds observed in the measured spectra of UPS and XPS.

3.1.1 Process of Photoemission

The process of photoemission of a single electron in a PES experiment can be described by a three-step model, which is illustrated in Figure 3.1.[209,216] This model is based on a purely phenomenological approach and the photoemission process can be better described by a one-step model.[217] However, the more intuitive three-step model has been proven quite successful in the description of the photoemission process and can describe many phenomena observed during PES experiments. The model consists of three individual steps, which are considered to be independent of each other:

1. Photoexcitation of an electron in the sample,
2. Transport of the electron to the sample surface,
3. Escape of the electron into the vacuum and detection.

Each of these steps will be treated in the following in more detail.

[46] This method is typically used for organic semiconductors. Another method employs the use of an low energy electron flood gun to compensate photoholes by introducing additional electrons.

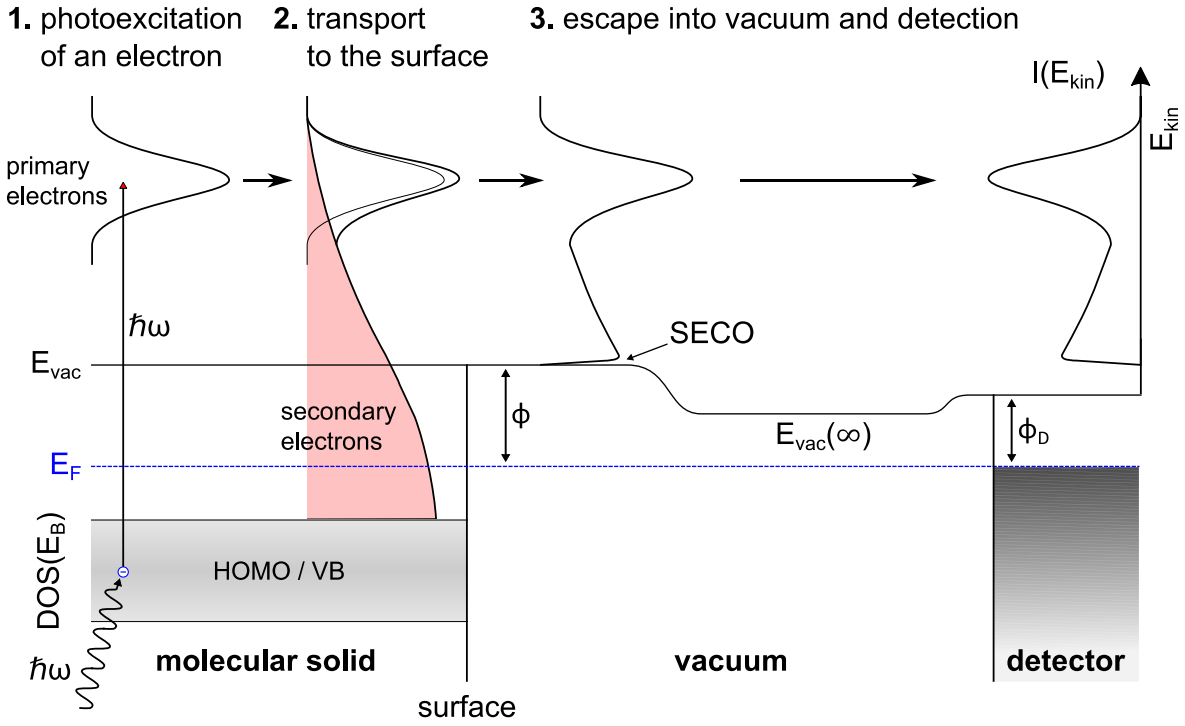

Figure 3.1 Three-step model of the PES measurement process. First, an electron is photoexcited by an incident photon. Second, it travels through the sample to the surface, on the way to which it can undergo scattering processes. Third, the electron escapes into the vacuum, if it is able to overcome the work function of the sample and, finally, is detected. Based on ref. [216] and ref. [218].

Step 1 – Photoexcitation of an electron in the sample

In the first step, an incident photon with energy $\hbar\omega$ hits the sample and is locally absorbed leading to the photoexcitation of an electron from the valance band (UPS) or atomic core levels (XPS) to empty states above the vacuum level E_{vac}. Hereby, the electron is excited from its initial state i with wavefunction ψ_i and energy E_i to the final state f with wavefunction ψ_f and energy E_f by the exciting electromagnetic field of the photon with vector potential $\boldsymbol{A}$. Following Fermi's golden rule in first order perturbation theory, the detected intensity I as a result of this photon-induced excitation to a final state $\psi_\mathrm{f} = \psi_{\boldsymbol{\kappa},\mathrm{s}}$ can be expressed as

$$I_{\boldsymbol{\kappa}}(\hbar\omega) \propto \frac{2\pi}{\hbar}\sum_{s}\left|\left\langle\psi_{\boldsymbol{\kappa},\mathrm{s}}\left|\frac{e}{m_\mathrm{e}c}\boldsymbol{A}\cdot\hat{\boldsymbol{p}}\right|\psi_\mathrm{i}\right\rangle\right|^2\delta(E_\mathrm{f}-E_\mathrm{i}-\hbar\omega)\ , \tag{3.2}$$

where $\hat{\boldsymbol{p}}$ is the momentum operator of the photoelectron with momentum $\boldsymbol{\kappa}$ as well as kinetic energy $E_\mathrm{kin} = \hbar^2\boldsymbol{\kappa}^2/2m_e + V_0$ (at a constant inner potential V_0),[47] m_e is the effective mass of the electron and c the velocity of light.[214] Here, the index s resemble a

[47]The final continuum state to which the electron is excited is assumed to be a parabolic free-electron like band in a constant inner potential V_0.[229] The delta-function $\delta(E_f - E_i - \hbar\omega)$ ensures the conservation of energy between the initial and final state.

set of quantum numbers containing all possible excitations of the final state, which will be discussed later. This equation is an appropriate basis for the theoretical description of most PES experiments.[48] At this point, it should be kept in mind that, while the measured intensity is proportional to the number of initial states for a given energy interval, the recorded spectrum is not per se proportional to the DOS of the sample, but only pointwise. Also, PES measures the final (N-1)-electron state after photoemission, which is the nearly fully relaxed positive polaron and is explicitly different form the initial N electron state (see also discussion in subsection 2.1.1).

During the photoexcitation, the remaining (N-1)-electron system can be further excited. In the case, where atoms themselves have a spin due to unpaired valence electrons, the new unpaired electron, which is left after photoemission, can couple to the spin of the unperturbed system. This will create several possible final state configurations and thus causes a multiplet splitting of the main photoelectron line. Furthermore, multi-electron processes give rise to several excitations. For example, in some cases, there is a finite probability that the remaining (N-1)-electron system is left in an excited state above the ground state. This leads to so-called shake-up lines a few eV higher in binding energy, since the kinetic energy of the photoelectron is reduced by the energetic difference between the excited and the ground state. For organic semiconductors, such lines are commonly observed in XPS, where the shake-up process is caused by the π-π* transition, schematically shown in Figure 3.2 a). High resolution spectra of the shake-up lines can be used to gain further insights into the charge redistribution within organic molecules upon photoexcitation.[219,220] Similarly, there are also shake-off lines, where the additionally excited electron goes to a continuum state above E_{vac}, or shake-down lines, where an excited state is relaxed, thus enhancing the kinetic energy of the photoelectron.

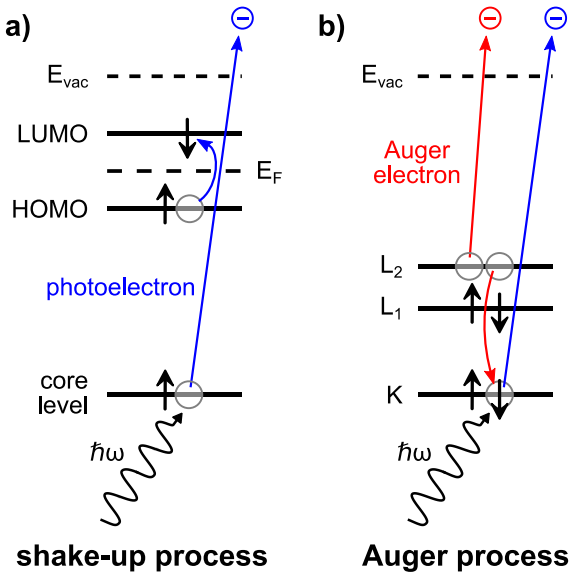

Figure 3.2 Multi electron processes. **a)** In a shake-up process, the outgoing photoelectron excites a π-π* transition, which lowers the kinetic energy of the photoelectron. b) In an Auger process, an electron from an outer shell falls into the empty state left by the photoelectron. Hereby, it transfers its energy to another electron in an outer shell, which is subsequently emitted as an Auger electron.

[48] For an actual calculation of the spectrum, more simplifications like the 'sudden approximation' have to be made, which, however, will not be discussed further at this point and the reader is referred to the respective literature.[214,216]

Another type of lines created during photoemission are Auger lines. Here, in addition to the emitted photoelectrons, Auger electrons can be emitted due to the relaxation of the created ions. In the Auger process, an electron from an outer shell falls into a lower shell left by a photoexcited electron, as illustrate in Figure 3.2 b). The hereby released energy is transferred to another electron in an outer shell, which is then emitted as an Auger electron. Since the energy difference between orbitals is fixed for each element, the emitted electron has a specific kinetic energy, which is independent from the incident photon energy used in the experiment. Auger electrons are usually labeled by three indices indicating the shell with the initial vacancy, the shell from which the electron relaxed and the shell from which the Auger electron was emitted. The main Auger series are the KLL, LMM, MNN and NOO series, which form rather complex patterns than single lines.

Step 2 – Transport of the electron to the sample surface

In the second step, the excited electrons travel to the surface of the sample. During their travel most of the electrons will undergo scattering processes with other electrons (mostly valence electrons) and only those which scatter elastically can be later traced back to the binding energy E_B of their initial state. These electrons are called primary electrons. Those which scatter inelastically lose a part or all of their kinetic energy E_{kin} and thus the information about their initial state.

The inelastic mean free path (IMFP) describes the mean distance an electron travels without inelastic scattering. In principle, the IMFP is a material specific quantity, however, a plot of the IMFP versus the kinetic energy of the electrons yields a somehow universal curve for all materials.[221] An analytical formula of the IMPF can be derived by modeling the electrons of a solid like a free electron gas. However, due to considerable scatter in the universal curve between materials, the IMFP for specific materials is usually derived by semi-empirical formulas.[221–224] For typical kinetic energies used in PES experiments, the IMPF lies in the region of 1-4 nm for XPS (E_{kin} = 200-1400 eV) and less than 2 nm for UPS (E_{kin} = 10-40 eV).

Due to the very short IMFP, a considerable amount of secondary electrons is created during photoemission experiments, which will contribute to a broad background. This background also leads to an asymmetrical form of photoelectron lines.[49] In general, three different models are used to describe the background of photoelectron lines. The first and simplest, yet physically unrealistic, is a linear background, where a straight line is drawn between the two endpoints of a peak. A more sophisticated model is the one developed by Shirley,

[49] Asymmetric line shapes can also have other origins. For example in metallic samples, the final hole state can couple to conduction electrons leading to an asymmetric tail at the high binding energy side of the photoelectron line. However, since metals were not studied by PES in this thesis, the line shapes asymmetry of metal core levels will not further be discussed at this point and the reader is referred to the respective literature.[375]

where each unscattered or elastically scattered photoelectron is assumed to be associated with a flat, continuous background of inelastically scattered electrons (assuming a constant scattering cross section).[225,226] This background is of the form

$$S_{\mathrm{S}}(E) \propto k \int_{E}^{\infty} (I(E') - S_{\mathrm{S},0}(E'))dE' \ , \tag{3.3}$$

where k is the constant inelastic energy loss cross section, $I(E)$ the measured spectrum at energy E and $S_{\mathrm{S},0}(E')$ the background intensity at lower binding energies before the line. The background intensity at a given energy is thus proportional to the total peak area above the background and to higher kinetic energy. The third and physically most realistic model was developed by Tougaard. It takes into account an energy loss cross section representing the probability of an electron at an energy offset undergoing a loss event and therefore contributing to the background.[225,227] The Tougaard background has the analytical form,

$$S_{\mathrm{T}}(E) \propto \int_{E}^{\infty} \frac{B(E'-E)}{(C+(E'-E)^2)^2} I(E')dE' \ , \tag{3.4}$$

where B and C are fitting parameters. However, since the Tougaard background needs a large energy range of up to 50 eV to give a reasonable fit,[50] the more easy-to-use Shirley background is commonly employed for most applications, which gives reasonable results when consistently used.

During the transport of the photoelectrons to the surface, there is also an enhanced probability for the electrons to undergo resonant scattering with electrons in the surface region (plasmons), which leads to a loss of a specific amount of energy. This energy loss produces a distinct, several eV broad feature at around 20-25 eV higher binding energy to the main photoelectron line, which is often termed energy or plasmon loss line.[228]

Step 3 – Escape of the electron into the vacuum and detection

In the third step, the electrons which are able to overcome the work function ϕ of the sample escape into the vacuum where they can be detected. Upon escape the sample, the electron's momentum component parallel to the surface $\boldsymbol{\kappa}_{||}$ is conserved, while the normal component $\boldsymbol{\kappa}_{\perp}$ is changed due to the change in potential. Thus, the parallel component can be expressed in dependence of the emission angle θ relative to the surface normal as

$$|\boldsymbol{\kappa}_{||}| = \kappa_{||} = \sqrt{\frac{2m_{\mathrm{e}}E_{\mathrm{kin}}}{\hbar^2}} \sin\theta \ , \tag{3.5}$$

[50] Which, of course, is very time-consuming and often does not yield qualitative better fits than the Shirley background.

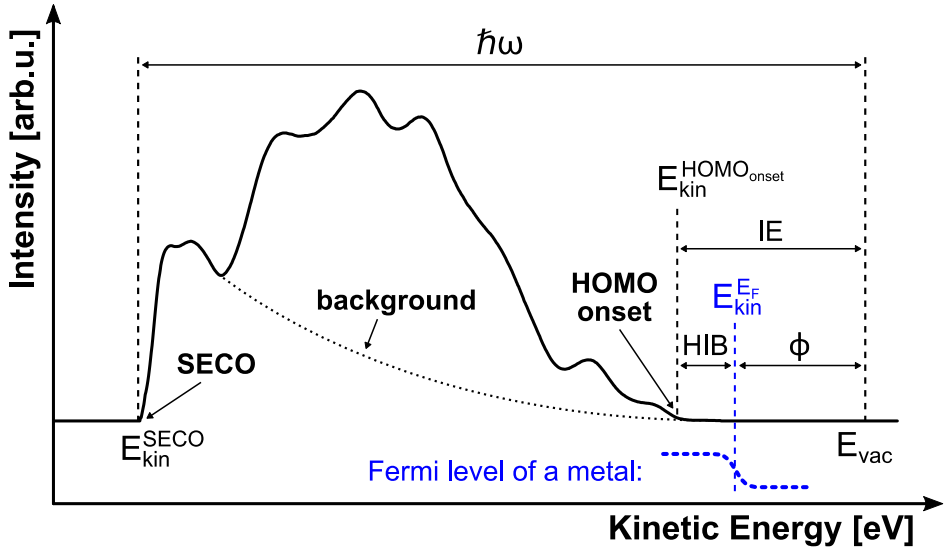

Figure 3.3 Typical spectrum of an organic semiconductor obtained by UPS. The binding energy of the spectra is given with respect to the Fermi level E_F, which is determined by measuring the Fermi edge of a metal.

where m_e is the free electron mass. Here, $\kappa_{||}$ is independent of the inner potential V_0, while $\kappa_{\perp}$ is not (for further details see e.g. ref. [229]). This relation shows that the band dispersion along $\kappa_{||}$ can be measured by changing the emission angle, which is performed via angle-resolved UPS (ARUPS).

During the escape of electron, however, the kinetic energy of some of the secondary electrons is too low to overcome ϕ. For this reason, a sharp decrease in intensity at low kinetic energies occurs in the recorded spectrum, which is called the secondary electron cutoff (SECO) and is used to determine the work function of the sample. Since the detector exhibits a work function ϕ_D, which is usually different from the sample work function ϕ, the potential in the region between sample and detector will gradually change. In the case $\phi_D > \phi$, electrons with kinetic energy $E_{kin} < (\phi_D - \phi)$ are unable to reach the detector and the exact position of the SECO cannot be measured. In order to overcome the detector work function, the sample is usually negatively biased when measuring the sample work function.

3.1.2 Ultraviolet Photoelectron Spectroscopy

Ultraviolet photoelectron spectroscopy (UPS) is a widely used technique to study the valence region of organic semiconductors and to determine their work functions. For this purpose gas discharge lamps are used as light sources which exhibit narrow lines. Most commonly employed are helium discharge lamps with their main emission lines of He I at 21.22 eV and He II at 40.81 eV).

A typical UPS spectrum is shown in Figure 3.3, where the number of detected electrons (usually normalized to counts per second) is plotted versus the kinetic energy E_{kin}. The electrons with the highest kinetic energy originate from the highest occupied states of the sample, i.e. the HOMO level of an organic semiconductor or the Fermi level of a metal. With decreasing kinetic energy the spectra shows the increasing secondary electron background, which ends in a sharp cutoff (SECO), where the electrons have a minimal kinetic energy $E_{\mathrm{kin}}^{\mathrm{SECO}}$. Since the sample and the detector are electrically connected and both have the same Fermi level in equilibrium, the minimal kinetic energy in the spectrum is defined by the difference of the work function of the sample ϕ and work function of the detector ϕ_{D},

$$E_{\mathrm{kin}}^{\mathrm{SECO}} = \phi - \phi_{\mathrm{D}} \,. \tag{3.6}$$

Thus, in order to calculate the sample work function, the detector work function has to be known, which, however, can be easily determined by measuring the kinetic energy of the Fermi edge of a metal,

$$\phi_{\mathrm{D}} = \hbar\omega - E_{\mathrm{kin}}^{\mathrm{E_F}} \,. \tag{3.7}$$

As evident from equations (3.1) and (3.7), the kinetic energy of the Fermi edge can be used as a universal reference point for the binding energy,

$$E_{\mathrm{B}} = \hbar\omega - E_{\mathrm{kin}} - \phi_D = E_{\mathrm{kin}}^{\mathrm{E_F}} - E_{\mathrm{kin}} \,. \tag{3.8}$$

Utilizing this relation, the work function ϕ, hole injection barrier HIB (defined as the energy difference between the Fermi level and the HOMO level onset), as well as the ionization energy IE can be determine from the UPS spectrum via

$$\phi = \hbar\omega - \left(E_{\mathrm{kin}}^{\mathrm{E_F}} - E_{\mathrm{kin}}^{\mathrm{SECO}}\right) - U_{\mathrm{BIAS}} \,, \tag{3.9}$$

$$HIB = E_{\mathrm{kin}}^{\mathrm{E_F}} - E_{\mathrm{kin}}^{\mathrm{HOMO_{onset}}} \,, \tag{3.10}$$

$$IE = \phi + HIB \,, \tag{3.11}$$

where U_{BIAS} is an applied bias to overcome the detector work function (see previous subsection).

Beside the primary emission lines, gas discharge lamps used for UPS also emit weak secondary emission lines. These lines will also photoexcite electrons and therefore lead to satellite features in the main spectrum, since they have a different photon energy than the primary emission line. In the case of helium I, the strongest secondary emission lines (denoted as β and γ) have a higher photon energy than the primary emission line α (as listed in

Table 3.1: Helium I emission lines. The relative intensities given here are approxi-mations and depend on the pressure in the discharge lamp. Data from ref. [230].

Emission Line		Energy [eV]	Approx. Intensity [%]
	α	21.22	100
He I	**β**	23.09	4
	γ	23.74	1

Table 3.1) and thus lead to satellite peaks at higher kinetic energy or lower binding energy, respectively. If one is not aware of the existence of these satellites or they are not properly removed from the spectra, one can easily confused satellite peaks at lower binding energies than the onset of the HOMO level with gap or tail states. Since the intensity of the emission lines is dependent on the pressure in the gas discharge lamp, the relative intensity of the secondary emission lines with respect to the primary is not fixed like and care has to be taken when removing these satellite peaks. The occurrence of satellite peaks can be avoided by using monochromatized light sources, where e.g. the light of a He gas discharge lamp is monochromated by employing a grating system.

3.1.3 X-Ray Photoelectron Spectroscopy

In contrast to UPS, X-ray photoelectron spectroscopy (XPS) is used to investigate atomic core levels. Since the binding energy of a core level is specific for each element, its chemical state, and chemical environment, XPS is widely used to study the chemical composition of surfaces, near surface bulk and interfaces by identifying and determining elemental concentrations and shifts in the core levels. Commonly, X-ray tubes are employed as photon sources, in which either an aluminum anode (Al-Kα, 1486.6 eV) or a magnesium anode (Mg-Kα, 1253.6 eV) is used to generate high energy photons.

In XPS spectra several types of lines are observed, most of which were already introduced in subsection 3.1.1. The main and most intense peaks in XPS spectra are the relatively symmetrical and narrow photoelectron lines, the shape of which will be addressed later on in this section. Due to spin-orbit coupling, doublet peaks are observed for orbitals with an angular momentum quantum number greater than zero, e.g. p, d and f orbitals. The p, d and f doublets have defined area ratios of 1:2, 2:3 and 3:4, respectively, while the energy distance between both components in the doublet is dependent on the specific orbital and element and can reach from less than 1 eV to over 100 eV.[228]

Table 3.2: Satellite lines of a non-monochromated Al-Kα and an Mg-Kα source. Displacements ΔE and relative intensities ΔI are given with respect to the primary line $\alpha_{1,2}$. Data taken from ref. [228].

	Al-Kα		**Mg-Kα**	
	ΔE [eV]	**ΔI [%]**	**ΔE [eV]**	**ΔI [%]**
$\alpha_{1,2}$	0	100	0	100
α_3	9.8	6.4	8.4	8.0
α_4	11.8	3.2	10.1	4.1
α_5	20.1	0.4	17.6	0.6
α_6	23.4	0.3	20.6	0.5
β	69.7	0.6	48.7	0.5

In most standard XPS setups, the X-ray sources are not monochromated and hence exhibit several minor lines at higher photon energies beside the characteristic main line. Similar to UPS, this gives rise to X-ray satellite peaks, exemplary shown in Figure 3.4 for a C1s core level. These peaks at lower binding energy have a defined relation of their relative intensity and displacement in binding energy to the main photoelectron peak, which is

characteristic for the anode material. Therefore, satellite peaks in XPS spectra can be removed from the spectra more easily than satellite peaks in UPS spectra. The energy displacements and relative intensities for satellites peaks of an Al-Kα and an Mg-Kα source are summarized in Table 3.2. Another type of lines are X-ray ghost lines which stem from contaminations in the X-ray anode. In most setups both an aluminum (Al) and a magnesium (Mg) anode are used, which can lead to Mg impurities in the Al anode and vice versa. These impurities typically lead to additional low intensity lines corresponding to the most intense lines in the spectra, having a characteristic energy displacement of the difference in photon energy, which is ±233 eV for the case of Al and Mg.

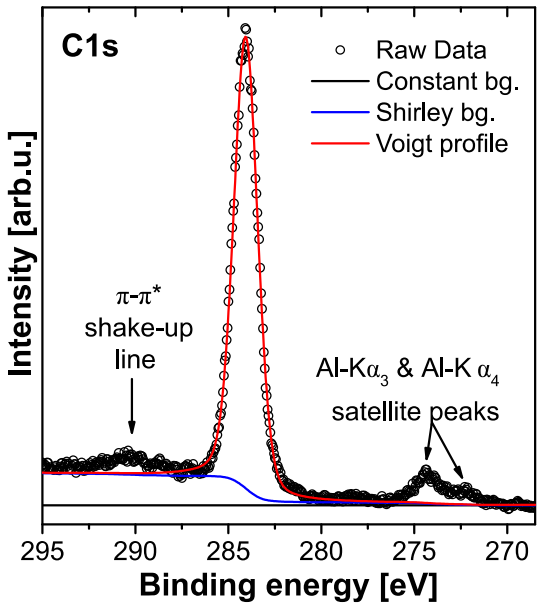

Figure 3.4 C1s core level of an organic semiconductor. The main peak can be described by a Lorentzian-Gaussian sum function (red) and is superimposed on a background, which can be described as a Shirley background (blue) and a constant background (black). The spectrum also shows the satellite peaks of a non-monochromated Al-Kα source at lower binding energy and the π-π* shake-up line at higher binding energy.

The line shapes of photoelectron lines in XPS spectra are defined by the photoemission process itself as well as by mechanisms of the experiment. A so-called natural broadening of photoelectron lines is caused by the lifetime of the core hole state created by photoemission. This lifetime leads to a shift in energy via the uncertainty principle, which results in a Lorentzian profile of the photoelectron line. The Lorentzian shape is considered to be the basic line shape, since other contributions (e.g. thermal broadening) can be minimized by for example cooling the sample. Experimental mechanisms like the instrumental response, thermal influences and the linewidth of the used X-ray source broaden the line further and are normally assumed to be Gaussian. Thus, photoelectron lines can be best described by a Voigt function, which is a convolution of a Lorentzian and a Gaussian function. The Voigt function is often approximated by a sum or product function of a Gaussian and a Lorentzian function, with which photoelectron lines can be nicely fitted as shown in Figure 3.4. The width ΔE_{FWHM} of a photoelectron line is usually given as the full width at half maximum (FWHM) and consists of several contributions (in Gaussian approximation)

$$\Delta E_{\mathrm{FWHM}} = \sqrt{\Delta E_0^2 + \Delta E_{\mathrm{T}}^2 + \Delta E_{\mathrm{p}}^2 + \Delta E_{\mathrm{a}}^2}\,, \tag{3.12}$$

where ΔE_0 is the natural line width, ΔE_T accounts for thermal broadening , ΔE_p is the width of the X-ray line and ΔE_a the analyzer resolution.

XPS spectra can be analyzed qualitatively by determining energetic shifts in line positions to receive information about the chemical environment of the specific elements. A different oxidation state, a chemical bond to an electron donating or withdrawing substituent, or an additional (partial) charge on an atom leads to a (small) redistribution of the atom's charge density. For this reason, the atom is exhibiting a slightly more positive or negative potential, which will effectively lower or enhance, respectively, the kinetic energy of a photoelectron originating from a core level of that atom. Thus, the determined effective binding energy $E_\mathrm{B,eff}$ will be energetically shifted from the 'normal' binding energy E_B of the atom by an energy ΔE_chem,

$$E_\mathrm{B,eff} = E_\mathrm{B} - \Delta E_\mathrm{chem} \,. \tag{3.13}$$

Information about the chemical environment of an atom can be deduced from the magnitude and sign of ΔE_chem. The origin of the chemical shift of the core levels always lies in changes in the valence states of the atom. In addition, since the binding energy is referenced to the Fermi level, shifts in core level binding energy can also be induced by shifts of the Fermi level in the gap of the organic semiconductor, caused by e.g. doping (compare section 2.2).

In addition, XPS can be also used quantitatively to determine the relative amount of different elementals present in the sample (or different species separated by a chemical shift). The area under a photoelectron line is proportional to the number of atoms of the respective element and can therefore be used for to determine the relative concentration of that element. Beside the number of atoms, the intensity (and thus the area) of a photoelectron line is also dependent on the flux of the X-ray photons, the photoelectric cross section of the atomic orbital, the angle between X-ray source and detector, the inelastic mean free path, and the transmission function of the analyzer. Most of these factors can be summarized in so-called atomic sensitivity factors (ASF), which are specific for each element, orbital and also the used analyzer.[228] The ratio between the numbers n_i of atoms of two elements in a sample (or two species of the same element in a different chemical environment) can thus be determined by their respective areas A_i via

$$\frac{n_1}{n_2} = \frac{A_1/ASF_1}{A_2/ASF_2} \,. \tag{3.14}$$

Since the IMFP of the photoelectrons is very short, an overlayer will significantly decrease the XPS signal from an underlying substrate or layer. For a substrate covered by a uniform and homogenous overlayer with thickness d, the ratio between the signal intensity of the overlay I_ovl and the substrate I_sub is given by

$$\frac{I_{\mathrm{ovl}}}{I_{\mathrm{sub}}}(\theta) = \frac{n_{\mathrm{ovl}}\sigma_{\mathrm{ovl}}\lambda_{\mathrm{ovl}}}{n_{\mathrm{sub}}\sigma_{\mathrm{sub}}\lambda_{\mathrm{sub}}}\left(\mathrm{e}^{d/(\lambda_{\mathrm{ovl}}\cos\theta)} - 1\right), \tag{3.15}$$

where σ_{i} is the cross section for the photoelectron emission.[223] As can be seen from this equation, when changing the angle θ relative to the sample's surface normal, the probed thickness is effectively change by $d_{\mathrm{eff}} = d/\cos\theta$. Thus, angle resolved XPS (ARXPS) can be used to study processes at surfaces or (buried) interfaces of samples consisting of (homogenously) stacked layers.

3.1.4 Inverse Photoelectron Spectroscopy

Inverse photoemission spectroscopy (IPES) is a technique to study the electronic structure of unoccupied states of surfaces and near-surface bulk of metals or semiconductors. The measurement process is basically a time-reversed process of PES. In IPES a collimated beam of energetically well-defined electrons produced by an electron gun is used to irradiate a sample. The electrons with kinetic energy E_{kin} couple to high lying unoccupied levels above the vacuum level and can then radiatively decay to lower lying unoccupied levels by emitting photons with energy $\hbar\omega$. Measuring the photon flux emitted from the sample can be used to map the electronic structure of the unoccupied states near the Fermi level, e.g. the LUMO, LUMO+1, etc. for an organic semiconductor. Similar to PES, IPES measures the energy levels of a nearly fully relaxed negative polaron, since the final state in the measurement process is an (N+1)-electron state.

In an IPES measurement, energy and electron momentum are conserved for elastic processes,[51] leading to the relation between the energy of the final state E_{f}, i.e. the unoccupied states, and the initial energy of the electrons E_i,

$$E_{\mathrm{f}} = E_{\mathrm{i}} - \hbar\omega\,. \tag{3.16}$$

As can be seen from this relation, IPES can be performed in two modes to get information about the energy of the final states E_{f}. The first mode is the so-called fluorescent mode, where the kinetic energy of the electron beam and hence E_{i} is fixed and a detector with a monochromator is used to scan the energy spectrum $\hbar\omega$ of the emitted photons. In return, in the so-called isochromat mode the energy E_{i} of the incident electrons is varied by varying E_{kin} and only photons with a fixed energy $\hbar\omega$ are detected by using a bandpass filter. The fluorescent mode has the advantage of having a better energy resolution than the isochromat mode, while the isochromat mode offers a stronger signal. The latter makes the isochromat mode the mode of choice for the investigation of organic semiconductors, since a weaker electron flux can be used to obtain a reasonable signal and thus sample damage by the incident electron beam can be reduced or even completely avoided.

[51] Similar to UPS, the electrons are also undergoing inelastic scattering processes before coupling to the high lying unoccupied states, therefore losing kinetic energy, which leads to a background in the IPES spectrum.

Similar to PES, the energy scale in IPES is calibrated by measuring the kinetic energy of the Fermi edge of a metal $E_{\mathrm{kin}}^{\mathrm{E_F}}$. IPES is able to measure the energy difference between the Fermi level and the LUMO, which is defined as the electron injection barrier

$$EIB = E_{\mathrm{kin}}^{\mathrm{LUMO_{onset}}} - E_{\mathrm{kin}}^{\mathrm{E_F}} . \tag{3.17}$$

Since there is no information about the position of the vacuum level in an IPES measurement, one has to align UPS and IPES spectra to be able to calculate the electron affinity of the sample,

$$EA = \phi - EIB , \tag{3.18}$$

with ϕ being the work function of the sample measured by UPS.

Due the conservation of momentum in the direction parallel to the surface, IPES can be also used to measure the dispersion of the unoccupied states by varying the incident angle of the electrons. Moreover, IPES is also a very surface sensitive technique. The inelastic mean free path and therefore the penetration depth of the used electrons with kinetic energies of typically 10 eV is in the order of 2 to 4 nm, making IPES a slightly less surface sensitive technique than UPS with an IMPF of less than 2 nm.[221]

Thus, in summary, UPS and IPES can be viewed as nearly fully complementary techniques, which are employed to measure the occupied and unoccupied DOS of samples.

3.2 Optical Absorption Spectroscopy

Optical absorption spectroscopy is a simple yet powerful experimental technique of the analytical chemistry to study the photo-physical properties of molecules. Since molecules have unique spectra of optical transitions, optical absorption spectroscopy allows the qualitative identification of the presence and kind of components in gaseous, liquid and solid samples. In addition, it is also used quantitatively to determine the amount of molecules contained in a sample as well as to study chemical reactions in solutions. For organic semiconductors, the transitions between HOMO and LUMO are usually of special interest with focus on the optical gap, which is

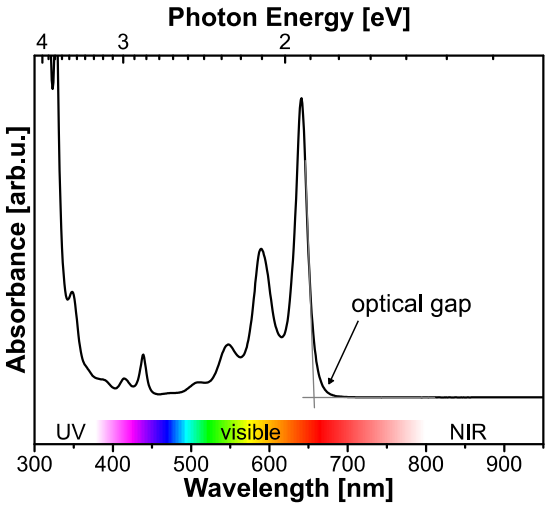

Figure 3.5 Typical optical absorbance spectrum of an organic molecule. The optical gap is determined by the onset of the absorption spectrum.

determined by the onset of the absorption spectra. A typical absorbance spectrum of an organic semiconductor is shown in Figure 3.5.

In general, optical absorption spectroscopy measures transitions between electronic states of organic compounds (compare subsection 2.1.2) by measuring the transmission of ultraviolet (UV: 200 to 400 nm), visible (Vis: 400 to 750 nm) and near infrared (NIR: 750 to 3000 nm) light through a sample. The intensity of electromagnetic radiation is attenuated when passing through an absorbing material, following an inverse exponential power law,

$$I = I_0 - \Delta I = I_0 e^{-\alpha(\lambda)\cdot d}, \tag{3.19}$$

where I is the intensity of the transmitted radiation, I_0 is the intensity of the incoming radiation, ΔI the change in intensity after transmission, $\alpha(\lambda)$ the material specific and wavelength λ dependent absorption coefficient and d the path length of the radiation in the sample. The change in intensity ΔI consists of several contributions arising from different interactions of the light with the material,

$$\Delta I = I_{\mathrm{abs}} + I_{\mathrm{sct}} + I_{\mathrm{ref}} + I_{\mathrm{int}} \approx I_{\mathrm{abs}} \ , \tag{3.20}$$

where I_{abs} arises from absorption of the light, I_{sct} from scattering, I_{ref} from reflection and I_{int} from interference effects. The latter three components are usually negligibly small or kept small, so that the change in intensity is mainly due to the absorption of the sample.

The basic measure of UV/Vis/NIR absorption spectroscopy is the absorbance A, or optical density,[52] which is defined as the negative logarithm of the transmittance T,

$$A = \log\left(\frac{I_0}{I}\right) = -\log(T) = \alpha^* x \quad with \quad \alpha^* = \frac{\alpha}{\ln(10)} \ , \tag{3.21}$$

where log() is the logarithm to base 10 and ln()the natural logarithm. For molecules in dilute solutions, molecule-molecule interactions are small and the molecules can be seen as nearly isolated. Here, the absorbance is given by the law of Beer-Lambert as a function of concentration c,

$$A = \varepsilon_\lambda \cdot c \cdot d \ . \tag{3.22}$$

Here, ε_λ is the decadic molar extinction coefficient, which is also a wavelength dependent quantity, and is usually reported for the maximum of an optical transition. During (chemical) reactions, there are points of specific wavelength in the optical absorbance spectra, where the extinction coefficients of reactant and product are the same and, consequently, the intensity of absorption stays constant during the reaction. These points

[52] Strictly speaking, the absorbance and optical density are not exactly the same, as the absorbance only includes absorption, while, in contrast, the optical density also includes scattering, reflection and interference. Since these three components are, however, usually neglected, the terms absorbance and optical density are used interchangeably.

are called isosbestic points and are an important indication of the linearity of the reaction (e.g. without formation of side-products).

As shown in equation (3.20), the measured changes in intensity are mainly due to absorption of the sample and reflection, scattering as well as interference are negligibly small. However, in cases, where they are not negligible, they lead to artifacts in the recorded absorbance spectra. Mostly elastic Rayleigh scattering will lead to a background which is increasing with decreasing wavelengths / increasing photon energies, since its intensity is proportional to $1/\lambda^4$ and E^4, respectively. In very homogenous thin films, interference will lead to enhanced transmission and therefore various dips in the absorbance spectra at specific wavelengths following the relationship $2d = (k + 1/2)\lambda$, where d is the thickness of the film.

Dual beam spectrophotometers are often used to perform optical measurements, where a beam of monochromatic light is split into a sample beam going through the sample to be measured and a reference beam. Here, the transmittance is recorded as the intensity difference between those two beams. The light in these spectrometers is usually generated by a deuterium lamp for the UV region and a halogen lamp for the visible and NIR region. After generation, the light is monochromated by using optical filters and grating systems and then split into the two beams. After passing through the sample chamber, the intensity of the beams is alternately measured via a photomultiplier for the UV and visible region, and a photoconductive or pyroelectric sensor for the NIR region and the transmittance for the specific wavelength is recorded.

With UV/Vis/NIR absorption spectroscopy, only electronic transitions are measured and in solution or solids, the vibronic structure often merges into a broad, sometimes even featureless band. To measure the vibronic transitions of molecules, infrared (IR) spectroscopy has to be employed.[53] IR spectroscopy is, however, only able to measure vibrations comprising a variation of the dipole moment. Such vibrations are thus called IR-active. A special version of IR spectroscopy is Fourier-transform infrared (FTIR) spectroscopy. In contrast to UV/Vis/NIR absorption spectroscopy, where only one wavelength is probed at a time, here, the IR light of a continuum source is used, which first enters an interferometer. In the interferometer, the beam is split into two beams following different paths and then combined again before it passes through the sample and is subsequently measured by a detector. The path lengths of one of the beam paths is always fixed, while the other is varied by length x. For different photon energies of the probing beam, the variation of x to constructive or destructive interferences and thus variations in the overall intensity $I(x)$, which is recorded by the detector as so-called interferogram. The

[53] Since FTIR spectroscopy, was only employed once in this thesis and only in order to extend optical spectra to lower photon energies, it will only be described briefly at this point.

spectrogram $I(\tilde{\nu})$ with dependence on the wavenumber[54] $\tilde{\nu}$ can be obtained from the interferogram by a Fast Fourier Transform algorithm, following the form

$$I(\tilde{\nu}) = \int_{-\infty}^{\infty} I(x) D(\tilde{\nu}) e^{i2\pi\tilde{\nu}x} dx \ , \tag{3.23}$$

where $D(\tilde{\nu})$ defines the bandwidth, where $D(\tilde{\nu}) = 1$ for detectable wavenumbers and 0 for the rest. The absorbance spectrum can be subsequently obtained via equation (3.21).

Compared to traditional scanning IR spectroscopic methods, FTIR has the advantage of a higher signal-to-noise ratio for a given scan-time, since information from all wavelengths are collected simultaneously. In addition, it has a higher throughput of light, since no entrance and exit slits are needed, also leading to a higher signal-to-noise ratio.[55] A third advantage is that the wavelength scale calibration is performed via a laser of a specific, known wavelength,[56] which more stable, since the scale does not depend on the mechanical movement of gratings and optical filters.

3.3 Cyclic Voltammetry

Cyclic voltammetry (CV) is the most common technique to study electrochemical reactions and to determine the oxidation and reduction potentials ($E_{\mathrm{ox}}/E_{\mathrm{red}}$, respectively) of organic semiconductors as well as molecules in general.[231] Although CV measurements were not performed by myself, redox-potentials measured by CV play an essential role in the discussion in chapter 5 and the theory behind CV shall thus be discussed at this point.

CV is principally similar to UPS/IPES, since both techniques measure the difference in total energy of a molecule between the N-electron ground state and the (N±1)-electron ionized state. However, there are fundamental differences in the measured values of the ionization process. The basic principle of a CV measurement is to cyclically sweep a potential between a working electrode and a reference electrode immersed in an analyte solution, while measuring the current response.[57] The plot of the measured current response in dependence of the applied voltage is called voltammogram, the typical form of which is displayed in Figure 3.6 and will be explained in the following. A fundamental equation to understand the processes occurring in an electrochemical cell is the Nernst equation, which

[54] The wavenumber $\tilde{\nu}$ is the inverse of the wavelength λ, thus directly proportional to the photon energy E.
[55] Although FTIR does not need entrance or exit slits, an aperture is required in order to restrict the convergence of the collimated beam in the interferometer. However, round apertures offer higher throughput than rectangular slits.
[56] A calibration has to be performed to define the point x = 0.
[57] In order to facilitate a good electrical conductivity of the solution, electrolytes are usually admixed to the analyte solution.

relates the potential of an electrochemical cell E to the formal potential $E^{0\prime}$ of the reversible process between oxidant (Ox) and reductant (Red) following

$$\mathrm{Ox} + z_\mathrm{e} e^- \rightleftharpoons \mathrm{Red} \ , \tag{3.24}$$

where z_e is the number of transferred electrons e^-.[58] The Nernst equation is expressed as

$$E = E^{0\prime} + \frac{RT}{z_\mathrm{e} F} \ln \frac{c_\mathrm{ox}}{c_\mathrm{red}} \ , \tag{3.25}$$

where R is the universal gas constant, T is the absolute temperature, F is Faraday's constant and c_i is the concentration of the respective species in the solution.[231] It predicts that, when a potential of $E = E^{0\prime}$ is applied to the electrochemical cell, the oxidant has to be reduced to its reductant form until both concentrations are equal, $c_\mathrm{ox} = c_\mathrm{red}$. This reduction is taking place at the working electrode of the electrochemical cell, which results in the measurement of a current as shown in Figure 3.6.

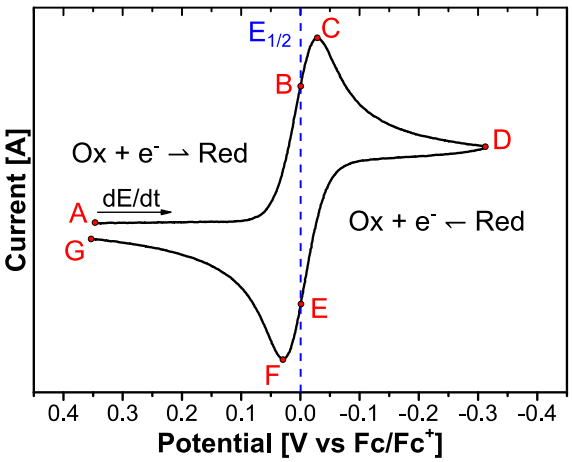

Figure 3.6 Typical cyclic voltammogram. Here, the reaction of the standard $\mathrm{Fc}^+ + e^- \rightleftharpoons \mathrm{Fc}$ is shown. The average between the peak potentials of forward and return scan marks the half-wave potential $E_{1/2}$, which is a good estimate of the formal potential. The potential in Volts is given with respect to the half-wave potential of $\mathrm{Fc/Fc}^+$ at 0 V (see text).

The following discussion of the oxidation / reduction processes, which lead to the typical form of the voltammogram as shown in Figure 3.6, is largely based on ref. [232] and assumes that a Nernstian equilibrium is instantly established for every change in potential. When the potential is scanned between point A and D, the oxidant is steadily reduced leading to a depletion of the oxidant at the working electrode. The maximum of current is achieved at point C, where the current is dominated by diffusion of oxidant species from the bulk solution to the electrode, where it is reduced. This leads to a built up of reductant species at the electrode, which form the so-called diffusion layer. At point C, the diffusion layer has grown so much that the mass transport of oxidant is slowed down leading to a decrease in current upon further scanning to point D. At point D, the switching potential (which is predefined before the measurement) is reached and the scan direction is reversed. Now, the formed reductant at the electrode gets oxidized back as the potential is scanned to point G leading to the formation of a

[58] In its original form, the Nernst equation relates the standard potential E^0 to the activities of the involved species. However, since the concentrations c of the species are more easily experimental accessible than the activities, the standard potential E^0 is replaced by the formal potential $E^{0\prime}$ and the activities are replaced by the concentrations.[231]

current of opposite sign. The maximum of this current is reached at point F, which is separated by 57mV/z_e from point C due to the diffusion of the analyte to and from the electrode.[231] The concentrations of oxidant and reductant are nearly equal at point B and E, which represent the average between the peak potentials of forward and return potential sweep and are thus easily accessible. This potential is called the half-wave potential $E_{1/2}$ and is a good estimate of the formal potential.

However, the formal potential is specific to the used experimental conditions and is only a relative measure of the ionization potential or the electron affinity in solution, since it is determined with respect to a reference electrode. Reported potentials are typically referenced to a standard measured under the same experimental conditions, often the ferrocene/ ferrocenium couple (Fc/Fc^+), since it has a well-defined redox-process and is stable in most employed solvents.[233] To calculate absolute values of the potentials, the potential of ferrocene with respect to the vacuum level has to be taken into account, which has been variously estimated to lie between -4.8 eV and -5.3 eV,[59] this value itself usually relying on estimation of the absolute value of the NHE (H_2/H^+) potential.[234,235] Thus, it is generally preferable to compare relative values referenced against Fc/Fc+ than to report absolute values. Similarly to the polarization energy in a thin film, which takes into account the environment of the charged molecule and its interaction with it, effects of solvent and electrolyte on the oxidation/reduction process of the molecule have to be considered. In analogy to equation (2.8) of subsection 2.1.1, the IE/EA in solution can be related to the IE/EA in gas phase by

$$IE_{\mathrm{sol}} = eE_{1/2}^{\mathrm{ox}} + C = IE_{\mathrm{gas}} - \Delta G_{\mathrm{solv}}^{+} \text{ and,} \tag{3.26}$$

$$EA_{\mathrm{sol}} = eE_{1/2}^{\mathrm{red}} + C = EA_{\mathrm{gas}} + \Delta G_{\mathrm{solv}}^{-}\,, \tag{3.27}$$

where e is the elementary charge, C the absolute potential of the used standard or reference electrode in the given solvent, and $\Delta G_{\mathrm{solv}}^{\pm}$ the total change in free energy of the oxidant and reductant upon solvation. Influences on the redox-potentials of different solvents and electrolytes are usually on the order of several 10 meV for typical molecular semiconductors and dopants, but can also reach values of a few 100 meV.[233,236]

The method to determine redox-potentials as described above is valid for reversible reactions. When the redox-process is quasi-reversible or even irreversible, the thermodynamically relevant formal potential cannot be reliably estimated. Moreover, determination of reliable values for polymers is also less straightforward.[235] Here, solution voltammo-grams can be complicated by slow diffusion, while the reversibility of that of films can be affected by relatively slow diffusion of charge-compensating electrolyte ions in and out of the films.

[59] For estimations in this thesis, the common value of -4.8 eV will be used following ref. [234].

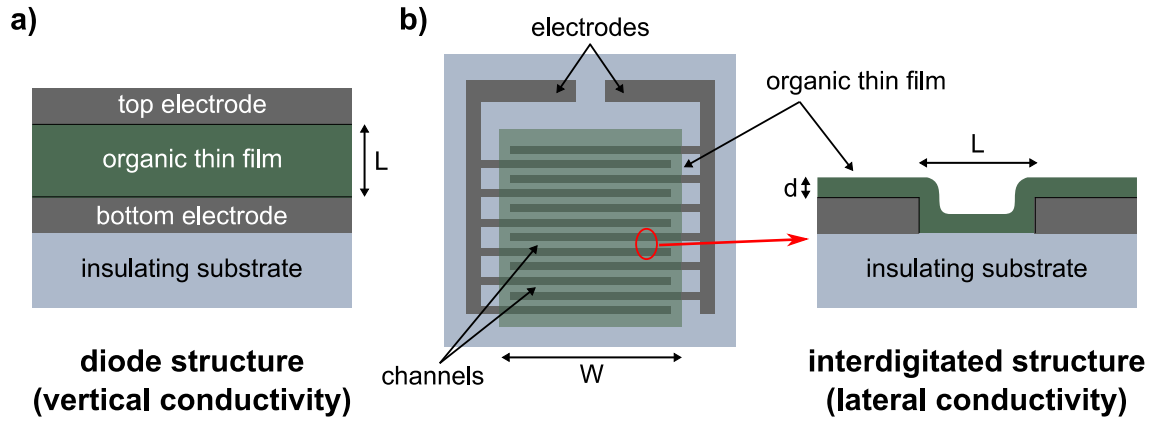

Figure 3.7 Different structures for IV-measurements. Currents can either be measured **a)** vertically in a (vertical) diode structure or **b)** laterally in an interdigitated structure (left – top view, right – side view). The interdigitated structure consists of multiple parallel connected channels in order to effectively decrease the measured resistance.

3.4 Electrical Conductivity Measurements

The electrical conductivity of an organic thin film can be determined from simple current-voltage (IV) measurements as described in subsection 2.1.3. Here, the current through an organic film between two metal contacts is measured for different applied biases. The conductivity σ of a sample can be determined from its IV characteristic in the Ohmic region via the relationship

$$\sigma = \frac{L}{R \cdot A}\,, \tag{3.28}$$

where R is the resistance given by the slope of the linear IV curve, L the length of the sample and A its cross sectional area. In general, the IV curve can be measured in two different configurations. The first one is the diode structure [shown in Figure 3.7 a)], where the organic thin film is sandwiched between two metal electrodes and the current is measured vertically to the main plane of the substrate. In the second configuration, the organic thin film is deposited onto a pre-patterned substrate, where the electrodes are interdigitated, forming multiple channels [shown in Figure 3.7 b)], and the current is measured laterally to the main plane of the substrate. The diode structure offers the advantage of being able to easily vary the thickness of the organic thin film (and therefore L of equation (3.28)) by changing parameters in the deposition process, whereas for the interdigitated substrates L is fixed and given by the width of the channels between the electrode fingers.[60] However, the diode structure has the disadvantage of needing a top

[60] In addition, in the diode structure, thin films of only a few 100 nm thickness or even lower can be used, while for the interdigitated structures 5 µm is commonly the lower limit of channel lengths.

metal contact, which has to be deposited onto the organic thin film and can easily lead to damage of the organic layer.

In the case of the interdigitated structure, multiple parallel connected channels are usually used in order to effectively decrease the measured resistance. This enables the measurement of higher currents and consequently increases the SNR. The conductivity of an organic thin film deposited on such a structure can be determined by

$$\sigma = \frac{L}{n \cdot R_{\mathrm{tot}} \cdot w \cdot d}, \tag{3.29}$$

where n is the number of channels, R_{tot} the overall resistance determined by the slope of the linear IV curve, w the width of the organic layer or the overlap between the finger electrodes, respectively, and d is the thickness of the organic layer [see also Figure 3.7 b)].

A drawback of determining the conductivity from simple IV-measurements is the prerequisite that the contact between electrode and organic films has to be Ohmic, which most often is not exactly the case. Thus, the measured resistance also includes the contact resistance R_{c}, which leads to an underestimation of the actual conductivity of the organic film. The so-called transmission line method (TLM) can be used to measure R_{c} by performing a series of IV-measurements on samples with a varying channel length. Here, the linear relation between the measured total resistance and the channel length can be extrapolated to a 'zero'-length semiconductor, which in fact is the contact resistance. To exclude the influence of contact resistance during the measurement completely, the four-point method can be used, where (in the linear geometry) the sample is contacted at four equally spaced points lying on a line. Here, a current is driven through the two outer contacts and the voltage drop at the inner contacts is measured, which makes it independent of the contact resistance.[237] However, due to notoriously low conductivity of organic materials, conventional four-point probes can usually not be used to measure the conductivity of these materials, since the spacing between the probes in conventional setups is usually several 100 µm large. In consequence, the current would have to be driven over a length of around 1 mm, which would require voltages over 100 V in order to create measureable currents for typical organic materials.

3.5 Scanning Force Microscopy

Scanning force microscopy (SFM) is a widely employed technique for topological imaging on the nanoscale. Here, a cantilever with a very sharp, microscopic tip is moved linewise over the surface of a sample and the deflection of the tip caused by atomic interactions between tip and surface can be measured with a resolution on the nanoscale.

The working principle of a SFM is schematically shown in Figure 3.8. Local attractive Van-der-Waals and repulsive Coulomb (and Pauli) forces lead to a bending of the cantilever. This deflection is measured by the deflection of a laser beam, which is reflected from the backside of the cantilever onto a position-sensitive photodiode. The photodiode usually consists of four quadrants and can therefore measure the position of the laser beam with a high precision.

A SFM can be operated in four different basic modes. The simplest mode is the contact mode, in which the tip moves over the sample surface, while always being in contact with the surface. Here, a feedback loop system keeps the tip at a constant force at which it is pressed on the sample, so that the height position of the tip always resembles the changes in height of the sample surface. For soft organic films, this mode is usual not the mode of choice, as the movements of the tip across the sample surface can easily damage the surface. More non-invasive modes are tapping modes, where the tip is oscillated near its resonance frequency and changes in its amplitude and phase due to the interaction with the surface are measured by a feedback loop system. In these cases, the feedback loop system keeps the tip at a constant height above the surface. Here, the recorded phase can give additional information about the surface. For example, if the attractive and repulsive interactions with the tip change, also the phase of the tip's oscillation can change and thus two different materials lying on the same height level can be distinguished in the phase image but not in the height image.

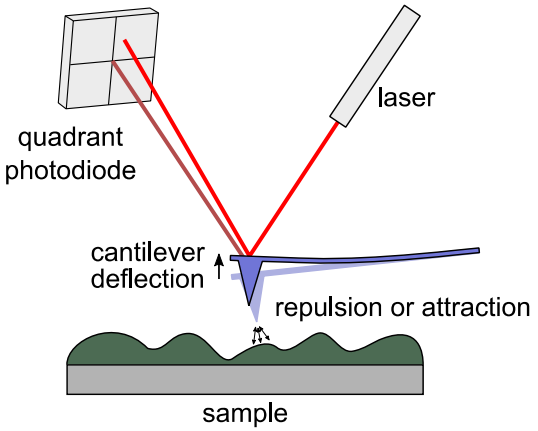

Figure 3.8 Working principle of a SFM. The bending of the cantilever caused by atomic forces between the tip and the sample surface is measured by the deflection of a reflected laser beam from which the height differences of the surface can be mapped.

There are three different tapping modes. In the so-called intermittent mode the tip is oscillated with a high amplitude and only touches the sample surface at the lowest point of its oscillation. This mode operates both in the attractive and repulsive regime of the tip-surface forces. More specialized modes are the non-contact mode operating only in the attractive region and the force-modulation mode operating only in the repulsive region. In the force-modulation mode the tip never leaves the surface during the oscillation (i.e. it is oscillated within the first view Å of the sample), whereas in the non-contact mode the tip never touches the surface. Usually the intermittent mode is the mode of choice for SFM measurements on organic thin films, since it combines the benefits of all other modes. Here, the lateral forces on the tip are much lower than in the contact mode, while also supplying additional information via the changes in the oscillation phase.

There is also a variety of more advanced modes utilizing specialized tips. To-date, available modes offer the possibility to probe thermal, electrical, conductive, frictional, shear and torsional force, or electrochemical properties of surfaces. For example, Kelvin probe force microscopy (KPFM) combines SFM and contact potential difference (CPD) measurements resulting in a mapping of the work function of the sample surface.

SFM measurements can also be used to determine the surface roughness of a sample. In general, roughness parameters quantify the vertical deviations from the mean image plane. They can be simply interpreted by comparison among samples, i.e. if the roughness parameter of one sample is higher than the one of another sample, the first sample is rougher. A widely used roughness parameter is the root mean square (RMS) roughness R_q, which is determined via

$$R_q = \sqrt{\frac{1}{n}\sum_{\mathrm{i}=1}^{n} z_i^2} \ , \tag{3.30}$$

where n is the number of data points and z_{i} the vertical distance from the i$^{\mathrm{th}}$ data point to the mean image plane.[238] Another common parameter to describe the surface roughness is the arithmetic average of the absolute values of the surface height deviations (commonly termed R_a).[238]

4 MATERIALS AND EXPERIMENTAL SETUPS

In this chapter, the materials used in this thesis will be introduced as well as the procedures, with which samples were prepared. Moreover, the experimental setups (the theory of which was described in the last chapter) and data analysis methods will be described.

4.1 MATERIALS

Throughout the work in this thesis, a large number of host and dopant materials in various combinations were investigated. The chemical structures of the materials used as well as their properties are summarized in Figure 4.1 and Table 4.1, respectively.

P-type materials: 1,3,6,8-tetra[bis(p-anisyl)amino]-4,5,9,10-tetramethoxypyrene (D_a) and 1,3,6,8-tetra[bis(p-anisyl)amino]pyrene (D_b) were synthesized by the group of Prof. Müllen (Max-Planck-Institut für Polymerforschung, Mainz) as described elsewhere.[239] The donor materials have been previously used as hole-transport materials in perovskite solar cells.[240,241] Sexithiophene (6T) and its more soluble, hexyl chain substituted derivative (DH6T) were purchased from Sigma Aldrich GmbH and H.C. Starck GmbH, respectively. 6T and DH6T are well studied oligothiophenes and have been previously used as active materials in p-type OFETs.[242–244] The polymer poly(3-hexylthiophene-2,5-diyl) (P3HT) is one of the most used and well-studied polymers in the field of organic electronics, as it is used as donor material in OPVs, p-type material in OFETs and as standard host material to study the behavior of newly synthesized p-dopants.[52,245,246] P3HT was purchased from Sigma Aldrich GmbH in its regioregularform[61] with a mass average molar mass of 50-100 kDa. The co-polymer indacenodithiophene-co-benzothiadiazole (IDT-BT) was recently synthesized by the group of Prof. McCulloch (Imperial College, London, UK) as a high-mobility p-type polymer and was used as donor material in organic solar cells as well as active layer in p-type organic field effect transistors (OFETs).[247–249]

N-type materials: In analogy to P3HT, which is the prototypical p-type/donor material in the field of organic electronics, the fullerene C_{60} (and its soluble derivative 1-(3-methoxy-carbonyl)propyl-1-phenyl[6,6]C_{61} – PCBM) is the prototypical n-type/acceptor material.[22,246] C_{60} was purchased from CreaPhys GmbH in a triple-sublimed grade. The perylene diimide derivatives perylene-3,4,9,10-tetracarboxylic dianhydride (PTCDA) and perylene-3,4:9,10-tetracarboxylic bis(benzimidazole) (PTCBI) are thermally resistant and inexpensive dyes used e.g. in car paint, which can also be used as hole-transport materials.[250,251] Both compounds were purchased from Sigma Aldrich GmbH. The fully

[61] Regioregular means the configuration of the alkyl-side chains between two monomer units is always head-to-tail. If the configuration is randomly head-to-tail, head-to-head, or tail-to-tail, it is called regiorandom.

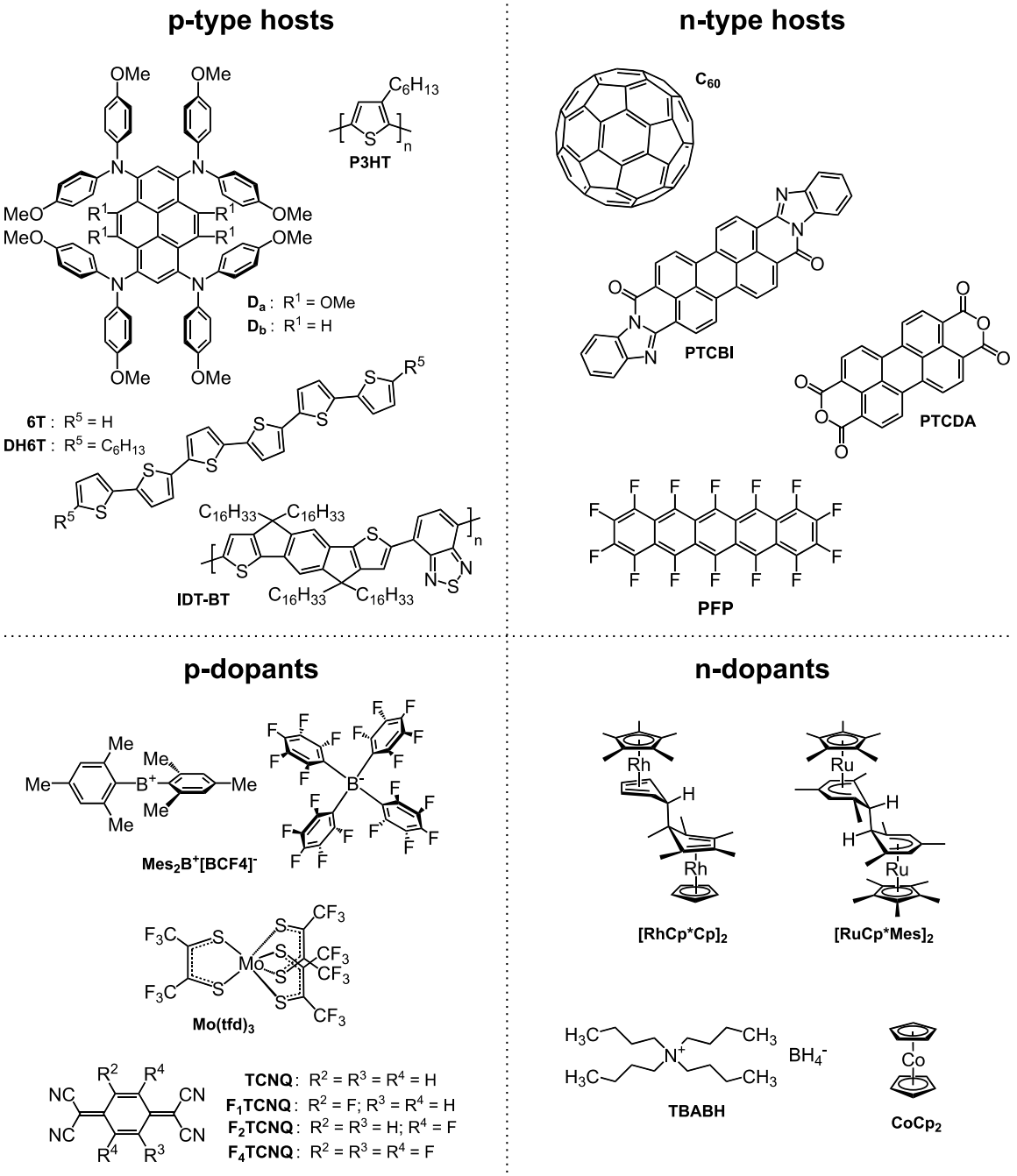

Figure 4.1 Summary of all host and dopant materials used during the work presented in this thesis.

fluorinated version of pentacene – perfluoropentacene (PFP) – is used as active n-type material in OFETs.[72,252] It was purchased from Kanto Denka Kogyo Co. Ltd.

P-dopants: The well-studied p-dopant series of increasingly fluorinated tetracyanoquinodimethane derivatives (F_xTCNQ, x=0,1,2,4) was purchased from TCI Europe N.V.[23,52] Tris[1,2-bis(trifluoromethyl)ethane-1,2-dithiolene] ($Mo(tfd)_3$) was recently introduced as alternative p-dopant with a similar strength as F_4TCNQ and the used material was synthesized by the group of Prof. Marder (School of Chemistry and Biochemistry,

Table 4.1 Properties of materials used. IE, EA, E_{ox}, E_{red}, and the optical gap were determined in this work, if not otherwise stated. If molecules are known to adopt a lying or standing orientation, both values of IE and EA are given. [a] EA of Mes_2B^+ is given as calculated by DFT.[253] [b] Converted from E_{ox}. [c] Effective reducing strength.[203]

	Material	Supplier	Sum formula	Molar mass [g/mol]	IE [eV]	EA [eV]	E_{ox} [V vs Fc/Fc$^+$]	E_{red} [V vs Fc/Fc$^+$]	Opt. gap [eV]
p-type hosts	D_a	Müllen group	$C_{76}H_{70}N_4O_{12}$	1231.4	4.7	--	-0.27	--	2.3
	D_b	Müllen group	$C_{72}H_{62}N_4O_8$	1111.3	4.9	--	-0.04	--	2.3
	6T	Sigma Aldrich	$C_{24}H_{14}S_6$	494.8	4.6/5.1 [256]	--	0.44 [254]	--	2.4
	DH6T	H.C. Starck	$C_{36}H_{38}S_6$	663.1	4.8/5.4 [257]	--	0.33 [254]	--	2.6
	P3HT	Sigma Aldrich	$(C_{10}H_{14}S)_n$	$(168.3)_n$	4.7	2.1 [255]	--	--	1.9
	IDT-BT	McCulloch group	$(C_{86}H_{140}N_2S_3)n$	$(1298.2)_n$	5.4	3.3	--	--	1.7
n-type hosts	C_{60}	CreaPhys	C_{60}	720.6	6.4 [255]	4.0 [255]	--	--	~1.6
	PTCDA	Sigma Aldrich	$C_{24}H_8O_6$	392.3	6.6	4.1	--	--	2.2
	PTCBI	Sigma Aldrich	$C_{36}H_{16}N_4O_2$	536.5	5.9	4.0	--	--	1.5
	PFP	Kanto Denka Kogyo	$C_{22}F_{14}$	530.2	--	3.6/4.1 [87]	--	-1.13 [72]	1.9
p-dopants	TCNQ	TCI Europe	$C_{12}H_4N_4$	204.2	--	4.2 [161]	--	-0.29	3.9
	F_1TCNQ	TCI Europe	$C_{12}H_3F_1N_4$	222.2	--	4.6 [161]	--	-0.18	3.9
	F_2TCNQ	TCI Europe	$C_{12}H_2F_2N_4$	240.2	--	4.6 [161]	--	-0.07	3.0
	F_4TCNQ	TCI Europe	$C_{12}F_4N_4$	276.2	--	5.1 [161]	--	0.13	3.0
	$Mo(tfd)_3$	Marder group	$C_{12}F_{18}MoS_6$	774.4	--	5.6 [171]	--	0.26 [171]	1.9
	$Mes_2B^+[CFB4]^-$	Fukushima group	$(C_{18}H_{22}B^+)(C_{24}F_{20}B^-)$	982.2	--	5.4 [a]	--	--	3.1
n-dopants	$[RhCp^*Cp]_2$	Marder group	$C_{30}H_{40}Rh_2$	606.5	2.8 [b]	--	-1.97 [c]	--	~3.3 [204]
	$[RuCp^*Mes]_2$	Marder group	$C_{38}H_{54}Ru_2$	713.0	2.8 [b]	--	-2.04 [c]	--	~3.3 [204]
	$CoCp_2$	Sigma Aldrich	$C_{10}H_{10}Co$	189.1	4.1 [188]	--	-1.33 [233]	--	3.3
	TBABH	Alfa Aesar	$(C_{16}H_{36}N^+)(B^-H_4)$	257.3	--	--	--	--	--

Georgia Institute of Technology, USA) as previously described.[171,258] The organic salt consisting of a diarylborinium ion (Mes_2B^+, Mes(mesityl) = 2,4,6-trimethyl-phenyl) and a tetrakis(pentafluorophenyl)borate anion ($[BCF4]^-$) was recently synthesized by the group of Prof. Fukushima (Chemical Resources Laboratory, Tokyo Institute of Technology, Japan) and introduced as a possibly very strong p-dopant.[253,259–261]

N-dopants: As described in subsection 2.2.3, organometallic dimers have been proven to be very powerful precursor-based n-dopants. In this work, the (pentamethyl-cyclopentadienyl)(cyclopentadienyl)rhodium dimer $[RhCp^*Cp]_2$ and (pentamethylcyclopentadienyl)(1,3,5-trimethylbenzene)ruthenium dimer $[RuCp^*Mes]_2$ have been used, which were synthesized by the group of Prof. Marder as previously described.[203,204,262] $CoCp_2$ is typically used as a reducing agent in organometallic chemistry and has also been shown to act as a strong n-type dopant.[188,233] It was purchased from Sigma Aldrich GmbH. The reducing agent tetrabutylammonium borohydride (TBABH) was used as an alternative to organometallic dimers as surface modifiers and has been previously shown to reduce the work function of gold.[263] It was purchased from Alfa Aesar, Thermo Fisher Scientific Inc.

All materials were used without further purification, except PTCBI, which was purified in three cycles via thermal gradient sublimation.

4.2 Sample Preparation

Nearly all of the sample preparation for the work presented in this thesis was performed under inert atmosphere or vacuum (unless otherwise stated). For the solution based preparation methods, a nitrogen-filled glovebox with water and oxygen levels below 1 ppm (for critical experiments below 0.1 ppm) was used. Thermal evaporation was performed in interconnected vacuum systems (see next section) with pressures of around 10^{-8} mbar or lower. Transports between the vacuum systems and glovebox were performed without air-exposure by using a specialized transfer rod, which could be sealed by a gate valve. Transfers were conducted with residual gas pressures below 10^{-2} mbar.

For solution processing, stock solutions with concentrations of around 1×10^{-3} M were prepared using dry and degassed solvents. Dichloromethane (DCM), chlorobenzene (CB), 1,2-dichlorobenzene (o-DCB) and tetrahydrofuran (THF) were purchased as anhydrous solvents from Sigma Aldrich GmbH (>99.9% purity, inhibitor-free) and further degassed via three freeze-pump-thaw cycles. To prepared solutions, the materials were weighed in air (except $CoCp_2$ and $Mes_2B^+[CFB4]^-$, which were only handled under inert atmosphere) and then transferred to the glovebox, where they were dissolved in appropriate amounts of the respective solvents. The stock solutions were stirred overnight to enable complete dissolution of the material and were subsequently used within the next few days. Mixed

solutions were always prepared from the stock solutions directly before deposition of thin films. The stock solutions were mixed in appropriate volume ratios to achieve the desired dopant concentrations. Drop-casting was performed by dropping appropriate amounts of solution (usually 50-100 µl) onto the cleaned substrates and letting the solvent dissipate. Spin-coating was performed with standard laboratory spin-coaters at various speeds (1000-6000 rpm) and times (1-2 min) to achieve the desired thicknesses by the static method, where an appropriate amount of solvent is first dropped onto the substrate (usually around 30 µl) and the substrate was subsequently set in rotation.

For thermal evaporation, the material was loaded into quartz glass crucibles which were wrapped with tantalum wire in order to resistively heat the material by a current flow through the wires. The crucibles were mounted into the respective vacuum chamber, which were pumped down until the desired pressure was reached. The evaporation rate was controlled by a quartz crystal microbalance (QCM) which was placed at the position of the sample in order to achieve a steady rate before the actual deposition, for which the QCM was retracted and the sample placed at its position. Typical evaporation rates ranged from 1 to 3 Å/min. For co-evaporation, both materials were heated simultaneously and their rates were measured individually by blocking the molecule beam from the respective other material with a shutter. From the rates the dopant concentration c could be estimated via

$$c \approx \frac{M_{\mathrm{host}}}{M_{\mathrm{dop}}} \cdot \frac{R_{\mathrm{dop}}}{R_{\mathrm{tot}}} \ , \tag{4.1}$$

where M_{host} is the molar weight of the host, M_{dop} is the molar weight of the dopant, R_{dop} is the evaporation rate of the dopant and R_{tot} is the total evaporation rate of dopant and host.

For PES and IPES measurements, thin films with thicknesses in the order of 10-20 nm were deposited onto glass substrates coated with an ultrasmooth indium tin oxide (ITO) film of 140 nm thickness (RMS roughness below 1 nm), which were purchased from Thin Film Devices Inc. The ITO substrates were cleaned by a detergent/solvent cleaning procedure, which consisted of scrubbing with a 2% Tergitol™ aqueous solution for 1 min, followed by rinsing with deionized water, sonication in 2% Tergitol™ aqueous solution for 10 min, copious rinsing and sonication in deionized water for 10 min, and finally sonication in ethanol and isopropanol (≥99.9%) for 10 min each. For the PES measurements of chapter 8, fluorine-doped tin oxide (FTO) coated glass sheets (Hartford Glass Inc.) were used as substrates. After initial washing with Hellmanex™ III detergent, substrates were immersed for 90 min in a H_2SO_4:H_2O_2 3:1 (v/v) piranha solution. Subsequently, the FTO substrates were rinsed with deionized water, and dried in an oven at 70 °C.

For optical absorption spectroscopy measurements, thin films were prepared on Suprasil© quartz glass substrates (Heraeus Quarzglas GmbH & Co.KG). The quartz glass substrates were cleaned by sonication in a 5% Hellmanex™ III detergent solution followed by extensive rinsing with deionized water and sonication in deionized water for 10 min. Subsequently, the substrates were dried in an oven at 70 °C. After all measurements were finished, the quartz substrates were recycled by immersing them in a H_2SO_4:H_2O_2 1:1 (v/v) piranha solution overnight, followed by extensive rinsing with water and the above described cleaning protocol. FTIR measurements were performed employing 1 mm thick substrates of non-doped silicon with a native oxide layer (Siegert prime grade), which were used as received.

For IV measurements, pre-patterned glass substrates with an interdigitated electrode structure were used. In the case of gold and aluminum electrodes, the substrates were patterned by thermal evaporation of the respective metal onto smooth borofloat glass substrates (CrysTec GmbH), which were covered with shadow masks. The interdigitated electrodes had a thickness of around 100 nm and contained 25 channels of 50 µm length and 5mm width. In the case of ITO electrodes, pre-patterned substrates were purchased from Ossila Ltd. The ITO IV-substrates consisted of 5 individual devices, each of which with 100 nm thick electrodes containing 5 channels of 50 µm length and 6mm width.

OFETs were fabricated using substrates with a thermally grown 300 nm thick SiO_2 layer as gate dielectric on which gold electrodes were deposited as source/drain contacts, with the source-drain channel length being 5 µm and the source-drain channel width 32 cm. The substrates were treated with a dodecyltrichlorosilane SAM to passivate the surface. The IDT-BT films were subsequently annealed at 150° C for 10 min in order to increase their crystallinity and thus achieve higher mobilities following literature protocols.[247,249,264,265]

4.3 Experimental Setups

All PES and IPES experiments were performed in interconnected vacuum-systems, which consisted of a sample preparation chamber (base pressure around 10^{-9} mbar) and an analysis chamber (base pressure < 10^{-9} mbar). UPS measurements were performed using the HeI photon line (21.22 eV) of a gas discharge lamp with low photon flux (attenuated by aluminum foils) in order to avoid radiation damage of the samples. The excitation sources for XPS measurements were non-monochromated Al Kα (1486.7 eV) and Mg Kα (1253.6 eV) sources. The spectra were collected in normal emission using a SPECS Phoibos 100 hemispherical electron energy analyzer with an energy resolution of 150 meV for UPS (determined from the Au Fermi edge) and 1.2 eV for XPS (determined from the $Au4f_{7/2}$ core level). The secondary electron cut-off (SECO) spectra were measured with a bias of −10 V

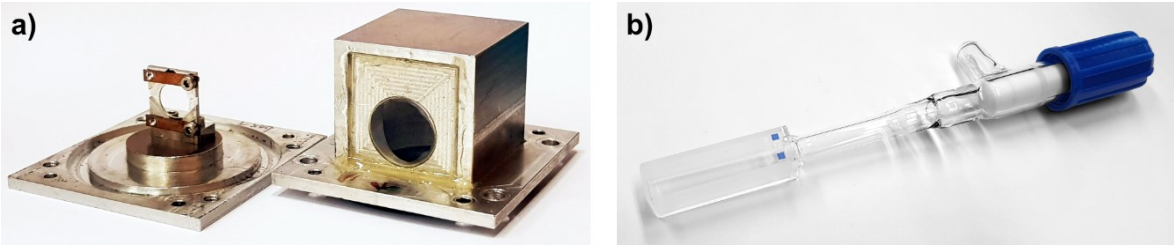

Figure 4.2 Images of the **a)** specialized boxes and **b)** cuvettes, which allowed optical absorption spectroscopy measurements to be performed in inert atmosphere. The thin film samples were mounted in the boxes and then sealed by using a vinyl gasket. Solutions for optical measurements were filled in the cuvettes, which could be sealed by a Teflon stopper.

applied to the sample to clear the detector WF. UPS measurements were performed at a pass energy of 2 eV, while XPS measurements were performed with a pass energy of 50 eV for survey scans and 20 eV for detail scans. IPES measurements (incident electron energy range: 5-15 eV, NaCl-coated photocathode, SrF2-window) were performed in the isochromat mode. The used IPES setup has a resolution of 1.3 eV (as determined from the broadening of the Fermi level of an Au reference). All UPS, XPS and IPES spectra were recorded at room temperature and in the order UPS, XPS, UPS, IPES, UPS, to check for sample damage.

Mono-UPS and Mono-XPS measurements were performed at FUNSOM, Soochow University in the group of Prof. Duhm (Jiangsu Key Laboratory, Institute of Functional Nano and Soft Materials (FUNSOM), Soochow University, Suzhou, China). The measurements were carried out in a customized SPECS UHV system, including an analysis chamber (base pressure – 2×10^{-10} mbar), an evaporation chamber (base pressure – 2×10^{-10} mbar). XPS was measured using a monochromatized Al Kα source (1486.7 eV) and UPS using the monochromatized He Iα excitation line (21.22 eV). The spectra were collected with a Specs PHOIBOS 150 hemispherical analyzer using a pass energy of 4 eV for UPS measurements and 50 eV / 20 eV for XPS survey / detail scans, respectively.

Optical absorption spectroscopy was performed using a Lambda 950 UV/Vis/NIR spectrophotometer (Perkin Elmer Inc.) with a step width of 1 nm. The optical measurements on thin films were performed with the samples mounted in specialized boxes with two quartz glass windows [see Figure 4.2 a)], which were sealed under nitrogen atmosphere using a vinyl gasket. A baseline spectrum of the boxes with a mounted clean quartz glass substrate was subtracted from the spectra before further analysis. For the optical measurements in solution, specialized quartz glass cuvettes [see Figure 4.2 b)] with a path length of 1 mm (or 10 mm) were used, which were sealed under nitrogen atmosphere using a Teflon stopper. 100 µl of the host stock solution (2 ml in the case of 10 mm cuvettes) were mixed with an appropriate amount of the respective donor stock solution and then filled with the respective solvent to a total volume of 300 µl (3 ml in the

case of 10 mm cuvettes). In this way, all of the measured mixtures contained the same concentration of host / dopant molecules and, therefore, the optical spectra can be compared without normalization. To extend the optical spectra to lower photon energies, FTIR spectroscopy measurements were performed under rough vacuum (around 5 mbar) using a Bruker IFS-66v/S spectrometer with a liquid nitrogen-cooled mid-range mercury cadmium telluride (MCT) detector. The spectra were recorded with a resolution of 4 cm^{-1}.

IV measurements were conducted using a Keithley SourceMeter 2400. Given the length of the channels of 50 µm, fields did not rise above 4000 Vcm^{-1}, which allowed a determination of the conductivity from the Ohmic region of the IV characteristics. The thickness of each film was measured by SFM separately for each sample after completion of all IV measurements.

SFM measurements were performed under ambient conditions using a Bruker Dimension Icon AFM. Height images were recorded in ScanAsyst (tapping) mode using silicon cantilevers with a typical resonant frequency of 70 kHz and a spring constant of 0.4 N/m. Film thickness were determined from height profiles measured on samples, which were scratched with a needle (syringe cannula). Using a needle will remove only the organic thin film, since the needle acts as a spring and, therefore, does usually not scratch the (hard) substrates, if only little force is applied. This procedure yielded scratches, which were 30-60 µm wide.

OFET, Cyclic voltammetry, and EPR measurements were performed by collaboration partners (as stated in the respective chapters) and details of the experimental and analysis procedures can be found in the respective references [A7] and [A8].

4.4 Data Analysis Methods

Recorded PES and IPES spectra have been recalculated to binding energy with respect to the Fermi level as stated in subsection 3.1.2, except the SECO spectra of UPS, which were calculated to effective kinetic energies resembling the work function by subtracting the applied bias. The onset of the HOMO, LUMO and also SECO were determined by the intersection of a horizontal baseline resembling a constant background and a line fitted to the linear part of the HOMO, LUMO or SECO, respectively. To account for the low resolution of the used IPES setup, the onset of the LUMO level as measured by IPES was corrected by an offset following the correction procedure described in appendix A. XPS peak fitting was performed using the software WinSpec 2.09. The peaks were fitted by a pseudo-Voigt function (as sum of a Gaussian and Lorentzian contribution) and a Shirley background. The binding energies of the core level positions are given with respect to the peak maxima. The error of the XPS binding energies obtained from peak fitting is estimated to be smaller than

50 meV, which was obtained from fitting procedures where the positions were purposely offset. In general, the error of the stated energy levels obtained from UPS and XPS are assumed to be around 50-100 meV also including sample to sample variation. For IPES, the error is much larger due to the large broadening of the used setup and assumed to be in the order of a few 100 meV.

For non-monochromatized UPS and XPS measurements, satellite correction procedures were performed were needed (e.g. in the case of HOMO onset scans in UPS or doublet core levels extending over 10 eV in XPS). It was assumed, that the satellite lines create a similar spectrum than the main lines. Thus, the satellite removal procedure consisted of creating satellite spectra by scaling the recorded spectrum to the appropriate satellite intensity and shifting it by the respective energy offsets as stated for He I, Al-Kα and Mg-Kα in Table 3.1 and Table 3.2 in subsections 3.1.2 and 3.1.3, respectively. Subsequently, the satellite spectra were subtracted from the recorded spectra in the overlapping energy region and the resulting spectra used for further analysis.

XPS detail scans of species with a very low intensity had to be recorded with several hundred scans and scan times in the order of several hours to obtain a reasonable signal-to-noise ratio (SNR). Due to their low intensity, these detail scans showed an additional background than only a Shirley background, which was the case for the B1s core level (189 eV) shown in chapter 7 and Rh3d doublet level (307 eV and 312 eV) shown in chapter 8. These backgrounds were attributed to the broad energy loss lines of the (high intensity) S2p (165 eV) and C1s (285 eV) core levels, respectively. To account for the energy loss lines, similar detail scans of the respective pristine host materials (P3HT, C_{60} and PTCBI, respectively) of these regions were recorded, which were smoothed using a 100-point second order Savitzky-Golay filter. The binding energies of the backgrounds were adjusted by the energy offset between the S2p/C1s core levels of the pristine sample and the doped samples, accounting for a shift of the Fermi level due to doping. Subsequently, the background spectra were subtracted from the B1s and Rh3d detail spectra by adjusting the intensity accounting for different X-ray intensities. An example of the background removal process in displayed in Figure B.3 in appendix B.

The recorded optical spectra were converted from wavelength to photon energies by using the known relation $E = hc/\lambda$ with $hc = 1239.84$ eV·nm. At the wavelengths of 861 nm and 319 nm, the used spectrophotometer undergoes a detector and lamp change, respectively, which leads to offsets (jumps) in the recorded UV/Vis/NIR spectra at these positions. To account for these offsets, the UV region (< 319 nm) and NIR region (> 861 nm) were aligned to the Vis region (319-861 nm) by shifting the intensity up or down with a constant offset. For some spectra (where stated), a background, taking into account Rayleigh scattering and an arbitrary linear background, with the form $A = a + bE + cE^4$ was subtracted before

analysis, where b and c are arbitrary fitting parameters, A is the absorbance, and E is the photon energy. In some cases, where the data was smoothed, a 100-point second order Savitzky-Golay filter was used. The recorded FTIR spectra were used to extend the spectra to lower photon energies. The intensity of the FTIR spectra was adjusted to the UV/Vis/NIR spectra by adjusting the absorbance in the overlapping region of 0.45 eV to 0.75 eV.

The recorded SFM images were analyzed with the software programs Gwyddion 2.44 and Nanoscope Analysis 1.9. In both cases a first-order line subtraction and plane correction were applied to the images to compensate for thermal drift and sample inclination. In addition, a linewise correction adjusting the line medians was applied. In the case of samples which showed the formation of large islands, these islands were excluded from the plane and linewise correction procedures, thus only taking into account the plane at the surface of the islands. Gwyddion was used to determine the sample thicknesses from the height profiles of the scratches, while Nanoscope Analysis was used to generate height images and for grain analysis. In addition, Nanoscope Analysis was also used to determine the root mean square (RMS) roughness of the samples.

5 PREDICTING ION PAIR FORMATION YIELD IN MOLECULAR DOPING

As highlighted in section 2.2, efficient doping of organic semiconductors relies on identifying appropriate molecular dopants that are capable of ionizing the host molecules with a high yield to facilitate the creation of mobile charges. This process requires an adequate energy alignment of the respective frontier molecular orbital energies. To select matching host/dopant pairs, many researchers rely on comparing solid-state IE/EA which are measured by UPS/IPES.[33–39,140,149,150,165,168,170,171,188,266–269] Alternatively, redox-potentials measured via cyclic voltammetry (CV) might serve to guide material selection. This has so far been done only in comparably few studies.[40,187],[A4] The aim of this section is to examine the practicality of redox-potentials measured via CV in solution versus IE/EA values measured by UPS/IPES on thin films for predicting the yield of ion pair formation.[62]

It should be noted here, that this section focuses entirely on ionization efficiency, which is the yield of ionized host molecules (monomer units in a polymer) per number of dopant molecules. Doping efficiency, on the other hand, is the yield of actual free charge carriers per number of dopant molecules. It is known, that ionization usually proceeds with a high efficiency (up to 100%, if host/dopant pairs are chosen adequately), whereas the generation of free charge carriers is notoriously low (in the order of 10%).[141,150] A systematic study relating ionization and doping efficiency has, however, not been conducted so far (to the best of my knowledge).

In sections 3.1 and 3.3, the experimental methods UPS, IPES, and CV have been explained in detail. As shown, energy level values determined by UPS/IPES depend strongly on the orientation of molecules with respect to the surface and inside the bulk,[87] whereas energy level values from CV are determined in an environment different to doped solid thin films and (to a lesser extent) depend on the experimental environment (solvent and electrolyte).[231,236] Thus, the values of both experimental approaches have their shortcomings, when they are used to evaluate IPA formation efficiency.

Although empirical linear relationships between the solid-state IE (EA) and the oxidation (reduction) potential of molecular org. semiconductors[270–273] as well as polymers[274,275] have been previously developed, there is considerable scatter in plots of oxidation (reduction) potential vs. IE (EA). Thus, the values in individual cases, especially for non-amorphous materials, can deviate by several 100 meV even up to 1 eV from the reported relationships due to the above described influences on the measured values of solid-state IE/EA and redox-potentials. Additionally, the differences between solvation energy and

[62] The literature cited here was chosen exemplarily, but is believed to adequately resemble the entire entity of molecular doping related literature. It should be noted, however, that the majority of researchers most likely uses a mix of energy levels estimated from different measurement methods, as e.g. ref. [153,376–378].

polarization energy are expected to strongly dependent on the size, shape, and charge distribution in the ions. These deviations are too large to make an accurate prediction of IPA formation in individual host/dopant systems based on such estimated values.

5.1 Comparison of Frontier Orbital Energy Levels

To investigate, which data-set is more practical for predicting the ion pair formation yield, we have chosen three different sets of host-dopant combinations, which, due to their structure, are all believed to undergo integer charge transfer only and do not form charge transfer complexes (see section 2.2 for details).

In Figure 5.1 the redox-potentials and the solid-state IE/EA of the investigated materials are juxtaposed. The redox-potentials for set I were measured by CV (see Figure B.1 in appendix B) and the IE for the donors D_x were determined by UPS (see Figure B.2), while IPES values were taken from literature.[161] The EA value of F_4TCNQ used here is slightly smaller than another previously reported value of 5.24 eV,[33] which is consistent within the assumed uncertainty of IPES and does not affect the following discussion. The energy levels[63] for set II and set III were taken solely from literature. [72,87,171,188,233,254,256,257] The values of the redox-potentials were measured under similar experimental conditions and reported with respect to the Fc/Fc^+ potential. They are also consistent with other reported values (except PFP, where no additional data was available).[276–279] In contrast, UPS/IPES data are only sparsely available. For 6T there are several other values of IE reported, all lying within the range of 4.6 eV to 5.3 eV. Here, however, the structure was not accounted for and can thus be assumed to be polycrystalline in the intermediate cases.[114,280–282] For PFP, an intermediate value of EA without well-defined orientation (like it would be measured conventionally without regard to film structure) can be estimated to be around 3.8 eV. This was done, following the values reported for pentacene, where the EA in lying and standing orientation is 2.35 eV and 3.14 eV, respectively, while an intermediate value of the EA for pentacene deposited on a rough ITO surface was found to be 2.70 eV.[87,283]

To a first approximation, the energy levels IE/E_{ox} of the donor and EA/E_{red} of the acceptor can be used to evaluate whether IPA formation is thermodynamically feasible or not. In a thermodynamic equilibrium, IPA formation is expected to occur with high yield when EA > IE or $E_{red} > E_{ox}$, respectively, while it should occur with only very low yield when EA < IE or $E_{red} < E_{ox}$. In the case of EA ≈ IE or $E_{red} \approx E_{ox}$, IPA formation can proceed with medium or high yield taking into account a thermal activation energy of ca. 25 meV at room temperature.

[63] Note: IE values reported for 6T[256] and DH6T[257] were maxima of the HOMO (estimated vertical IE), rather than onsets of ionization (estimated adiabatic IE). The values used here are, however, the onset values and thus 400-500 meV lower than those previously reported.

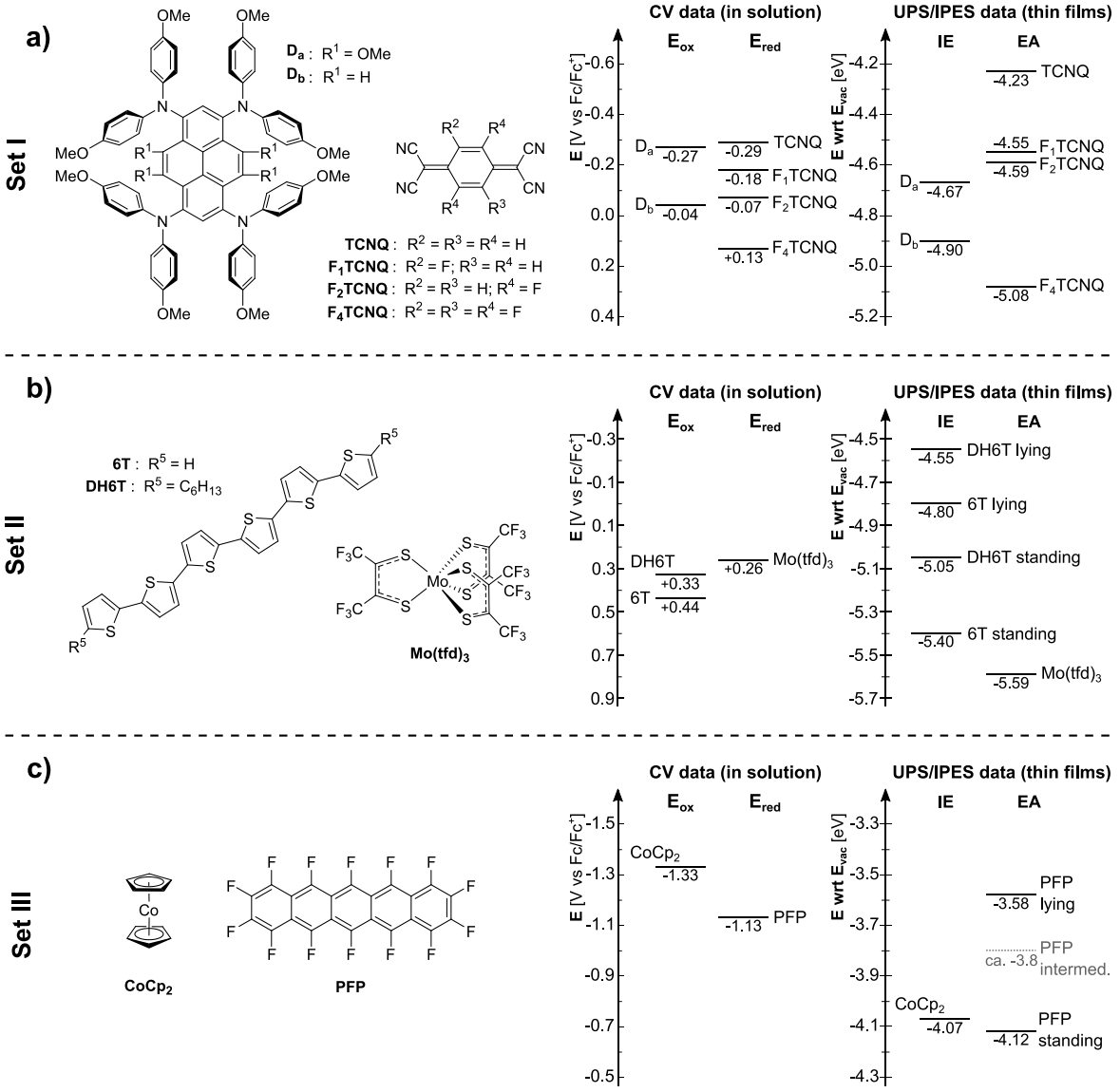

Figure 5.1 Chemical structures (left) and energy level diagrams (right) deduced from CV and UPS/IPES data of the used materials. **a)** Set I: Used donor hosts D_x and acceptor dopants F_xTCNQ. Redox-potentials and IE were measured in this work, EA of F_xTCNQs taken from literature.[161] **b)** Set II: Donor hosts 6T/DH6T and acceptor dopant molybdenum $Mo(tfd)_3$. All energy levels were taken from literature.[171,254,256,257] **c)** Set III: Acceptor host PFP and donor dopant $CoCp_2$. All energy levels were again taken from literature[72,87,188,233] and the intermediate EA for PFP (grey) was estimated by comparison of the EA of pentacene in different orientations.[87,283] The energy scales were aligned by using the estimation of the absolute position of the Fc/Fc^+ potential with respect to the vacuum level E_{vac} lying at 4.8 eV.[234] This figure will be published in ref. [A7].

For almost every material combination, both the CV and the UPS/IPES data-sets predict different outcomes for the IPA formation yield. When looking only for high IPA yield, the prediction can be reduced to a simple yes/no question. Thus, by comparing the redox-potentials of set I [Figure 5.1 a) – left diagram], one would expect integer charge transfer for D_a to be possible with all F_xTCNQs. For D_b, however, IPA formation should only clearly occur with F_4TCNQ and F_2TCNQ, and not for F_1TCNQ and TCNQ. When comparing IE and EA

values [Figure 5.1 a) – right diagram], IPA formation of both semiconductors should noticeably occur only with F_4TCNQ, but not TCNQ. For F_1TCNQ and F_2TCNQ, IPA formation might still be feasible for D_a, considering the small difference between IE/EA and taking into account the polarization energies of around 100 meV not captured by UPS/IPES (see subsection 2.1.1). Additionally $D^+..A^-$ Coulombic interactions (also not captured by UPS/IPES performed on individual material thin films) can further stabilize the ion pairs.

A comparison of the IE/EA values of set II [Figure 5.1 b) – right diagram] shows that, although there is a difference of 500/600 meV between the IE in lying and standing configuration of DH6T/6T, respectively, all IE values are considerably lower than the EA of $Mo(tfd)_3$. Thus integer charge transfer between DH6T/6T and $Mo(tfd)_3$ should be clearly possible. In contrast, the reported redox-potentials [Figure 5.1 b) – left diagram] suggest IPA formation to be energetically unfavorable. For set III, the reported redox-potentials [Figure 5.1 c) – left diagram] suggest integer charge transfer between PFP and $CoCp_2$ to be clearly possible, whereas the situation of IE/EA values [Figure 5.1 c) – right diagram] is more complicated. Here, it is not clear which of the EA values should be given preference when evaluating the possibility of IPA formation, since for PFP in standing configuration the EA is slightly higher than the IE of $CoCp_2$, but for PFP in lying configuration the EA is significantly lower. Additionally, the estimated intermediate EA for PFP in a polycrystalline configuration is lower than the reported IE of $CoCp_2$. Thus, if the EA of PFP would be measured without regard of its film structure, one would assume IPA formation to be energetically unfavorable.

To establish which of these opposing sets of IPA prediction is more useful in practice, optical absorption spectroscopy measurements were performed, both with solutions and thin films in a molar semiconductor / dopant ratio of 1:1 (except for set III – see below). The results of these measurements will be shown and discussed for each set separately in the following subsections.

5.2 Material Set I

The results of the optical absorption measurements of set I are summarized in Figure 5.2 and Figure 5.3. Since neither the donors nor the acceptors absorb in the spectral region up to around 2.0 eV, features emerging in this region upon mixing can reliably be assigned to ionized semiconductor or acceptor molecules by comparison with reference spectra as shown in Figure 5.2 and thus give clear evidence for IPA formation only.[24] To ionize the donors and acceptors, iron(III) chloride ($FeCl_3$) and potassium iodide (KI) were added in increasing amounts to the donor and acceptor solutions, respectively, and the evolution of the ionized peaks was followed. Figure 5.2 shows the optical spectra of the systems

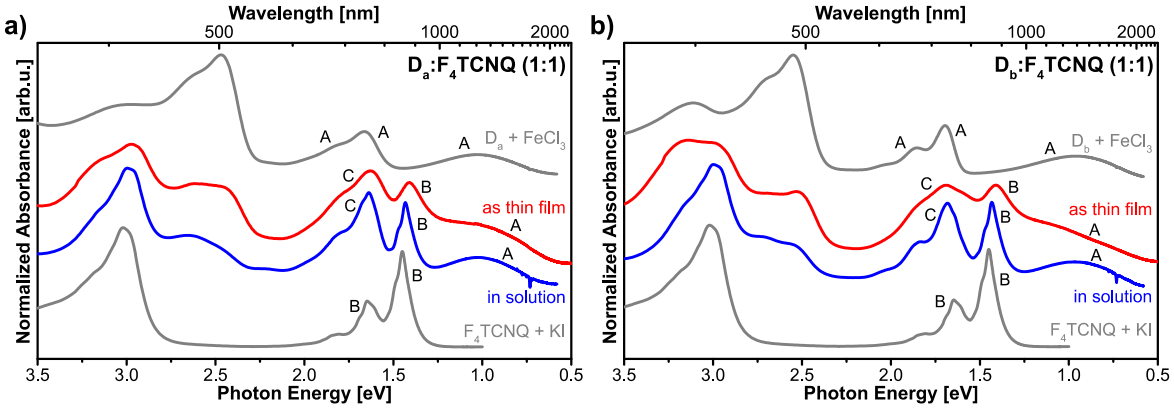

Figure 5.2 Comparison of the optical spectra of **a)** D_a:F_4TCNQ and **b)** D_b:F_4TCNQ of solutions and thin films with reference spectra. To create donor cations D_x^+, the respective solutions were mixed with $FeCl_3$, and for F_4TCNQ anions, the solution was mixed with KI. By comparison with the reference spectra the new emerging peaks in the range of 0.5 to 2.0 eV can be attributed to the cation features of D_x (A), the anion features of F_4TCNQ (B) and a superposition of both (C). The spectra of F_4TCNQ + KI were recorded by Paul Zybarth (Institut für Physik, Humboldt-Universität zu Berlin). This figure will be published in ref. [A7].

D_x:F_4TCNQ (both in solution and as thin films) in comparison to the optical spectra of the ionized D_x / F_4TCNQ in solution. Since the peaks related to the F_xTCNQ radical anion are very similar (compare SI of ref. [155]), the systems with F_4TCNQ are shown here as representatives for all systems. Figure 5.2 shows that the spectra of the mixed solutions and thin films are very similar. The features of the spectra of the mixed thin films are slightly red-shifted and broadened in comparison to the spectra of the mixed solutions, as it would be expected. By comparing the spectra of the mixed systems with the reference spectra of the ionized donors / acceptors, the feature at 1.0 eV can be associated with the cation of the donors (A), the one at 1.4 eV with the anion of the acceptors (B) and the features at 1.6 eV to 1.8 eV can be identified as a superposition of both cation and anion features (C).

The optical spectra of solutions [Figure 5.3 a) and b)] show that just a fraction of molecules undergoes ionization for nearly half of the material pairs. Following the Beer-Lambert law, this fraction can be estimated from the absorbance of the optical transitions of the respective species, as summarized in Table 5.1, in each case assuming all molecules in D_x:F_4TCNQ to be ionized. This observation of a fractional amount of ionized molecules is in line with a thermodynamic equilibrium based on the energetic difference ΔE of the redox-potentials from CV in Figure 5.1. By considering the equilibrium relation of single integer charge transfer $\mathrm{D} + \mathrm{A} \rightleftharpoons \mathrm{D}^+ + \mathrm{A}^-$ and following Nernst's equation the percentage of ionized molecules (P) can be estimated from the difference in redox-potentials (ΔE) considering thermal energy at room temperature. From Nernst's equation (see equation (3.25)in section 3.3), we get

$$ln\,K = \frac{z_e F \Delta E}{RT} \quad with \quad \Delta E = E_{1/2}^{red} - E_{1/2}^{ox} \tag{5.1}$$

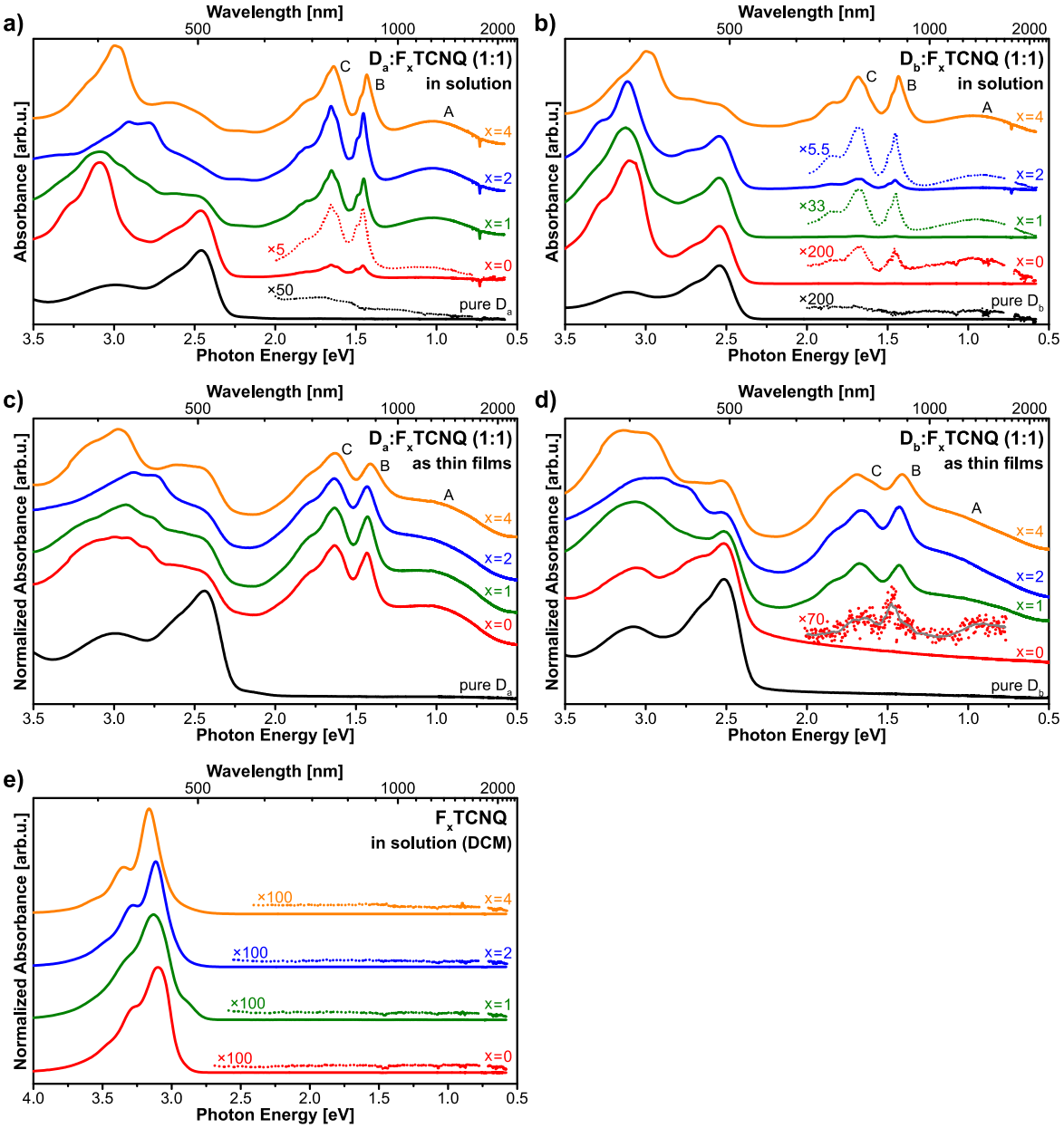

Figure 5.3 Optical spectra of **a)** D_a:F_xTCNQ in solution, **b)** D_b:F_xTCNQ in solution, **c)** D_a:F_xTCNQ in thin films, **d)** D_b:F_xTCNQ in thin films, and **e)** pure F_xTCNQ in solution. For the purpose of clarity, the spectra of pure F_xTCNQ are shown separately in e) and not in a)-d). The new emerging features in the range of 0.5 to 2.0 eV can be attributed to the cation features of D_x (A), the anion features of F_xTCNQ (B) and a superposition of both (C). The solution spectra show that only in the systems of D_a:F_2TCNQ, D_a:F_4TCNQ and D_b:F_4TCNQ nearly all the molecules get ionized, while in the others only a fraction does. In thin films, however, nearly all dopant molecules become ionized in all of the systems except D_b:TCNQ. For the systems with fractional ionization yield, the spectral regions of ca. 0.5 - 2.0 eV were enlarged for better visibility (dashed lines). For D_b:TCNQ in a thin film, a background was subtracted from this spectral region and the data was smoothened due to a small signal-to-noise ratio (grey line). This figure will be published in ref. [A7].

where $ln\,K$ is the natural logarithm of the equilibrium constant K, z_e the number of moles of transferred electrons, F Faraday's constant, R the gas constant, T the absolute temperature (here 20° C – 293.15 K), $E_{1/2}^{red}$ the half-wave reduction potential of the

acceptors and $E_{1/2}^{\mathrm{ox}}$ the half-wave oxidation potential of the donors. The equilibrium constant K in solution can be expressed as the reaction quotient,[284]

$$K = \frac{c_{D^+} \cdot c_{A^-}}{c_D \cdot c_A} \tag{5.2}$$

with the concentration c_{i} of the respective species, considering ideal behavior with activity coefficients of 1. Our measurements indicate that in the investigated systems there is always only 1 electron transferred, thus $c_{\mathrm{D}^+} = c_{\mathrm{A}^-}$ and $z_{\mathrm{e}} = 1$. The solutions were mixed in a molar ratio of one acceptor per one donor molecule, therefore $c_{\mathrm{D}} \approx c_{\mathrm{A}}$.[64] Since we assume no side reactions to take place, $c_{\mathrm{A}} + c_{\mathrm{A}^-} = c_{\mathrm{A}}^0$, where c_{A}^0 is the starting concentration of acceptors in the mixed solution. Based on these considerations, we can estimate the percentage P of molecules, which undergo charge transfer ($P = c_{\mathrm{A}^-}/c_{\mathrm{A}}^0$) in solution via

$$P = \frac{\sqrt{e^{\frac{F\Delta E}{RT}}}}{\sqrt{e^{\frac{F\Delta E}{RT}}} + 1} \,. \tag{5.3}$$

This formula shows the dependence of the charge transfer probability on temperature and the energetic difference in redox-potentials for a donor-acceptor system undergoing single charge transfer. It can also be easily modified to accommodate different molar mixing ratios than 1:1.

Table 5.1 summarizes the percentages of molecules undergoing charge transfer estimated from the optical spectra (P_{exp}) and the theoretically estimated percentages (P_{theo}). As can be seen, both reveal the same trend with reasonable quantitative agreement. Quantitative differences likely arise from the (small) influences of the electrolyte being present during the CV measurements, weak ion-pairing effects, and non-ideal behavior of the molecules in solution (activity coefficients smaller 1).

The situation changes when turning towards thin solid films. While in solution for nearly half of the semiconductor-dopant combinations only a fraction of the molecules was ionized, the optical spectra of the thin films [Figure 5.3 c) and d)] demonstrate that in almost every system nearly all molecules undergo charge transfer. The clear exception is D_b:TCNQ, where about 1% of the molecules are ionized in the thin film, comparable to the amount found in solution. In the case of D_b: F_1TCNQ, only an estimated 70% of the molecules undergo charge transfer, which is still much higher than the percenttage in

[64] Equation (5.3) can be extended to molar ratios of 1:r (dopant:host), which then reads $P = \frac{\sqrt{r \cdot \exp(\dots)}}{\sqrt{r \cdot \exp(\dots)}+1}$. In cases of $E_{red} \approx E_{ox}$, where $\exp(\dots) \approx 1$ and thus, the IPA yield for 1:1 ratios is only medium, P increases drastically for low dopant concentrations with r >> 1. In such cases, low dopant concentrations of a few percent (as commonly used) have a higher ionization efficiency.

solution of about 3%. This transition from partial to (nearly) complete ionization yield was observed to take place during deposition of the thin films (dropcasting), where the color of the respective samples changed during drying. Consequently, the difference in IPA formation yield for solution versus the solid is to be sought in (small) changes of the effective E_{ox} and E_{red} when changing the state of aggregation. In fact, in solution E_{ox} of D_b is within ca. 100 meV of E_{red} of F_1TCNQ and F_2TCNQ, so that already small stabilizing effects (e.g., polarization or charge delocalization beyond the initial ion pair, i.e. $D^+..A^-$ Coulombic interactions) in the solid as compared to solution would suffice to invoke the observed effect. The same argumentation applies for the pairing D_a:TCNQ. Additionally, possible (partial) planarization of the arylamine groups in the solid might lower E_{ox} of the semiconductor molecules compared to the solution, making IPA with all dopants more probable in thin films.

Table 5.1 Charge transfer probability (P_{theo}) as function of the difference in electrochemical potential (ΔE) in comparison with measured yield of ionized molecules in solution (P_{exp}). Both calculated and experimental results show the same trend and are in reasonable quantitative agreement. This table will be published in ref. [A7].

	ΔE [mV]		**P_{theo} [%]**		**P_{exp} [%]**	
	D_a	**D_b**	**D_a**	**D_b**	**D_a**	**D_b**
TCNQ	-22	-246	39	0.8	20	0.5
F_1TCNQ	89	-135	85	7	75	3
F_2TCNQ	197	-27	98	37	100	18
F_4TCNQ	398	174	100	97	100	100

In contrast, using IE and EA values from UPS/IPES does not allow a reliable estimation on whether IPA is likely to occur for a given material pair (except for the two obvious combinations with F_4TCNQ). This can be rationalized when considering that the F_xTCNQs employed here do form polycrystalline thin films, and substantial effects of molecular arrangement on IE/EA values are expected due to the numerous highly polar intra-molecular bonds. This can be easily seen in comparison with the CV data, where each additional fluorine substitution lowers E_{red} by roughly 100 meV, which is not the case for the solid-state EA.

5.3 Material Set II

For set II, the obtained optical spectra are summarized in Figure 5.4. Again, neither the host molecules nor the dopant absorb in the spectral region up to around 1.5 eV and emerging features in this region are assigned to ionized species. Reference spectra of ionized species were recorded of solutions, where $FeCl_3$ was added generate cations of the oligothiophenes and lithium iodide (LiI) to generate anions of $Mo(tfd)_3$, respectively.

Figure 5.4 a) shows the optical spectra of 6T and DH6T in solution (DCM). Due to poor solubility of both compounds in DCM, saturated solutions were used. Upon addition of

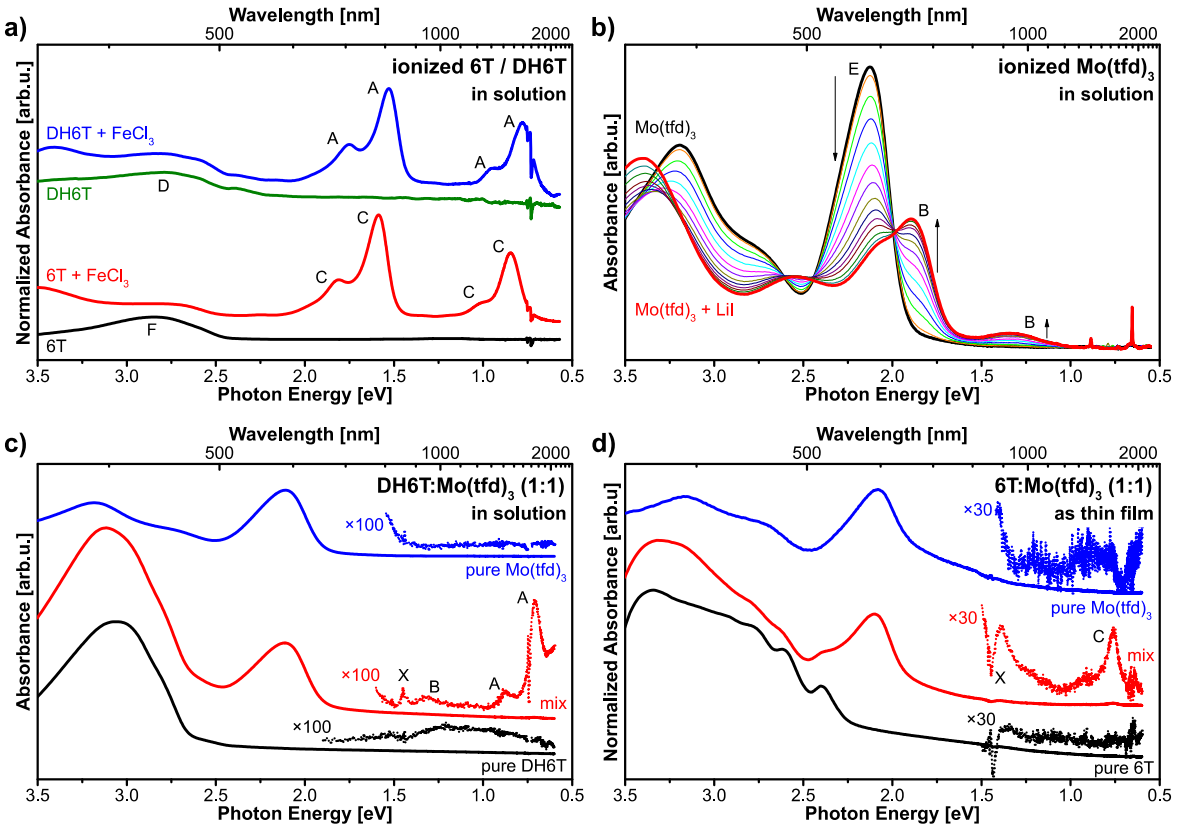

Figure 5.4 Optical spectra of **a)** ionized 6T / DH6T in solution, b**)** ionized $Mo(tfd)_3$ in solution, **c)** DH6T:$Mo(tfd)_3$ in solution, and **d)** 6T:$Mo(tfd)_3$ as thin films. To create donor cations $(DH)6T^+$, the respective solutions were mixed with $FeCl_3$, and for $Mo(tfd)_3$ anions, the solution was mixed with LiI. The newly appearing features in the region up to 1.5 eV can be assigned to belong to ionized DH6T (A), ionized $Mo(tfd)_3$ (B), and ionized 6T (C), while the neutral features of these compounds are marked with D, E and F, respectively. For c) and d) a background was subtracted from the spectral regions of ca. 0.5 to 1.5 eV (see experimental section for details) and these regions were enlarged for better visibility (dashed lines). The signals at 1.44 eV (X) are artefacts from the photo-spectrometer occurring from a change of detectors. The spectra of the mixed materials both in solution and in thin film reveal only a small number of molecules being ionized. The reference spectra a) and b) were recorded by PD Dr. Andreas Opitz and Stephan Lüdtke (Institut für Physik, Humboldt-Universität zu Berlin). This figure will be published in ref. [A7].

$FeCl_3$, both spectra show similar new features in the region up to 2.0 eV. The positions of these new features are at 0.78 eV, 0.94 eV, 1.53 eV and 1.75 eV for DH6T and 0.85 eV, 1.01 eV, 1.59 eV and 1.81 eV for 6T, while the positions of the main neutral 6T and DH6T features are at 2.85 eV and 2.79 eV, respectively. These values are comparable to previously reported values for the cation of 6T.[93] Figure 5.4 b) shows the optical spectra of a titration series of LiI to a $Mo(tfd)_3$ solution ($CHCl_3$). Here, with increasing LiI concentration, the feature of the neutral molecule at 2.13 eV is decreasing, while two new features at 1.89 eV and 1.34 eV are increasing. The spectra are in good agreement with previously reported spectra for the reduction of $Mo(tfd)_3$ with ferrocene.[171]

The absorption spectra of DH6T:$Mo(tfd)_3$ in solution and a co-evaporated thin film of 6T:$Mo(tfd)_3$ a shown in Figure 5.4 c) and d), respectively. The (background corrected)

regions up to 1.5 eV reveal only a small amount of molecules to be ionized. In solution optical transitions for both ionized DH6T and ionized $Mo(tfd)_3$ can be found, while in the thin film only transition of ionized 6T are visible. This is most likely due to the weak molar absorptivity of the signal of ionized $Mo(tfd)_3$ at around 1.34 eV, which is buried in the noise and the artefact (marked with X) stemming from the detector change of the used spectrometer at 1.44 eV.

In literature, the molar absorptivity of 6T is reported to be 5.0×10^4 $M^{-1}cm^{-1}$ (at 436 nm in THF)[254] and 6.0×10^4 $M^{-1}cm^{-1}$ (at 432 nm in DCM)[285] and for its cation $6T^+$ to be 4.3×10^4 $M^{-1}cm^{-1}$ (at 780 nm in DCM),[286] while for DH6T, it is reported to be 5.3×10^4 $M^{-1}cm^{-1}$ (at 440 nm in THF)[254]. Since the molar absorptivity for 6T and DH6T in THF is roughly the same, it is assumed at this point that the molar absorptivities for the cations are roughly the same. Based on Figure 5.4 a) and the reported molar absorptivity of $6T^+$ at 780nm (1.59 eV), the molar absorptivity of the cation feature at 0.84 eV is calculated to be around 2.8×10^4 $M^{-1}cm^{-1}$. Using these values of molar absorptivities and the intensity ratios of the signals of ionized and neutral DH6T/6T species (0.6% and 2.2%, respectively), the ratio between ionized and neutral species is estimated to be in the order of 1% for DH6T:$Mo(tfd)_3$ in solution and 4% for 6T:$Mo(tfd)_3$ in a thin film. Thus, both in solution and in thin films only a small percentage of molecules is found to be ionized. This is in line with the calculated amount of molecules undergoing charge transfer based on equation (5.3) (ca. 20% for DH6T and ca. 3% for 6T), keeping in mind that the reported literature values were measured under slightly different experimental conditions (see above).[171,254] While UPS/IPES data shows a huge energetic offset between the EA of the acceptor and the IE of the donors in favor of charge transfer, CV data predict the process to be energetically unfavorable, again in agreement with the obtained results.

Additionally, AFM measurements were performed on the (co-)evaporated thin films of 6T:$Mo(tfd)_3$, the images of which are summarized in Figure 5.5.[65] The image of the pure $Mo(tfd)_3$ film in Figure 5.5 a) shows that $Mo(tfd)_3$ tends to form large islands with heights up to 200 nm (the nominal thickness of the film was in the order of 50 nm). On the other hand, pure 6T forms a homogenous film with a RMS roughness of 8-10 nm and consists of grains with diameters in the order of 150 nm, as shown in Figure 5.5 b). The images of the mixed film in Figure 5.5 c) show a different morphology. The film consists of many large islands up to 100 nm in height and 300 to 500 nm in diameter. Changing the color scale of the images, the surface at the bottom of the islands becomes visible, see Figure 5.5 d). The surface shows a morphology similar to the surface of the pure 6T film, although the density of the islands makes an unambiguous determination of the surface morphology difficult.

[65] Since the thin-films of the other systems were prepared by drop-casting etc., AFM measurements of these films did not yield useful results due to largely inhomogeneous films.

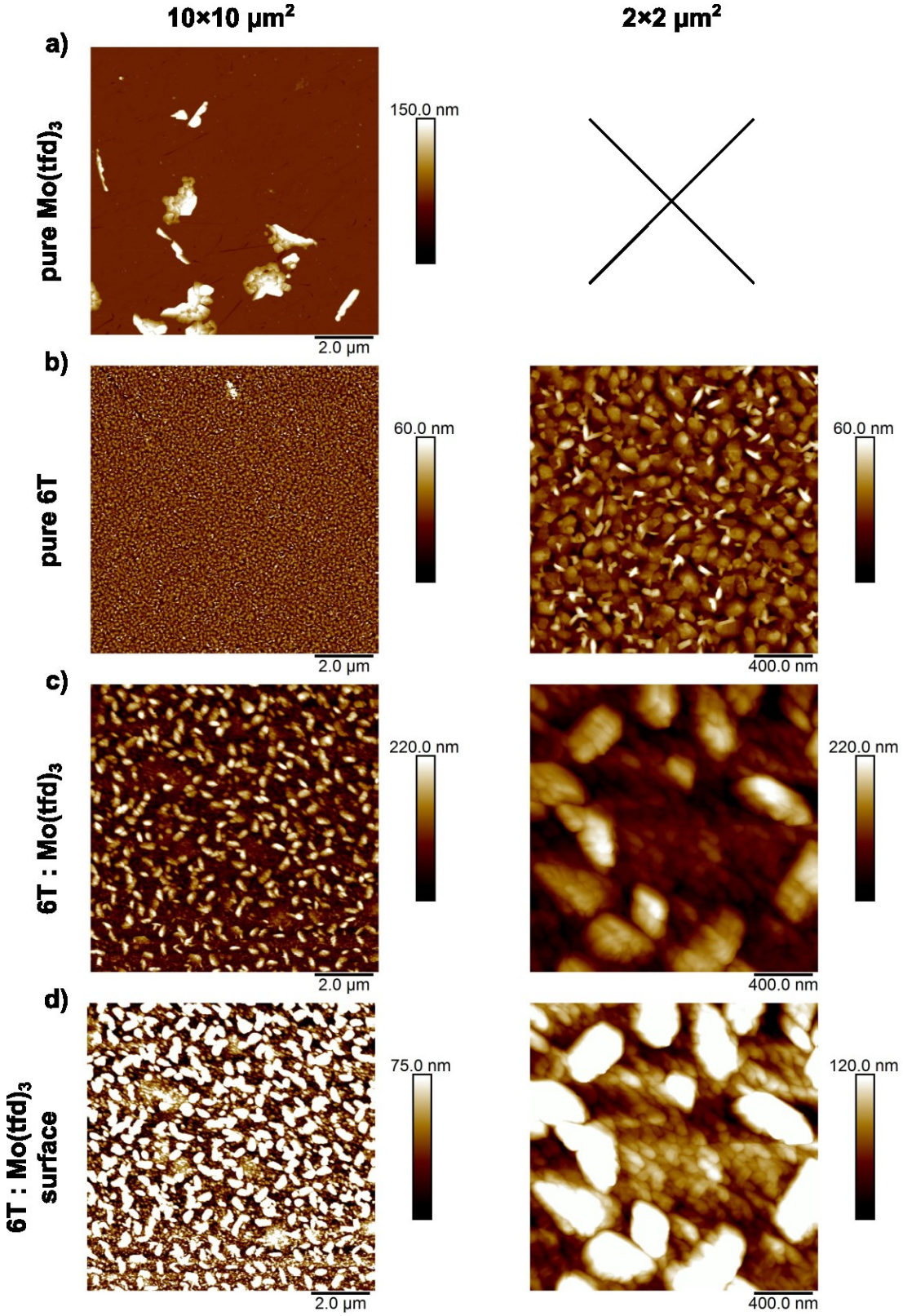

Figure 5.5 AFM images with size 10×10 µm² (left) and 2×2 µm² of **a)** pure $Mo(tfd)_3$, **b)** pure 6T, **c)** mixed 6T:$Mo(tfd)_3$, and **d)** mixed 6T:$Mo(tfd)_3$ with a different color scale to focus on the surface. Pure $Mo(tfd)_3$ grows in large islands, while pure 6T grows in a homogeneous film with grains of diameter in the range of 150 nm. The mixed film shows a morphology which indicates that 6T and $Mo(tfd)_3$ form separated crystalline phases, where $Mo(tfd)_3$ grows in islands and 6T as homogenous film in between the islands.

These measurements indicate, that 6T and $Mo(tfd)_3$ do not mix, but rather form separate crystalline phases with $Mo(tfd)_3$ growing in islands and 6T as film in between the islands. This is in line with the observation that the positions of the optical transitions of both materials in the mixed film do not shift significantly compared to the transitions of the pure films (less than 30 meV, see Figure 5.4). If the materials would mix, one would expect the optical transitions of the two species to be blue-shifted compared to the transitions of the pure films, since the strong molecule-molecule interaction of pure crystalline phases (causing a red-shift compared to isolated molecules) is reduced in a mixed phase. However, additional structure-resolvingmeasurements like X-ray diffraction (XRD) are needed to further confirm this hypothesis. However, these measurements still confirm that there is only limited interaction between 6T and $Mo(tfd)_3$.

5.4 Material Set III

The experimental conditions used to measure IPA formation for set III are different from the other two sets, since in this case it was not possible to achieve molar 1:1 mixing ratios. Since the solubility of PFP in the used solvent (DCM) is poor and not even concentrations of 0.1 mM could be achieved without precipitants of non-dissolved PFP being present, saturated PFP solutions (< 0.1 mM) were used and mixed with (excess) $CoCp_2$. This approach was chosen to show the general feasibility of IPA formation between PFP and $CoCp_2$ in solution, since it was found that the PFP anions are not stable in solution (the peak associated with ionized PFP at 0.65 eV measured on a PFP solution with excess $CoCp_2$ vanished during the course of an hour, while the peak of neutral PFP re-appeared in part). This observation is not surprising, since the anions of PFP can be expected to be air- and moisture sensitive. According to the specification sheet of the commercially purchased, anhydrous DCM (Sigma Aldrich, anhydrous, ≥99.8%), the used DCM still contains up to 10 ppm of water. However, 10 ppm water correspond to a molar concentration of 0.5 mM (by using the general convention of 1 ppm ≈ 1 mg l^{-1}). Due to the low solubility and thus the used low concentration of PFP (< 0.1 mM), the amount of PFP (thus PFP anions) and water in the DCM solution can be assumed to be in the same order of magnitude, explaining the instability of the PFP anions in this setup. Therefore, using lower concentrations with fully dissolved PFP (in the order of 10^{-5} M) would not have been beneficial to determine the IPA formation yield.

Additionally, due to the low solubility of PFP, it was not possible to deposit useable thin films from solution. Furthermore, the vacuum deposition of $CoCp_2$ is also rather complicated – due to its high vapor pressure, $CoCp_2$ has to be introduced to the vacuum system from an ampoule via a leak valve[188] – and thus depositing mixed thin films in a molar 1:1 ratio cannot be achieved easily. For this reason, mixed films of PFP:$CoCp_2$ were

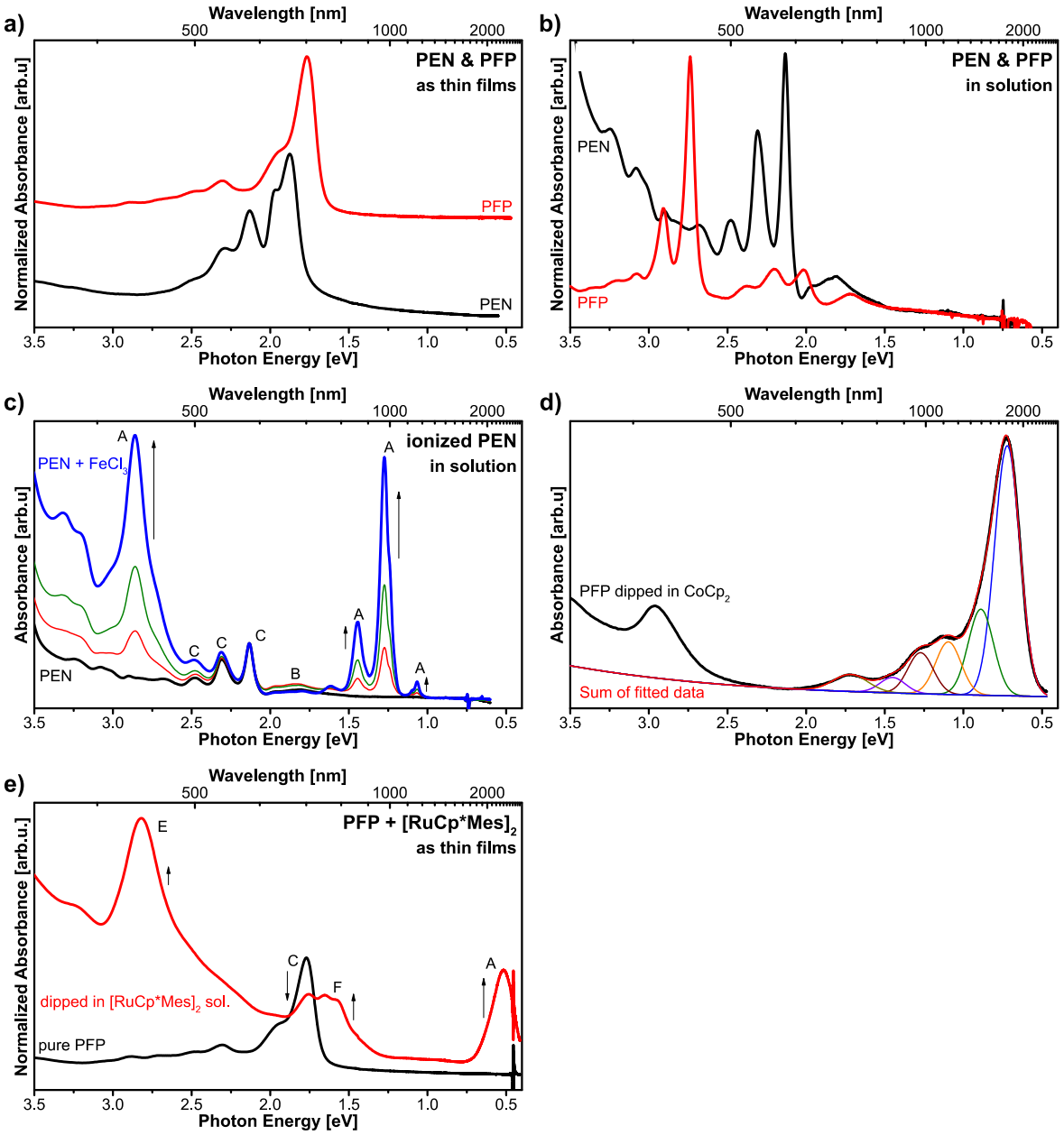

Figure 5.6 Optical spectra of **a)** pentacene (PEN) and PFP as thin films and **b)** in solution. Both spectra show similar optical features, especially in solution, where just the intensity of the features is different. The features at 1.7 eV and 1.8 eV for PFP and PEN in solution, respectively, stem from non-dissolved particles. **c)** Optical spectra of PEN cations generated by titration with a $FeCl_3$ solution. The features can be assigned to PEN cations (A), non-dissolved PEN (B) and neutral PEN (C). **d)** Spectra of PFP film dipped in a $CoCp_2$ solution. The features in the spectral region of 0.5 to 2.0 eV were fitted with Gaussian peaks to reveal the optical structure of ionized PFP. **e)** Optical spectra of a PFP thin film dipped in a $[RuCpMes]_2$ solution. The features are assigned to neutral PFP (C), PFP^- (A) and PFP^{2-} (F) (details see text). The optical spectra of ionized PEN displayed in c) were recorded by PD Dr. Andreas Opitz (Institut für Physik, Humboldt-Universität zu Berlin). This figure will be published in ref. [A7].

fabricated by dipping a vacuum deposited PFP thin film (ca. 50 nm) into a 2 mM solution of $CoCp_2$ in DCM, and by sequentially spin-coating the 2mM $CoCp_2$ solution onto a PFP film. In both cases, incorporation of $CoCp_2$ into the thin film is sought to occur due to swelling of the PFP thin film caused by the DCM solution.

The reference spectra for ionized PFP are displayed in Figure 5.6. Reference spectra for the $CoCp_2$ cation can be found in literature with its lowest transition lying at around 3 eV.[233,276] For PFP it was not possible to generate anions by reduction with KI or LiI, nor cations by oxidation with $FeCl_3$. Also spectro-electrochemical measurements did not yield reasonable results. Therefore, the appearing features in the spectral region of 0.5 to 2.0 eV for PFP:$CoCp_2$ thin films and solutions (Figure 5.7) will be assigned to belong to the PFP anions by comparison with the optical spectra of PEN cations. The main reasoning here is the similarity of the optical spectra of PEN and PFP, and that usually the optical features of anions and cations are very similar.[287] PEN cations were generated by titration of a $FeCl_3$ solution to a saturated PEN solution (DCM), the optical spectra of which are displayed in Figure 5.6 c).

Figure 5.6 a) and b) show the optical spectra of pure PEN and PFP in thin films and solutions, respectively. As can be seen, the optical features are very similar, with the main difference of the PFP spectra being red-shifted to the PEN spectra by 110 meV for the thin films and 155 meV for the solutions. Especially in solution, the features of the first optical transitions show the same structure (only the intensity of the transitions being different) and are separated by ca. 170 meV. The features of the saturated pure PFP and PEN solutions at 1.7 eV and 1.8 eV can be assigned to non-dissolved particles, since the respective thin films show absorption features at these energies and they are not present in literature spectra of solutions.[72] Figure 5.6 c) shows the optical spectra of PEN cations. Here, upon titration of $FeCl_3$ new features are emerging in the spectral range of 0.5 to 2.0 eV (labeled A) and the positions of the first four strong transitions are lying at 1.07 eV, 1.27 eV, 1.44 eV, and 1.61 eV (thus all separated by 170 to 200 meV). The neutral features (C) at 2.13 eV and 2.31 eV are not vanishing upon $FeCl_3$ titration, since due to poor solubility a saturated PEN solution was used with non-dissolved PEN still being present. Thus, when PEN is ionized – ionized PEN is more soluble – some of the non-dissolved PEN particles will dissolve, basically keeping the neutral PEN concentration constant. To compare the structure of the newly appearing features in the thin films of PFP:$CoCp_2$, the features in the spectral region of 0.5 to 2.0 eV of the PFP thin film dipped into a $CoCp_2$ solution were fitted by using Gaussian peaks and a background (as described in the experimental section). Figure 5.6 d) shows the fitted spectrum, which reveals the first four strong transitions to lie at 0.72 eV, 0.89 eV, 1.10 eV, and 1.27 eV. Again, all features are separated by 170 to 200 meV, similar to the structure of PEN cations with of course the intensity of the transitions being different. In general, for PEN and PFP, the energetically lowest transition is strongest in the

thin films. When we assume that the red shift of PEN to PFP and from solution to thin films is the same for the ionized species, we can estimate the position of the first transition for ionized PFP species. The red shift from solution to thin film of the first optical transition for PEN is 270 meV, while the red shift of PEN to PFP thin film is 110 meV. Applying these shifts to the energetically lowest transition of PEN cations at 1.07 eV, the estimated position for the first transition of ionized PFP is 0.69 eV. This value is very close to the position of the energetically lowest transition of the PFP+$CoCp_2$ thin film [Figure 5.6 d)] at 0.72 eV. Therefore, by comparison of the structure of the optical features and the shifts in PEN and PFP thin films and solutions, we can safely assign the newly appearing features in the optical spectra of PEN+$CoCp_2$ displayed in Figure 5.7 to belong to ionized PFP.

Additionally, a thin film of PFP was dipped in a $[RuCp^*Mes]_2$ solution (Toluene) and the resulting spectrum is shown in Figure 5.6 e). Here, after dipping, the feature of neutral PFP (C) decreases, while new features are emerging at 0.52 eV (A), 1.57 eV (F), 1.65 eV (F) and 2.82 eV (E). By comparison with Figure 5.6 d), the features A and E, might be assigned to the anion PFP^-, both peaks are blue-shifted by ca. 200 meV and 140 meV, respectively.[66] However, the additional features F are not observed in mixed PFP:$CoCp_2$ thin films and solutions. Thus, they probably stem from the dianions PFP^{2-}, as $[RuCp^*Mes]_2$ is a much stronger reducing agent than $CoCp_2$.[67] Thus, the spectrum of the PFP+$[RuCp^*Mes]_2$ thin film supports the assignment of features to ionized PFP, but due to possible formation of dianions cannot serve as a standalone reference spectrum.

The results of the optical measurements of the mixed PFP+$CoCp_2$ solutions and thin films are displayed in Figure 5.7. Upon (excess) exposure of a saturated PFP solution to $CoCp_2$ the optical transitions of neutral PFP are seen to vanish [Figure 5.7 a)], while a new feature at 0.65 eV emerges indicating that nearly all PFP molecules are ionized. In the case of the PFP film dipped into a $CoCp_2$ solution [Figure 5.7 b) – bottom], the signal of neutral PFP at 1.77 eV vanishes nearly completely, while the feature at 0.73 eV assigned to ionized PFP is emerging. The newly appearing transition at 2.96 eV coincidentally lies at the same position of the cation $CoCp_2^+$.[276,288] However, since the absorption of $CoCp_2^+$ is relatively weak[288] and PFP^- is expected to have a rather strong absorption, the peak at 2.96 eV is more likely a higher energy peak of PFP^-, as it was also observed (although slightly blue shifted) in the spectrum of the PFP+$[RuCp^*Mes]_2$ thin film [Figure 5.6 e)]. In the spectra of the step-wise sequentially spin-coated $CoCp_2$ on top of a PFP film [Figure 5.7 b) – top], the optical transitions of ionized PFP and $CoCp_2$ are appearing gradually, while at the same time the

[66] The monomer cation $[RuCp^*Mes]^+$ has no absorption feature at 2.8-3.0 eV (compare ref. [A4]), thus E can be assigned to PFP^-.

[67] Optical transitions of doubly charged ions are usually blue shifted to the transitions of singly charge ions and energetically lie in between the transitions of the neutral molecules and singly charge ions.[93]

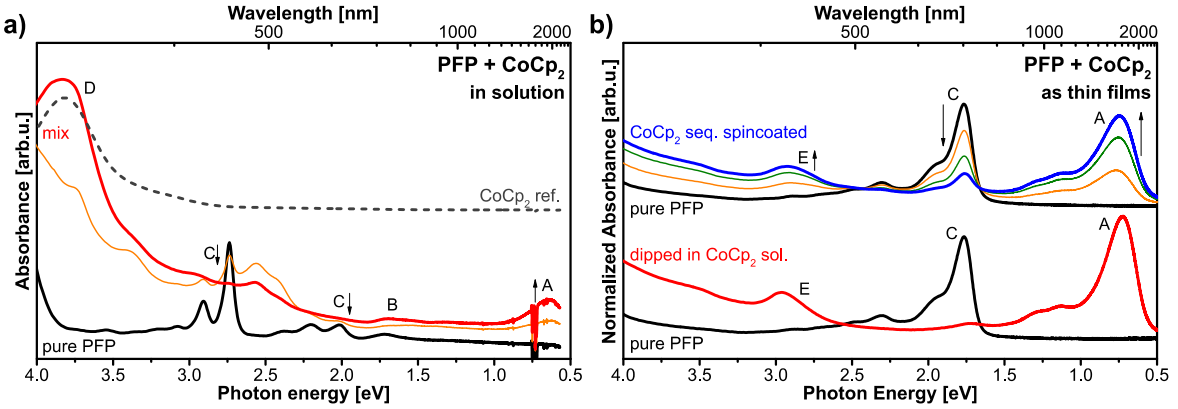

Figure 5.7 Optical spectra of **a)** PFP mixed with (excess) $CoCp_2$ (the mixed solution of the spectra shown as red curve contains double the amount of $CoCp_2$ than the mixed solution, whose spectra is shown as orange curve), and **b)** PFP thin films, dipped in a $CoCp_2$ solution (bottom) and processed via sequential spin-coating (top). The newly appearing optical transitions upon mixing in solution were assigned to ionized PFP (A) and neutral $CoCp_2$ (D), while the features of neutral PFP (C) are vanishing. The transitions at around 1.7 eV (B) belong to non-dissolved PFP being present in the saturated PFP solutions and are not changing significantly upon mixing. In thin films, the newly appearing feature at around 2.96 eV (E) is most likely a higher energy peak of PFP^- (compare Figure 5.6e), which coincidently lies at the same position as $CoCp_2^+$.[276,288] This figure will be published in ref. [A7].

feature of neutral PFP is vanishing. This illustrates the possibility of the sequential processing method to control the mixing or dopant concentration by choosing appropriate preparation conditions. Both the spectra of solutions and thin films point towards efficient IPA formation of PFP^-:$CoCp_2^+$, although its yield could not be quantified in this case. Equation (5.3) predicts nearly all molecules for the pair PFP:$CoCp_2$ to undergo charge transfer (98%), whereas the prediction from UPS/IPES data is ambiguous. In the case of the intermediate EA of PFP, the data would suggest IPA formation to be energetically unfavorable. Thus, the results of set III still indicate redox-potentials from CV to be more reliable for the prediction of IPA formation.

5.5 Summary

The results from the investigated host/dopant sets show that using IE and EA values from UPS/IPES does not allow a reliable estimation on whether IPA is likely to occur for a given material pair, whereas CV data are able to provide a reasonable prediction. For set I, the redox-potentials were used to quantitatively predict the fraction of neutral and ionized molecules in mixed solution as expected from thermodynamics. In thin solid films, solid-state effects influence the effective E_{ox} and E_{red} compared to solution. However, here the CV data still provided a useful basis to estimate the IPA formation yield in the solid. For set II, the UPS/IPES data revealed a huge energetic offset between the EA of the acceptor and the IE of the donors in favor of charge transfer, while CV data predicted the process to

be energetically unfavorable, in agreement with the obtained results. Here, even the knowledge of the difference in IE for different film structures did not help for the prediction of possible IPA formation. For set III, the prediction from UPS/IPES data was ambiguous and in the case of the intermediate EA value of PFP, the data would suggest IPA formation to be energetically unfavorable. The CV data on the other hand predicted IPA formation to be energetically favorable, which was corroborated by the results of (excessively) doped solutions and thin films.

Overall, our results suggest that CV data reveal characteristics on the molecular scale that are relevant for IPA formation in mixed semiconductor-dopant films. This is most likely due to the fact that CV probes nearly isolated molecules. In addition, ionic species are more stabilized in polar solvents (containing electrolytes) than in neutral solids, which more-or-less models the mutual Coulombic stabilization of oppositely charged molecules in doped films. In contrast, UPS/IPES data include surface and collective electrostatic sample properties on and above the meso-scale that are not reliable parameters for dopant selection.

6 N-DOPING OF A P-TYPE POLYMER

In principle, organic semiconductors should be equally able to transport p-type and n-type charge carriers. However, most organic semiconductors show a high asymmetry between electron and hole mobilities, where the hole mobility exceeds the electron mobility by several orders of magnitude, rendering them intrinsically p-type.[41] This asymmetry was recently related to an universally present trap level at around 3.6 eV below the vacuum level caused by an oxygen/water complex.[42] Due to this trap level, polymers exhibiting good n-type behavior with high electron mobilities of up to 3.1 cm^2/Vs usually have an electron affinity of 3.7-4.0 eV, which lies just below the found trap level.[43–45]

Here, we investigate the n-type doping of the predominantly p-type co-polymer IDT-BT, in order to assess whether a p-type polymer can successfully be n-doped and possibly be rendered n-type in accordance. IDT-BT was previously used as donor material in organic solar cells and as active layer in p-type organic field effect transistors (OFETs), for which hole mobilities of 0.8-3.6 cm^2/Vs were reported.[247,249,265,289–292] As n-dopants, the organo-metallic dimers $[RhCp^*Cp]_2$ and the slightly stronger $[RuCp^*Mes]_2$ are used, the doping mechanisms of which are explained in detail in subsection 2.2.3. Recent studies showed that the n-doping of n-type co-polymers like P(NDIOD-T2)[68] or P(BTP-DPP)[69] by organometallic dimers leads to an enhancement of the mobility by a factor of around 10 and an increase in conductivity over several orders of magnitude.[206,208,293]

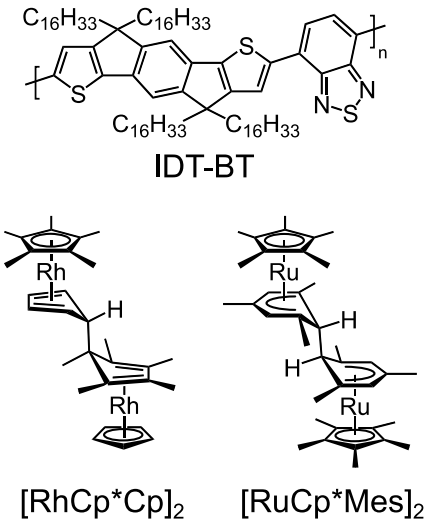

Figure 6.1 Chemical structures of the host polymer IDT-BT and the organometallic dimers $[RhCp^*Cp]_2$ and $[RuCp^*Mes]_2$.

Figure 6.1 shows the chemical structures of the host polymer IDT-BT and the two dopants. At first, the capability of the organometallic dimers to successfully n-dope IDT-BT is investigated by employing optical absorption spectroscopy and the influence of light irradiation on the doping process is examined. Following, the electronic structure of doped films is explored by combined UPS and IPES measurements and the changes in conductivity upon doping are determined by current-voltage measurements. Finally, a short attempt to fabricate OFETs employing such doped layers is presented.

[68] Poly{[N,N'-bis(2-octyldodecyl)-naphthalene-1,4,5,8-bis(dicarboximide)-2,6-diyl]-*alt*-5,5'-(2,2'-bithiophene)}.
[69] Poly((*E*)-3-(5-([8,8'-biindeno[2,1-b] thiophenylidene]-2-yl)thiophen-2-yl)-2,5-bis(*n*-icosyl)-6(thiophen-2-yl)-pyrrolo[3,4-*c*]pyrrole-1,4(2*H*,5*H*)-dione).

6.1 Doping Capability and Activation by Light Irradiation

At first, optical absorption spectra of mixed solutions were recorded to investigate the capability of the two organometallic dimers to effectively dope IDT-BT. Since absorption spectra of solutions are usually less broad than spectra of thin films and also show a smaller background due to less scattering, new transitions appearing in the optical gap of the polymer, associable with the formation of polarons, can be observed easier in solution. In subsection 2.2.3, it was highlighted that the doping of low electron affinity materials with organometallic dimers can be activated or enhanced by irradiation of the doped material with light. To study the effect of light irradiation on the absorption spectra of the mixed IDT-BT:dimer solutions, the solutions were irradiated with a high intensity red LED (625 nm), since IDT-BT shows a strong transition at this wavelength and host absorption was found to be the first step in the activation process of doping. The results of these investigations are summarized in Figure 6.2.[70]

Figure 6.2 a) and c) show the absorption spectra of solutions of IDT-BT mixed with $[RhCp^*Cp]_2$ and $[RuCp^*Mes]_2$, respectively, which were mixed in a molar 2:1 ratio corresponding to a dopant concentration of 50%.[71] This large dopant concentration was chosen with the expectation of obtaining strong polaron features in the event of any doping, which are easily observable by optical absorption spectroscopy. From the spectrum of the pure IDT-BT solution, the optical gap of IDT-BT was determined to be 1.7 eV. Both mixed solutions (red lines) show the emergence of two major absorption features in the optical gap of IDT-BT at 1.29 eV and 0.65 eV, which are similar in intensity for both dopants. Since the dimers and their cationic monomers show no absorption in the NIR and visible range,[203,204] these features can be assigned to belong to the negative polaron of IDT-BT. However, the absorption feature of neutral IDT-BT at 1.87 eV only decreases to around 85% of the intensity of the pure IDT-BT solution, which points towards a low ionization efficiency in this very high dopant concentration regime. In addition, the doping in solution was found to be not stable over time, since the signal of the IDT-BT polarons decreases while at the same time the signal of neutral IDT-BT increases again. Here, the doping with the slightly weaker $[RhCp^*Cp]_2$ is decaying faster than the doping with $[RuCp^*Mes]_2$, since the intensity of the polaron signal in the case of $[RhCp^*Cp]_2$ decreases to around 44% of its original value within 30 min, while in the case of $[RuCp^*Mes]_2$ the intensity decreases to only 77% in the course of 3 hours. The increase in intensity of the signal of neutral IDT-BT points towards a

[70] Note: the following is a purely qualitative investigation. To determine rate constants of the reaction between the polymer and dopants, or degradation of the doped state, a more detailed quantitative analysis has to be conducted, for which, however, the experimental results are clearly not sufficient. Nonetheless, here, it is sufficient to know the qualitative behavior of n-doping the polymer IDT-BT.

[71] Here, the reported molar ratios correspond to the number of polymer units per dimer molecules (thus, mixed materials), whereas the dopant concentrations c are calculated based on the number of monomeric cations N_{D^+} related to the number of polymer units N_P, in the form $c = N_{D^+}/(N_{D^+} + N_P)$.

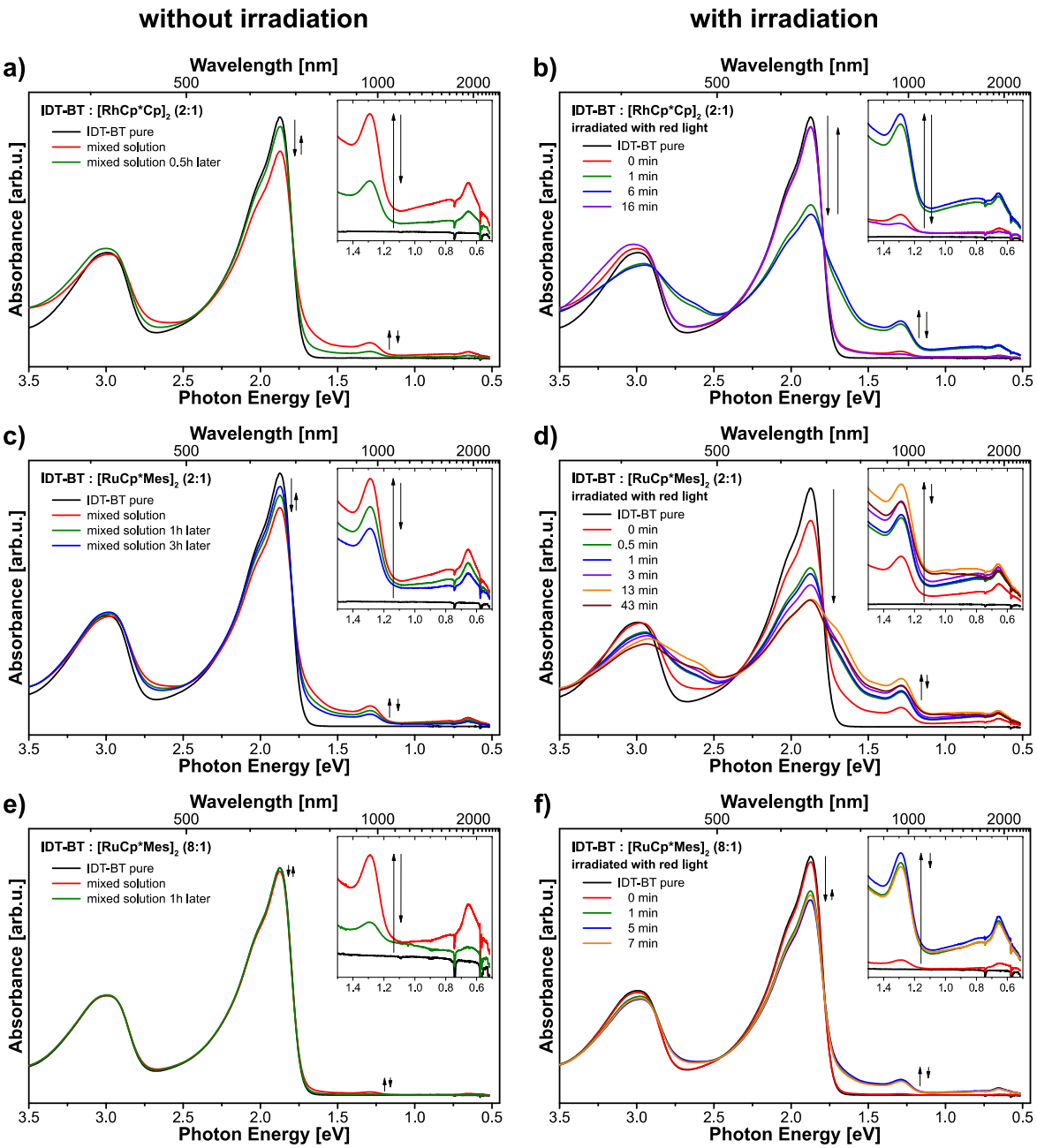

Figure 6.2 Optical absorption spectra of mixed solutions of **a)** IDT-BT:$[RhCp^*Cp]_2$ (2:1), **c)** IDT-BT:$[RuCp^*Mes]_2$ (2:1), and **e)** IDT-BT:$[RhCp^*Cp]_2$ (8:1). **b)**, **d)**, and **f)** show the systems of a), c), and e), respectively, after irradiation with high intensity red light (625 nm). The insets show an enhanced view of the regions of 0.5 to 1.5 eV. The formation of polarons can be observed in all systems (after mixing of the solutions) by the increase of the respective features at 1.29 eV and 0.65 eV. However, without irradiation, the doping is unstable and the polaron features decrease over the course of a few hours, while the feature of neutral IDT-BT increases again. Upon irradiation, the polaron features are significantly increased. However, prolonged irradiation is detrimental and leads to (partial) degradation.

back-reaction from the polaronic to the neutral state, possibly accompanied by partial degradation.[72] A completely reversible reaction would also involve the monomer cations to form dimers again. However, optical absorption spectroscopy is most likely not able to detect the re-formation of dimers, since the dimers show only a very weak absorption at around 3.5 eV,[204] and no distinct changes in intensity at around 3.5eV could be observed in the recorded spectra of the solutions.

The formation of polarons can be greatly enhanced by the irradiation with red light, as evidenced by the increase in intensity of the polaron features shown in Figure 6.2 b) and d). As can be seen, an irradiation of only 1 min with the high intensity light is sufficient to significantly increase the intensity of the polaron signals, while at the same time the intensity of the neutral feature is decreased. In the case of $[RhCp^*Cp]_2$, the polaron intensity reaches a maximum after around 6 min of irradiation. A prolonged irradiation, however, has severe negative effects, as the polaron features decrease slightly below the starting value. In the case of $[RuCp^*Mes]_2$, the formation of polarons under irradiation proceeds similarly. Here, after around 13 min the intensity reaches its maximum value. The maximum intensity of the $[RuCp^*Mes]_2$ doped IDT-BT is slightly higher (20% of the initial neutral IDT-BT feature) than in the case of $[RhCp^*Cp]_2$ (15% of the initial neutral IDT-BT feature). Moreover, a prolonged irradiation with red light leads to a decrease of the polaron features, whereas the intensity of the neutral feature stays at the same level, pointing towards degradation of IDT-BT. In addition, the spectra up to the irradiation time of 13 min exhibit an isosbestic point at (1.785 ± 0.003) eV, which clearly indicates a direct transition from neutral to polaron state without degradation occurring in the meantime. The spectrum of the 43 min irradiated sample, however, strays from that point by 24 meV (distance of spectra to isosbestic point at the same intensity), clearly indicating degradation occurring under prolonged irradiation.

Since the ionization efficiency was found to be low in the case of the 50% concentration (even with irradiation, the neutral signal only decreases to 55% of its original value), also a lower dopant concentration for the more stable system with $[RuCp^*Mes]_2$ was investigated. Here, a molar ratio of 8:1 (20%) was used, which is still a high dopant concentration compared to the usually used concentrations in the range of a few percent, but was chosen to provide a clearly observable polaron signal. The respective optical spectra are summarized in Figure 6.2 e) and f). Here, also polaron formation can be observed, which again is unstable over time, since the polaron features decrease to 29% of their initial intensity. Upon irradiation, the polaron features significantly increase in intensity and reach a maximum value after around 5 min of irradiation. Here, the minimum

[72] At this point, however, the data is not sufficient to clearly distinguish between a reversible (back-) reaction and degradation.

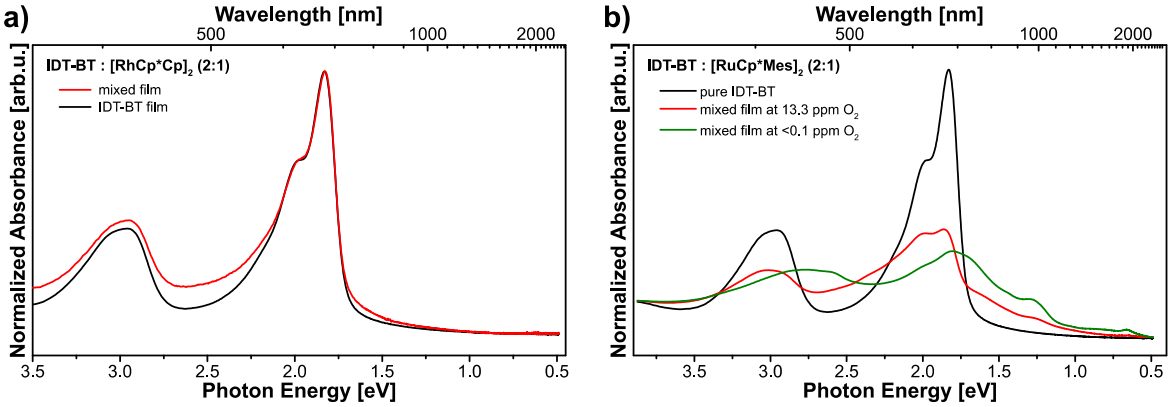

Figure 6.3 Optical absorption spectra of thin films of **a)** IDT-BT:$[RhCp^*Cp]_2$ and **b)** IDT-BT:$[RuCp^*Mes]_2$ in a molar ratio of 2:1. The inset in a) shows an enhanced view of the spectral region of 0.5-1.5 eV. As can be seen, the polaron formation proceeds much more efficiently in the case of $[RuCp^*Mes]_2$ than in the case of $[RhCp^*Cp]_2$. In Fig b), the effect of increased partial oxygen pressure in the glovebox is shown. The spectrum of a sample (green line) prepared at ideal glovebox conditions (partial pressure of O_2 below 1 ppm) shows strong polaron absorption features. In contrast, the spectrum of a sample prepared at O_2 partial pressure of 13 ppm (red line) shows a significant decrease of the polaron features, while the neutral features are more enhanced than in the other case of 0.1 ppm O_2. This clearly demonstrates the high oxygen sensitivity of the doped samples. In Fig b), the spectra were normalized to the intensity at 3.9 eV.

intensity of the neutral IDT-BT feature is around 82% of the intensity of a neutral IDT-BT solution, which points towards a higher ionization efficiency under illumination compared to the 50% doping case, where the minimal intensity was 55%.[73] Further irradiation of a few minutes leads again to a decrease in intensity of the polaron features, indicating that after around 5 min the maximal achievable ionization is reached. The results of the mixed solutions with different dopant concentrations clearly show that the doping in solution is not stable over time, but irradiation can enhance the reaction between dimers and IDT-BT. A prolonged irradiation, however, has detrimental effects leading to (partial) degradation of the system.

To investigate polaron formation in thin films, mixed films were fabricated by drop-casting mixed IDT-BT:dimer solutions (molar ratio of 2:1). The optical spectra of these films are shown in Figure 6.3. In the case of $[RhCp^*Cp]_2$ (Figure 6.3a), polaron features of the spectrum of the mixed film (red line) are barely observable. In the enhanced view of the 0.5-1.5 eV region, only a small feature at around 0.65 eV is visible, while no feature at 1.29 eV can be observed. The incorporation of $[RhCp^*Cp]_2$ rather leads to enhanced scattering in the film amounting for the additional background which is increasing with increasing photon energy. In the case of the slightly stronger $[RuCp^*Mes]_2$, the mixed film (green line)

[73] For a molecular system, a decrease of the neutral feature to 75% would be expected in a case of 4 host molecules per 1 dopant ion and single integer charge transfer. This can, however, not be related par for par to a polymer system, since here, a polaron can extend over a few monomer units and is thus not limited to a singular molecular unit.

shows strong polaron features similar to the ones in solution, whereas the neutral feature is significantly decreased. While in solution both dimers show similar intensities of the polaron features, here, the polaron features are much stronger in the case of $[RuCp^*Mes]_2$ than in the case of $[RhCp^*Cp]_2$. This might be related to the fact that the doping with $[RhCp^*Cp]_2$ was found to be less stable in solution (it significantly decreases over the course of 30 min) and the thin film preparation was performed via drop-casting from chlorobenzene solutions, which took around 40-60 min for the films to dry.[74] For this reason, only $[RuCp^*Mes]_2$ was used for the following investigations.

Furthermore, Figure 6.3 b) shows the spectra of two IDT-BT films mixed with $[RuCp^*Mes]_2$, which were prepared in a glovebox at different partial pressures of oxygen. The spectrum of the sample (green line) prepared at an O_2 partial pressure below 0.1 ppm (good glovebox conditions) shows strong polaron absorption features. In contrast, the spectrum of a sample prepared at an O_2 partial pressure of 13 ppm (red line) shows significantly smaller polaron features and more enhanced features of neutral IDT-BT. In both cases the partial pressure of H_2O was below 0.1 ppm, thus these results can be clearly linked to a high sensitivity of the doped films towards oxygen. For this reason, doped films were only prepared under good glovebox conditions with partial pressures of O_2 and H_2O always below 0.1 ppm.

Since in solution the formation of polarons can be enhanced by irradiation with red light, in the following the influence of red light irradiation of the mixed solutions before film preparation and also irradiation of thin films subsequent to preparation will be investigated. For solutions mixed in a molar 2:1 ratio, the maximum intensity of the polaron signal was achieved after around 10 min of irradiation, thus thin films were prepared, where the solutions were irradiated for 0 min, 0.5 min, 2 min, and 10 min prior to spin-coating. The obtained spectra are summarized in Figure 6.4 a). All spectra show similar polaron intensities, except the case of 10 min solution-irradiation, where the polaron features show a slightly smaller intensity and also the features of neutral IDT-BT at 1.8 eV and 2.0 eV are more pronounced. In addition, the thin films were irradiated with red light after the first recording of the optical absorption spectra. Figure 6.4 b) shows that an irradiation of 2 min leads to a small enhancement in the intensity of the polaron features (dashed lines), which is more pronounced for the cases of 0 min and 0.5 min solution-irradiation. Longer irradiation was found to not further increase the intensity of the polaron features (not shown here). Thus, solution-irradiation shows no benefit for films mixed in a

[74] This could be partially avoided by using a more volatile solvent like tetrahydrofuran, with which drop-casted films should dry within a few minutes. A change of solvent was, however, not attempted at this point, as tetrahydrofuran was expected to lead to bad film formation during spin-coating. Spin-coating was performed in order to produce homogenous thin films of a few 10 nm, which were used for UPS/IPES and IV measurements presented in the next subsection.

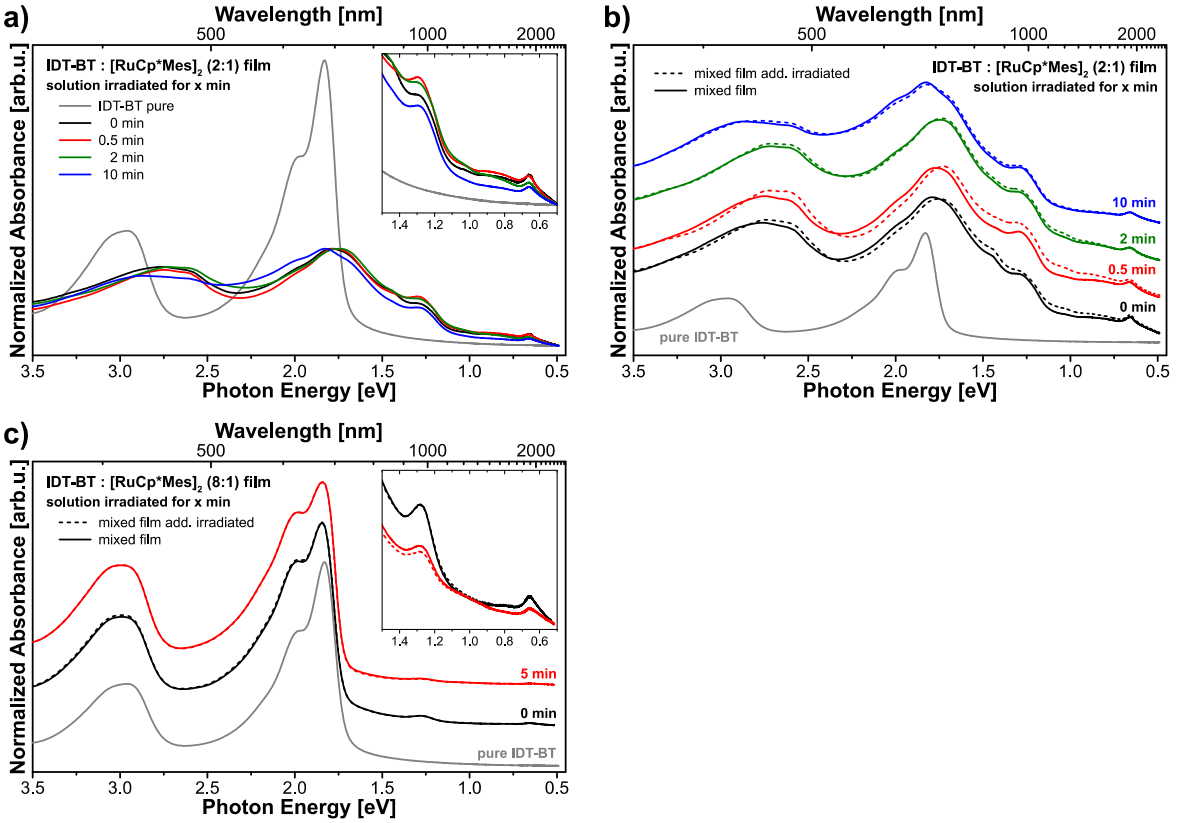

Figure 6.4 Optical absorption spectra of IDT-BT:[RuCp*Mes]$_2$ thin films in a molar ratio of **a)** and **b)** 2:1, and **c)** 8:1, where the respective mixed solutions were irradiated with red light prior to film formation. The insets show an enhanced view of the region from 0.5 eV to 1.5 eV. As can be seen, the irradiation of the solutions has no beneficial effect and can be even detrimental to polaron formation, if the solution is irradiated for a too long time. While irradiation of the samples after film preparation leads to slightly enhanced polaron features in the case of a molar 2:1 ratio, it has no beneficial effect in the case of a molar 8:1 ratio.

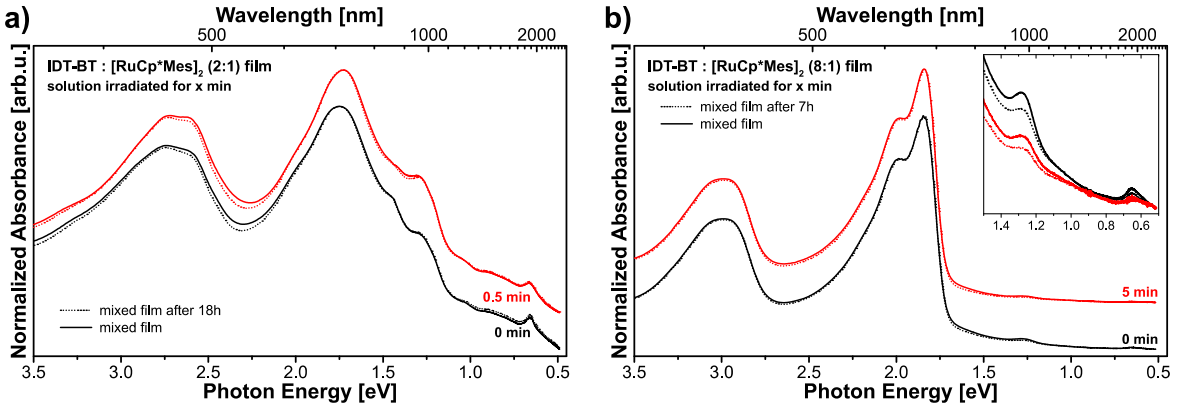

Figure 6.5 Optical absorption spectra of IDT-BT:[RuCp*Mes]$_2$ thin films in a molar ratio of **a)** 2:1 and **b)** 8:1 measured after different times. The absorption spectra of the thin films in a 2:1 ratio show no significant change after storage under inert atmosphere for 18 h (dotted lines) and doping in this case can be assumed to be stable at least for several days. In the case of the 8:1 ratio, however, the polaron features (inset) markedly decrease already after 6 h storage in inert atmosphere.

2:1 ratio and can even be slightly detrimental, when the solution is irradiated for a too long time.

Furthermore, thin films mixed in a molar 8:1 ratio were prepared to study the effect of irradiation in the case of a lower dopant concentration. Since for solutions mixed in this ratio the maximum polaron intensity was found after irradiation of around 5 min, the solutions were irradiated for 0 min and 5 min prior to drop-casting. The spectra shown in Figure 6.4 c) display a much smaller intensity of the polaron features for the sample, solution of which was irradiated prior to film preparation, compared to the sample directly cast from solution without irradiation. This behavior was confirmed by three different pairs of similarly prepared thin films, which were prepared on different days from different stock solutions and all showed a similar behavior. In contrast to the samples of 2:1 molar ratio, additional irradiation of the films [dashed lines, Figure 6.4 c)] shows no enhancement in intensity of the polaron features. Rather, the intensity of the polaron features of the solution-irradiated film is slightly decreased, while the features of the non-solution-irradiated film stay the same. Thus, irradiation in general seems to have a detrimental effect on polaron formation.

To check for stability of the doped films over time, some of the mixed thin films were stored for several hours under inert atmosphere and afterwards optical absorption spectra of those samples were recorded again, which are displayed in Figure 6.5. The absorption spectra of the thin films in a 2:1 ratio in Figure 6.5 a) show no significant change after storage in inert atmosphere for around 18 h (dotted lines) and doping can thus be assumed to be stable for at least several days. In the case of the 8:1 ratio in Figure 6.5 b), however, the polaron features markedly decrease already after 6 h storage in inert atmosphere. This observation is in line with the found decrease in conductivity of n-doped IDT-BT over the course of a few hours (see next subsection). Thus, in the case of lower dopant concentrations, the n-doping of IDT-BT is not stable and already starts to decay slowly within a few hours. This instability of doping might be caused by the trace amounts of oxygen and water still present in the inert atmosphere as well as within the solutions and thin films. The discussion on stability will be continued in the next subsection with the discussion of the obtained conductivity data.

With regard to chapter 7, it should be noted at this point that no indication of possible bipolaron formation was found in any of the recorded optical spectra. I.e., only two major absorption features in the optical gap of IDT-BT at 1.29 eV and 0.65 eV were observed indicative of polaron formation (compare section 2.1.2 and chapter 7).

6.2 Electronic Structure and Electrical Properties of Doped Films

The changes in the electronic structure of IDT-BT thin films upon n-doping with $[RuCp^*Mes]_2$ were determined by combined UPS/IPES measurements, the spectra of which are displayed in Figure 6.6 a). The electronic band onsets display a low intensity compared to the rest of the valence and conduction features, which is typical for polymers and can be also observed e.g. for P3HT (compare section 5.3 and ref. [294]). For this reason, an enlarged view of the region around the Fermi level is shown in Figure 6.6 b) for the spectrum of pure IDT-BT. From the spectrum, the ionization energy is determined to be 5.4 eV, which is consistent with previously reported values.[247,248] The determination of the electron affinity is a bit more difficult due to the large broadening of the IPES setup of 1.3 eV. Due to this large broadening the onset, which is extracted by linear extrapolation of the CB slope [red lines in Figure 6.6 b)], has to be corrected for the broadening. A detailed

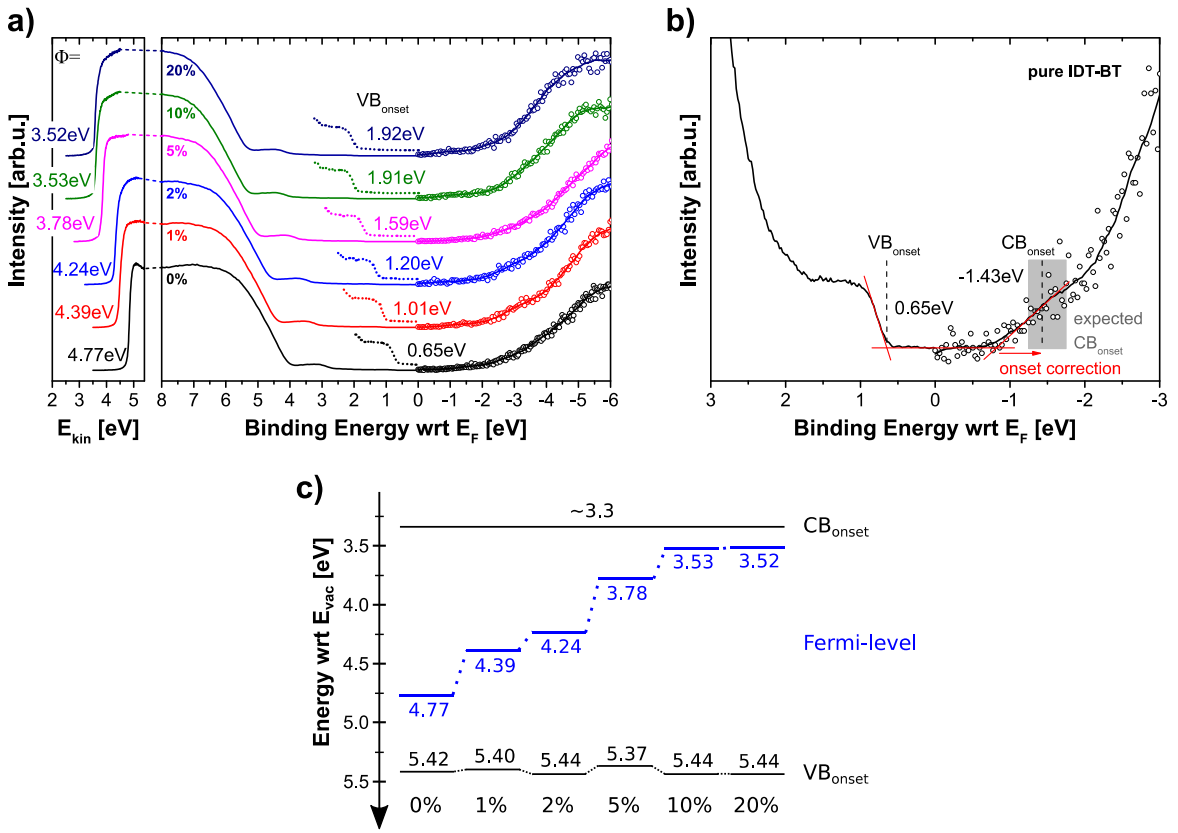

Figure 6.6 a) Combined UPS/IPES spectra of $[RuCp^*Mes]_2$ doped IDT-BT films with increasing dopant concentration. The dotted lines show the enlarged VB onsets. The IPES data (circles) were smoothed using a 32 point Savitzky-Golay filter (lines). **b)** Enlarged view of the region around the Fermi level of a pure IDT-BT film from which the VB onset was determined to be 0.65 eV and the CB onset to be -1.43 eV. The determined CB onset had to be corrected for the broadening of the IPES setup and the corrected value lies well within the range (grey area), where the CB onset was expected (see text). **c)** Energy level diagram deduced from the UPS/IPES spectra. With increasing dopant concentration the Fermi level is shifted upwards until it is pinned 0.2 eV below the CB onset.

explanation of the onset correction procedure can be found in Appendix A.[75] The correction offset for IDT-BT was calculated to be 0.61 eV and with the linear extrapolated onset of -0.82 eV, the electron affinity can be estimated to be around 3.3 eV. However, since the electron beam of the IPES setup lead to some radiation damage of the sample, witnessed by a large broadening of the valence region measured by UPS after the IPES measurement, the feasibility of the determined EA value has to be checked. Reported values for the exciton binding energy[76] of other polymers like e.g. P3HT, PFO[77], and P(NDIOD-T2) lie in the range of 0.2-0.7 eV.[43,208,255,294–298] Using the determined optical gap of IDT-BT of 1.7 eV and the IE of 5.4 eV, the EA can be expected to lie in the range of 3.0-3.5 eV. The determined value lies well within this range and can thus be considered to be reliable.

With increasing dopant concentration, the spectra shift to increasingly higher binding energies accompanied by an according decrease in work function. The energy level diagram displayed in Figure 6.6 c) summarizes the determined VB onsets and work functions. The IPES spectra of the doped films, however, exhibit an even larger broadening than the spectrum shown in Figure 6.6 b), which made it impossible to reliably determine the CB onsets. Thus, the CB onset was considered to stay constant, since also the VB onset was found to be constant. The diagram shows that with increasing dopant concentration, the Fermi level shifts throughout the transport gap of the polymer until it gets pinned ca. 0.2 eV below the CB onset at a dopant concentration of around 10%. This behavior is very indicative of successful n-doping.

In order to measure p-type and n-type conductivity separately from each other, different electrode materials were used for the interdigitated substrates on which IV measurements were performed. For the n-type measurements, thermally evaporated aluminum contacts were chosen and for the p-type measurements, thermally evaporated gold contacts.[78] Aluminum with a work function of around 4.0 eV was thought to mainly inject electrons, since the electron injection barrier is much smaller than the hole injection barrier in a scenario of vacuum level alignment as shown in Figure 6.7 a), while the gold contact with a work function of around 4.9 eV should mainly inject holes.[79]

[75] For molecular systems, the correction procedure depends on determining the FWHM of the HOMO level assuming a Gaussian distribution of the level. In the case of the polymer IDT-BT, the VB was also assumed to have a Gaussian shape and thus a Gaussian function was fitted to the valence band maximum at around 1.0 eV. The fit determined this Gaussian function to have a FWHM of 0.84 eV.

[76] Or values determined from separately reported electron affinities (IPES) and optical gaps.

[77] Poly(9,9-dioctylfluorenyl-2,7-diyl).

[78] Thermal evaporation leads to polycrystalline contacts.

[79] Polycrystalline aluminum exhibits a work function of 4.3 eV,[379,380] while polycrystalline gold has a work function of 5.1 eV (both under UHV conditions).[381] However, here, it has to be taken into account that the electrodes were exposed to an inert atmosphere at atmospheric pressure, which leads to surface contamination of the electrodes and partial oxidation of the aluminum. The work function of aluminum with a native oxide layer is around 3.7 eV,[208] whereas the one of dirty gold is around 4.8 eV (own measurement). Thus, the work function of aluminum was assumed to be around 4.0 eV and the one of gold to be around 4.9 eV.

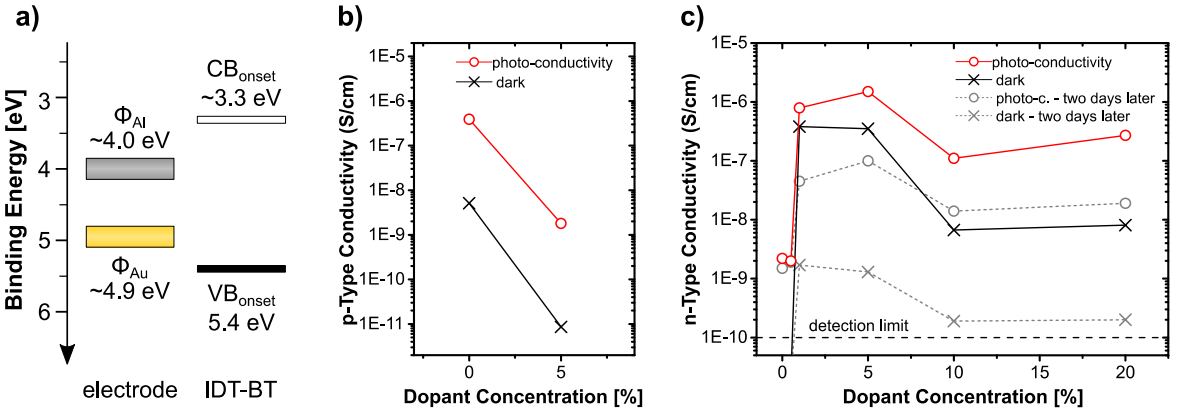

Figure 6.7 a) Work functions of the used electrodes as well as valence and conduction band onsets of IDT-BT, shown for vacuum level alignment. **b)** p-type conductivity and **c)** n-type conductivity of pristine and $[RuCp^*Mes]_2$ doped IDT-BT. Upon doping, the p-type conductivity decreases, while the n-type conductivity increases, both of which pointing towards a significant increase in mobile n-type charge carriers. However, the n-type conductivity was found to be not stable over time and decrease again about two orders of magnitude within two days (grey dashed lines).

Figure 6.7 b) shows the p-type conductivity and photo-conductivity (under red-light illumination) of pristine and 5% $[RuCp^*Mes]_2$ doped IDT-BT. As can be seen, both dark and photo-conductivity are decreased by around three orders of magnitude, while the decrease in dark conductivity is higher than the decrease in photo-conductivity. The change in n-type conductivity for a range of dopant concentrations is shown in Figure 6.7 c). The conductivity of the pristine film was below the detection limit of the used system, which lies in this case at around 10^{-10} S/cm, but a photo-conductivity of around 2×10^{-9} S/cm was observed.[80] Upon doping, the dark and also photo-conductivities increase by several orders of magnitude. The maximal conductivity was achieved with a dopant concentration of a few percent (1% and 5%). At higher dopant concentrations the conductivity decreases again, which is generally related to a decrease of mobility, since the dopants are disturbing the structure of the semi-crystalline IDT-BT film. Both, the decrease in p-type conductivity and the increase in n-type conductivity indicate a significant increase in mobile negative charge carriers upon doping. However, in both cases the changes in conductivity could partially also be related to a change in contact resistance to the electrodes. Since the films were deposited by solution processing of mixed solution, not yet reacted dimers from the solution could interact with the electrode surfaces, effectively decreasing the work function of both electrode materials (see section 5.4 for a discussion about work function

[80] For the p-type conductivity measurements, interdigitated substrates with gold electrodes with a 5 µm spacing were used, since IDT-BT films on substrates with 50 µm did not show any dark conductivity for yet unknown reasons. Unfortunately, 5 µm spaced substrates with aluminum electrodes were not available, thus substrates with 50 µm spacing were used, where the detection limit lies higher than for the 5 µm spaced substrates.

modification of electrodes with the dimers). In the case of the gold electrodes, this would increase the hole injection barrier, while in the case of aluminum, it would decrease the electron injection barrier, thus, effectively increasing and decreasing the contact resistance, leading to lower p-type and higher n-type conductivity, respectively.

The n-type conductivity was, however, found to not be stable over time. The conductivity of the 5% doped film already decreases by one order of magnitude from 3×10^{-7} S/cm to 2×10^{-8} S/cm within four hours. After two days stored under inert atmosphere, the conductivity of all doped samples decreases by around two orders of magnitude [grey dashed lines in Figure 6.7 c)]. This decrease in n-type conductivity over time is consistent with the intensity decrease of the polaron features in the optical spectra. However, this is still somewhat surprising, since we recently were able to show that the doping of a molecular organic semiconductor with an electron affinity of around 2 eV by the same organometallic dimer can be activated by UV light irradiation and the increased conductivity was stable for over a year.[A4] However, in this case the thin films were fabricated by co-evaporation of the small molecules in UHV and also measured as well as stored in UHV. Here, on the other hand, thin films were prepared from solutions in inert atmosphere. Although, (commercially available) dry solvents were used, which were thoroughly degassed, there is most likely still water present in the solvent, the concentration of which was estimated to be around 0.5 mM (see discussion in subsection 5.1.4). Here, the concentrations of around 5 mM are just one order of magnitude above the estimated water concentration.[81] In addition, residual water present in the polymer powder[82] or adsorbed at the used vials and substrates[83] can get dissolved in the prepared solutions. Such residual water molecules were recently shown to fill voids present in the microstructure of amorphous and semi-crystalline polymer films and were even found to be detrimental to device performance in p-type OFETs.[299,300]

To explain the negative effects of residual water and oxygen, just the redox potentials of simple water and oxygen reduction can be used, although in general, there are several other reactions possible, involving an interplay of water and oxygen. The potential of water reduction is estimated to lie at around -1.1 V vs Fc/Fc^+ and the one of oxygen at around -1.2 to -1.4 V vs Fc/Fc^+.[203,301] Unfortunately, there was no cyclic voltammetry data available for IDT-BT, but from the electron affinity of 3.3 eV, the reduction potential of IDT-BT can be estimated to lie around -1.5 V vs Fc/Fc^+ (using the conversion shown in subsection 3.3). The redox-potentials illustrate that the oxidation of negative IDT-BT polarons by reduction of water or oxygen is energetically favorable. Let us compare these consideration to other

[81] Here, mol-concentrations are related to the molecular weight of the monomer unit of the polymer.
[82] The polymer was weighed in air and then transferred to the glovebox.
[83] The vials and substrates (except IV substrates) were heated to 70° C before transfer to the glovebox, which, however, will not get rid of all water molecules adsorbed on the vials walls.

polymers like P(NDIOD-T2) or P(BTP-DPP), where successful n-doping by organometallic dimers was reported.[206,208,293] The reduction potential of P(NDIOD-T2) was reported to lie at -1.0 V vs Fc/Fc^+ and thus, n-doping of P(NDIOD-T2) should be mostly insensitive to influences by oxygen and water.[43] For P(BTP-DPP), there are also no information about its redox-potentials available, but its ionization energy was reported to be 4.9 eV and its optical gap to be 1.2 eV.[293] Based on these values, the electron affinity and its reduction-potential can be assumed to be similar to IDT-BT and n-doped P(BTP-DPP) films should thus also be highly sensitive to oxygen and water. In the presented study, there were no information made about the stability of doping. However, in this publication, the thin films were prepared by sequential processing, where the dopant was cast on top of the already dried polymer film and films were additionally annealed, which might lead to a more stable doping than the here used method of casting mixed solutions.[84] All in all, the instability of n-doping of IDT-BT (slow decay over several hours) is most likely related to the trace amounts of water and oxygen still being present even under optimized conditions.

6.3 Application in Organic Field Effect Transistors

To assess the ability of n-doping to turn the p-type polymer to n-type, OFETs comprised of pristine and doped IDT-BT films were fabricated in collaboration with Dr. Simon Dalgleish (Institut für Physik, Humboldt-Universität zu Berlin). The characterization measurements and analysis of the data were performed by Simon Dalgleish.

At first bottom-gate bottom-contact OFETs were fabricated on Si^{++}/SiO_2 substrates with gold source/drain electrodes. The substrates were passivated using a dense silane SAM formed from dodecyltrichlorosilane (it should be noted at this point, that for yet unknown reasons, the wetting of the chlorobenzene solution on the silane SAM treated SiO_2 was poor). The output and transfer characteristics of pristine and 5% $[RuCp^*Mes]_2$ doped IDT-BT are shown in Figure 6.8 and the extracted mobilities, threshold voltage and ON/OFF ratios summarized in Table 6.1. For the pristine film, the output characteristics for gate voltages V_{GS} up to 3 V show nearly ideal behavior and the devices easily reach saturation in the used source-drain voltages V_{DS} ranges [inset in Figure 6.8 a)]. However, for higher V_{GS} up to 10 V, the output curves show a sigmoidal shape, which is indicative of non-negligible contact resistance. The output characteristics of the 5% doped film [Figure 6.8 d)] show much lower source-drain currents I_{DS} than the pristine films. Moreover, the output curves

[84] Unfortunately, using the sequential deposition method was not possible with IDT-BT, since the dopant has to be dissolved in a solvent which is orthogonal to the polymer. However, the dimers can only be dissolved in a limited number of solvents (chlorobenzene, di-chlorobenze, tetrahydrofuran, and toluene), in all of which also IDT-BT shows a high solubility.[249]

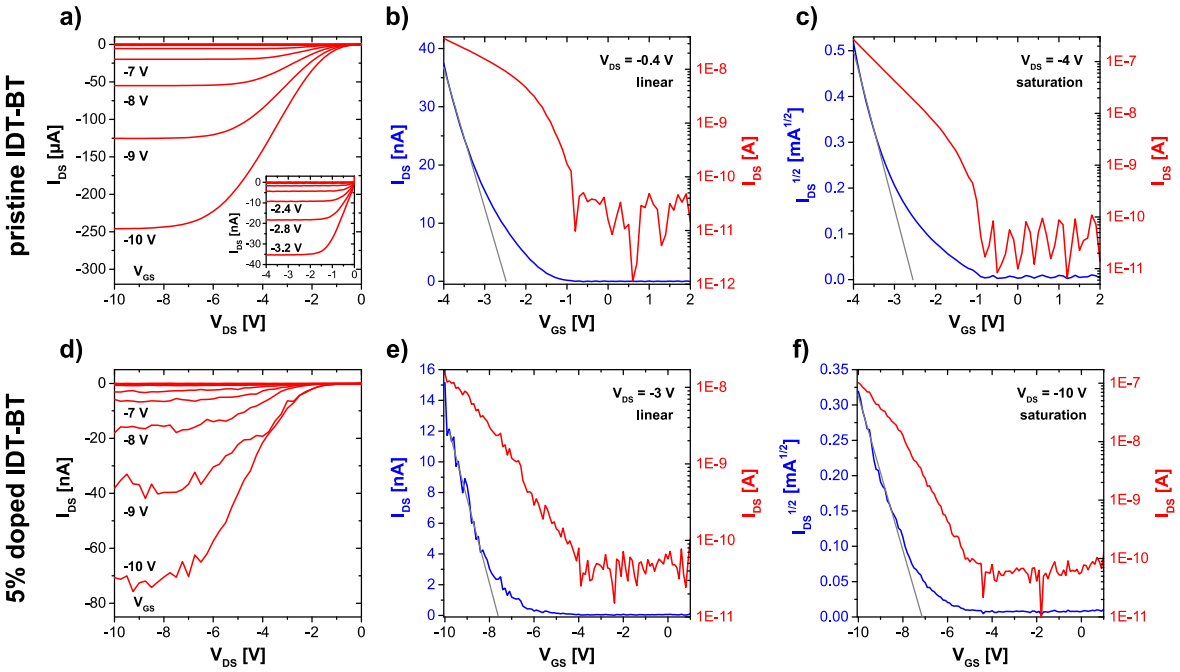

Figure 6.8 **a), d)** Output and **b), c), e), f)** transfer characteristics of OFETs employing pristine and 5% $[RuCp^*Mes]_2$ doped IDT-BT layers, respectively. The sigmoidal shape of the output characteristics points towards non-negligible contact resistance, which is increased upon doping. For the doped film, however, no n-type transport could be observed. Data kindly provided by Dr. Simon Dalgleish.

Table 6.1 Device characteristics of OFETs employing pristine and 5% $[RuCp^*Mes]_2$ doped IDT-BT. Using the reliability factor, the effective mobility μ_{eff} can be calculated from measured mobility μ_{meas}, which accounts for non-ideal behavior of the transfer characteristics. Upon doping the mobility is decreased and the threshold voltage V_{th} is largely shifted to more negative values. In addition, the ratio between on and off current is decreased by one order of magnitude upon doping. Data kindly provided by Dr. Simon Dalgleish.

		μ_{meas} [cm^2/Vs]	μ_{eff} [cm^2/Vs]	V_{th} [V]	on/off
pristine	linear	8.2×10^{-5}	3.6×10^{-5}	-2.4	$>10^3$
	saturation	3.2×10^{-4}	4.7×10^{-5}	-2.5	$>10^4$
5% doped	linear	4.1×10^{-6}	7.5×10^{-7}	-7.6	$>10^2$
	saturation	8.2×10^{-5}	3.6×10^{-5}	-7.0	$>10^3$

are very noisy compared to Figure 6.8 a), where the currents are in the same order of magnitude, and also have a more extreme sigmoidal shape.

The transfer characteristics for the pristine and 5% doped film in both linear and saturation regime are shown in Figure 6.8 b) and c) as well as Figure 6.8 e) and f), respectively. From Figure 6.8 b), the (linear) mobility μ_{meas} of pristine IDT-BT was determined to be 8.2×10^{-5} cm^2/Vs. Accounting for non-ideality, the reliability factor[85] was calculated to be

[85] The reliability factor is basically a measure for the deviation of the transfer characteristics from ideal behavior. It is defined as the ratio between the maximal experimentally achieved channel conductivity and the maximal conductivity of an ideal FET of same mobility. For further details see ref. [302].

around 44% from which an effective mobility μ_{eff} of 3.6×10^{-5} cm^2/Vs can be defined.[302] The mobility was also found to be field dependent, as it increased up to $\mu_{eff} = 9.1\times10^{-5}$ cm^2/Vs for larger V_{GS} ranges up to -6V. The determined p-type mobility of pristine IDT-BT is much lower than the previously reported values of 0.8-3.6 cm^2/Vs.[247,249,265,289–292] This might be related to the bad wetting of the chlorobenzene solution on the silane SAM modified surface leading to not ideal film structures, the use of bottom-gate bottom-contact devices (for the reported mobilities, optimized top-gate bottom-contact devices were used) and the fact, that the device structure in general was not optimized. Upon doping the effective mobility of the linear region decreases from 3.6×10^{-5} cm^2/Vs to 7.5×10^{-7} cm^2/Vs and the effective mobility of the saturated region slightly decreases from 4.7×10^{-5} cm^2/Vs to 3.6×10^{-5} cm^2/Vs. The decrease in mobility can generally be associated with a disturbance of the semi-crystalline microstructure of IDT-BT caused by the dopants. In addition, the decrease of the linear mobility is much larger than the decrease in the saturation mobility, which points towards an increased contact resistance, possibly induced by interaction of non-reacted dimers with the source/drain contacts. The shift in threshold voltage V_{th} is, however, more dramatic. Here, V_{th} shifts from -2.4 V to -7.6 V in the linear regime (-2.5 V to -7.0 V in the saturation regime), which correlates with the observed shift in Fermi level upon doping (see Figure 6.6). Also, the on/off ratio decreases by roughly one order of magnitude, which is mainly due to a decrease in the on-current rather than an increase in off-current. This shows that upon n-doping the p-type behavior is reduced. However, no n-type transport could be observed, when scanning V_{GS} in the positive region.

In order to facilitate n-type transport, the device architecture was changed. Aluminum was used as drain/source contact material and the SiO_2 dielectric was not passivated with a silane SAM in order to increase wetting of the chlorobenzene solution. Here, the idea was that non-reacted dimers in the mixed solution would suffice to passivate the SiO_2 surface. However, these devices did not show any n-type transport and a bad p-type behavior due to the large hole injection barrier to the aluminum contacts. The observation of no detectable n-type transport is most likely related to surface hydroxyl-groups, which, contrary to our expectations, were not successfully (or just partially) passivated by the dimers. Furthermore, the non-observation of n-type transport could also be related to the instability of n-doping over time. At this point in the experiments, it was discovered that the n-type conductivity already decreases about one order of magnitude during the course of a few hours. For this reason, the experiments on OFETs were not continued, as the effort of optimizing the device architecture[86] was deemed to be too much for the possible gain in

[86] Silane SAMs as passivation layer could not be used due to bad wetting of the chlorobenzene solution and other at this time available passivation layers were not compatible with the following spin-coating of a chlorobenzene solution. Changing the architecture to top-gate was also not feasible as there was no possibility to fabricate top gate electrodes under inert atmosphere.

knowledge. Nonetheless, the presented OFET results are consistent with the data presented in the previous sections, e.g. the shift of the Fermi level upon doping.

6.4 SUMMARY

In summary, it was shown that the p-type polymer IDT-BT can successfully be n-doped by using organometallic dimers. This was observed by the formation of negative polarons in optical absorption spectroscopy. In addition, the Fermi level is shifted away from the valance band upon doping and at a dopant concentration of around 10% gets pinned near the conduction band onset. Furthermore, doping leads to an increase in n-type conductivity by several orders of magnitude, while at the same time the p-type conductivity is decreased. The approach to achieve n-type transport in OFETs employing doped IDT-BT layers was, however, not successful. Moreover, it was discovered that the n-type doping in solution as well as in thin films cast from solution is not stable over time. This is evidenced by the n-type conductivity decreasing again over two orders of magnitude in the course of a few days. This instability of n-doping was related to the presence of residual water and oxygen, which leads to a degradation of the formed negative polarons.

7 BIPOLARON FORMATION IN P3HT

The type of charge carriers formed upon charge injection into or doping of conjugated polymers with a non-degenerate ground state like P3HT has been a widely discussed topic. Some studies support the formation of mainly polarons, while others suggest the formation of mainly bipolarons.[46–51,92,303–305] Today, it is commonly accepted that molecular doping of polymers, in general, leads to the formation of polarons as charge carriers.[21,22,52,53] Bipolaron formation in P3HT has been previously reported to occur upon electrochemical doping and doping with $FeCl_3$.[90,306–308] However, no direct evidence has been reported so far for bipolaron formation to also occur during the molecular doping of P3HT.[87]

Here, the possibility of bipolaron formation during p-type doping of P3HT with the organic salt $Mes_2B^+[BCF4]^-$ is investigated. Their chemical structures are displayed in Figure 7.1. The recently developed dopant consists of the two-coordinate boron cation Mes_2B^+ and the chemically stable and inert counteranion $[BCF4]^-$.[253,261] The counteranion $[BCF4]^-$ is a weakly coordinating anion, meaning strong interactions with other molecules/ions are suppressed and therefore it does not induces structural changes in the other ions.[309] This counteranion was recently used in combination with the cation trityl to successfully p-dope different polymers and enhance the p-channel performance of OFETs comprised of such doped polymer layers.[310] Due to the exceptionally electron-deficient nature of Mes_2B^+, it can serve as a strong one-electron oxidant and was previously used to p-doped carbon nanotubes and the surface of transition metal dichalcogenide monolayers.[259,260] $Mes_2B^+[BCF4]^-$ is thus expected to be a very strong p-dopant, possibly exceeding the doping strength of other commonly used molecular p-dopants like F_4TCNQ or F_6TCNNQ.

In this chapter, first, the doping process of the organic salt will be explored. Second, the transition from polaron to bipolaron formation will be studied by optical absorption and electron paramagnetic resonance (EPR) spectroscopy. Subsequently, the changes in conductivity upon doping and the effect of thermal annealing on the conductivity is shown. In the following, the influence of doping on the electronic structure and chemical shifts in the core-levels of P3HT will be investigated by UPS and XPS measurements using monochromated light sources (mono-UPS / mono-XPS). Finally, the effect of air-exposure on doped films will be presented.

Most of the presented results will be published in the joint manuscript [A8], where the doping of P3HT with $Mes_2B^+[BCF4]^-$ is compared to the doping with the strong Lewis acid

[87] $FeCl_3$ is normally not classified as a molecular dopant, the class of which is usually comprised of organic molecules, but rather as a small inorganic Lewis acid dopant (see also subsection 2.2.2).

BCF3,[88] since $[BCF4]^-$ contains just one fluorinated phenyl-ring more than BCF3. The doping of P3HT with BCF3 is the topic of the Master's thesis of Dominique Lungwitz (Institut für Physik, Humboldt-Universität zu Berlin) and will thus not be present here.

7.1 Doping Process

The doping process of the organic ionic salts is different than the doping process of other molecular dopants like e.g. F_4TCNQ, where an electron is transferred from the host to the p-dopant and the ionized dopant then acts as the counteranion. In the case of the salt $Mes_2B^+[BCF4]^-$, the electron is transferred from P3HT to the boron cation Mes_2B^+ forming the neutral radical $Mes_2B^\bullet$. This process is illustrated in Figure 7.1. Here, $[BCF4]^-$ acts as the counteranion to the positive polaron formed in P3HT. The formed radical $Mes_2B^\bullet$ is most likely reacting with another $Mes_2B^\bullet$ radical via hydrogen abstraction to form the dimesitylborane dimer $[Mes_2BH]_2$, which is the known stable form of dimesitylborane.[311–313] This reaction was shown to occur when decamethylferrocene is oxidized by $Mes_2B^+[BCF4]^-$ yielding the corresponding ferrocenium salt with $[BCF4]^-$ as well as $[Mes_2BH]_2$.[259] It is anticipated that the formation of $[Mes_2BH]_2$ is occurring similarly during the doping process of P3HT.

Since both Mes_2B^+ and $[BCF4]^-$ contain boron in different oxidation states, XPS detail scans of the B1s region can be used to differentiate between cation and counteranion. Figure 7.2 shows the B1s detail scans of a thick (10 nm) and thin (2 nm) multilayer of the pure ionic salt as well as doped P3HT thin films at different dopant concentrations.[89] The spectrum of the 10 nm thick multilayer (black line) shows two clearly distinguishable features at 193.6 eV and 188.5 eV (the small features in between the two high intensity features are probably belonging to impurity or side-product species containing neutral boron). The feature at higher binding energy can be ascribed to the positively charged boron and thus Mes_2B^+. A positive charge on an atom will yield a positive potential, which is experienced by the electron leaving the 1s core level and will therefore reduce the kinetic energy of the leaving electron. Similarly, a negative charged atom will show a higher kinetic energy and thus lower binding energy of the 1s core level. The reported binding energy of neutral boron is 189.4 eV, which lies between the just reported binding energies of negatively and positively charged boron.[228] The spectrum of the 2 nm thin multilayer also shows two main features, which are separated by 4 eV from each other. In contrast to the thick multilayer, where both features have nearly the same intensity, here, the feature of B^+ shows only ca. half

[88] Tris(pentafluorophenyl)borane. This compound is commonly abbreviated as BCF.[181] Here, however, it will be abbreviated as BCF3 to distinguish it from the counteranion $[BCF4]^-$.

[89] Here, the definition of the dopant concentration c is based on the molar number of counteranions N_{D^-} with respect to the number of polymer 3HT units N_P, in the form $c = N_{D^-}/(N_{D^-} + N_P)$, similar to section 5.2.

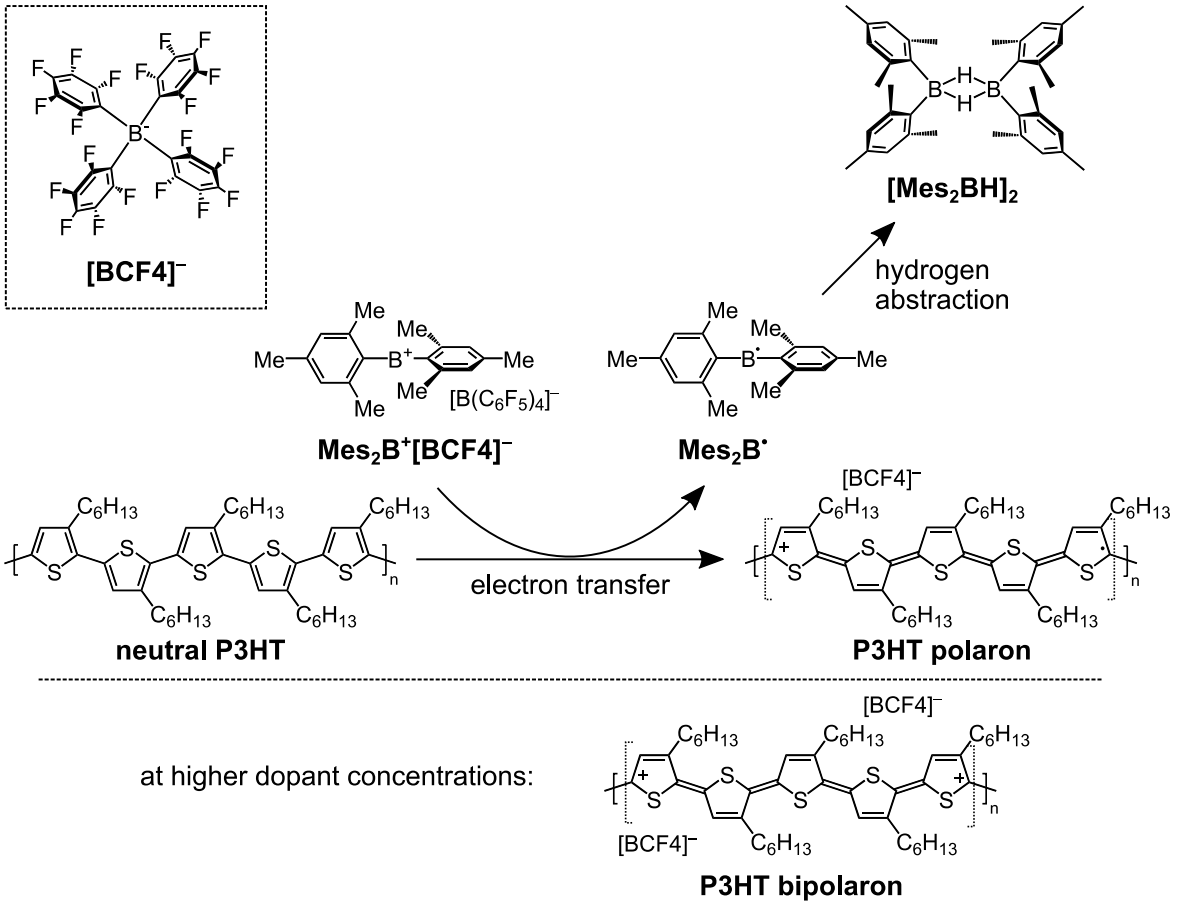

Figure 7.1 Proposed mechanism of the doping of P3HT with the organic salt $Mes_2B^+[BCF4]^-$. Upon doping an electron is transferred from a segment of P3HT to Mes_2B^+ and the neutral radical $Mes_2B^\bullet$ reacts with another radical to the dimer $[Mes_2BH]_2$ via hydrogen abstraction. The formed polaron in P3HT is stabilized by the counteranion $[BCF4]^-$. At higher dopant concentrations, the formation of bipolarons is possible. The mechanism is based on the oxidation mechanism of decamethylferrocene by $Mes_2B^+[BCF4]^-$.[259] The figure will be published in ref. [A8].

the intensity of the one of B^-. This can be related to Mes_2B^+ also undergoing a reaction with the ITO substrate used in the PES measurements similar to the described doping process.

Here, electrons are transferred from the ITO to the salt (most likely also associated with the formation of $[Mes_2BH]_2$), which leads to the formation of an interface dipole at the interface of ITO. This was found to lead to an increase of the effective work function from 4.6 eV for bare ITO to around 5.8 eV for both multilayers. For the thin multilayer, the B1s spectrum, however, shows no feature at equal intensity which could be attributed to neutral boron from $[Mes_2BH]_2$. This observation is even more striking, in the case of the doped P3HT films also shown in Figure 7.2. Here, only the feature of B^- is observed, the intensity of which is increasing with increasing dopant concentrations (the shift in the core level can be associated with the shift in Fermi level, see discussion in subsection 7.4). For higher dopant concentrations of above 20%, a small intensity feature of B^+ can be observed, which is most likely due to a small portion of non-reacted ionic salt.

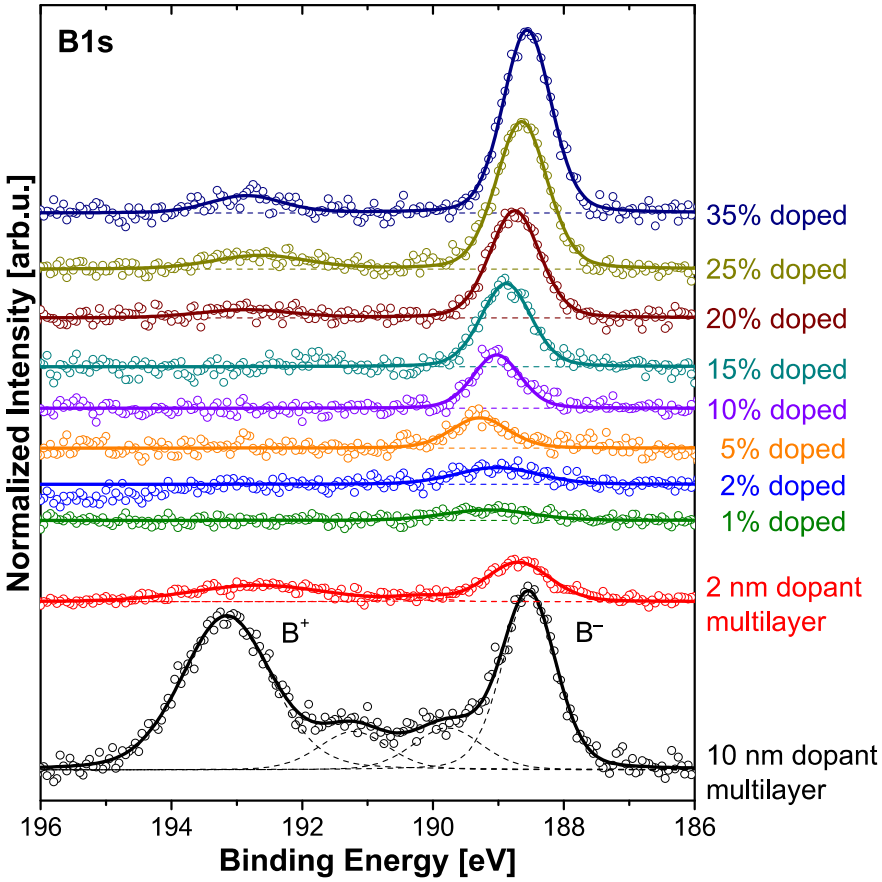

Figure 7.2 Mono-XPS detail scans of the B1s region of a 10 nm thick (black line) and a 2 nm thin (red line) multilayer of $Mes_2B^+[BCF4]^-$ as well as doped P3HT films with increasing dopant concentration (others). The thick multilayer shows two distinct features at 193.6 eV and 188.5 eV, which are assigned to positively (Mes_2B^+) and negatively charge boron ($[BCF4]^-$), respectively. In the thinner multilayer, the intensity of the B^+ feature is decreased compared to the B^-, since the dopant is also interacting with the ITO substrate. The doped P3HT layers only show the feature of B^-, except in the cases of higher dopant concentrations, where the re-appearance of the B^+ feature is related to non-reacted dopants. This indicates that for doped P3HT only the counteranions $[BCF4]^-$ are still present in the film. The B1s spectra of the doped P3HT films are normalized with respect to the area of S2p resembling the amount of P3HT. The spectra of the multilayers are normalized according to their thickness. The figure will be published in ref. [A8].

The absence of any features of neutral (or positively charged) boron features (except in the high dopant concentration cases) indicates that the formed $[Mes_2BH]_2$ is not present in the doped P3HT films. It is assumed that the dimer is either removed during the spin-coating process or when exposing the films to UHV before the XPS measurements. In the second case, it could be possible that $[Mes_2BH]_2$ sublimes under UHV conditions and thus desorbs from the doped films as soon as they are transferred to the vacuum systems and brought into UHV. Since there is no information available about sublimation points for these compounds, the following discussion is based on melting points in comparison to other molecules. The melting point of $[Mes_2BH]_2$ is around 165 °C,[311] which is similar to that of BCF3 of 130 °C and $CoCp_2$ of 170 °C,[314,315] both of which are known to easily sublime in

UHV at room temperature.[90,188] On the other hand, the small molecule F_4TCNQ, for example, has a melting point of 290-300 °C,[316,317] is known to be non-volatile under UHV conditions at room temperature and can thus be nicely thermally evaporated in UHV.[33] On another note, molecules with high melting points (> 300 °C) are generally considered suitable for molecular beam deposition as molecules with low melting points (< 130 °C) are known to already sublime at room temperature in UHV.[318] Thus, it is likely that $[Mes_2BH]_2$ desorbs from the doped films under UHV conditions, although it cannot be excluded that $[Mes_2BH]_2$ is already removed during the spin-coating process. To further test this hypothesis, optical absorption spectra of doped P3HT thin films were recorded before and after an overnight exposure to UHV (see section 7.5). However, there was no significant change observed in optical spectra up to 4.0 eV. But since the optical absorption of $[Mes_2BH]_2$ is unknown and lies most likely in the high UV region, further experiments are needed to clarify at which stage $[Mes_2BH]_2$ is removed and, if it is still present in thin films under atmospheric pressure, what its influence on the electrical properties would be.

7.2 Polaron to Bipolaron Transition

The optical absorption spectra of increasingly $Mes_2B^+[BCF4]^-$ doped P3HT are summarized in Figure 7.3. The absorption spectrum of neutral P3HT shows the typical optical signature of regioregular P3HT with well resolved features at around 2.1 eV, 2.2 eV, and 2.4 eV.[303,319,320] The absorption spectrum of regioregular P3HT films consists of two parts, where the lower energy part is ascribed to interchain states of aggregates in the crystalline regions of the film and the higher energy part to intrachain states of twisted chains in more disordered areas.[319] From the absorption spectrum, the optical gap of P3HT is determined to be 1.9 eV. Upon doping at low concentrations (1% and 5%), the emergence of new features at 0.4 eV and 1.3 eV in the optical gap of P3HT is observed, which are usually related to the P1 and P2 transitions of positive P3HT polarons, reported to lie in the range of 0.4-0.5 eV and 1.3-1.5 eV, respectively.[38,49,50,52,150,175] For higher dopant concentrations starting at 10%, these features are shifting to higher photon energies, i.e. from 0.4 eV to 0.5 eV and from 1.3 eV to 1.5 eV (also compare Figure 7.10 in subsection 7.5). Starting at around 15% dopant concentration, two additional features at 1.8 eV and 2.1 eV emerge, which are further increasing in intensity with increasing dopant concentration, indicating the formation of other species than polarons.[91] The emergence of such features in doped P3HT thin films has (to the best of my knowledge) never been reported so far.

[90] The described behavior of BCF3 stems from own experience.

[91] It should be noted at this point, that the newly emerging transition at 2.12 eV is not the same as the transition of interchain aggregates of neutral P3HT, which lies at 2.06 eV.

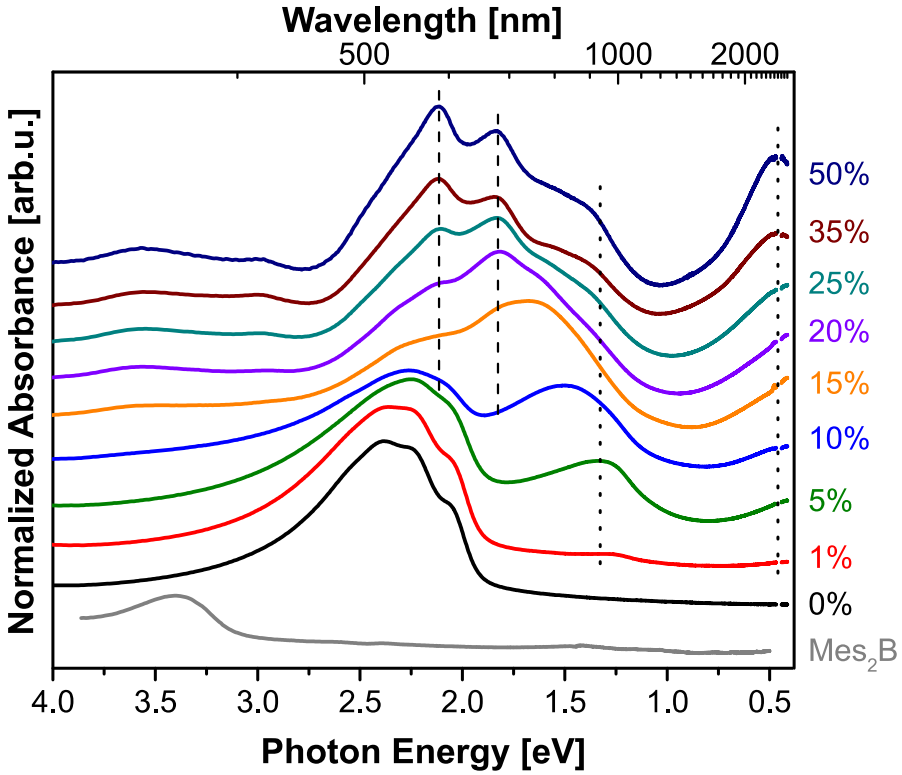

Figure 7.3 Optical absorption spectra of increasingly $Mes_2B^+[BCF4]^-$ doped P3HT. At low dopant concentrations of a few percent, two new absorption features emerge at 0.4 eV and 1.3 eV (marked by dotted lines), which are attributed to the formation of P3HT polarons. At higher dopant concentration, these features shift to 0.5 eV and 1.5 eV, respectively. At 15% dopant concentration, two additional absorption features emerge at 1.8 eV and 2.1 eV (marked by dashed lines), which are increasing with increasing dopant concentration. In accordance with EPR measurements, these features can be assigned to bipolarons. The figure will be published in ref. [A8].

In order to further examine the origin of these absorption features, EPR measurements were conducted on doped P3HT films. The EPR measurements were performed by Dr. Claudia Tait (Berlin Joint EPR Lab, Fachbereich Physik, Freie Universität Berlin).[92] In general, EPR spectroscopy can be used to determine the number of charge carriers with unpaired spins. Therefore, it can be used to distinguish between polarons with an unpaired spin and spin-less bipolarons. Figure 7.4 shows the determined number of unpaired spins in dependence of the dopant concentration of $Mes_2B^+[BCF4]^-$ doped P3HT films in comparison to F_4TCNQ and BCF3doped P3HT thin films. For all three p-dopants, the data reveals a strict linear increase in polaron concentration with increasing dopant concentration in the regime of 0.01% to 10%, which is indicated by the drawn lines with slope 1 in the logarithmic plot in Figure 7.4. Interestingly, these lines reveal the formation of polarons to proceed with a different efficiency for the three dopants. Here, F_4TCNQ seems to have the polaron formation efficiency in the order of 60%, while it is only around

[92] Further details on the experimental and evaluation procedures as well as a discussion on the change in the EPR signal shape can be found in our joint publication ref. [A8].

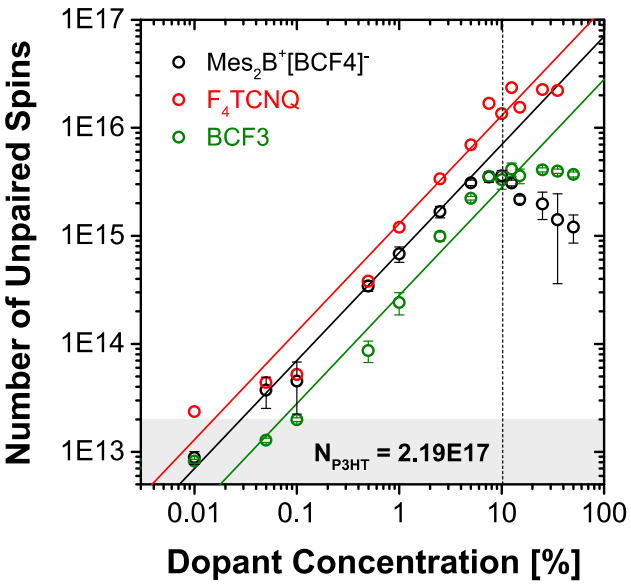

Figure 7.4 Number of unpaired spins N in dependence of the dopant concentration c of $Mes_2B^+[BCF4]^-$, F_4TCNQ, and BCF3 doped P3HT films as determined by quantitative EPR measurements. The lines with slope 1 indicate a linear correlation between N and c in the regime of 0.01% to 10%. The grey area shows the background number of spins measured on pristine P3HT. At c ≈ 10%, N saturates for F_4TCNQ and BCF3 doped P3HT, while it decreases for $Mes_2B^+[BCF4]^-$, indicating the formation of spin-less bipolarons. N-values were determined from three independently performed doping series (two in the case of F_4TCNQ) and the error bars shown are the standard deviations (not shown in the case of F_4TCNQ). The number of polymer units N_{P3HT} was kept constant at 2.19×10^{17} for all samples. Data kindly provided by Dr. Claudia Tait (Berlin Joint EPR Lab, Fachbereich Physik, Freie Universität Berlin). The figure will be published in ref. [A8].

30% for $Mes_2B^+[BCF4]^-$ and around 15% for BCF3. For F_4TCNQ, this finding is in accordance with the ionization efficiency in P3HT thin films determined form optical measurements of around 70% (for solutions an efficiency of 50-70% was found).[150] However, for BCF3, higher ionization efficiencies were estimated by optical measurements, which lie in the region of 50-70%, similar to F_4TCNQ.[181]

For higher dopant concentrations (>10%), however, the number of spins does not increase linearly with the dopant concentration anymore and the dopants F_4TCNQ and BCF3 show a different behavior than $Mes_2B^+[BCF4]^-$. Here, at around 10% dopant concentration, the number of spins goes into saturation for F_4TCNQ and BCF3, indicating that the formation of polarons stops at around 10% and further introduced dopants do not ionize P3HT units anymore. In contrast, for $Mes_2B^+[BCF4]^-$, the measured number of spins starts to decrease at around 10% and continues to decrease with further increasing dopant concentration, indicating that at around 10% a transition of the type of charge carriers occurs, most likely from polarons to spin-less bipolarons. As discussed in subsection 2.1.1, polarons in polymers extend over several monomer units and it is energetically unfavorable for two polarons to exist in close vicinity to each other. Consequently, there must be a maximum concentration of dopants at which the formation of additional polarons is energetically not feasible. Theoretical studies showed that doubly charged, moderately sized oligomers can support two polarons, but upon an oligomer length of less than seven units, the formation

of bipolarons is energetically more stable than two neighboring polarons.[321–323],[93] This would correspond to a limit of the dopant concentration of around 14% for the transition between polarons and bipolarons to occur. The presented EPR data suggests this transition to be reached at around 10% dopant concentration, which is in close agreement with the theoretical results. Accordingly, above 10% dopant concentration, bipolarons have to be formed in P3HT in order for P3HT to further transfer electrons to the dopants. Here, it seems that the dopants F_4TCNQ and BCF3 do not possess the required oxidation strength to facilitate the transition from polarons to bipolarons, while $Mes_2B^+[BCF4]^-$ does.

The EPR determined transition from polarons to bipolarons at around 10% dopant concentration is in accordance with the spectral changes in Figure 7.3, which also start to occur between 10% and 15% dopant concentration. The emerging features at 1.8 eV and 2.1 eV can thus be assigned to belong to P3HT bipolarons.[94] The here presented optical absorption features of P3HT bipolarons are, however, in contrast to the optical spectra associated with P3HT bipolarons, which have been previously reported in literature.[90,93,306–308] These differences shall thus be discussed in more detail at this point.

Oligomers are often considered to be a model system for polymers, as polymers consists of segments with an effective conjugation length and are thus basically comprised of oligomer units.[93,106,324,325] Following this thought, 6T (or other shorter oligothiophenes) could be used as model system for polythiophene. The absorption spectra of ionized 6T reveal two major absorption features in the optical gap of 6T at 0.8 eV and 1.6 eV for 6T cations, and only one absorption feature at 1.2 eV for 6T dications.[93] Thus, in general one could also assume a single optical transition to be present for P3HT bipolarons, which should be located between the two polaron transitions P1 and P2. However, recent studies revealed fundamental differences in the doping process of oligothiophenes and polythiophenes, demonstrating that oligomers cannot always serve as model systems for polymers.[24,52],[A2] In addition, the origin of the optical transitions in oligomers and polymers is different (see subsection 2.1.2). The optical transitions in positively ionized (small) molecules (thus also short oligomers) occur between the states of the split HOMO level (which is split into a singly occupied and a singly unoccupied level) and the LUMO as well as also the HOMO-1 level. In contrast, in polymers the transitions occur between the valence and conduction band of the neutral polymer and localized states created by polarons within the optical gap of the polymer.[97] While the comparison between the absorptive transitions seems to hold for polymer polarons and oligomer cations,[93,324]

[93] These calculations are experimentally supported by recent work on the reduction of oligofluorenes, where it was shown that side-by-side polarons can only exist on oligomers with a length of more than five repeat units.[382]

[94] However, the possible formation of other also spin-less charge carriers cannot be ruled out.

there has been no indication so far for it to also hold in the case of polymer bipolarons and dications (at least to the best of my knowledge).

Studies on electrodeposited and -doped[95] P3HT and, similarly, of P3HT doped by exposure to FeCl3 vapor, have also claimed the formation of bipolarons to occur at a certain doping level. Here, the optical spectra of such deposited and doped P3HT films show the emergence of a feature at around 800 nm (1.55 eV) and a broader feature in the NIR region maximizing at around 2500 nm (0.5 eV) for low dopant concentrations, which was associated with the formation of a polaronic state.[306–308,326] Simultaneously with the emergence of the new features, the neutral feature of P3HT at around 500 nm (2.5 eV) is decreased, similarly to the spectra in Figure 7.3. In contrast, the feature at 800 nm decreases again in intensity for higher dopant concentrations, while at the same time, the neutral absorption of P3HT is nearly completely bleached and an increase of a very broad absorption is observed in the NIR region extending from 800 nm to higher wavelengths, which was associated with the transition from polarons to bipolarons. No additional features are observed in the region down to 300 nm (4.1 eV). However, none of these studies show direct evidence for the formation of bipolarons. Moreover, older studies on highly doped polythiophene and poly(3-methylthiophene) showed that the frequency-dependent absorption at high dopant concentrations is more characteristic of the free-carrier spectrum of a metallic state by comparison to the spectra of heavily doped polyacetlyene.[46,327],96

In another recent study, P3HT films prepared via spin-coating were electrochemically oxidized and optical absorption measurements at different applied voltages were coupled with EPR measurements.[90] Here, it was shown that until a certain applied potential the number of unpaired spins detected by EPR increases, while at the same time new optical transitions are observed at 1.7 eV and 0.5 eV related to the formation of polarons. After exceeding this potential, the number of unpaired spins decreases again followed by a decrease in intensity of the transition at 1.7 eV, while the NIR transition at 0.5 eV increases and shifts to the mid-IR region and maximizes at 0.35 eV. Consequently, these absorption features were attributed to the formation of bipolarons. No additional features in the region from 2.0 eV to 3.5 eV were observed. These findings are in strong contrast to the results presented in this section and the differences have to most likely be sought in the

[95] During electrodeposition, P3HT is electrochemically polymerized from 3-hexythiophene units at an electrode by applying a series of potential steps. Doping is carried out by incorporation of counteranions into the film and its extent can be controlled by the last applied resting potential.

[96] Note: In publications from the 80s and 90s, the transitions at around 0.5-0.6 eV and 1.5 eV in doped polythiophene and derivatives were associated with the formation of bipolarons, as it was believed that these two features arise from transitions between the valence band and two localized empty energy levels in the gap of the polymer.[46] This assignment has, however, been revised in later years.[49] See also the discussion on the theory of optical transitions of polarons in subsection 2.1.2.

different doping mechanisms (electrochemical vs. molecular doping). However, no satisfactory explanation has been found so far.

Furthermore, it was demonstrated lately that by employing special processing conditions, charge transfer complexes (CPXs) can also be achieved in mixed P3HT:F_4TCNQ thin films, which was evidenced by partial charge transfer measured via FTIR.[154] Hitherto, CPX formation was only observed to occur for small molecules.[155,328,329],[A2] For the CT complex of P3HT:F_4TCNQ, absorption features were found at around 1.0 eV, 2.0 eV and 3.4 eV, and displayed a very large broadening of around 0.7-1.0 eV FWHM (estimated from the reported absorption spectrum in ref. [154]). In comparison, the absorption features displayed in Figure 7.3 and Figure 7.10 do not show broad transitions at these energies and the observed transitions at 1.8 eV and 2.1 eV are rather sharp compared to the polaron absorption features. However, the absorption features of CPX complexes are known to shift in energy depending on the dopant and interaction of the involved HOMO and LUMO levels,[97] thus the observation of no features at these energies cannot rule out CPX formation.[155],[A2] Nonetheless, since the orbitals of the involved frontier levels of host and dopant have to strongly overlap for CPX formation to occur,[155],[A2] and since $[BCF4]^-$ is a weakly coordinating anion,[309] CPX formation is very unlikely to occur between P3HT and $[BCF4]^-$.

To briefly summarize this subsection, the results presented so far for the doping of P3HT wiht $Mes_2B^+[BCF4]^-$ indicate a transition of polaron to bipolaron formation to occur at a dopant concentration of around 10%, although the optical absorption results are in contrast to previous reports of bipolaron formation.

7.3 Conductivity and Influence of Thermal Annealing

Conductivity measurements of pristine and $Mes_2B^+[BCF4]^-$ doped P3HT were conducted as in-plane measurements of thin films spun-coat on substrates with interdigitated ITO electrodes. Since the work function of ITO lies between 4.4-4.6 eV and the ionization energy of P3HT is 4.7 eV (see next subsection), the hole injection barrier can be considered to be minimal and contact resistance to be negligible. Figure 7.5 a) shows the increase in conductivity upon doping. As can be seen, the conductivity is highly increasing with increasing dopant concentration until around 15%, where it reaches a value of 0.5 S/cm, which is four orders of magnitude higher than the conductivity of pristine P3HT. Going to higher dopant concentration the conductivity quickly decreases and nearly falls back to the order of magnitude of pristine P3HT. This behavior is similar to what was observed for the

[97] For the series TCNQ to F_6TCNNQ this shift was found to be 0.4-0.5 eV.[155],[A2]

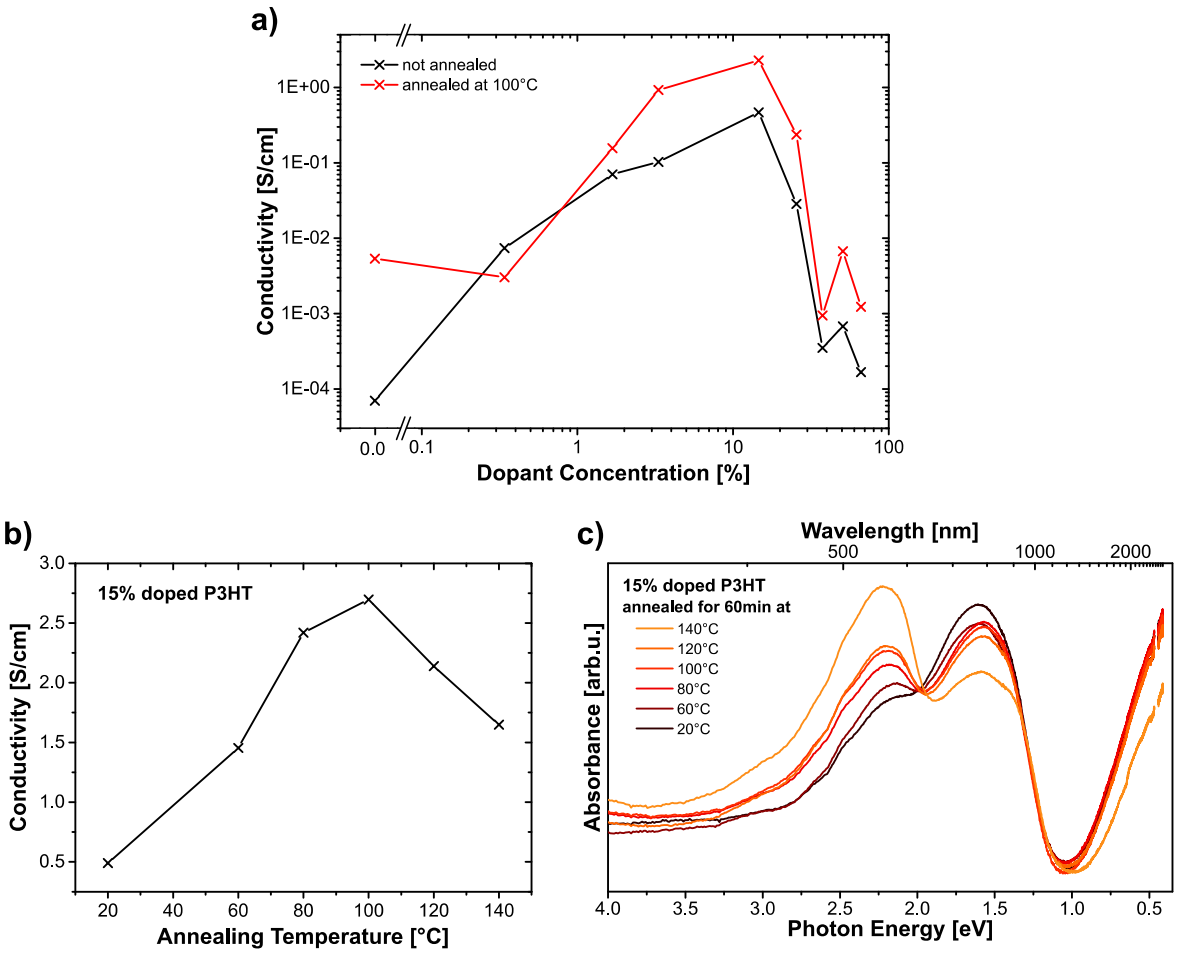

Figure 7.5 a) Conductivity of $Mes_2B^+[BCF4]^-$ doped P3HT thin films. The data shows a strong increase of the conductivity over four orders of magnitude until a dopant concentration of 15%, after which the conductivity is decreasing again. Thermal annealing of the thin films at 100 °C can further enhance the conductivity. **b)** Conductivity of a 15% $Mes_2B^+[BCF4]^-$ doped P3HT film in dependence of the temperature at which the film was annealed. Thermal annealing can increase the conductivity from 0.5 S/cm up to 2.8 S/cm until an annealing temperature of 100 °C, after which the conductivity decreases again. **c)** Optical absorption spectra of a 15% $Mes_2B^+[BCF4]^-$ doped P3HT film in dependence of the temperature at which the film was annealed. Already at 60 °C annealing temperature, the P2 feature at 1.5 eV starts to decrease, while the neutral feature at 2.2 eV increases again. Surprisingly, the P1 feature at 0.5 eV stays nearly constant in intensity and only at an annealing temperature of 140 °C, it gets strongly decreased. Data recorded by Naoki Tanaka (Chemical Resources Laboratory, Tokyo Institute of Technology, Japan). Fig. a) will be published in ref. [A8].

doping of P3HT with F_4TCNQ, where maximal conductivities of 1-3 S/cm could be achieved at dopant concentrations of around 10-25%.[24,152–154] The decrease of the conductivity at higher dopant concentrations is related to a change in the quality of the microstructure of the thin film as well as the formation of scattering centers and traps for the free charge carriers upon excessive incorporation of dopant molecules, all of which will decrease the mobility of P3HT and thus also the overall conductivity of the film.[24,151,328] The EPR data presented in Figure 7.4 provide additionally insights into the change in conductivity of F_4TCNQ doped thin films. EPR shows an increase in the number of unpaired spins until a dopant concentration of around 10%, after which the number of spins saturates. Thus, the

strong increase in conductivity until around 10% is related to the formation of additional free charge carriers, however at higher dopant concentration no more additional free charge carriers are created and the conductivity is decreasing because of the decrease in mobility upon introduction of more dopants.[98] For $Mes_2B^+[BCF4]^-$, the results of the previous subsection suggest a polaron to bipolaron transition to occur at this dopant concentration. Thus at this point it is unclear, if the decrease in conductivity can be purely related to a decrease of mobility, or is the formed bipolarons are less mobile than polarons, thus also leading to a decrease in conductivity. This discussion will be continued in subsection 7.5.

P3HT films are often thermally annealed in order to increase the crystallinity of the thin films and with it the charge carrier mobility.[330–333] To assess the influence of thermal annealing on the conductivity of the doped P3HT films, the films were annealed at 100 °C for 60 min. Figure 7.5 a) (red line) shows, that upon thermal annealing, the conductivity of all films (with the exception of the 0.3% doped sample) can be enhanced by two orders of magnitude in the case of the pristine P3HT film and by up to one order of magnitude for the doped films. However, since a recent study of our group showed, that thermal annealing leads to a de-doping of F_4TCNQ doped P3HT films already at rather low annealing temperatures of 80 °C, the effect of thermal annealing was investigated in more detail by conductivity and optical measurements of a 15% doped film.[334] Figure 7.5 b) shows the conductivity at different annealing temperatures. Up to a temperature of 100 °C the conductivity of the film can be increased from 0.5 S/cm to 2.8 S/cm. At higher annealing temperatures, the conductivity decreases again, but not dramatically. The optical spectra of the 15% doped film displayed in Figure 7.5 c), however, show that already at an annealing temperature of 60 °C, the polaron transition P2 at 1.5 eV gets decreased in intensity, while the intensity of the transition of neutral P3HT at 2.2 eV increases. Higher annealing temperatures amplify the decrease and increase, respectively. Surprisingly, the polaron transition P1 at around 0.5 eV stays nearly constant in intensity up to an annealing temperature of 120 °C. The P1 transition gets first significantly lowered only at a temperature of 140 °C, where also the decrease of the P2 transition as well as the increase of the transition of neutral P3HT is stronger than at the other temperatures. These data confirm that thermally-induced de-doping is also taking place in the case of $Mes_2B^+[BCF4]^-$ doped P3HT. For this reason, doped films were not annealed for all other conducted experiments.

[98] Assuming that the ratio between additional free charge carriers and created polarons is nearly independent of dopant concentration.

7.4 Electronic Structure and Core Level Analysis

The changes in the electronic structure of P3HT films upon increased doping with $Mes_2B^+[BCF4]^-$ were investigated via mono-UPS measurements, the spectra of which are displayed in Figure 7.6 a). The valence band spectrum of pristine P3HT in Figure 7.6 b) shows the typical structure, with a prominent peak at around 3 eV binding energy attributed to a localized, non-bonding π-band and a comparably flat and broad feature between 0.2 eV and 2.0 eV attributed to the frontier π-band delocalized over the polymer chain.[332,335,336] From the work function of 4.52 eV and the valence band onset at 0.22 eV, the ionization energy of pristine P3HT can be calculated to be 4.74 eV, in good agreement with previously published values.[332,335,337] Upon doping, the Fermi level is shifted towards the valence band onset until it gets pinned at 80 meV above the onset for a dopant concentration of 10%. The detail scans of the Fermi level region displayed in Figure 7.6 c) show that there is no formation of additional density of states beyond the Fermi level with increasing dopant concentration (except the typical linear background, which is similar in all cases), which was observed for non-monochromatized UPS measurements and was the reason for conducting mono-UPS measurements in the first place.[99] For low dopant concentrations till 5%, the shift in work function is following the shift of the valence band onset, keeping the ionization energy constant at around 4.7 eV, as shown in the deduced energy level diagram in Figure 7.6 d). However, for dopant concentrations of 10% and higher, the work function is strongly increased up to 5.4 eV at 35%, indicating an increase in ionization energy of P3HT. A similar increase in ionization energy was also observed for electrodeposited and doped thin films of P3HT via UPS measurements.[307,326] This increase might seem surprising at first sight, since usually the ionization energy or electron affinity of the host material are reported to be constant during doping (like in Figure 6.6 of chapter 6),[52,149,168,176,206,338] and only for some crystalline materials the ionization energy is seemingly increased, which is, however, related to a broadening of the HOMO or LUMO level upon doping.[339,340] In most of these case, however, the dopant concentrations are usually in the range of a few mol-percent and typically do not exceed the 10% range, whereas here the increase in ionization energy is observed only for dopant concentrations of 10% and above.

The increase in ionization energy can be related to a significant increase in hole density / loss of electron density near the Fermi level, which is shown in Figure 7.6 e). The mono-UPS spectra displayed in Figure 7.6 e) are corrected for a numerical Shirley background, normalized to the localized π-band peak and the binding energy is shifted so that position of the localized π-band peak is matched, which is similar to setting the binding energy with

[99] The observed density of state beyond the Fermi-level in non-monochromatized UPS spectra are most likely related to satellite peaks from HeIβ and γ radiation, which cannot be completely removed by a numerical satellite-removal algorithm (see chapter 4 for details).

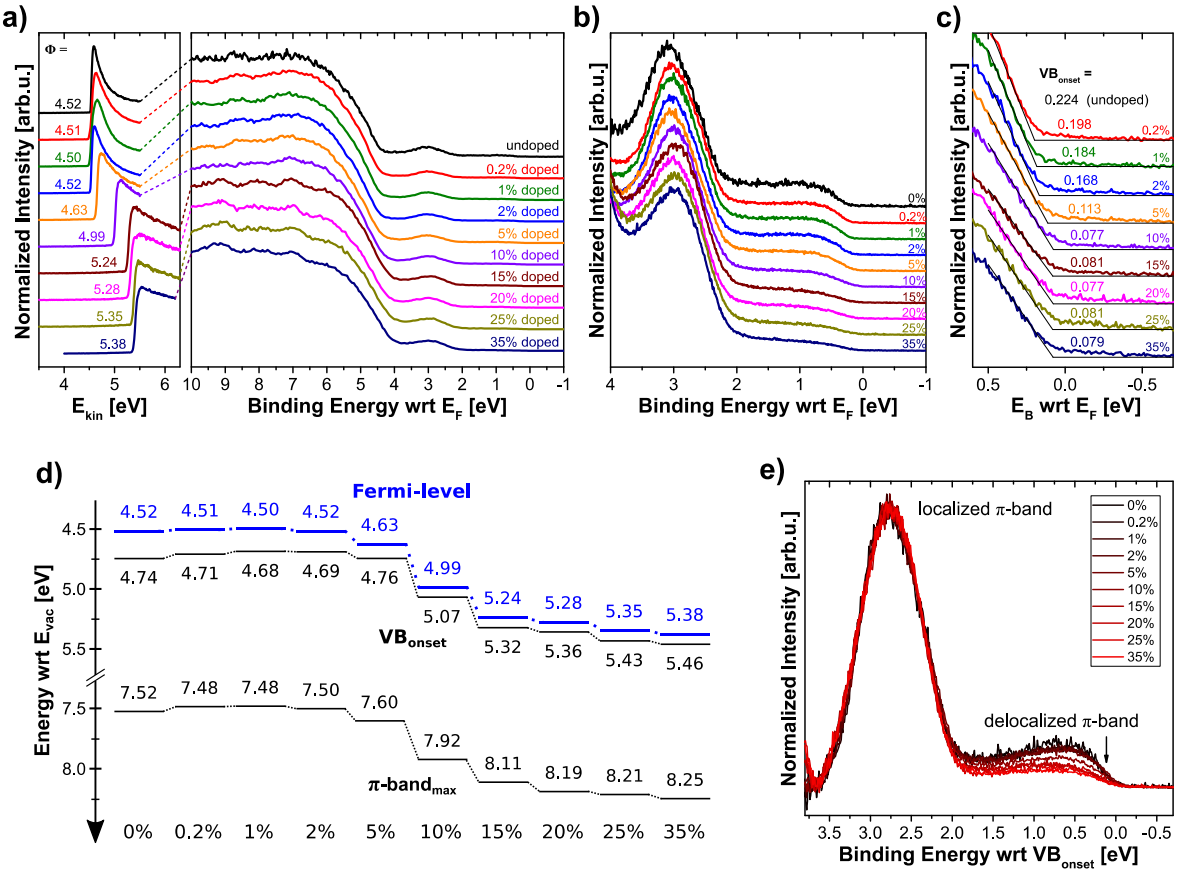

Figure 7.6 a) Mono-UPS spectra of $Mes_2B^+[BCF4]^-$ doped P3HT films. **b)** Detail scans of the valence band and **c)** detail scans of the Fermi level region. Till a dopant concentration of 5% the Fermi level gets shifted towards the valence band onset, while the ionization energy stays nearly constant. Upon a dopant concentration of 10%, the Fermi level gets pinned at around 80 meV above the valence band onset and the ionization energy is continuously increased with further increasing dopant concentration. **d)** From mono-UPS spectra deduced energy level diagram showing the positions of the Fermi-level, the onset of the valence band (VB_{onset}) and the peak position of the localized π-band (π-$band_{max}$) with respect to the vacuum level. **e)** Valence band spectra corrected by a numerical Shirley-background, normalized and shifted to the localized π-band. While the localized π-band stays nearly constant throughout all dopant concentrations with no additional broadening, the delocalized π-band near the Fermi level is continuously being depleted, showing a significant increase in hole density. The depletion sets in most strongly at the dopant concentration of 10%. This figure will be published in ref. [A8].

respect to the valence band onset within a tolerance of 100 meV (see also Figure 7.7). As can be clearly seen in Figure 7.6 e), the localized π-band peak is nearly unchanged for all doping levels. However, at higher doping levels, there is a strong depletion of the delocalized π-band near the Fermi level, which is increasing with higher dopant concentration. This decrease in electron density or equivalently increase in hole density is becoming significant at the dopant concentration of 10% and can thus explain the observed increase in ionization energy setting in at 10%.

The core level positions determined by mono-XPS measurements basically follow the changes in the work function. Figure 7.7 shows the relative shifts in binding energy of the

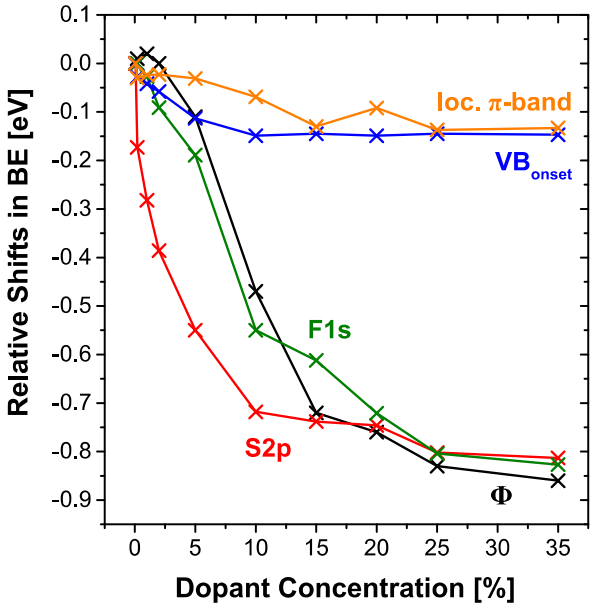

Figure 7.7 Relative shifts in binding energy (BE) of the work function, valence band onset and position of the localized π-band as well as of the positions of the S2p and F1s core levels with respect to the values of pristine P3HT. The relative shifts of the F1s core level are given with respect to the F1s core level position of the 0.2% doped sample, as the WF is not significantly changed compared to the pristine P3HT film. The shifts in the core-levels basically follow the shift in work function, while the valence band onset as well as the loc. π-band position get pinned at around 10% dopant concentration.

core levels of S2p (neutral component – see below) and F1s, which are exemplarily chosen for P3HT and $[BCF4]^-$, respectively, as well as the relative shifts of the work function ϕ, the onset of the valence band and the position of the localized π-band peak from mono-UPS. As can be seen, the relative shifts of the core levels follow the trend of the work function, indicating that the ionization energies of the core levels stay nearly constant. Only the shifts of the S2p core level in the low dopant concentration region up to 10% are much higher than the respective shifts in work function, which might be related to the influence of polaron and bipolaron formation (see below), for which, however, no satisfactory explanation has been found yet. In contrast, the peak position of the localized π-band basically follows the shift in the VB onset, which at first is also following the shift in work function, but at a concentration of around 10% gets pinned. This data shows only the ionization energy of the valence band electrons beeing significantly increased for higher doing concentrations, related to the increased hole density in the delocalized π-band.

Since, the C1s spectra of doped films contain too many contributions to perform an adequate deconvolution appropriately accounting for all chemical shifts, only the sulfur core levels were analyzed.[100] Figure 7.8 a) and b) show the deconvolution of the S2p and S2s core levels at each dopant concentration, respectively. The scan of the S2p level of pristine P3HT shows the typical doublet with a spin-orbit splitting between the $S2p_{3/2}$ and $S2p_{1/2}$ components of 1.18 eV and an intensity ratio of 0.5, as expected for an S2p doublet.[228] The S2s feature shows a much higher Lorentzian line shape than the S2p

[100] The C1s spectrum of doped C1s should be composed of at least 8 different contributions, two stemming from $[BCF4]^-$ (C-F and C-B), and two each for neutral, polaronic and bipolaronic 3HT (C-S and C=C). A deconvolution of so many contributions would make it rather arbitrary without proper theoretical support.

feature, indicating a lower lifetime of the core hole state created by photoemission. The parameters for S2p and S2s were kept constant in the deconvolution and in the following all references will be made only to the $S2p3_{/2}$ component, keeping in mind that the same applies to the $S2p_{1/2}$. Upon doping the core levels shift to lower binding energies, with the relative shift being very similar between S2p and S2s, while the line shape shows the emergence of new components. In the doping regime up to 5%, the S2p feature can be fitted with two doublet components with an energy difference of 0.4 eV. The new component at 0.4 eV higher binding energy is increasing with increasing dopant concentration and can thus be related to the formed polarons. At 10% dopant concentration, there is a broad new component emerging located at 2.0 eV to higher binding energies compared to the neutral component, which is further increasing with increasing dopant concentration. In accordance with the EPR and optical absorption spectroscopy presented in subsection 7.2, this new component can be related to the formation of bipolarons. The deconvolution of the S2s detail scans show similar results with the polaron and bipolaron components also being shifted to 0.4 eV and 2.0 eV higher binding energy, respectively, compared to the neutral component. XPS measurements reported for electrodeposited and doped P3HT show a similar development of the S2p line shape upon increased dopant concentration, where the components for polarons and bipolarons were reported to be 0.7-0.8 eV and 2.0-2.1 eV shifted to higher binding energies compared to the neutral component, respectively.[306,307,326] These results are in reasonable agreement with the fitting parameters obtained here, keeping in mind that the reported values are based on a different deconvolution procedure.

The relative changes in the areas of the different components are visually summarized in Figure 7.8 c). At 10% dopant concentration, the contribution associated with bipolaron formation appears and is increasing with increasing dopant concentration. However, at the same time the contribution associated with polaron formation is also increasing, which is strongly contradictory to the EPR results shown in Figure 7.4, where the amount of polarons to start to decrease at 10% dopant concentration. This conflict can be resolved, when considering that bipolarons also have contributions to the polaron and neutral features. Theoretical calculations performed on thiophene-oligomers suggest that polarons and bipolarons are delocalized over a hexamer unit.[325,341] The calculations show that the two positive charges in a bipolaron are mostly localized at the end of the hexamer unit, while the one positive charge in a polaron unit is completely delocalized over the hexamer unit. Following, the relative charge density in a polaron leads to one XPS component of the S2p core level, which according to the calculations should be 0.3 eV shifted to higher binding energies compared to the neutral component. This is in reasonable agreement with the obtained shift of 0.4 eV. For a bipolaron, however, the differently distributed relative charge density leads to three components for the bipolaron:

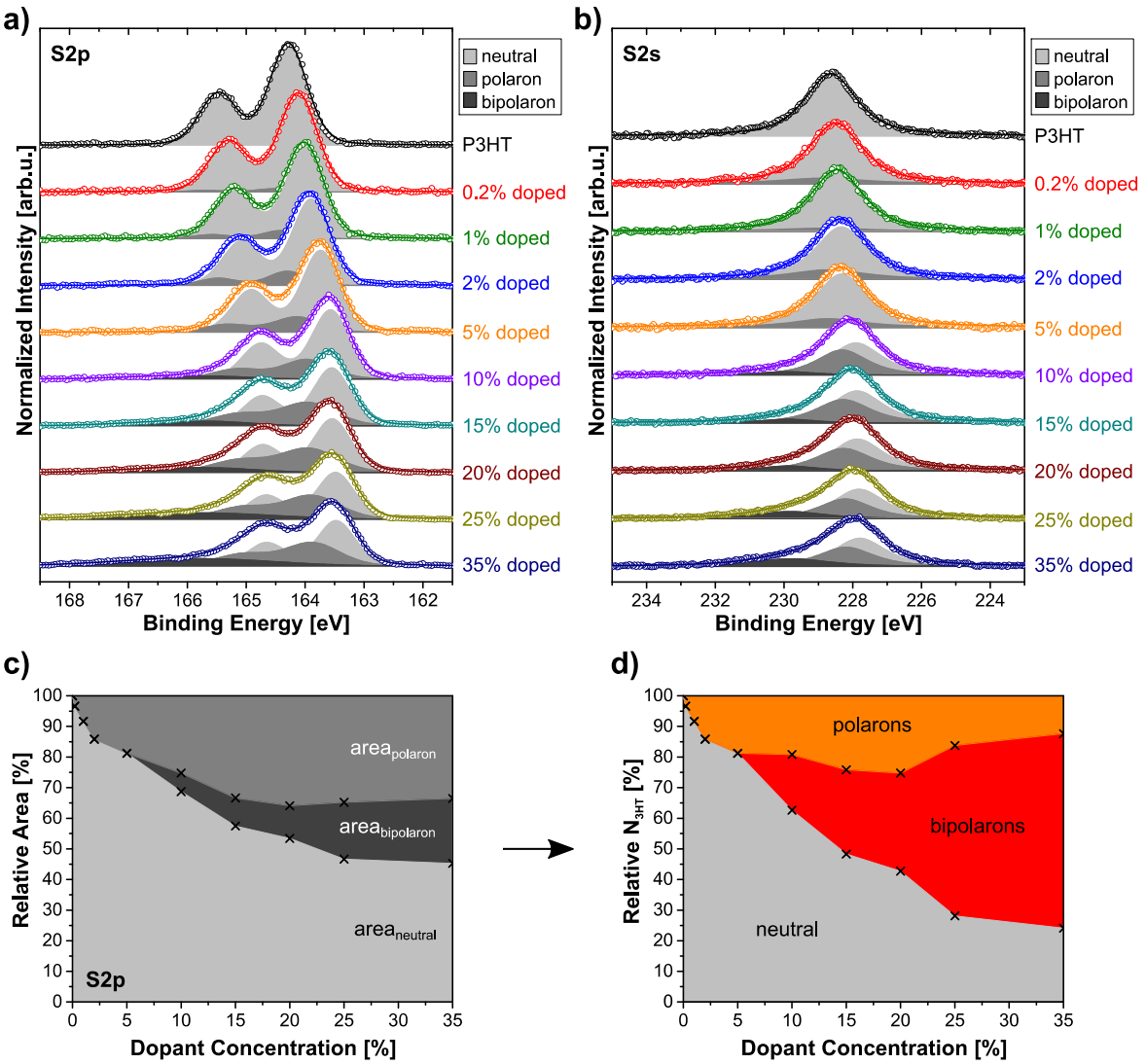

Figure 7.8 Deconvolution of the **a)** S2p and **b)** S2s core levels from XPS detail scans in dependence of the dopant concentration. Circles display the raw data. Both core levels are shifting to lower binding energies with increasing dopant concentration in accordance with the shifts in vacuum level. Upon doping till a 5% dopant concentration, the deconvolution reveals a new component at 0.4 eV higher binding energies, which is associtated with the formation of polarons. Starting at 10% dopant concentration a third component has to be taken into account, which is located at 2.0 eV higher binding energies and is associated with the formation of bipolarons. **c)** Relative areas of each component of the S2p core level as deduced from the deconvolution in Fig a. Here, the amount of polarons is increasing till around 20%, at which point it is going into saturation, which is in strong contrast to the EPR results. **d)** Relative amount of neutral 3HT units and 3HT units contained by polarons (orange) and bipolarons (red). Here, it is taken into account that the formation of bipolarons leads to equal contributions to all three components (based on the hexamer model). These results are in reasonable quantitative agreement with the EPR results. This figure will be published in ref. [A8].

one for the outer to thiophene units being even further shifted to higher BE, one for the 2nd and 5th unit displaying a similar shift in BE as the polaron contribution, and one for the inner two units lying at a similar BE as the neutral component.[325,341] Thus, assuming the formation of bipolarons leads to equal contributions to all three found components, the

number of affected thiophene units can be calculated assuming that the neutral and polaron component have a contribution from bipolarons similar in area to the component at 2.0 eV higher binding energy, as visualized in Figure 7.8 d). Here, the relative amount of polarons is increasing till around 15-20% and then decreasing again. The EPR results show the amount of polarons at around 2% and 35% dopant concentration to be similar and at around 50% of the maximal amount of polarons at 10% dopant concentration, which is in good agreement with the results shown in Figure 7.8 d).

Based on this hexamer unit model, the amount of charges per thiophene unit can be calculated, which should be equal to the dopant concentration. Table 7.1 shows this calculated quantity in dependence of the nominal dopant concentration and the dopant concentration estimated from the F/S area ratio taking into account that each $[BCF4]^-$ molecules contains 20 fluorine atoms, while each 3HT monomer only one sulfur atom. The dopant concentration estimated from the F/S area ratio is mostly lower than the nominal dopant concentra-tion, but still in reasonable quantitative agreement. Reasons for the XPS estimated concentrations being lower (or slightly higher in the case of 0.2% and 1%) than the nominal can be sought in the film preparation process (e.g. weighing of polymer and dopant or mixing of stock solutions) as well as not completely accurately calibrated atomic sensitivity factors on which the estimations are based.[102] The calculated average number of charges per monomer-unit show a very good quantitative agreement with the values estimated from the F/S area ratio.

Table 7.1 Nominal dopant concentrations as well as concentrations estimated from the F/S area ratios and the average amount of charge per thiophene unit based on the hexamer model. All values in %. This table will be published in ref. [A8].

nominal	based on F/S area ratio	based on hexamer unit[101]
0.2	0.65	0.57
1	1.16	1.39
2	1.95	2.36
5	3.33	3.13
10	6.85	9.26
15	12.26	13.21
20	15.68	14.88
25	22.04	21.25
35	26.23	23.24

However, the above made considerations have several weak points, which shall be discussed now. The main assumptions are that the spatial configuration of the polaron and bipolaron delocalization does not change upon increasing dopant concentration and that the delocalization of polarons and bipolarons extends over the same number of monomer

[101] Calculated via $(1[e^-] \cdot P_{polaron} + 2[e^-] \cdot P_{bipolaron})/6$, where P_i is the percentage of polarons and bipolarons, respectively.

[102] Note: the dopant concentrations in this chapter are, however, still reported as the nominal values, since the F/S area ratios of nominally 25% doped samples, which were prepared independently and measured on a different XPS system, showed the dopant concentration to be between 25-27%.

units, namely six units. For the doping of P3HT with F_4TCNQ, it was shown that the spatial delocalization does indeed not change with different dopant concentrations.[267] However, the combined optical and FTIR spectra of the $Mes_2B^+[CFB4]^-$ doped P3HT films presented in Figure 7.10 indicate a change in delocalization of the polarons with increasing dopant concentration (see discussion in the next subsection). Most of the recent publications also show experimental and theoretical indications that polarons are in fact delocalized over only quarterthiophene units and not over sexithiophene units.[24,152,267,342–344] Moreover, there is no strict reason why polarons and bipolarons should show the same spatial delocalization. Another weak point is that only intra-chain delocalization was considered to play a role in the formation of polarons and bipolarons and inter-chain delocalization was neglected. However, there is theoretical and experimental work suggesting that polarons are also delocalized over a few neighboring polymer chains, thus showing 2D instead of only 1D (on a single chain) electronic behavior.[49,344,345] Therefore, more theoretical support is needed in order to make more accurate predictions about polaron / bipolaron formation based on XPS measurements.

Another hypothesis which shall be discussed here, is the possibility of the observed components at higher binding energy in the S2p (and S2s) core level to stem from enhanced shake-up transitions, like it was suggest for the $ClO4^-$ doping of P3MT.[346] Here, the authors found a similar line shape for the S2p (and in their case also C1s) core level as shown in Figure 7.8 a) and advocated these asymmetrical line shape to stem from π-π* shake-up transitions, which are enhanced in intensity and also shifted in binding energy upon doping. In order to discuss this hypothesis, first the shake-up transitions of S2p and C1s are compared and following the C1s spectrum of the 35% doped P3HT sample is deconvoluted. For pristine P3HT, the π-π* shake-up transition for the S2p core level is located at around 2.6 eV to higher binding energies than the $S2p3_{/2}$ line position and its area is around 1.8% of the area of the S2p doublet, as shown in the deconvoluted S2p spectrum in Figure 7.9 a). The energetic distance of the shake-up line to the main $S2p3_{/2}$ line is very similar to the transport gap of P3HT, reported to be 2.6 eV.[294] The deconvolution of the C1s spectrum of pristine P3HT in Figure 7.9 b) shows a main contribution at 285.3 eV attributed to single- and double-bonded carbon species (C-C, C=C) in the 3HT unit and a smaller feature with the set intensity ratio of 1:4 relative to the C-C/C=C contribution. This smaller feature is shifted 490 meV to higher binding energies and attributed to carbon species bound to the sulfur atom in the thiophene unit (C-S), similar to what has been reported for P3HT before.[347] In addition, there is also a small contribution present at 284.6 eV, which was attributed to adventitious carbon contami-nations. The shake-up line was found at around 2.4 eV higher binding energy than the main C-C line and its area is around 2.3% of the combined C-C and C-S area, similar to the shake-up line of S2p.

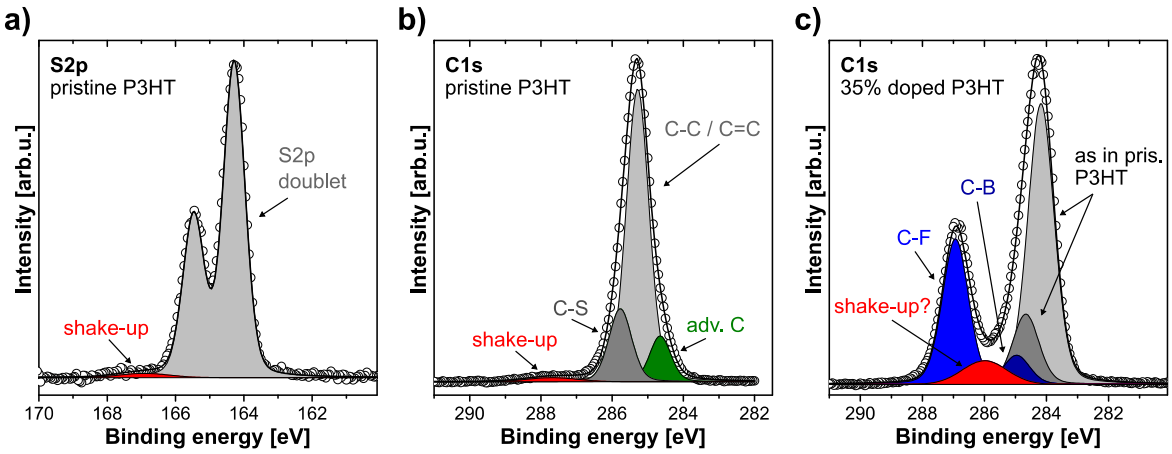

Figure 7.9 Deconvolution taking into account shake-up lines for **a)** S2p and **b)** C1s of pristine P3HT as well as **c)** C1s of 35% doped P3HT. Circles display the raw data. In S2p and C1s of pristine P3HT the shake-up transition lies at 2.4-2.6 eV higher binding energy than the main contribution and amounts for around 2%. The C1s spectrum of 35% doped P3HT can be fitted with two contributions of 3HT (C-C and C-S) as well as two contributions of $[CFB4]^-$ (C-F and C-B), which were linked to the amount of fluorine from the F1s line. The rest of the spectrum can be fitted by one feature at 1.9 eV higher binding energy, the area of which is ca. 12% of the area of C-S and C-C. This feature can be misinterpreted as an enhanced shake-up transition (see text for discussion).

Assuming that the changed line shape upon doping results only from an enhancement and energetic shift of the shake-up contribution, the S2p spectrum of the 35% doped P3HT film [Figure 7.8 a)] can be fitted with only a S2p doublet and a broad peak for the assumed shake-up line. Here, the shake-up transition is located at ca. 1.7 eV higher binding energy and its area is 37% of the doublet area. Proceeding similarly, the C1s spectrum of 35% doped P3HT can be fitted by five contributions, as shown in Figure 7.9 c). The main contribution stems from C-C and C-S species similar to pristine P3HT, while the prominent feature at higher binding energy stems from fluorine bonded species (C-F) from $[BCF4]^-$. Here, the C-F contribution was linked to the amount of fluorine determined from the F1s core level in a ratio as found for $Mes_2B^+[BCF4]^-$ multilayers.[103] Another contribution of $[BCF4]^-$ are boron bonded carbon species (C-B), which have an intensity ratio of 1:5 compared to the C-F contribution and are located at around 2 eV to lower binding energy as determined from the $Mes_2B^+[BCF4]^-$ multilayers. The last contribution to the spectrum in Figure 7.9 c), is located at 1.9 eV to higher binding energy than the C-C contribution and it area is around 12% of the combined C-S and C-C area. These results show, that if the additional contributions to the S2p and C1s line shape would stem from enhanced shake-up contributions, that the enhancement of the S2p shake-up line with a factor of around 20 would be much stronger than the enhance-ment of the C1s shake-up line with a factor of around 5. This is considered to be highly unlikely, because there is no obvious reason

[103] The ratio between F and C-F should be one. However, due to a large screening of the C-F species from fluorine atoms, the ratio was found to be 0.6 for the $Mes_2B^+[BCF4]^-$ multilayers.

that the shake-up transition (which for pure P3HT is in the same order of magnitude) gets much more enhanced for the S2p level compared to the C1s level. Here, it is much more likely that the asymmetry of the line shape of S2p as well as C1s to higher binding energies stems from polaronic and bipolaronic contributions. The reason for the contribution of the C1s level to be smaller than the contribution of the S2p level lies in the fact that for C1s only the four carbon atoms in the aromatic ring are affected by the formation of polarons and bipolarons, while the six carbon atoms in the alkyl chain should be nearly unaffected by the formation.[341] Thus, they should lie at the same position as neutral C-C and contribute to the prominent feature at around 284 eV in the spectrum in Figure 7.9 c).

7.5 Influence of Air-Exposure

In order to study the influence of low pressure in high vacuum (HV) and also the influence of air, optical spectra of $Mes_2B^+[CFB4]^-$ doped P3HT thin films for various dopant concentrations were recorded after preparation in inert atmosphere, after exposure to HV overnight, and after air-exposure for a few hours. The optical spectra are summarized in Figure 7.10 a). After the overnight exposure to HV, the optical spectra (thin solid lines) show only negligible changes. Thus, the presence of $[Mes2BH]_2$ as side-product of the doping process can neither be confirmed nor excluded, since the optical absorption of $[Mes2BH]_2$ is unknown and lies most likely in the high UV region. Further experiments are therefore needed to clarify at which stage $[Mes2BH]_2$ is removed from the film, as XPS detail scans of B1s show no sign of neutral or positively charged boron species being present in doped P3HT films.[104]

Upon exposure to air, the optical spectra of the doped films are significantly changed [dashed lines in Figure 7.10 a], especially for highly doped films. Here, the features at 1.8 eV and 2.1 eV, previously identified to belong to bipolarons (see section 7.2), are vanishing, while at the same time the polaron features at around 0.5 eV and 1.5 eV are increasing in intensity. For the dopant concentrations up to 15%, the P1 feature at 0.5 eV is increasing around 70-80%, while for the higher dopant concentrations, it is only increasing about 20%. This clearly shows that upon air-exposure, there is a transition from bipolarons back to polarons. Figure 7.10 b) shows combined optical and FTIR spectra of the doped films after air-exposure.[105] The combined spectra show that with increasing dopant concentration the position of the polaron features P1 and P2 undergo a blue-shift, i.e. from 0.4 eV to 0.5 eV

[104] Here, nuclear magnetic resonance (NMR) or IR spectroscopy under inert atmosphere could be useful to clarify this question, since both techniques have been previously used to study $[Mes_2BH]_2$.[311,312]

[105] Unfortunately, there was no possibility of performing FTIR spectra without air exposure. Since the transition from bipolarons to polarons was found to set in rapidly after air-exposure, it was not possible to expand the spectra of the doped films taken in inert atmosphere to the MIR region.

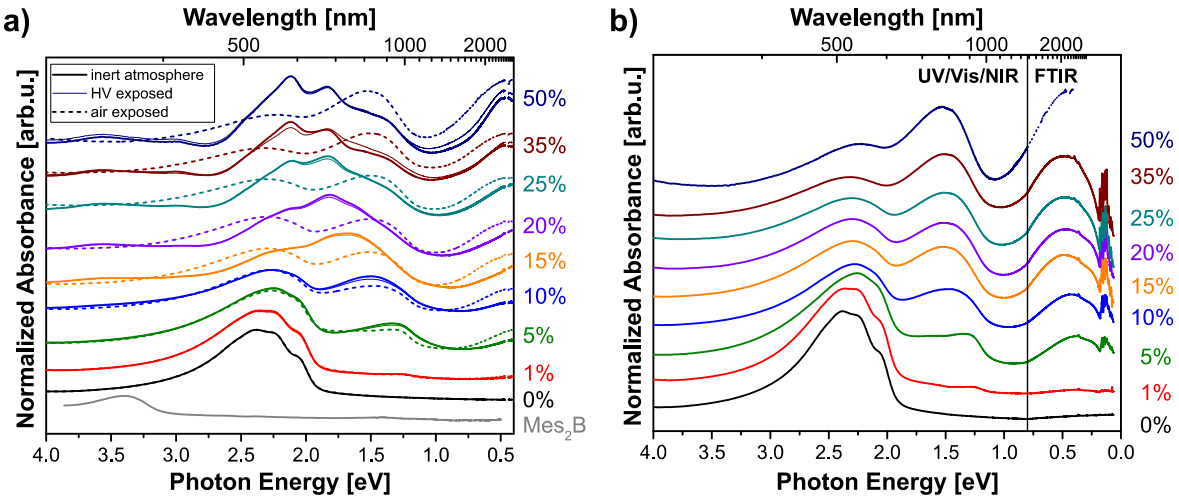

Figure 7.10 a) Optical absorption spectra of $Mes_2B^+[CFB4]^-$ doped P3HT thin films after preparation in inert atmosphere, overnight HV exposure and air-exposure of a few hours, respectively. Upon HV, exposure the spectra show only negligible changes, while they are significantly changed after air-exposure. Here, the features associated with bipolarons at 1.8 eV and 2.1 eV are vanishing, while the P1 and P2 features of polarons at 0.5 eV and 1.5 eV, respectively, are increasing, showing a clear transition from bipolarons to polarons. **b)** Combined optical and FTIR spectra of the doped thin films after air-exposure. The FTIR spectrum of the 50% doped film is missing due to very bad SNR ratio, instead the NIR spectrum measured with optical spectroscopy is shown (dotted line). The structure in the region below 0.2 eV is caused by IR-active vibrations (IRAV) of P3HT. This figure will be published in ref. [A8].

and from 1.3 eV to 1.5 eV, respectively. These shifts indicate a stronger localization of the polaron with increasing dopant concentration, since delocalization was shown to lead to a red-shift of the polaron transitions.[344,348] This localization of polarons is most likely caused by adecrease in crystallinity of the P3HT microstructure with increasing dopant concentration.[174] In addition, the combined spectra of Figure 7.10 b) also show both polaron transitions to increase in intensity compared to the transition of neutral P3HT at around 2.3 eV without going into saturation.

Since the results of the optical measurements clearly show a transition from polarons back to bipolarons occurring after air-exposure of the films, conductivity measurements were performed in order to assess the effect of bipolarons on the charge transport in P3HT. For this reason, samples with 2% and with 25% dopant concentrations were prepared, as the 2% doped sample is mainly comprised of polarons, while the 25% doped sample has a high degree of bipolarons [see Figure 7.8 d)]. As reference, one sample of each dopant concentration was kept under inert atmosphere and also the change in conductivity of a pristine P3HT sample upon air-exposure was measured. Figure 7.11 shows the time dependent change in conductivity, where t = 0 marks the moment of air-exposure. Directly after preparation, P3HT exhibits a conductivity of around 1×10^{-6} S/cm, 2% doped P3HT 7×10^{-4} to 2×10^{-3} S/cm and 25% doped P3HT around 3×10^{-5} S/cm, similar to what was shown in Figure 7.5 (differences are related to the use of different batches of P3HT). Upon air-

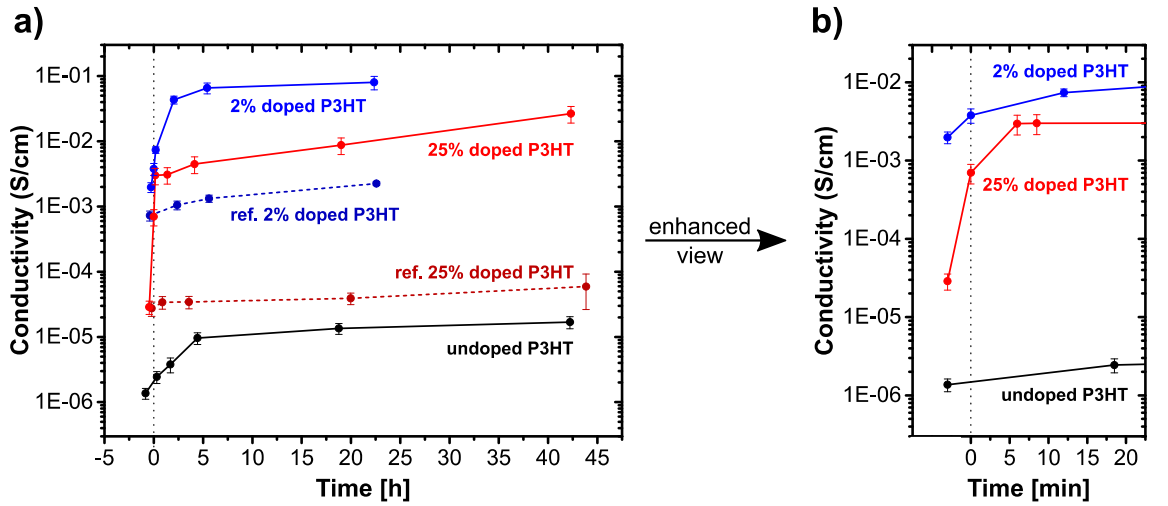

Figure 7.11 a) Time-dependent conductivity of pristine, 2% and 25% doped P3HT upon air-exposure. Here, t=0 marks the moment of air-exposure. While the reference samples kept in inert atmosphere stay nearly constant in conductivity, the conductivity of the air-exposed samples is increased by a few orders of magnitude. This is related to oxygen doping of P3HT for pristine and 2% doped P3HT, while in the case of 25% doped P3HT, it is a combination of bipolaron to polaron transition and oxygen doping. **b)** Enhanced view of the changes in conductivity in the first 20 min after air-exposure. For better visibility, the conductivity values of the samples after preparation in inert atmosphere and before air-exposure are shown at the same point in time. As can be seen, the increase in conductivity over up to two orders of magnitude sets in directly after air-exposure for 25% doped P3HT. In contrast, the conductivity of pristine and 2% doped P3HT increases only slightly within the first 20 min of air-exposure. This figure will be published in ref. [A8].

exposure, the conductivity of pristine P3HT is slowly increased about one order of magnitude within the course of several hours. This increase in conductivity is attributed to p-doping of P3HT by oxygen, which is proceeding slowly and saturation of the conductivity is reached after around 4-5 hours similar to what has been reported previously.[157,349–353] The 2% doped sample shows a similar increase in conductivity over nearly two orders of magnitude within the same time-scale. The reference sample kept under inert atmosphere, on the other hand, shows also shows a slight increase in conductivity, which, however, is in the same order of magnitude. This shows that also already doped samples are further p-doped by oxygen. In contrast, the increase in conductivity of the 25% sample sets in rapidly. Figure 7.11 b) shows that while the conductivity of pristine and 2% doped P3HT increases only slightly upon air-exposure, the conductivity of 25% doped P3HT increases already over one order of magnitude directly after air-exposure and over two orders of magnitude after 10 min, nearly reaching the conductivity of the 2% doped sample. Over the whole measured time period of 44 h, the conductivity of the air-exposed sample increases over a total of three orders of magnitude, whereas the reference sample in inert atmosphere stays constantly at its original conductivity.

In accordance with the optical spectra in Figure 7.10, the rapid conductivity increase of the 25% doped sample can be related to a transition from bipolarons to polarons upon air-exposure, while the additional slow increase over several hours is most likely also related

to doping by oxygen similar to pristine and 2% doped P3HT. The rapid increase over two orders of magnitude associated to bipolaron to polaron transition also indicates that bipolaronic charge carriers are less mobile than polaronic charge carriers assuming that the total number of holes is contained during the transition. Such a behavior was also observed for the doping of P3HT with $FeCl_3$, where the mobility of polarons was estimated to be two orders of magnitude higher than that of bipolarons.[308] This difference in mobility can most likely be related to the fact that a bipolaron induces stronger polarizations in its vicinity and consequently, it does have to carry a larger polarization cloud with it, which effectively decreases its mobility.

7.6 SUMMARY

In summary, doping of the polymer P3HT with the organic salt $Mes_2B^+[CFB4]^-$ was investigated via a multi-experimental approach. It was shown that the doping at high dopant concentrations leads to the formation of bipolarons. Upon doping, electrons are transferred from P3HT chains to Mes_2B^+, while the formed positive polarons (and bipolarons) in P3HT are stabilized by the weakly coordinating counteranion $[CFB4]^-$. The formed neutral radical $MesB^\bullet$ is most likely forming the dimer $[Mes_2BH]_2$ via hydrogen abstraction, which, at least under UHV conditions, is no longer present in the doped P3HT films as evidenced by XPS detail scans of the B1s core level.

Optical absorption spectroscopy revealed the formation of polarons at low dopant concentrations up to 10% by observation of the typical polaron transitions P1 and P2, which were found to be blue shifting with increasing dopant concentration. This blue shift indicates a stronger localization of the polarons on individual polymer chains most likely due to a decrease in microstructural crystallinity of the P3HT films. Starting at a dopant concentration of 15%, new features are emerging at 1.8 eV and 2.1 eV, which have never been observed for P3HT so far. By comparison with EPR spectroscopy, these new features can be attributed to belong to spinless charge carriers (most likely bipolarons). The EPR determined number of unpaired spins was found to linearly increase with increasing dopant concentration till around 10%, upon which it starts to decrease again. EPR measurements of similarly p-doped P3HT films with F_4TCNQ and BCF3 revealed also a linear increase in the number of spins with increasing dopant concentration until 10%, at which, in contrast, the number of spins goes into saturation. This indicates, that the dopants F_4TCNQ and BCF3 do not possess the required doping strength to induce the formation of bipolarons. In the case of F_4TCNQ and BCF3, the doping efficiency is related to the equilibrium between ionized host and ionized dopant (as e.g. shown in section 5.2) and is decreasing with increasing dopant concentrations. In contrast, in the case of the organic salt, the charge transfer to the cation is important for the doping strength and doping

efficiency of the organic salt. After accepting an electron, however, the former cation is taken out of the equation due to its dimerization with another radical and thus the formed polarons/bipolarons only have to be balanced by the counteranions. This likely explains the fact that the optical features attributed to bipolarons have never been observed before by molecular doping of P3HT. The observed optical features of P3HT bipolarons in this work are, however, in conflict with previously reported optical absorption features associated with the formation of P3HT bipolarons.[46,50,90,306,308,324]

The electronic structure of doped P3HT films was investigated by mono-UPS measurements. Here, it was shown that upon doping the Fermi level gets shifted towards the valence band of P3HT and at a dopant concentration of around 10% gets pinned at 80 meV above the valence band onset. Starting at 10%, the ionization energy of 4.7 eV of pristine P3HT was found to increase with further increasing dopant concentration up to 5.4 eV for 35%. This increase in ionization energy was associated with the observed strong depletion of the delocalized π-band near the Fermi level, showing a significant increase in hole density. XPS detail scans of the S2p and S2s core levels revealed the formation of a second component to the line shapes for low dopant concentrations up to 5%, which was associated to polaron formation. Starting from 10% dopant concentration, a third component at 2.0 eV higher binding energies was observed, which kept increasing with further increasing dopant concentration and was associated to the formation of bipolarons in accordance to the optical and EPR measurements. By comparison with the C1s core level, the possibility of these components belonging to enhanced shake-up transitions was excluded.

Upon air-exposure, a transition from bipolarons back to polarons was observed by optical absorption spectroscopy. This transition was found to set in rapidly within the first few minutes of air-exposure. Conductivity measurements in inert atmosphere showed an increase in conductivity over four orders of magnitude up to a dopant concentration of around 15%, after which the conductivity decreased nearly back to the level of pristine P3HT. The strong decrease in conductivity at dopant concentrations above 15% was linked to the bipolaronic charge carries being less mobile than polaronic charge carries, since upon air exposure of 25% doped P3HT, the conductivity increases rapidly by two orders of magnitude and after longer air-exposure increase to nearly the same level as 2% doped P3HT. The involved mechanisms in the transition from bipolarons to polarons are, however, not yet understood and have to be explored in future experiments.

All in all, this is the first time that the formation of bipolarons was conclusively proven to occur for the doping of the polymer P3HT with a molecular dopant comprised of an organic salt.

8 ELECTRODE MODIFICATION FOR USE IN PEROVSKITE SOLAR CELLS

To date, the most efficient perovskite solar cells (PSCs) employ TiO_2 as electron transport material (ETM).[12,54,55] However, TiO_2 based PSCs were shown to be unstable under UV irradiation and, thus, exhibit short device lifetimes.[56,57] An alternative approach is to use organic ETMs like fullerene derivatives, which reduces hysteresis in the current-voltage characteristics leading to higher stabilized power outputs and thus increased lifetimes of the devices.[58,354,355] In addition to fullerenes, perylene diimides (PDI) derivatives have been used as ETM materials.[61,62,356–358] However, although organic transport layers have been used relatively early in the development of PSCs,[13] they are currently mostly employed as hole transport layers while still metal oxides are employed as electron transport layers (ETL).[12] One reason could be the low compact between those organic ETMs and transparent conductive oxide substrates like ITO and FTO, which are commonly used as transparent electron selective contacts.[12] Lowering the work function of electrodes is a common method to achieve Ohmic contacts (and thus higher compact) between organic ETLs and electrodes due to Fermi level pinning of the ETL at the low-WF electrode (see also subsection 2.1.4).[108] Recently, organometallic dimers have been shown to effectively reduce the work function of several electrode materials.[132,359] The aim of this work is to extend the use of organometallic dimers to the technological relevant FTO in order to minimize electron-collection losses at the interface between organic electron transport layers (ETL) and FTO used as electron-selective contacts in PSCs.

Here, first the modification of FTO with the organometallic dimer $[RhCp^*Cp]_2$ is studied and different modification methods are compared. This is followed by an analysis of the energy level alignment at the interface between (un-)modified FTO and organic ETL materials. As ETM material, the perylene diimide derivative PTCBI is compared to C_{60}. Furthermore, possible diffusion of the dimer into the ETL and subsequent doping is investigated. Finally, the application of such modified electron selective contacts in PSCs is demonstrated.

This study was performed in collaboration with Federico Pulvirenti (School of Chemistry and Biochemistry, Georgia Institute of Technology, Atlanta, USA) and most of the results presented here were published in ref. [A6].

8.1 MODIFICATION OF FTO

Vacuum deposition of the dimer $[RhCp^*Cp]_2$ onto piranha-cleaned FTO leads to an effective reduction of the electrode work function, as evidenced by the UPS measurements shown in Figure 8.1 a). The initial work function of clean FTO of 4.6 eV is reduced by 1.0 eV, when a nominally 1 nm thick layer of $[RhCp^*Cp]_2$ is deposited onto the surface. Deposition of a thicker layer (nominally 10 nm) leads to a further reduction to 3.3 eV. At the same time the

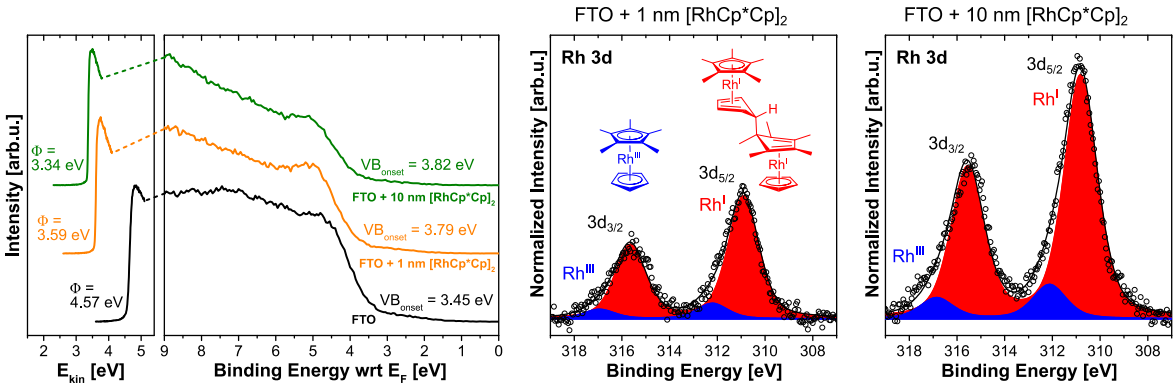

Figure 8.1 a) UPS spectra of bare FTO as well as FTO with a nominally 1 nm and 10 nm thick $[RhCp^*Cp]_2$ layer. Upon deposition of the dimer, the work function of FTO is reduced by 1.0 and 1.3 eV, respectively. **b)** XPS detail scan of the Rh 3d region of the 1 nm thick dimer layer on FTO and **c)** of the 10 nm thick dimer layer on FTO. Both detail scans show the major component to belong to unreacted dimers (red) and a minor component of around 14% to belong to the monomer cations (blue). Both regions have been normalized to the area of Sn3d. Published in ref. [A6].

Table 8.1 XPS binding energies and peak area ratios for $[RhCp^*Cp]_2$-covered FTO. All values are in eV (except ratios). The position of the Rh^{III} 3d peaks was fixed to be at a distance of 1.3 eV from the Rh^{I} 3d peaks to allow consistent fitting. Table published in ref. [A6].

	Sn $3d_{5/2}$	C 1s	Rh^{I} $3d_{5/2}$	Rh^{III} $3d_{5/2}$	Rh^{III} / Rh^{I}	Rh / Sn
FTO	487.22	285.62	--	--	--	--
FTO + 1 nm $[RhCp^*Cp]_2$	487.27	286.17	310.91	312.21	0.13	1.6×10^{-2}
FTO + 10 nm $[RhCp^*Cp]_2$	487.29	286.23	310.82	312.12	0.14	3.5×10^{-2}

VB onset shifts by 340 meV and 370 meV to higher binding energies, respectively.[106] Upon adsorption of the dimer, the core level of tin Sn $3d_{5/2}$ belonging to the FTO substrate, only increases slightly in binding energy from 487.22 eV to 487.27-487.29 eV, respectively, which is associated with a change in surface band bending of FTO (see Table 6.1).[360] Thus, these shifts in the energy levels point towards the formation of an interface dipole at the surface of FTO due to electron transfer from the dopant to the FTO. This electron transfer is associated with a dissociation of the dimer into two monomer cations, which results in an interface dipole (i.e. positive potential) at the interface leading to the interface dipole and thus the appreciable reduction in work function.

The formation of monomer cations can be observed by XPS. The central Rh atom of the monomer cation is in formal oxidation state III, while Rh in the dimer is in oxidation state I. A change in oxidation state from I to III is associated with a shift of the Rh 3d signal to higher binding energies, which normally is in the order of 1.0 to 1.4 eV.[361] Following the work of Akaike et al., the energetic difference in binding energies between the 3d signals of Rh^{I} and

[106] However, in this case, it is not possible to distinguish between the VB and HOMO features stemming from FTO and the dimer, respectively.

Rh^{III} was in all cases assumed to be 1.3 eV in order to allow a consistent deconvolution. The XPS details scans of the Rh3d region of 1 nm and 10 nm thick films are shown in Figure 8.1 b) and c), respectively. Due to spin-orbit coupling the Rh 3d signal is split into two components, $3d_{5/2}$ and $3d_{3/2}$, whose energy splitting was found to be 4.63 eV and intensity ratio to be 0.61. The splitting in energy is slightly lower than the literature value of 4.74 eV and also the intensity ratio of 0.61 is slightly lower than the value of 0.67, which would be normally expected for a 3d feature.[228] Since the shift in binding energy between the oxidation states I and III applies equally to $3d_{5/2}$ and $3d_{3/2}$, only the $3d_{5/2}$ component will be discussed in the following.

As can be seen from both spectra, the $3d_{5/2}$ component consists of two contributions, with the main one lying at 310.8-310.9 eV and a smaller intensity shoulder at higher binding energy. The main contribution was associated to belong to Rh^{I}, unreacted dimer, and accordingly the shoulder at 312.1-312.2 eV to belong to Rh^{III}, monomer cation [see deconvolution in in Figure 8.1 b) and c)]. The XPS spectra reveal the evaporated films to mainly consist of unreacted dimers and only the dimeric molecules directly in contact witf the FTO surface are undergoing charge transfer. However, the area ratio between Rh^{III} and Rh^{I} stays nearly the same (see Table 6.1). In addition, the area ratio of Rh to Sn only increases by a factor of about 2, which is muss less than would be expected for a closed homogeneous layer of 10 nm thickness compared to a layer of 1 nm thickness. As shown in subsection 3.1.3, the ratio between the intensity from the substrate I_{sub} and a closed overlayer to I_{ovl} should rather follow an exponential function proportional to $\exp(t/\lambda_{ovl})$, where t is the thickness of the overlayer and λ_{ovl} its IMPF. Assuming an IPMF of 3-4 nm at around 1200 eV for organic compounds,[222,224] the ratio of Rh / Sn should increase by a factor of 10 to 20. This points towards a Stranski-Krastonov growth mode, where the monomer cations cover the substrate followed by partial island formation of the dimers. An alternative explanation would be that some of the molecules desorb again from the surface during/after deposition.

To further investigate whether the dimeric molecules grow by the Stranski-Krastonov mode, AFM measurements were performed on the samples, the images of which are shown in Figure 8.2 a). The dimer covered FTO samples show similar surface morphologies as the unmodified FTO. FTO has a very high RMS surface roughness of 13 nm and 15 nm for 2×2 μm^2 and 10×10 μm^2 probing areas, respectively. The RMS roughness of dimer-covered FTO is of the same order of magnitude for the same probing areas, but it decreases with as the dimer layer thickness increases. Thus, the organic layer seems to even out the high roughness of FTO. However, due to the high surface roughness, changes in the morphology of modified FTO with thicknesses of the organic layers in the order 5-20 nm cannot be observed. As a reference, a nominally 5 nm thick film of dimers was vacuum deposited on a quartz glass, which has a very smooth surface (RMS roughness of 0.5 nm). In this case, no

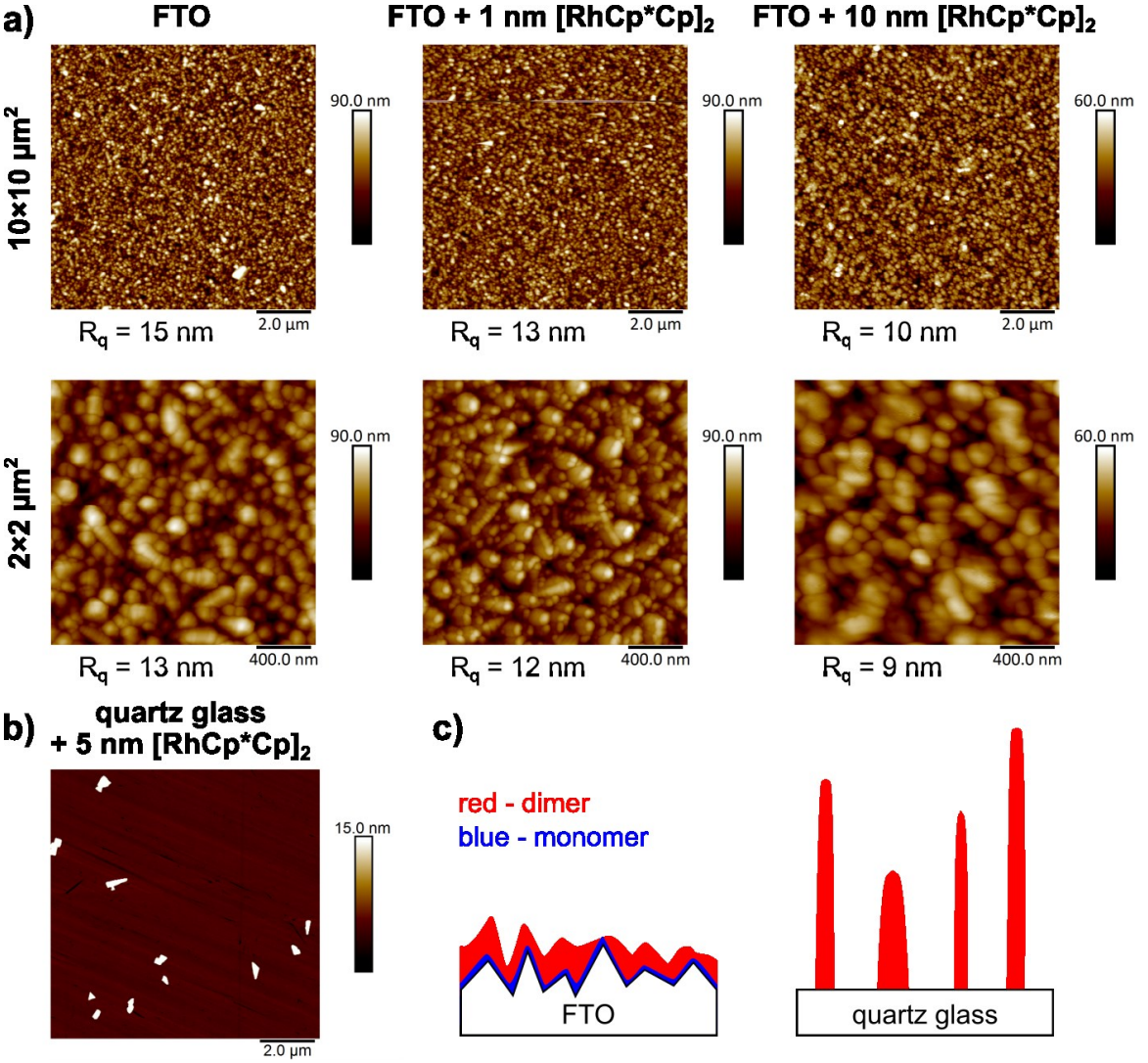

Figure 8.2 a) 10×10 µm^2 and 2×2 µm^2 AFM images of FTO, FTO modified with 1 nm $[RhCp^*Cp]_2$, and FTO modified with 10 nm $[RhCp^*Cp]_2$. FTO has a very high RMS surface roughness of 15 nm. The morphology of the FTO is preserved upon modification, however, the dimer layer seems to slightly smooth the surface, since the roughness tends to decrease with a thicker dimer layer. Due to the high surface roughness, island formation in the order of a few 10 nm cannot be observed. **b)** 10×10 µm^2 of a nominally 5 nm $[RhCp^*Cp]_2$ layer on quartz glass. The dimers do not interact with the substrate and thus form large islands with heights up to 200 nm. **c)** Deduced growth modes of $[RhCp^*Cp]_2$ on FTO (left) and quartz glass (right).

charge transfer between the dimer and the quartz substrate is expected as quartz is an insulator. The AFM image displayed in Figure 8.2 b) shows that on quartz large islands of dopants are formed following the Volmer-Weber growth mode. Such islands have an average height in the order of 50-100 nm, with outliers reaching up to 200 nm. However, islands were not observed when the dimer was deposited on FTO. From these measurements, it can be deduced that $[RhCp^*Cp]_2$ growth modes are substrate dependent, as shown in a simple schematic in Figure 8.2 c). In the case of quartz, where there is no interaction between the dimer and the substrate, the dimers tend to form large islands, probably without even forming a completely closed monolayer at the interface to the

substrate. In contrast, the dimers deposited on FTO interact with the substrate and form a mono-layer (or even multilayers) of monomer cations directly at the interface with the metal oxide, while unreacted dimers form additional layers and small sized islands on top of the monomer-layer. Due to the high surface roughness, it could be possible that the nominally 1 nm thick layer of $[RhCp^*Cp]_2$ does not even completely cover the whole FTO surface, which would explain the ratio of Rh^{III} / Rh^{I} to seemingly stay constant.

Vacuum deposition is a rather wasteful deposition method, as a lot of the thermally evaporated organic is deposited on the chamber walls and not on the desired substrate (from experience, around 10 mg are needed to deposit a few 10 nm thick films).[107] As an alternative, solution-processing of the dimer via dip-coating was investigated in another context, where a solution containing only a few mg of dopants, can be used for multiple samples. Here, the FTO substrates were dipped in 2 mM solutions of $[RhCp^*Cp]_2$ in toluene followed by rinsing with toluene to get rid of species not adsorbed on the substrate. The dipping time of FTO samples in the dimer solutions was varied from 1 min up to 10 min. As the UPS spectra of samples show [see Figure 8.3 a)], using dip-coating can reduce the work function of FTO from 4.6 eV to 3.3 eV, which is comparable to the work function of FTO modified by vacuum deposition of the dimer. The XPS details scans of the Rh3d region of substrates dipped for 1 min and 10 min are shown in Figure 8.3 b) and c), respectively. Here, the Rh $3d_{5/2}$ signals show again to contributions, the main one lying at 310.7 eV and 311.0 eV, respectively. In contrast to vacuum deposited samples where the second Rh $3d_{5/2}$ contribution is shown at high binding energies, with solution-processed samples the detail scans show a smaller intensity shoulder is at lower binding energies. In accordance with the positions found for evaporated (sub-)monolayers, i.e. 309.3 eV for Rh^{I} and 310.6 eV for Rh^{III}, the main peak was assigned to belong to the monomer cation, while the shoulder at 309.4 eV and 309.7 eV, respectively, was assigned to un reacted dimer. This assignment is further strengthened by the data displayed in Table 8.2. The FTO samples dipped longer in $[RhCp^*Cp]_2$ solutions also display a lower work function and a higher Rh^{I} to Rh^{III} ratio. Thus, with longer dipping time a denser monolayer is formed probably accompanied by bilayers of unreacted dimer. The increase in Rh^{I}/Rh^{III} ratio is also accompanied by shifts of the Rh^{III} 3d core level to higher binding energies, which is in the same order of magnitude as the shifts of the work function. It should be noted that the Rh/Sn ratios are always in the same order of magnitude regardless of the dipping time, possibly because of the high surface roughness of the FTO substrates used.

The assignment of the Rh^{I} and Rh^{III} signals seems to be in conflict with the assignment of the Rh 3d features for the vacuum deposited samples, where the peak at around 310.9 eV was assigned to Rh^{I} and should thus be further discussed at this point (especially since

[107] This high usage can be further minimized with a more sophisticated deposition system.

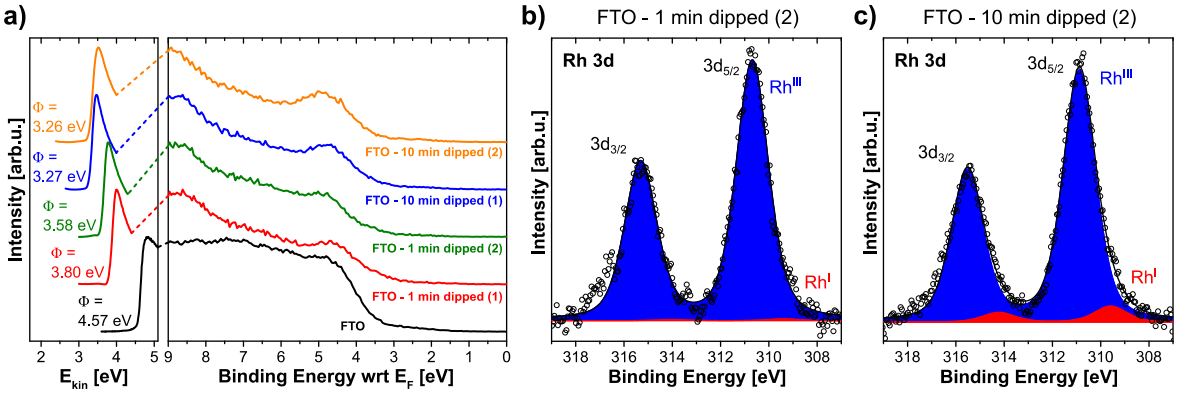

Figure 8.3 a) UPS spectra of bare FTO as well as FTO dipped into a 2 mM $[RhCp^*Cp]_2$ solution for 1 min and 10 min (two samples were analyzed for each dipping time). With increasing dipping time, the work function of FTO is continuously reduced. **b)** XPS detail scan of the Rh 3d region of FTO dipped for 1min (sample 2) and **c)** of FTO dipped for 10 min (sample 2). Both detail scans show the major component to belong to monomer cations (blue). With decreasing work function the amount of unreacted dimers (red) is increased.

Table 8.2 XPS binding energies and peak area ratios for FTO dipped into a 2 mM $[RhCp^*Cp]_2$ solution for different dipping times (two samples were analyzed for each dipping time). All values are in eV (except ratios). The position of the Rh^{I} 3d peaks was fixed to be at a distance of 1.3 eV from the Rh^{III} 3d peaks to allow consistent fitting. With increasing Rh^{I}/Rh^{III} ratio, the peak position of Rh^{III} $3d_{5/2}$ is further shifted to higher binding energies.

	Sn $3d_{5/2}$	C 1s	Rh^{I} $3d_{5/2}$	Rh^{III} $3d_{5/2}$	Rh^{I} / Rh^{III}	Rh / Sn
FTO	487.22	285.62	--	--	--	--
FTO dipped for 1 min (1)	487.16	285.84	--	310.54	--	6.1×10^{-2}
FTO dipped for 1 min (2)	487.29	286.02	309.38	310.68	0.01	4.7×10^{-2}
FTO dipped for 10 min (1)	487.24	286.25	309.59	310.89	0.06	6.9×10^{-2}
FTO dipped for 10 min (2)	487.23	286.32	309.72	311.02	0.12	6.3×10^{-2}

Sn $3d_{5/2}$ is located at nearly the identical position – see Table 8.2). The difference in binding energies of around 1.3 eV between the two oxidation states is relatively small, and in agreement with what has been observed in previous studies on Rh-based dopants.[132,172] Although the formal oxidation states are I and III, there is considerable covalency and charge delocalization onto the ligands in both $[RhCp^*Cp]_2$ and $[RhCp^*Cp]^+$. Thus, differences in the microscopic environment of the Rh species can have comparable effects on the binding energy as the oxidation state. According to the NIST XPS database, the position of Rh^{III} can lie between 308.0 to 312.2 eV, depending on the compound and chemical environment.[362]

The dip-coating process, followed by washing with toluene is believed to remove most of the unreacted dimer, which leaves primarily Rh^{III} cations on the surface. The thick evaporated layers of the dimer, on the other hand, are believed to mainly consist of unreacted dimers, where only a small fraction of them is expected to be oxidized to the cation monomer. Thus, differences in binding energies for the two Rh 3d components

between differently prepared samples presumably arise from large differences in the chemical environments. In the solution-processed monolayers of FTO, the dopant species are all in close proximity to the negatively charged oxide surface, while in the thick layers of evaporated dopants, most dopant species will be surrounded by neutral dopant molecules.

In the context of solution-processing of the rhodium-based dimer, also an alternative method was investigated employing the inexpensive reducing agent tetrabutylammonium borohydride (TBABH), which shall be briefly reported here.[108] TBABH was previously found to reduce the work function of gold by around 0.7 eV.[263] In principle, TBABH can be processed by dipping and washing similarly to the processing of $[RhCp^*Cp]_2$. Kelvin probe measurements (performed in air) of such modified FTO substrates show a reduction in work function by up to 0.6 eV. However, since TBABH has a very low melting point of 124-128 °C, this ammonium salt can be expected to easily sublime in vacuum (melting points and sublimation in vacuum are discussed in detail in section 7.1). It is likely that because of sublimation, UPS measurements of FTO samples dipped for 10 min in a 10 mM solution of TBABH in acetonitrile did not show any reduction in work function and XPS measurements did not show any signals attributable to TBABH (e.g. N1s and B1s core levels).

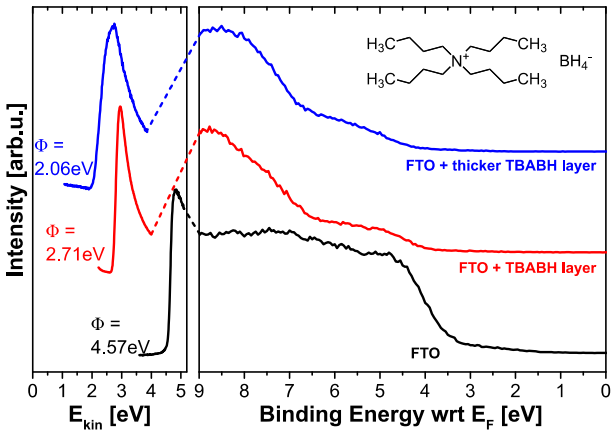

Figure 8.4 UPS spectra of FTO modified with drop-cast layers of TBABH of different thicknesses. The thicker TBABH layer (blue – drop-cast using 100µl) shows a decrease in work function of 2.5 eV, which is larger than the decrease in work function induced by the thinner layer (red – drop-cast using 20µl) of 1.9 eV. The sample marked in blue was assumed to be thicker than the other one (red), since no XPS signal of Sn 3d from the substrate could be observed, while it was easily observed for the other one. The inset shows the chemical structure of TBABH.

In order to show the general possibility of work function reduction by TBABH, thick multilayers were prepared by drop-casting TBABH solutions onto the FTO substrates and not washing the metal oxide with solvent. The thickness was varied by dropping different amounts (i.e. 20µl and 100µl) of 10 mM acetonitrile solution of TBABH. While AFM measurements were not performed, one layer can be assumed to be considerably thicker than the other, since XPS measurements showed no signal of the Sn 3d core level of the substrate for this layer, while it was easily observable for the other one. The UPS spectra of these films are displayed in Figure 8.4

[108] The price of organometallic dimers from Sigma-Aldrich (Merck KGaA) ranges around 300 € for 25 mg, which is in the order of 12 000 €/g, whereas TBABH can be purchased for around 10 €/g (as of 2018-09-14).

and show a reduction of the work function of FTO by 1.9 eV for the thinner and 2.5 eV for the thicker TBABH layer. However, the work function of TBABH modified FTO substrates as analyzed by UPS is stable over time and increases again. For the thinner layer, the work function increases from 2.7 eV to 3.2 eV within two days of storage in UHV, which is accompanied by a decrease of the C/Sn ratio, suggesting slow sublimation of the TBABH layer. For the thicker layer, the increase in work function is occurring at a slower rate, i.e. from 2.1eV to 3.0 eV in one month, while also after a month-long exposure in UHV, the Sn 3d core level was not observable via XPS. A deeper discussion of the modification of FTO with TBABH and its application in perovskite solar cells can be found in ref. [A9].

8.2 The Interface between Modified FTO and Organic ETMs

To understand how the dimer $[RhCp^*Cp]_2$ affects the energy level alignment at the FTO/ETM interface, vacuum-processible ETMs were used in order to avoid loss of the soluble dopant molecules during the deposition of the ETMs. As organic ETM, the vacuum-processable and nearly insoluble perylene derivative PTCBI is compared to the prototypical fullerene C_{60}. The electronic structure of C_{60} has been widely studied and its ionization energy (IE) and electron affinity (EA) were reported to be 6.4 eV and 4.0 eV, respectively.[88,207,255,363] However, since a complete description of the electronic structure of PTCBI is missing, it will at first be investigated in comparison to another perylene derivative, PTCDA, whose electronic structure has been previously reported.[100,363–368]

Combined UPS and IPES spectra of PTCBI and PTCDA are shown in Figure 8.5 a) and b), respectively. Since the resolution of the used IPES setup is very large (1.3 eV), the LUMO level onsets determined from the IPES spectra have to be corrected (see subsection 3.1.4 and appendix A). For this reason, the detail scans of the valence region were fitted with 3 and 2 Gaussian contributions for PTCBI and PTCDA, respectively. The width of the HOMO feature was determined to be 620-640 meV. Based on these values, the correction offset for the LUMO onsets was determined to be 700 meV (see appendix A for more details). From the HOMO and (corrected) LUMO level onsets, the IE and EA of PTCBI were determined to be 5.9 eV and 4.0 eV, respectively, yielding a transport gap of 1.9 eV as indicated in Figure 8.5 a). The measured IE is in good agreement with previously determined values of 5.8-6.2 eV.[369–371] For PTCDA, IE and EA were determined to be 6.6 eV and 4.1 eV, thus showing an energy gap of2.5 eV. Previously, IEs for PTCDA have been reported to lie in the range of 6.4-6.8 eV, which is in agreement with the hereby measured IE.[364–368] The reported EA of 4.1 eV and the reported transport gap of 2.5 eV are in very good agreement with the determined values, proving the validity of the used correction method for the LUMO level onset.[100,363] In addition, the optical gap of PTCBI is 1.5 eV [see Figure 8.7 b)] thus, PTCBI has an exciton binding energy of 0.4 eV, which is similar to the exciton binding

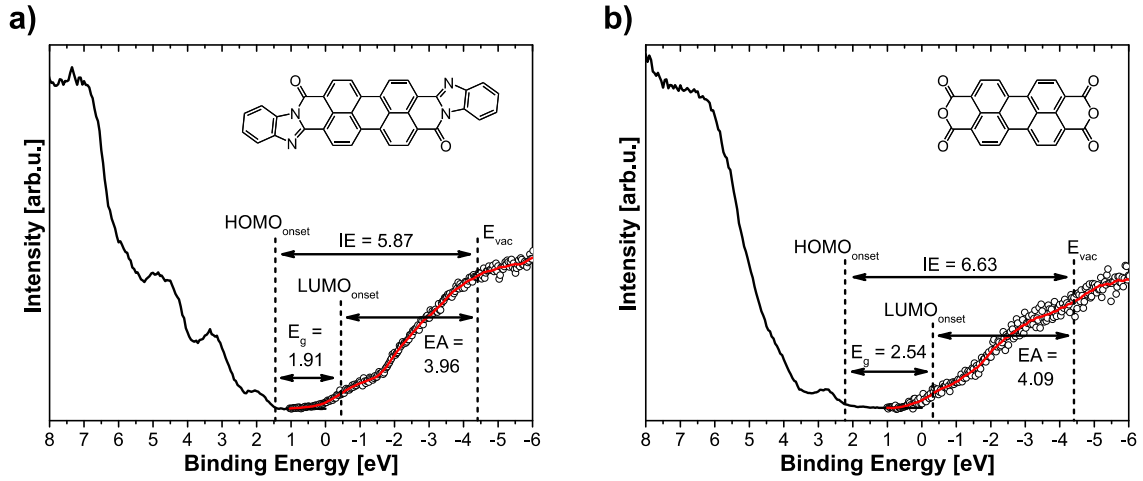

Figure 8.5 Combined UPS/IPES spectra of **a)** PTCBI and **b)** PTCDA. The inset shows the chemical structures of PTCBI and PTCDA, respectively. IPES data (circles) was smoothed for better visibility (red curve). The IE, EA and E_g for PTCBI and PTCDA were obtained from the UPS/IPES spectra, as indicated. Fig a) was published in ref. [A6].

energy of 0.3 eV reported for PTCDA.[100] The electron affinity of PTCBI is very similar to that of C_{60} (both around 4.0 eV). In addition, initial experiments showed that perovskite solar cells fabricated using PTCBI outperform devices fabricated using PTCDA. Therefore, the following discussion will be focused on PTCBI instead of PTCDA.

C_{60} and PTCBI were vacuum deposited onto clean FTO and on FTO modified by vacuum deposition of $[RhCp^*Cp]_2$. Figure 8.6 shows the recorded UPS spectra of FTO/ETM and FTO/$[RhCp^*Cp]_2$/ETM samples. Upon deposition of C_{60} and PTCBI, the work function of FTO (4.6 eV) decreases to 4.4 eV and 4.3 eV, respectively, which is related to the push-back effect. The IE of C_{60} is determined to be 6.2 eV, which is a bit lower, than the previously reported ionization energies of 6.4 eV (see above). The work function of the ETM layers on modified FTO, containing nominally 1 nm and 10 nm thick dimer interlayers, is further reduced and about 4.1 eV, which is close to the EA of both materials. The work function of the sample 1 nm $[RhCp^*Cp]_2$ + 5 nm C_{60} is lower than that 10 nm $[RhCp^*Cp]_2$ + 6 nm C_{60} due to the dependence of Fermi level pinning on the thickness of the organic layer(see subsection 2.1.4 and note the different thickness of C_{60} for these specific samples). The onsets of the HOMO levels are shifted to higher binding energy with respect to the HOMO onset of the ETM on clean FTO, in accordance with the shift of the Fermi level. Given the low WF of modified FTO of 3.6 eV and 3.3 eV, respectively, these results suggest Fermi level pinning at the LUMO of the ETM to take place, which results in the desired Ohmic contact between FTO and the ETM.

Given the effective ionization energy of the dimer of 2.8 eV and the high electron affinity of C_{60} and PTCBI of 4.0 eV, it can be expected that the dimer efficiently n-dopes both ETMs.

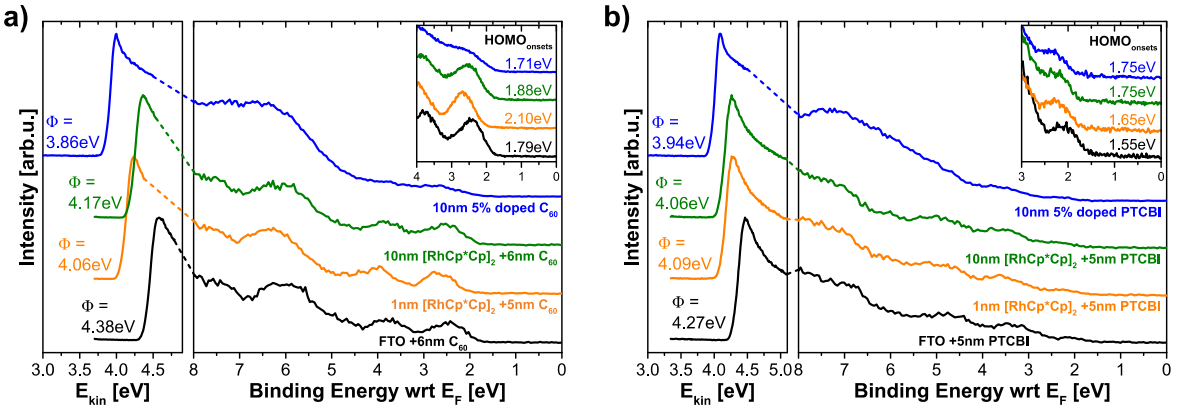

Figure 8.6 UPS spectra of **a)** C_{60} and **b)** PTCBI on (un-)modified FTO as well as 5% doped C_{60} and PTCBI, respectively. The insets show the detail scans of the HOMO level onsets. Depositing the ETMs on $[RhCp^*Cp]_2$ modified FTO leads to Fermi level pinning at the LUMO of the ETMs at around 4.1 eV. The valence features of the doped films are broadened and their work function is further reduced, both typical features of doping. Published in ref. [A6].

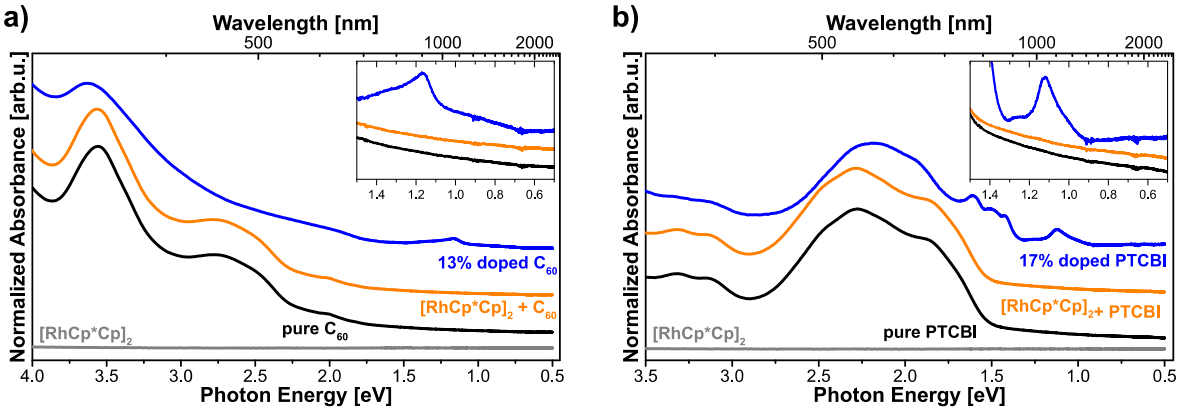

Figure 8.7 Optical absorption spectra of pure ETM, sequentially deposited $[RhCp^*Cp]_2$ + ETM, and doped ETM for **a)** C_{60} and **b)** PTCBI. The insets show an enlarged view of the NIR region from 0.5 to 1.5 eV. $[RhCp^*Cp]_2$ shows no absorption in the investigated range (its absorption starts at around 4.5 eV). Doped C_{60} shows a new absorption feature in the optical gap at 1.16 eV, which is associated with the C_{60} anion by comparison with literature.[192] Doped PTCBI shows a similar feature at 1.11 eV, which, accordingly, is attributed to the PTCBI anion. In contrast, the sequentially deposited films show no absorption in the NIR range.

To show that the dimer does indeed n-dope both ETMs, mixed thin films were prepared via co-evaporation of the dimer and the respective ETM. The dopant concentrations were calculated from the evaporation rates to be around 5%.[109] UPS spectra of the co-evaporated films are also shown in Figure 8.6 (blue lines). The doped films show a further reduction of the work function to 3.9 eV and a broadening of the valence band features, which are typical signatures of doping. In addition, UV/Vis/NIR spectra of doped C_{60} (13%) and PTCBI (17%) deposited on quartz glass show new features emerging in the optical gap

[109] Dopant concentrations are given here as molar concentrations with respect to the dimer, not the monomer. To obtain the dopant concentrations with respect to the monomer units, the given concentrations just have to be doubled.

of the materials, as shown in Figure 8.7. The new transition in the doped C_{60} film at 1.16 eV (1065 nm) is attributable to the C_{60} anion.[192] A similar feature is found for PTCBI at 1.11 eV (1120 nm) and in accordance is attributed to the PTCBI anion. These results clearly show the ability of the dimer to efficiently n-dope both C_{60} and PTCBI. Thus, it can be expected that ETM molecules near the interface of modified FTO will be n-doped by unreacted dimers and diffusion of the dimers into the ETL might be possible. However, the UV/Vis spectra of sequentially deposited films of 10 nm $[RhCp^*Cp]_2$ + 25 nm ETM on quartz glass (also shown in Figure 8.7) exhibit no visible absorption features in the NIR region, in contrast to the spectra of the doped ETM films. For this reason, it can be assumed that diffusion of the dimer into the ETL upon deposition of the organic film is only very minimal and probably limited to only the direct interface between dimer and ETM (a further discussion on diffusion is presented in the next subsection).

XPS detail scans of the Rh 3d region are shown in Figure 8.8. In accordance with the UV/Vis/NIR spectra shown in Figure 8.7, the Rh 3d spectra of the bilayer samples consist mainly of Rh^{I} associated with unreacted dimers, as can be seen in Figure 8.8 a), b), d), and e). These results are very similar to the results of the vacuum deposited dimer on FTO shown in the previous section. Here, however, the Rh^{III}/Rh^{I} ratios shown in Table 8.3 are smaller than the ones of the neat dimer films on FTO, but are in the same order of magnitude, at least for the PTCBI samples. This might be related to the much smaller signal-to-noise ratio (SNR) of the scanned regions and the fact, that the regions had to be corrected for a background before deconvolution (see experimental section 4.4 as well as Figure B.3 in appendix B). Additionally, ARXPS measurements were performed at 45° and 60° relative to normal emission, in order to effectively increase the thickness of the sample by a factor of 1.41 and 2, respectively. However, the obtained changes in the area ratios were inconclusive, probably due to the high surface roughness of FTO (15 nm) and shall thus not be discussed here.

In contrast to the assignment of Rh 3d of the sequentially deposited films, the main features of the Rh 3d regions of the co-evaporated films [Figure 8.8 c) and f)] are attributed to belong to Rh^{III} associated with monomer cations, since the UV/Vis/NIR spectra shown in Figure 8.7 exhibit absorption features of the ETM anions. The deconvolution of these regions reveal only little unreacted dimers to be present, i.e. 4.6% for doped C_{60} and 2.5% for doped PTCBI. Furthermore, the determined area ratios of Rh/C for doped C_{60} and Rh/N for doped PTCBI displayed in Table 8.3 can be used to calculate the dopant concentrations based on their stoichiometry, which are 10% and 8%, respectively.[110] The calculated dopant concentrations are in reasonable agreement with the dopant concentrations calculated from the evaporation rates of around 5%.

[110] For the dopant concentration of C_{60}, it has to be considered that the dimers also contribute to the C 1s peak. This can be easily done by calculating the appropriate area of C 1s related to the dimer with respect to the area of the Rh 3d peak and subtracting it from the total C 1s area to receive the area of C1s related to C_{60}.

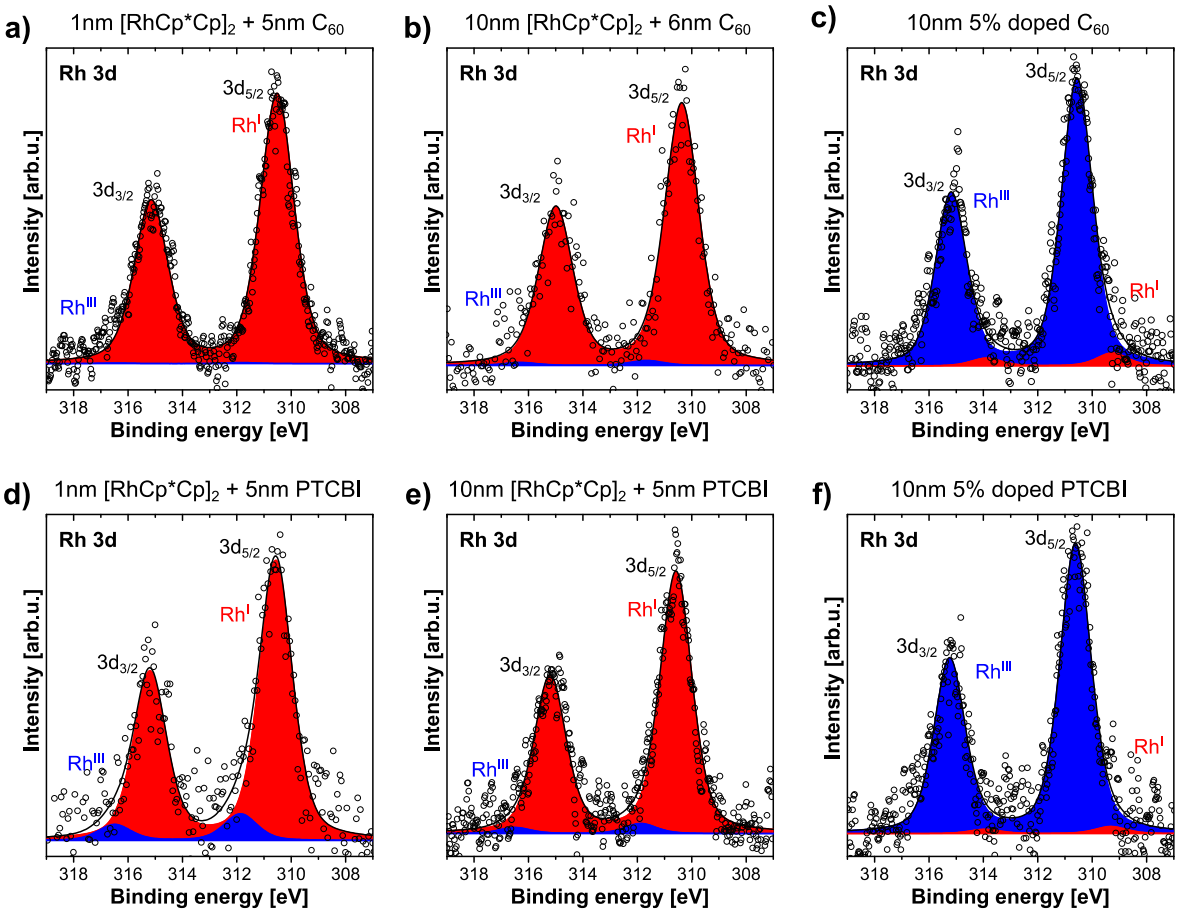

Figure 8.8 XPS detail scans of the Rh 3d region of 1/10 nm $[RhCp^*Cp]_2$ + 5 nm ETM (**a**, **b**, **d**, **e**) as well as of the 5% doped ETM films (**c**, **f**). While the major component of Rh 3d of the sequentially deposited films belongs to the unreacted dimers (Rh^I – red) in accordance with the Rh 3d spectra found for the dimers on FTO, the major component of the doped films belongs to the monomer cations (Rh^{III} – blue) in accordance with the Rh 3d spectra of the monomer cation monolayers. Published in ref. [A6].

Table 8.3 XPS binding energies and peak area ratios for the pure ETM, sequentially deposited $[RhCp^*Cp]_2$ and ETM, and 5% doped ETM films. All values are in eV (except ratios). For the last column (Rh/X), X denotes C for C_{60} and N for PTCBI. From these ratios, the dopant concentration of the doped film can be calculated, which are 10% for C_{60} and 8% for PTCBI, which is in reasonable agreement with the nominal value. Published in ref. [A6].

	C 1s	N 1s	Rh^I $3d_{5/2}$	Rh^{III} $3d_{5/2}$	Rh^{III} / Rh^I	Rh / X
6 nm C_{60}	285.22	--	--	--	--	--
1 nm Rh + 5 nm C_{60}	285.41	--	310.52	311.82	0.004	4×10^{-3}
10 nm Rh + 6 nm C_{60}	285.28	--	310.36	311.66	0.02	2×10^{-3}
5% doped C_{60}	285.38	--	309.26	310.56	21.8	3×10^{-3}
5 nm PTCBI	285.23	398.90	--	--	--	--
1 nm Rh + 5 nm PTCBI	285.30	398.98	310.57	311.87	0.10	3×10^{-2}
10 nm Rh + 5 nm PTCBI	285.29	398.96	310.58	311.88	0.04	2×10^{-2}
5% doped PTCBI	285.30	398.98	309.32	310.62	40.6	4×10^{-2}

The conflicting assignment of the Rh 3d features at 310.6 eV to belong to Rh^{I} in one case and Rh^{III} in the other (despite the position of the other species being very similar – see Table 8.3), can be resolved considering again different chemical environments of the respective species. This is closely related to the assignment of Rh^{I} and Rh^{III} features of solution-processed monolayers and co-evaporated thick multilayers, as presented in the last subsection. In the co-evaporated films the ionized dopant species will likely be in close proximity to both neutral and negatively charged ETM molecules, while in the thick films (both with and without ETM overlayer), most dopant species will be surrounded by neutral dopant molecules. As explained previously, the different chemical environment is believed to have a similar influence on the binding energy as the change in oxidation state does. Additionally, the assignment is in-line with the other results presented in this section.

8.3 Diffusion of Dimers into the Organic Layers

To study the possible diffusion of $[RhCp^*Cp]_2$ in to the ETM, the sequentially deposited films of 10 nm $[RhCp^*Cp]_2$ and 25 nm ETM on quartz glass were sequentially annealed at increasing temperatures and their optical absorption measured. Due to light scattering in the thin films, the optical absorption spectra exhibit a background in the NIR region (as can be seen in the insets in Figure 8.7), which increases with increasing photon energy. Since the background hinders the observability of features related to ETM anions, the spectra were corrected for a background assuming Rayleigh scattering (for details see experimental section 4.4). The background corrected spectra of the NIR region of 1.0 to 1.5 eV are displayed in Figure 8.9. Since the measurement box used to conduct these experiments under inert atmosphere shows no absorption features in the region 1.04 to 1.44 eV (see Figure B.4 in appendix B), features in this region can be reliably assigned to sub-gap transitions of the samples.

Figure 8.9 shows that directly after deposition, both films exhibit no visible absorption features in the NIR region. Assuming the 10 nm thick dimer layer would completely diffuse into the 25 nm thick ETL, a dopant concentration of 20-30% would be expected for such a layer, which should show absorption features in the NIR region of similar intensity than the co-evaporated films.[111] However, upon sequentially heating the samples at 100 °C, 150 °C, 185 °C and 200 °C for at least 60 min each time, NIR absorption features similar to those of doped films appear in this region and thus can be assigned to belong to ionized ETM

[111] The dopant concentration c can be calculated taking into account the density ρ and molecular mass M of the involved molecules and the thickness d of the respective layers. The densities and molecular masses are 1.55 g/cm^3 and 638.5 g/mol for the dimer, 1.54 g/cm^3 and 720.6 g/mol for C_{60}, and 1.70 g/cm^3 and 536.5 g/mol for PTCBI, respectively. The molar ratio N_H/N_D between host and dimer can then be calculated via $N_H/N_D = \rho_H d_H/M_H \cdot M_D/\rho_D d_D$. Following c is calculated from the ratio via $c = 1/(N_H/N_D + 1)$.

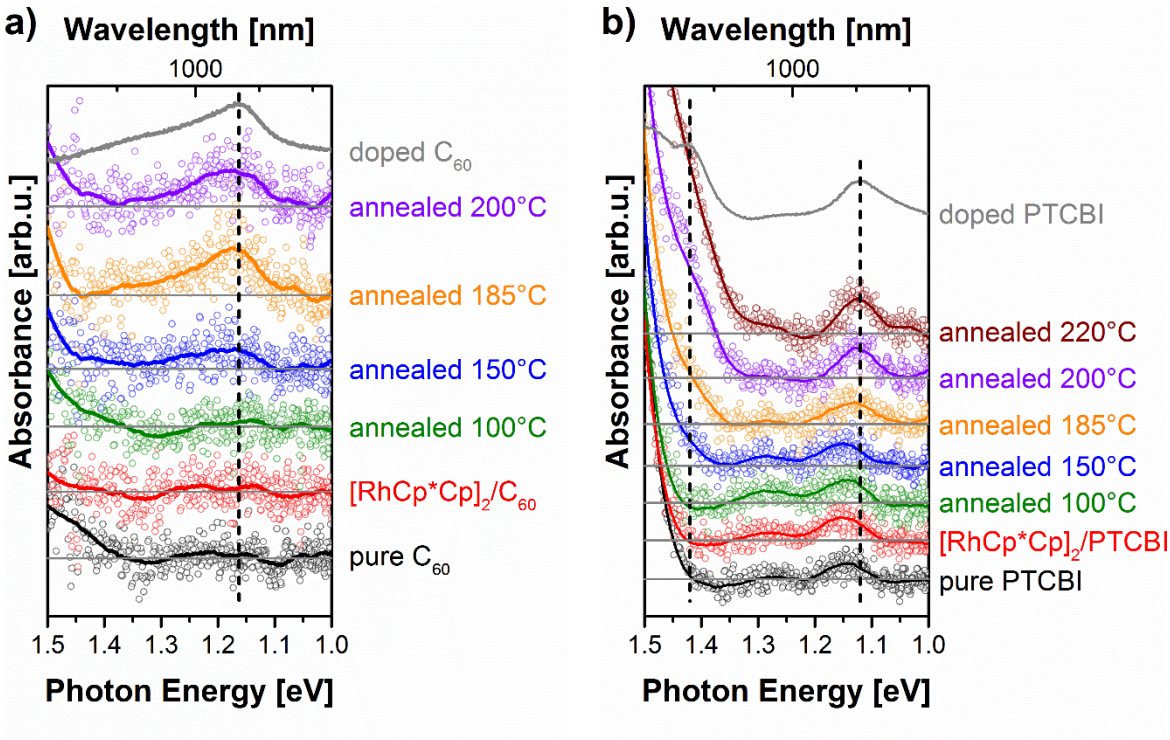

Figure 8.9 Background corrected NIR absorption spectra of sequentially deposited $[RhCp^*Cp]_2$ and ETM at increasing annealing temperatures for **a)** C_{60} and **b)** PTCBI. The data (circles) was smoothed (line) for better visibility. As can be seen from the spectra, annealing leads to the appearance of NIR absorption features which are very similar to those of the doped ETM films. Published in ref. [A6].

molecules. These features maximize at 185 °C for C_{60} and 200 °C for PTCBI, and further annealing at higher temperatures does not increase the intensity of the absorption features. A formal dopant concentration[112] of these films can be estimated using the intensity of the anion features as follows. Since the absorbance A is proportional to the total number of molecules N within the film, with ϵ being the extinction coefficient and d the thickness of the film,

$$A = \epsilon d \propto \epsilon N \,, \tag{8.1}$$

the dopant concentration c can be expressed as

$$c = \frac{N_{H^-}}{N_H + N_{H^-}} \approx \frac{N_{H^-}}{N_H} = \frac{\epsilon_H A_{H^-}}{\epsilon_{H^-} A_H} \,, \tag{8.2}$$

where the subscript H denotes the ETM molecule and H^- the ionized ETM molecule. By comparing the intensities of the optical features, the intensity ratios f can be calculated,

$$A_{H^-}^{bi} = f_1 \cdot A_{H^-}^{co} \quad and \quad f_2 \cdot A_H^{co} = A_H^{pure} \,, \tag{8.3}$$

[112] Here, "formal" means that the dopant molecules are assumed to be homogenously dispersed throughout the organic layer. While there is a gradient of diffused dopants expected to occur, the formal concentration is used to receive information about the relative number of diffused dopants.

where the superscripts bi, co, and pure denote the sequentially deposited (bilayer), doped (co-evaporated) and pure ETM films, respectively. Combined with the heights of the ETM layer of the pure $d_{\mathrm{H}}^{\mathrm{pure}}$ and sequentially deposited film $d_{\mathrm{H}}^{\mathrm{bi}}$ measured by AFM (see later), the formal dopant concentration c_{bi} can thus be estimated via

$$c_{bi} \approx \frac{f_1}{f_2} \frac{d_H^{pure}}{d_H^{bi}} c_{co} \,, \tag{8.4}$$

where the dopant concentration of the doped c_{co} films is used, which was calculated from the evaporation rates. Here, the thickness of the ETM layer of sequentially deposited film is assumed to mainly consist of neutral ETM molecules. The appearance of the NIR absorption features, thus, corresponds to an increase in formal dopant concentration from 0% to 0.6% for C_{60} and 1% for PTCBI. This increase suggests that diffusion of the dimer into the ETL upon deposition of the organic film is only very minimal and probably limited to only the direct interface between dimer and ETM, while annealing promotes the reaction of the dimer with the ETM molecules, possibly also allowing limited diffusion of the bulky dimer into the organic layers.

AFM measurements of the samples were performed after the annealing experiment.[113] The obtained images of the pure, doped and sequentially deposited C_{60} films are displayed in Figure 8.10. The AFM images of pure C_{60} [Figure 8.10 a)] show a very smooth surface with an RMS roughness of around 1 nm. Doped C_{60} [Figure 8.10 b)] exhibits a morphology, very similar to undoped C_{60} with nearly the same surface roughness. The image of the sequentially deposited $[RhCp^*Cp]_2$ + C_{60} film in Figure 8.10 d, however, shows a completely different morphology. Here, the film consists of islands with a layer in between them. The surface in between the islands shows a morphology similar to that of C_{60} and the roughness of this surfaces is in the order of 1-2 nm. This points towards a growth mode of the sequentially deposited film, where first $[RhCp^*Cp]_2$ grows in islands on the quartz substrate [see Figure 8.2 c)] and afterwards the C_{60} layer grows in between the islands, as shown in a simple schematic in Figure 6.2 d). The height of the layer in between the islands was measured to have a thickness of 22 nm. The AFM images of PTCBI show in principle the same behavior, however, the image quality is poor, because PTCBI has a high sticking coefficients and, thus, PTCBI molecules tend to easily attach to the AFM tip, which leads to artefacts and distortions of the image.

A grain analysis shows the film displayed in Figure 8.10 c) to have a density of 0.48 islands/µm^2 with the islands having an average height of around 100 nm (in reference to the surface in between the islands) and an average diameter of 300 nm. Assuming the

[113] Since the n-doped films were considered to be highly air-sensitive and AFM measurements could only be conducted in air, it was not possible to perform the AFM measurements in between the annealing steps. This slightly limits the explanatory power of the following discussion.

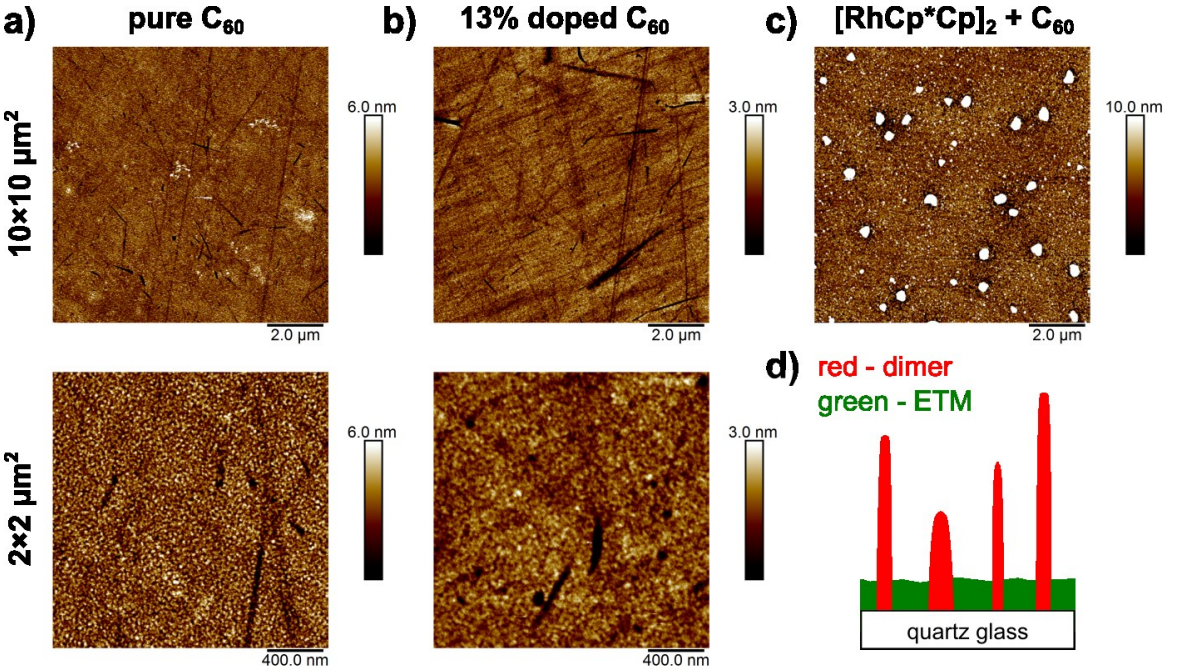

Figure 8.10 AFM images of **a)** pure C_{60}, **b)** 13% $[RhCp^*Cp]_2$ doped C_{60}, and **c)** sequentially deposited $[RhCp^*Cp]_2$ + C_{60} (after annealing). While both pure and doped C_{60} show a very smooth surface with a RMS roughness of around 1 nm and a very similar morphology, the sequentially deposited film shows a completely different structure. Here, the film consists of islands with an average height of 100 nm and a layer between the islands. Since this layer shows a similar morphology to pure C_{60} and has a RMS surface roughness of around 1-2 nm, it was concluded that first the dimer grows in islands and the afterwards deposited ETM as layer between the islands. **d)** From AFM image deduced growth mode of sequentially deposited $[RhCp^*Cp]_2$ + ETM on quartz glass.

islands to be cylinders, the whole volume of the islands (including the thickness of the layer in between the islands) is 0.4 μm^3, which leads to an effective thickness (flat, homogenous layer of 100 μm^2 size) of 4 nm. This effective thickness is in the same order of magnitude as the nominal thickness of the $[RhCp^*Cp]_2$ layer of 10 nm, which is a further indication of the assumed growth mode. However, this growth mode has implications on the size of the interface between $[RhCp^*Cp]_2$ and the ETM. Taking the parameters of the grain analysis, the effective interface of this growth mode is only in the order of 1% of the interface of two flat layers on top of each other.[114] As consequence, the formal dopant concentration of a sequentially deposited film growing in a bilayer structure [like it was assumed for FTO, see Figure 8.2 c)] could be higher than the here found 1% (after annealing), but should still be mostly limited to the vicinity of the interface.

[114] To increase the significance of this discussion, a full AFM study on FTO would need to be conducted, where all samples are measured in inert atmosphere before and after each annealing step. This was, however, not possible with the used setup and was also deemed to be unnecessary, since the optical absorption spectra show the principal possibility of interface doping and diffusion of the dimers into the organic layer.

8.4 Application in Perovskite Solar Cells

To evaluate the electrical consequences of modifying the electron-selective contact in PSCs by introducing an interlayer of $[RhCp^*Cp]_2$ between the FTO electrode and the ETM, n-i-p PSCs were fabricated. In addition, the ability of PTCBI to be used as ETM in PSCs was investigated in comparison to C_{60}. PSCs were fabricated by Federico Pulvirenti and shall thus only be discussed briefly at this point. Further details and discussions can be found in his doctoral thesis and ref. [A6].

The used device architecture consists of FTO (bare or modified with 10 nm of $[RhCp^*Cp_2]$) + ETM (C_{60} or PTCBI) + $CH_3NH_3PbI_3$ + spiro-OMeTAD + Ag. Table 8.4 summarizes the average device parameters for PSCs with vacuum processed $CH_3NH_3PbI_3$. PSCs containing non-modified FTO and PTCBI as ETM exhibit similar short circuit currents (j_{SC}) and fill factors (FF) as similar devices containing C_{60} as ETM. However, they also exhibit slightly lower open-circuit voltages (V_{OC}), which leads to lower power conversion efficiencies (PCE). While the stabilized power conversion efficiency[115] (η_{MPP}) for the cells containing C_{60} was even slightly higher than the PCE, η_{MPP} of the cells containing PTCBI was lower than the respective PCE. Upon introduction of the $[RhCp^*Cp]_2$ interlayer, η_{MPP} of the PTCBI cells greatly improves from an average of 6.8% to 9.2%, while also the PCE improves from 8.6% to 10.4%. This increase in PCE is due to an increase in j_{SC} and FF, suggesting that the quality of the

Table 8.4 Average device performance parameters of PSCs containing an evaporated active perovskite layer. While the introduction of an interlayer greatly improves the efficiency of devices containing PTCBI as ETM, the effect is negligible for devices containing C_{60}. Five devices were averaged per parameter. Data kindly provided by Federico Pulvirenti. Published in [A6].

	j_{SC} [mA/cm²]	V_{OC} [mV]	FF [%]	PCE [%]	η_{MPP} [%]	R_{sh} [Ωcm²]
C_{60}	17.1 ± 0.3	988 ± 6	55 ± 1	9.3 ± 0.3	9.5 ± 0.4	133 ± 6
$[RhCp^*Cp]_2$ + C_{60}	17.5 ± 0.2	994 ± 5	59 ± 1	10.1 ± 0.3	10.0 ± 0.3	245 ± 14
PTCBI	17.4 ± 0.8	928 ± 21	54 ± 1	8.6 ± 0.7	6.8 ± 0.8	147 ± 19
$[RhCp^*Cp]_2$ + PTCBI	19.9 ± 0.2	935 ± 7	56 ± 1	10.4 ± 0.1	9.2 ± 0.1	190 ± 20

Table 8.5 Device performance parameters of the best performing PSCs containing a solution processed active perovskite layer. While the introduction of an interlayer improves the performance of the cells containing PTCBI, they are still outperformed by the cells containing only C_{60} without an interlayer. Data kindly provided by Federico Pulvirenti. Published in ref. [A6].

	j_{SC} [mA/cm²]	V_{OC} [mV]	FF [%]	PCE [%]	η_{MPP} [%]
C_{60}	22.3	1070	68	15.7	16.0
PTCBI	22.2	1040	61	13.7	12.7
$[RhCp^*Cp]_2$ + PTCBI	20.1	1070	67	14.6	14.2

[115] The stabilized power conversion efficiencies were measured by holding the devices at the voltage of the maximum power point determined from their J-V characteristics for 50s.

FTO/ETM interface is improved. For the cells containing C_{60}, the PCE and FF was found to only increase slightly and the increase in η_{MPP} is negligible. In addition, introduction of the interlayer lead to a higher shunt resistance (R_{sh}) in both cases.

Furthermore, PSCs were fabricated by solution processing the active layer $CH_3NH_3PbI_3$ from a methylamine/acetonitrile precursor solution and the perovskite layer was annealed for 60 min at 100 °C to ensure its full crystallization. Both ETMs are insoluble in methylamine/ acetonitrile,[A6] which prevents the formation of pinholes in the ETL during the deposition of the active layer. In the case of $[RhCp^*Cp]_2$-modified FTO, annealing the devices promotes interfacial doping and limited diffusion of the dopants into the ETL, as it was shown in the last subsection. The device parameters of the best devices, achieved with optimized processing conditions, are summarized in Table 8.5. For PTCBI, η_{MPP} can reach up to 12.7% which is further increased to up to 14.2% when modified FTO is used. Here, the increase mainly results in a drastic increase in FF from 61% to 67%, while at the same time j_{SC} is slightly decreased. Here, the increase in FF is larger than the one found for the evaporated cells summarized in Table 8.4. While in both cases, modification of FTO leads to Ohmic contacts, it can be assumed here that the level of interfacial doping is increased in the solution processed devices due to the additional annealing step. However, even with the modified FTO/ETM interface the stabilized power conversion efficiency of PTCBI is still lower than the one of C_{60} of 16% without FTO modification.[116] The fact, that the solution processed cells exhibit much larger efficiencies than evaporated cells is, however, not fully understood yet.

8.5 Summary

In summary, it was shown that vacuum deposition of $[RhCp^*Cp]_2$ on FTO effectively decreases the work function of FTO by up to 1.3 eV. This decrease in work function is associated with an electron transfer from the dimers to the electrode, which leads to the formation of monomer cations on the metal oxide surface and introduces an interfacial dipole. In addition, multilayers of unreacted dimers are still present, which can later react with sequentially deposited ETMs. Alternatively, FTO can also be modified by solution processing the dimer, leading to comparable work function reductions. In contrast to vacuum sublimation, solution processing leads to the formation of only a layer of monomer cations with little unreacted dimers being present. Another method to effectively decrease the work function of FTO involves the inexpensive reducing agent TBABH, which can lead to a similar decrease in work function, but was found to be only somewhat durable in UHV when processed as thick layer via drop-casting.

[116] Solution processed cells containing modified FTO and C_{60} were, however, not fabricated.

Furthermore, the electronic structures of PTCBI and PTCDA were studied, which were found to a have very similar electron affinities to C_{60} and thus could replace C_{60} as ETM in PSCs. Devices built on PTCBI outperformed devices built on PTCDA, therefore the investigation focused on PTCBI as compared to C_{60}. When C_{60} and PTCBI are deposited on top of modified FTO, the Fermi level gets pinned at the LUMO of the ETM leading to the formation of Ohmic contacts. In addition, unreacted dimers at the interface can n-dope the ETM molecules in the direct vicinity of the interface. The ability of $[RhCp^*Cp]_2$ to effectively dope both ETM materials was confirmed by optical absorption and UPS measurements on co-evaporated samples. Moreover, it was shown that annealing of sequentially deposited samples increases the level of interfacial doping and can even lead to moderate diffusion of the dopants into the organic layer.

Perovskite solar cells based on PTCBI as ETM show higher stabilized power conversion efficiencies, when $[RhCp^*Cp]_2$-modified FTO electrodes are used as electron selective contacts. Here, the introduced Ohmic contact and interfacial doping of the ETM leads to a minimization of electron collection losses and thus a better device performance. However, the PTCBI containing PSCs are still outperformed by PSCs containing C_{60} as ETM fabricated under comparable conditions. In contrast to PTCBI containing PSCs, the introduction of the $[RhCp^*Cp]_2$ interlayer leads to only negligible increases in efficiency for C_{60} containing PSCs. Nonetheless, this study indicates PDI derivatives to be suitable materials for use as ETMs in PSCs and shows the potential of using modified Ohmic contacts to increase device performance.

9 CONCLUSION AND OUTLOOK

The aim of the work presented in this thesis was to contribute to a better understanding of the mechanisms and processes involved in the molecular doping of organic semiconductors. For this reason, primarily ultraviolet, X-ray, and inverse photoelectron spectroscopy (UPS, XPS and IPES, respectively) were employed to elucidate the electronic structure of doped thin films as well as chemical and doping induced shifts of the core levels. With nearly the same importance, optical absorption spectroscopy measurements were performed to qualitatively and quantitatively identify neutral and ionized species in mixed solutions as well as in doped thin films. Furthermore, current-voltage (IV) measurements were conducted to track changes in conductivity upon doping and scanning force microscopy (SFM) was used to analyze the changes in thin film morphology. These experimental techniques were employed to study a variety of different topics related to the molecular doping of organic semiconductors. The topics ranged from i) the question which experimentally determined energy level values should be used to guide host-dopant selection, over ii) the n-doping of a p-type polymer, iii) the first indication of bipolaron formation in the polymer P3HT employing molecular dopants, and finally, iv) the application of with organometallic n-dopants modified electrode contacts in perovskite solar cells.

Ad i)

In the first part, the practicality of two different material parameters to predict ion pair formation in molecular doping was explored. In general, the energy levels of organic semiconductors can be determined via redox-potentials measured by cyclic voltammetry (CV) in solution or via solid state ionization energies (IE) and electron affinities (EA) measured by UPS/IPES on solid thin films. Three different sets of host-dopant material pairs were investigated, where the redox-potentials and the IE/EA data sets predicted different yields of ion pair formation. Here, each material pair consisted of a planar material component and one with a non-planar but rather bulky three-dimensional structure. These combinations were chosen in order to minimize the possibility of ground-state charge transfer complex (CPX) formation, since CPX formation is known to occur between different molecules with a planar structure, which allow an overlap of the involved frontier orbitals.[24,155,328] The results from optical absorption spectroscopy measurements of all three systems clearly showed that using IE and EA values from UPS/IPES does not allow a reliable estimation on whether IPA is likely to occur for a given material pair, whereas CV data are able to provide a reasonable prediction. These findings were attributed to the CV data revealing characteristics on the molecular scale that are relevant for IPA formation in mixed semiconductor-dopant films. This is most likely due to CV probing nearly isolated

molecules. In addition, ionic species are more stabilized in polar solvents (containing electrolytes) than in neutral solids, which approximately models the mutual Coulombic stabilization of oppositely charged molecules in doped films. In contrast, UPS/IPES data include surface and collective electrostatic sample properties on and above the meso-scale that are not reliable parameters for dopant selection. The molar mixing ratio of 1:1 investigated in this study is far from conditions employed in devices, where dopant concentrations of a few mole-percent are used (IPA formation yield and thus doping efficiencies are correlated with mixing / dopant concentrations). Nonetheless, the findings can also be applied for devices as they provide information about the general feasibility of IPA formation.

In conclusion, it is recommended to evaluate IPA formation yield, hence doping efficiency and electrical properties, of doped organic semiconductors with respect to both, redox-potentials from CV and IE/EA values from UPS/IPES. Here, it should be fully taking into account how each method has shortfalls in accounting for the actual physical environment (e.g. dielectric constant) and the Coulombic interaction between the oppositely charged ions within the doped film. In this study each material pair always consisted of one planar component, the IE/EA of which is likely significantly affected by strong polar and/or π-π intermolecular interactions leading to the huge differences in IE/EA and the redox-potentials. To further generalize the results of this study, also material pairs have to be investigated where both components have a bulky three-dimensional structure, but IE/EA and redox-potentials still predict different IPA yields. Another interesting question involves the dependence of doping efficiency on the 3D structure and size of the dopant molecule. Here, it should be investigated whether the increase in dopant size (by e.g. substitution of side-groups like alkyl-chains), while keeping the energy levels nearly constant, can decrease the Coulomb binding energy of the host-dopant ion pair and thus lead to the increase of free charge carriers.

Furthermore, only the ionization efficiency was investigated, whereas for applications the doping efficiency, i.e. the yield of actual free charge carriers per number of dopant molecules, is of more importance. Thus, a next step to further improve the understanding of molecular doping and its application in organic electronic devices would be to systematically investigate the relation between ionization and doping efficiency as well as the influence of the energy levels of the neutral as well as ionized species. A first step in this direction was recently reported, where molecular doping was explained to be a two-step process consisting of single-electron transfer between host and dopant molecules (hence ionization) and a subsequent dissociation of the Coulombic bound ion pair.[372] For the investigated systems, it was shown that the dissociation energy is in the order of only a few 10 meV despite the actual Coulomb binding energy of the ion pair being in the order of several 100 meV, which was claimed to result from energetic disorder within the

semiconductor film. However, more systems need to be studied as well as weaker dopants to be included in order to further prove this hypothesized model.

Ad ii)

In the second part, the n-doping of the p-type polymer IDT-BT with organometallic dimers was investigated. It was shown that IDT-BT can be rendered n-type upon doping. This was observed by the formation of negative polarons upon doping and the continuous shift of the Fermi level away from the valance band with increasing dopant concentration, which at a dopant concentration of around 10% was pinned near the conduction band onset. Furthermore, upon doping an increase in n-type conductivity by several orders of magnitude was observed, while at the same time the p-type conductivity was found to decrease. However, the approach to achieve n-type transport in OFETs consisting of doped IDT-BT layers was not yet successful. Moreover, it was discovered that the n-type doping in thin films cast from solution is not stable over time and the doping-induced n-type conductivity is decreasing again over two orders of magnitude within a few days stored under ideal inert conditions. This instability of the doped system was related to the presence of residual water (and oxygen) leading to degradation of the formed negative polarons.

From the presented results, it can be concluded that, while n-type doping of low EA polymers is generally possible, great care needs to be taken in removing residual water, e.g. from the polymer powder before preparation of a polymer solution, and shielding the doped film from water and oxygen by e.g. proper encapsulation. Such procedures should in general result in stable n-doping of polymer films, since in one of our recent studies we were able to show successful and stable n-doping of a low EA molecule with organometallic dimers. Here, the doped films were fabricated via co-evaporation and thus incorporation of residual water molecules can be expected to be very low.[A4] Furthermore, other preparation techniques like sequential processing might lead to less water incorporation. In sequential processing, the dopant is deposited either from solution or by thermal evaporation subsequent to the preparation of the polymer film and doping is achieved via diffusion of the dopant into the film. Here, residual water could be removed from the pristine polymer film by an annealing step subsequent to spin-coating of the polymer. Another strategy to achieve highly conductive n-type polymer layers with low EA would involve the development of dopants or additives, which are actually not strong enough to create negative polarons within the polymer, but only passivate the trap states caused by oxygen/water complexes.

Ad iii)

In the third part, the p-doping of the polymer P3HT with the recently developed organic salt $Mes_2B^+[CFB4]^-$ was investigated via a multi-experimental approach. The general doping

mechanism of the ionic salt involves electron transfer from P3HT chains to the cation Mes_2B^+ and a stabilization of the formed positive polarons (and bipolarons) by the weakly coordinating counteranion $[CFB4]^-$. The hereby created neutral radical $MesB^\bullet$ is most likely reacting via hydrogen abstraction to form the dimer $[Mes_2BH]_2$, which, at least under UHV conditions, was found to be no longer present in the doped P3HT films.

Strong evidence was provided that upon high dopant concentrations above 10% bipolarons are forming in P3HT. The most striking indication of bipolaron formation was provided by EPR spectroscopy. Here, the determined number of unpaired spins was found to linearly increase with increasing dopant concentration till around 10% proving the formation of polarons. For higher concentration, however, the number of unpaired spins is decreasing again, which is consistent with the transition of polarons to spinless bipolarons. This formation of bipolarons was shown to lead to new optical transitions at 1.8 eV and 2.1 eV, which have never been reported for P3HT so far. The observed transitions are, however, in conflict with previously reported optical spectra of bipolarons in P3HT. This conflict could not satisfactorily be completely resolved. The main assumption is that the previously reported optical spectra of highly doped P3HT do not show bipolaronic behavior but rather a metallic like state of the polymer. Continuing, mono-chromatized UPS measurements showed a strong depletion of the delocalized π-band near the Fermi level indicating a significant increase in hole density. This was accompanied by a strong increase of the ionization energy from 4.7 eV of pristine P3HT up to 5.4 eV for 35% doped P3HT. Consistent with the optical and EPR results, XPS detail scans of the sulfur core levels revealed the emergence of polaronic and bipolaronic components upon doping. For low dopant concentrations up to 5%, a component associated to polaron formation emerges at 0.4 eV higher binding energy than the neutral component. Starting from 10% dopant concentration, a third component at 2.0 eV higher binding energies was observed, which was associated to the formation of bipolarons. By a detailed comparison between the EPR results and the deconvoluted XPS spectra, it was concluded that bipolaron formation also leads to contributions to the formerly polaronic and neutral components. However, further theoretical support is needed in order to make more accurate predictions about polaron / bipolaron formation based on the XPS measurements.

Surprisingly, upon air-exposure a back-transition from bipolarons to polarons was found to be occurring. This transition sets in rapidly within the first few minutes of air-exposure. The conductivity of a mainly polaronic sample (2% dopant concentration) is only increasing slowly upon air-exposure, which is associated with oxygen doping of the P3HT. In contrast, the conductivity of a mainly bipolaronic sample (25% dopant concentration) increases rapidly over two orders of magnitude after air-exposure. After long time exposure over a few days, the conductivity of the formerly bipolaronic sample increased to nearly the same level as the 2% doped sample. This finding indicates bipolaronic charge carriers to be less

mobile than polaronic ones. So far, however, it is unclear why air-exposure induces a transition from bipolarons to polarons and the involved mechanisms have to be explored by future experiments. Moreover, it was not tested if the transition is reversible and if by storing the samples again in inert atmosphere or even exposing them to UHV leads to the re-formation of bipolarons. This process might be possible, since it is known that the p-doping of P3HT with oxygen is (at least partially) reversible.[350,351] Nonetheless, due to the facts that bipolarons can be formed in P3HT via doping with $Mes_2B^+[CFB4]^-$ and that air-exposure leads to a back-transition from bipolarons to polarons, this system is predestined for further studies about the different behavior and characteristics of polaronic and bipolaronic charge carriers. Moreover, the actual doping strength of $Mes_2B^+[CFB4]^-$ has yet to be determined. Since the presented results suggest the salt to have a greater doping strength than F_4TCNQ and even F_6TCNNQ, $Mes_2B^+[CFB4]^-$ could be used to dope organic materials with ionization energies around 6 eV, which so far has been the regime of metal oxides. In addition, $Mes_2B^+[CFB4]^-$ could also be employed in future studies to induce bipolarons in other polymers or small molecules with similar ionization energies to P3HT, in order to improve the understanding of bipolaron formation.

Ad iv)

In the last part of this thesis, the modification of the electron-selective contacts in organic inorganic metal halide perovskite solar cells (PSCs) was studied by inserting an interlayer of $[RhCp^*Cp]_2$ between the FTO electrode and organic electron transport layer (ETL) consisting of either C_{60} or PTCBI. It was shown that $[RhCp^*Cp]_2$ can effectively decreases the work function of FTO by up to 1.3 eV, since the dimer readily transfers electrons to the electrode leading to the formation of monomer cations on the metal oxide surface and the introduction of an interfacial dipole. Deposition of C_{60} or PTCBI on top of modified FTO leads to Fermi level pinning and thus the formation of Ohmic contacts. Due to multilayers of unreacted dimers being present, the interlayer can induce interfacial doping of the ETL, which was found to increase upon annealing at temperatures above 100 °C. In addition, annealing can even lead to moderate diffusion of the dopants into the organic layer. PSCs based on PTCBI as ETM were shown to have increased stabilized power conversion efficiencies, when modified FTO electrodes are used. However, PSCs fabricated under comparable conditions and using C_{60} as ETM still outperform those with PTCBI and, in contrast, exhibit only negligible increases in efficiency upon introduction of an interlayer.

Nonetheless, this study shows the potential of using interlayers of organometallic dimers to modify FTO contacts, which leads to a minimization of electron collection losses and thus a better device performance of PSCs. In addition, PDI derivatives were found to be suitable replacements for fullerenes as ETM in PSCs and future investigations could explore the potential of other PDI derivatives. The next step in the future development of highly efficient PSCs would be to explore the combination of interlayers of organometallic dimers

with other organic ETMs to replace metal oxides. This approach has the potential to increase the operational stability of PSCs and could thus aid in the already started process of commercializing perovskite solar cells.

Overall, this thesis explored several topics of fundamental and applicational relevance to the area of molecular doping of organic semiconductors. It was shown which basic material parameters can be reliably used to predict the yield of ion pair formation upon doping, which enables a better selection of system appropriate dopants. In addition, it was demonstrated that n-doping can successfully (although not yet long-term stably) render a predominantly p-type polymer n-type. Further developing this approach will likely reduce the still present asymmetry between hole and electron conductivities of organic semiconductors and thus aid in the design of highly efficient organic n-type transistors. Moreover, this is the first time that the formation of bipolarons for the p-doping of the polymer P3HT with a molecular dopant has been conclusively demonstrated via a multi-experimental approach. And, last but not least, it was shown how organic n-dopants can be used to further improve the efficiency of perovskite solar cells by minimizing electron collection losses. With this work, I hope to have contributed to advance the field of molecular doping and the understanding of its basic mechanisms as well as its application in devices.

APPENDIX

A INFLUENCE OF INSTRUMENTAL BROADENING AND EA CORRECTION PROCEDURE

In this appended section, the influence of instrumental broadening on the HOMO and LUMO onset positions in UPS and IPES, respectively. First, a quick review on the Gaussian function is given, which is normally assumed to be the shape of HOMO and LUMO levels. Then, the instrumental broadening of the UPS and IPES systems used in this work will be determined. Finally, the correction procedure for the electron affinity measured by IPES will be described, which loosely follows the procedure described by Krause et al. for the deconvolution of their IPES data.[100] This section was similarly published in the appendix of my Master's thesis (B. Wegner, *Activation of Organometallic Dimers as n-Dopants for a Low Electron Affinity Organic Semiconductor*, Institut für Physik, Humboldt-Universität zu Berlin, Berlin, 2015).

A Gaussian distribution function as shown in Figure A.1 is of the general form

$$y(x) = A \cdot e^{-\frac{1}{2}\left(\frac{x-\mu}{\sigma}\right)^2}, \qquad \text{(A.1)}$$

where A is the height of the distribution, μ its center position and σ^2 its variance. The full width at half maximum (FWHM) w is given by

$$w = 2\sqrt{2\ln(2)} \cdot \sigma\,. \qquad \text{(A.2)}$$

The convolution of two Gaussian functions yields another Gaussian function, with a new center and variance [373],

$$\mu_{new} = \mu_1 + \mu_2\,; \qquad \text{(A.3)}$$

$$\sigma_{\text{new}} = \sqrt{\sigma_1^2 + \sigma_2^2}\,. \qquad \text{(A.4)}$$

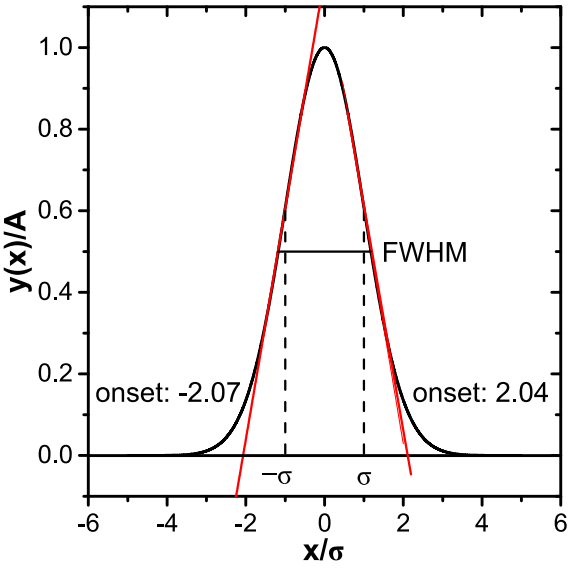

Figure A.1 A Gaussian distribution function of form (A.1). By linear extrapolation, the onset is determined to lie at a distance of around 2σ to the peak center μ.

As described in section 4.4, the onset of HOMO/LUMO levels in UPS and IPES spectra is commonly determined by the intersection of a horizontal baseline with a straight line extending the nearly linear part of the Gaussian envelope function of the HOMO/LUMO level. As determined in Figure A.1, the onset lies at a distance of around 2σ to the peak center μ. Since usually the width of a Homo/LUMO levels is given by the FWHM, the onset of levels at distance to the maximum of the level in terms of FWHM w is

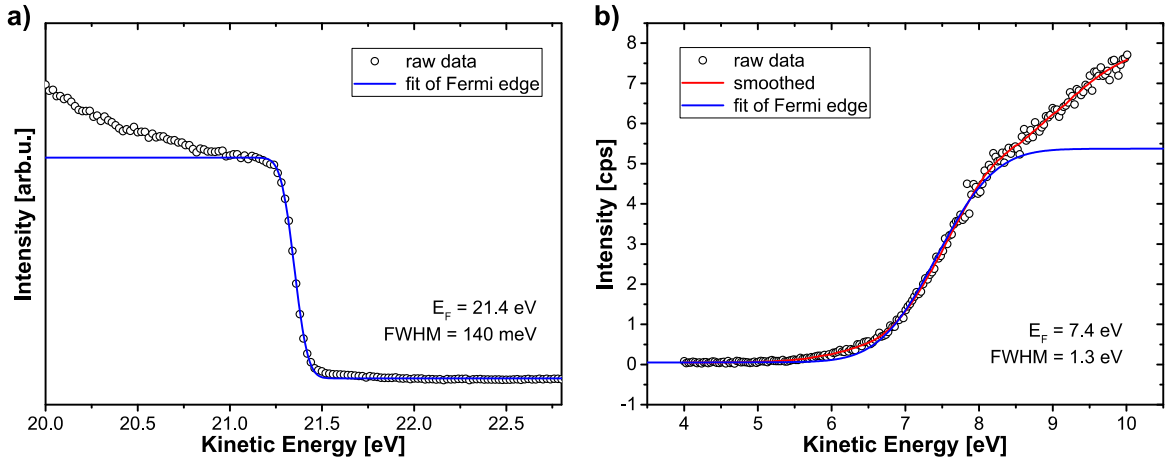

Figure A.2 Fermi edge of a gold sample measured by **a)** UPS and **b)** IPES. While the used UPS setup has only an instrumental broadening of around 140 meV, the IPES setup displays a large instrumental broadening of around 1.3 eV.

$$x_{\text{onset}} \approx 2\sigma = \frac{w}{\sqrt{2\,ln(2)}}\,. \tag{A.5}$$

The instrumental broadening of a UPS and IPES setup is usually assumed to be Gaussian (see section 3.1) and can be experimentally estimated by the broadening of the Fermi edge of a metallic calibration sample, which is used to calibrate the binding energy scale of the setup. Figure A.2 shows the Fermi edge of a gold sample as measured by UPS and IPES. The Fermi edge is described by Fermi-Dirac statistics given in equation (2.6) (section 2.1.1). However, since a convolution of a Fermi function and a Gaussian function can only be solved numerically, the Fermi function has to be approximated by a convolution of a step-function and a Gaussian function in order to receive an analytical function for the broadened Fermi edge,[117] which is of the form

$$y(E) = \frac{A}{2}\left[1 + \text{erf}\left(\frac{2\sqrt{\ln(2)}}{w}(E - E_F)\right)\right] + y_0\,, \tag{A.6}$$

where, A is the height of the step, $\text{erf}()$ is the error function, w is the FWHM of the Gaussian broadening and y_0 is an additional constant background.[374] Using this function, the data of Figure A.2 was fitted yielding a broadening of 140 meV for the used UPS setup and a large broadening of 1300 meV for the used IPES setup.

[117] At T = 0 K, the Fermi function resembles a step function. For T > 0, the Fermi function can be described by a convolution of a step function with a thermal broadening function, the explicit form of which can be found in ref. [374]. This broadening function with width $\frac{7}{2}k_BT$, which is around 90 meV at a room temperature of 300 K, can reasonably well be approximated by a Gaussian function.[374]

While the position of the Fermi level as well as the maxima of the HOMO and LUMO levels are unaffected by the experimental broadening, the onset positions are shifted, which leads to an underestimation of the injection barriers, i.e. the energetic distance between the onsets and the Fermi level. Taking into consideration equations (A.4) and (A.5), the offset x_{off} induced by instrumental broadening can be calculated via

$$x_{\mathrm{off}} = \frac{\sqrt{w_{\mathrm{int}}^2 + w_{\mathrm{broad}}^2} - w_{\mathrm{int}}}{\sqrt{2\ln(2)}}\,, \tag{A.7}$$

where w_{int} is the intrinsic width of the HOMO/LUMO level and w_{broad} is the instrumental broadening. For typical organic semiconductors, the intrinsic width of HOMO and LUMO lies in the range of 500-1000 meV. For the used UPS setup, the offset x_{off} is less than 10 meV (also taking into account thermal broadening of 90 meV), which is negligible. However, for the used IPES setup with the large instrumental broadening of 1300 meV (here thermal broadening can be neglected), x_{off} is in the order of 500-800 meV and thus has to be taken into account when determining EIB and EA.

However, all IPES spectra measured in this thesis were too broad to be properly deconvoluted. To still get an estimate by which offset the obtained electron affinities should be corrected, it was assumed that the HOMO and LUMO levels of the respective materials have nearly the same intrinsic width. The width of the HOMO level was determined by fitting the valence region measured by UPS with Gaussian functions. A typical valence band deconvolution is shown in Figure A.3 for PTCBI, the UPS spectrum of which is also displayed in Figure 8.5 a) (section 8.2). Here, the width of the HOMO level was determined to be 600 meV, which following equation (A.7) leads to a correction factor x_{off} of 700 meV for the determined EA of PTCBI (as used in 8.2).

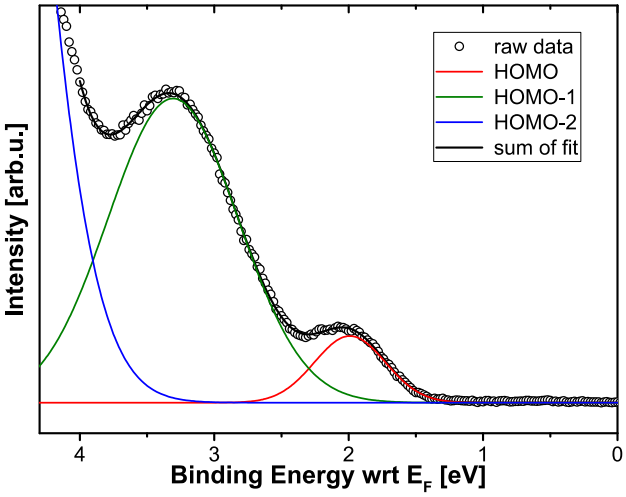

Figure A.3 Deconvolution of the valence region of PTCBI (Figure 8.5a in section 8.2) assuming three Gaussian contributions for the HOMO, HOMO-1 and HOMO-2 levels.

B ADDITIONAL FIGURES

In this appended section, additional experimental figures are shown, which are not essential for the main discussion and only support non-central points. Therefore, they were deemed to rather distract the reader from the main arguments than help in their understanding and were placed here instead of the relevant sections.

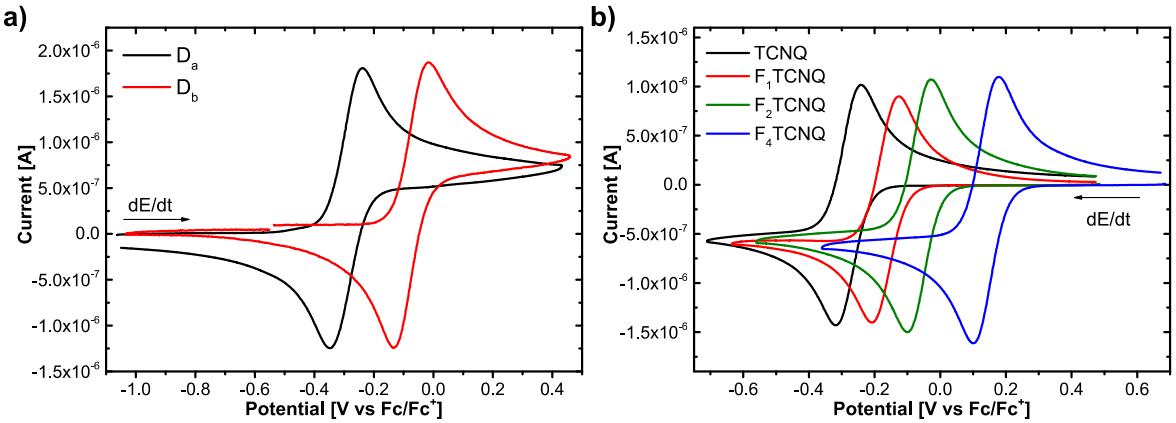

Figure B.1 Cyclic voltammetry measurements for the used **a)** donors Dx and **b)** the acceptors FxTCNQ of chapter 5. The scanning direction is indicated with an arrow marked by dE/dt. Voltammograms kindly provided by Dr. Lutz Grubert (Institut für Chemie, Humboldt-Universität zu Berlin).

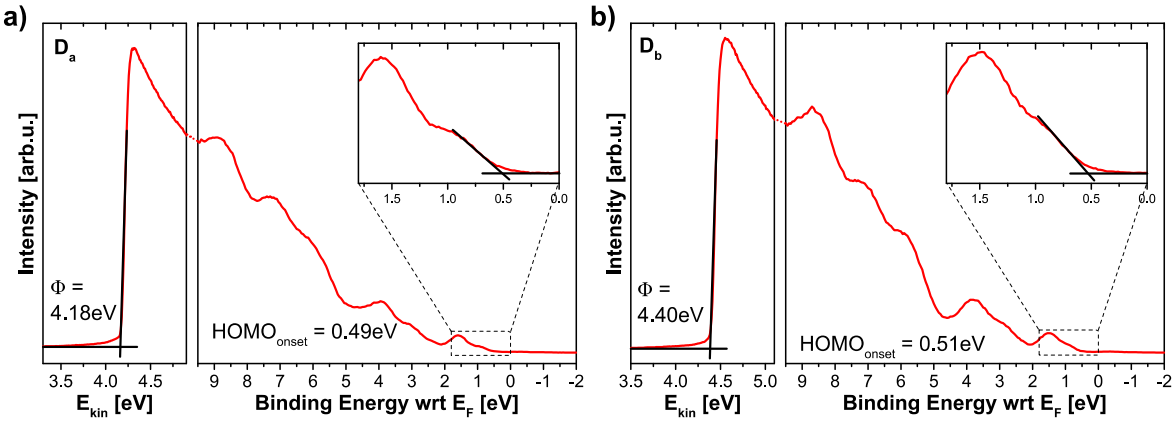

Figure B.2 UPS Spectra of the donors **a)** D_a and **b)** D_b of chapter 5. The left panel shows the SECO with respect to the kinetic energy E_{kin} from which the work function Φ of the samples was determined. The right panel shows the valence structure of the molecules with respect to the binding energy E_b, where 0 eV corresponds to the Fermi level E_F. The inlet in the right panel shows the onset of the HOMO level magnified for better visibility.

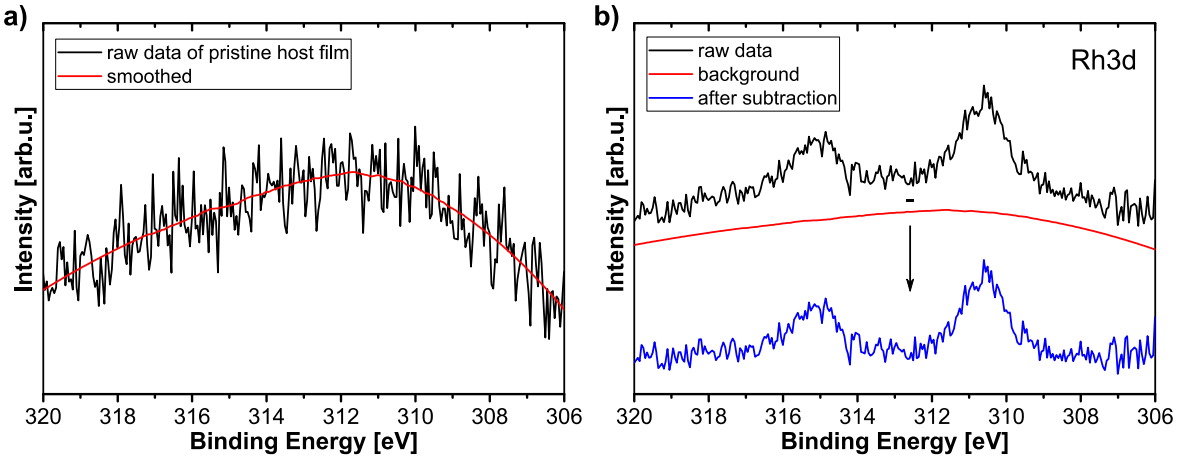

Figure B.3 Example of how the background of XPS detail scans of core levels with a very low intensity was removed (here for the Rh3d core level of Figure 8.8 in chapter 8). **a)** The background in the specific region of the pristine host film (here C1s energy loss line of PTCBI) was smoothed by a using a 100-point second order Savitzky-Golay filter. **b)** The background was fitted to the respective detail scan and subtracted from the data, as described in section 4.4.

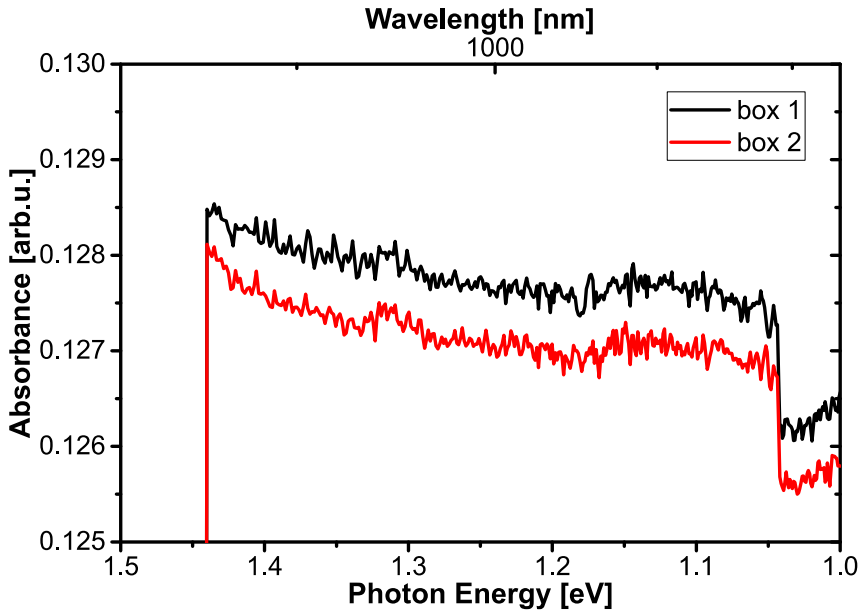

Figure B.4 Optical absorption spectrum in the region 1.0-1.5 eV of the specialized boxes used to perform optical absorption spectroscopy measurements in inert atmosphere. The abrupt changes in signal at 1.04 eV and 1.44 eV are artefacts of the spectrophotometer caused by a change of the grating and detector at these positions, respectively. Since there are no distinct absorption features of the reference box visible in the range of 1.04-1.44 eV, features in this range appearing in Figure 8.9 (chapter 8) can reliably be assigned to sub-bandgap features of the respective samples.

RECORD OF PUBLICATIONS

Publications which comprise parts of the work presented in this thesis are marked with bold index numbers.

[A1] M. Timpel, M. V. Nardi, S. Krause, G. Ligorio, C. Christodoulou, L. Pasquali, A. Giglia, J. Frisch, B. Wegner, P. Moras, N. Koch, Surface Modification of ZnO(0001)–Zn with Phosphonate-Based Self-Assembled Monolayers: Binding Modes, Orientation, and Work Function, *Chem. Mater.* **2014**, 26, 5042.

[A2] H. Méndez, G. Heimel, S. Winkler, J. Frisch, A. Opitz, K. Sauer, B. Wegner, M. Oehzelt, C. Röthel, S. Duhm, D. Többens, N. Koch, I. Salzmann, Charge-transfer crystallites as molecular electrical dopants, *Nat. Commun.* **2015**, 6, 8560.

[A3] M. Timpel, M. V. Nardi, G. Ligorio, B. Wegner, M. Pätzel, B. Kobin, S. Hecht, N. Koch, Energy-Level Engineering at ZnO/Oligophenylene Interfaces with Phosphonate-Based Self-Assembled Monolayers, *ACS Appl. Mater. Interfaces* **2015**, 7, 11900.

[A4] X. Lin, B. Wegner, K. M. Lee, M. A. Fusella, F. Zhang, K. Moudgil, B. P. Rand, S. Barlow, S. R. Marder, N. Koch, A. Kahn, Beating the thermodynamic limit with photo-activation of n-doping in organic semiconductors, *Nat. Mater.* **2017**, 16, 1209.

[A5] M. Timpel, H. Li, M. V. Nardi, B. Wegner, J. Frisch, P. J. Hotchkiss, S. R. Marder, S. Barlow, J.-L. Brédas, N. Koch, Electrode Work Function Engineering with Phosphonic Acid Monolayers and Molecular Acceptors: Charge Redistribution Mechanisms, *Adv. Funct. Mater.* **2018**, 28, 1704438.

[A6] F. Pulvirenti, B. Wegner, N. K. Noel, G. Mazzotta, R. Hill, J. B. Patel, L. M. Herz, M. B. Johnston, M. K. Riede, H. J. Snaith, N. Koch, S. Barlow, S. R. Marder, Modification of the fluorinated tin oxide/electron-transporting material interface by a strong reductant and its effect on perovskite solar cell efficiency, *Mol. Syst. Des. Eng.* **2018**, 3, 741.

[A7] B. Wegner, L. Grubert, D. Chercka, A. Opitz, A. Röttger, Y. Zhang, S. Barlow, S. R. Marder, S. Hecht, K. Müllen, N. Koch, Predicting the Yield of Ion Pair Formation in Molecular Electrical Doping from Redox-Potentials, *in preparation.*

[A8] B. Wegner, A. Mansour, D. Lungwitz, C. Tait, N. Tanaka, T. Zhai, S. Duhm, J. Behrends, Y. Shoji, A. Opitz, T. Fukushima, N. Koch, Bipolaron Formation in P3HT Induced by Molecular Doping Using a Boron-Based Ionic Salt, *in preparation.*

[A9] F. Pulvirenti, J.B. Patel, B. Wegner, X. Jia, S.M.A.R. Kandada, E. Longhi, C.S. Acuna, C. Fuentes-Hernandez, B. Kippelen, N. Koch, L.M. Herz, M.B. Johnston, H.J. Snaith, S. Barlow, S. R. Marder, A comparison of modifiers of the FTO/ETM interface in perovskite solar cells, *in preparation.*

REFERENCES

[1] H. Akamatu, H. Inokuchi, Y. Matsunaga, *Nature* **1954**, *173*, 168.

[2] H. Inokuchi, *Bull. Chem. Soc. Jpn.* **1954**, *27*, 22.

[3] C. K. Chiang, C. R. Fincher, Y. W. Park, A. J. Heeger, H. Shirakawa, E. J. Louis, S. C. Gau, A. G. MacDiarmid, *Phys. Rev. Lett.* **1977**, *39*, 1098.

[4] A. J. Heeger, *Angew. Chemie Int. Ed.* **2001**, *40*, 2591.

[5] A. G. MacDiarmid, *Angew. Chemie Int. Ed.* **2001**, *40*, 2581.

[6] H. Shirakawa, *Angew. Chemie Int. Ed.* **2001**, *40*, 2574.

[7] S. Reineke, *Nat. Mater.* **2015**, *14*, 459.

[8] J. K. Borchardt, *Mater. Today* **2004**, *7*, 42.

[9] K. Myny, S. Steudel, S. Smout, P. Vicca, F. Furthner, B. van der Putten, A. K. Tripathi, G. H. Gelinck, J. Genoe, W. Dehaene, *Org. Electron.* **2010**, *11*, 1176.

[10] J. S. Chang, A. F. Facchetti, R. Reuss, *IEEE J. Emerg. Sel. Top. Circuits Syst.* **2017**, *7*, 7.

[11] X. Wu, S. Mao, J. Chen, J. Huang, *Adv. Mater.* **2018**, *30*, 1705642.

[12] Z. Shi, A. Jayatissa, *Materials* **2018**, *11*, 729.

[13] O. Malinkiewicz, A. Yella, Y. H. Lee, G. M. Espallargas, M. Graetzel, M. K. Nazeeruddin, H. J. Bolink, *Nat. Photonics* **2014**, *8*, 128.

[14] J. S. Heo, J. Eom, Y.-H. Kim, S. K. Park, *Small* **2018**, *14*, 1703034.

[15] J. Onorato, V. Pakhnyuk, C. K. Luscombe, *Polym. J.* **2017**, *49*, 41.

[16] A. Heinrichsdobler, J. C. Roigk, F. Schirmeier, C. J. Brabec, T. Wehlus, *Adv. Mater. Technol.* **2017**, *2*, 1700166.

[17] M. Schwoerer, H. C. Wolf, *Organic Molecular Solids*, WILEY-VCH Verlag GmbH & Co. KGaA, Weinheim, **2007**.

[18] Y. Yamamoto, K. Yoshino, Y. Inuishi, *J. Phys. Soc. Japan* **1979**, *47*, 1887.

[19] J. Kido, T. Matsumoto, *Appl. Phys. Lett.* **1998**, *73*, 2866.

[20] G. Parthasarathy, C. Shen, A. Kahn, S. R. Forrest, *J. Appl. Phys.* **2001**, *89*, 4986.

[21] I. E. Jacobs, A. J. Moulé, *Adv. Mater.* **2017**, *29*, 1703063.

[22] B. Lüssem, M. Riede, K. Leo, *Phys. status solidi* **2013**, *210*, 9.

[23] K. Walzer, B. Maennig, M. Pfeiffer, K. Leo, *Chem. Rev.* **2007**, *107*, 1233.

[24] I. Salzmann, G. Heimel, M. Oehzelt, S. Winkler, N. Koch, *Acc. Chem. Res.* **2016**, *49*, 370.

[25] S. Reineke, F. Lindner, G. Schwartz, N. Seidler, K. Walzer, B. Lüssem, K. Leo, *Nature* **2009**, *459*, 234.

[26] C. Murawski, C. Fuchs, S. Hofmann, K. Leo, M. C. Gather, *Appl. Phys. Lett.* **2014**, *105*, 113303.

[27] F. Selzer, C. Falkenberg, M. Hamburger, M. Baumgarten, K. Müllen, K. Leo, M. Riede, *J. Appl. Phys.* **2014**, *115*, 054515.

[28] X. Lei, F. Zhang, T. Song, B. Sun, *Appl. Phys. Lett.* **2011**, *99*, 233305.

[29] T. Matsushima, C. Adachi, *Appl. Phys. Lett.* **2008**, *92*, 063306.

[30] B. D. Naab, S. Himmelberger, Y. Diao, K. Vandewal, P. Wei, B. Lussem, A. Salleo, Z. Bao, *Adv. Mater.* **2013**, *25*, 4663.

[31] S. Olthof, S. Singh, S. K. Mohapatra, S. Barlow, S. R. Marder, B. Kippelen, A. Kahn, *Appl. Phys. Lett.* **2012**, *101*, 253303.

[32] J. H. Oh, P. Wei, Z. Bao, *Appl. Phys. Lett.* **2010**, *97*, 243305.

[33] W. Gao, A. Kahn, *Appl. Phys. Lett.* **2001**, *79*, 4040.

[34] S. Tanaka, K. Kanai, E. Kawabe, T. Iwahashi, T. Nishi, Y. Ouchi, K. Seki, *Jpn. J. Appl. Phys.* **2005**, *44*, 3760.

[35] Y. Zhang, B. de Boer, P. W. M. Blom, *Phys. Rev. B* **2010**, *81*, 085201.

[36] K. Leo, M. Hummert, in *Handb. Org. Mater. Opt. (Opto)Electronic Devices Prop. Appl.* (Ed.: O. Ostroverkhova), Woodhead Publishing Limited, **2013**.

[37] D. Di Nuzzo, C. Fontanesi, R. Jones, S. Allard, I. Dumsch, U. Scherf, E. von Hauff, S. Schumacher, E. Da Como, *Nat. Commun.* **2015**, *6*, 6460.

[38] L. Müller, D. Nanova, T. Glaser, S. Beck, A. Pucci, A. K. Kast, R. R. Schröder, E. Mankel, P. Pingel, D. Neher, W. Kowalsky, R. Lovrincic, *Chem. Mater.* **2016**, *28*, 4432.

[39] K. Kang, S. Watanabe, K. Broch, A. Sepe, A. Brown, I. Nasrallah, M. Nikolka, Z. Fei, M. Heeney, D. Matsumoto, K. Marumoto, H. Tanaka, S. Kuroda, H. Sirringhaus, *Nat. Mater.* **2016**, *15*, 896.

[40] Y. Karpov, T. Erdmann, I. Raguzin, M. Al-Hussein, M. Binner, U. Lappan, M. Stamm, K. L. Gerasimov, T. Beryozkina, V. Bakulev, D. V. Anokhin, D. A. Ivanov, F. Günther, S. Gemming, G. Seifert, B. Voit, R. Di Pietro, A. Kiriy, *Adv. Mater.* **2016**, *28*, 6003.

[41] A. Köhler, *Nat. Mater.* **2012**, *11*, 836.

[42] H. T. Nicolai, M. Kuik, G. A. H. Wetzelaer, B. de Boer, C. Campbell, C. Risko, J. L. Brédas, P. W. M. Blom, *Nat. Mater.* **2012**, *11*, 882.

[43] H. Yan, Z. Chen, Y. Zheng, C. Newman, J. R. Quinn, F. Dötz, M. Kastler, A. Facchetti, *Nature* **2009**, *457*, 679.

[44] S. Holliday, R. S. Ashraf, A. Wadsworth, D. Baran, S. A. Yousaf, C. B. Nielsen, C.-H. Tan, S. D. Dimitrov, Z. Shang, N. Gasparini, M. Alamoudi, F. Laquai, C. J. Brabec, A. Salleo, J. R. Durrant, I. McCulloch, *Nat. Commun.* **2016**, *7*, 11585.

[45] K. J. Fallon, N. Wijeyasinghe, E. F. Manley, S. D. Dimitrov, S. A. Yousaf, R. S. Ashraf, W. Duffy, A. A. Y. Guilbert, D. M. E. Freeman, M. Al-Hashimi, J. Nelson, J. R. Durrant, L. X. Chen, I. McCulloch, T. J. Marks, T. M. Clarke, T. D. Anthopoulos, H. Bronstein, *Chem. Mater.* **2016**, *28*, 8366.

[46] T.-C. Chung, J. H. Kaufman, A. J. Heeger, F. Wudl, *Phys. Rev. B* **1984**, *30*, 702.

[47] J. L. Bredas, G. B. Street, *Acc. Chem. Res.* **1985**, *18*, 309.

[48] K. E. Ziemelis, A. T. Hussain, D. D. C. Bradley, R. H. Friend, J. Rühe, G. Wegner, *Phys. Rev. Lett.* **1991**, *66*, 2231.

[49] R. Österbacka, C. P. An, X. M. Jiang, Z. V. Vardeny, *Science* **2000**, *287*, 839.

[50] C. Wang, D. T. Duong, K. Vandewal, J. Rivnay, A. Salleo, *Phys. Rev. B* **2015**, *91*, 085205.

[51] C. Cobet, J. Gasiorowski, D. Farka, P. Stadler, in *Ellipsom. Funct. Org. Surfaces Film.* (Eds.: K. Hinrichs, K.-J. Eichhorn), Springer International Publishing AG, Berlin, Heidelberg, **2018**.

[52] I. Salzmann, G. Heimel, *J. Electron Spectros. Relat. Phenomena* **2015**, *204*, 208.

[53] S.-J. Yoo, J.-J. Kim, *Macromol. Rapid Commun.* **2015**, *36*, 984.

[54] W. S. Yang, B. Park, E. H. Jung, N. J. Jeon, Y. C. Kim, D. U. Lee, S. S. Shin, J. Seo, E. K. Kim, J. H. Noh, S. Il Seok, *Science* **2017**, *356*, 1376.

[55] J.-P. Correa-Baena, M. Saliba, T. Buonassisi, M. Grätzel, A. Abate, W. Tress, A. Hagfeldt, *Science* **2017**, *358*, 739.

[56] S. K. Pathak, A. Abate, P. Ruckdeschel, B. Roose, K. C. Gödel, Y. Vaynzof, A. Santhala, S.-I. Watanabe, D. J. Hollman, N. Noel, A. Sepe, U. Wiesner, R. Friend, H. J. Snaith, U. Steiner, *Adv. Funct. Mater.* **2014**, *24*, 6046.

[57] T. Leijtens, G. E. Eperon, S. Pathak, A. Abate, M. M. Lee, H. J. Snaith, *Nat. Commun.* **2013**, *4*, 2885.

[58] K. Wojciechowski, T. Leijtens, S. Siprova, C. Schlueter, M. T. Hörantner, J. T. Wang, C. Li, A. K.-Y. Jen, T. Lee, H. J. Snaith, *J. Phys. Chem. Lett.* **2015**, *6*, 2399.

[59] S. N. Patel, A. M. Glaudell, K. A. Peterson, E. M. Thomas, K. A. O'Hara, E. Lim, M. L. Chabinyc, *Sci. Adv.* **2017**, *3*, e1700434.

[60] J. M. Kim, S. J. Yoo, C. K. Moon, B. Sim, J. H. Lee, H. Lim, J. W. Kim, J. J. Kim, *J. Phys. Chem. C* **2016**, *120*, 9475.

[61] J. Min, Z.-G. Zhang, Y. Hou, C. O. Ramirez Quiroz, T. Przybilla, C. Bronnbauer, F. Guo, K. Forberich, H. Azimi, T. Ameri, E. Spiecker, Y. Li, C. J. Brabec, *Chem. Mater.* **2015**, *27*, 227.

[62] M. Kaltenbrunner, G. Adam, E. D. Głowacki, M. Drack, R. Schwödiauer, L. Leonat, D. H. Apaydin, H. Groiss, M. C. Scharber, M. S. White, N. S. Sariciftci, S. Bauer, *Nat. Mater.* **2015**, *14*, 1032.

[63] G. Hadziioannou, P. F. van Hutten, Eds. , *Semiconducting Polymers - Chemistry, Physics and Engineering*, WILEY-VCH Verlag GmbH & Co. KGaA, Weinheim, **2007**.

[64] W. Brütting, C. Adachi, Eds. , *Physics of Organic Semiconductors*, WILEY-VCH Verlag GmbH & Co. KGaA, Weinheim, **2012**.

[65] N. Koch, N. Ueno, A. T. S. Wee, Eds. , *The Molecule-Metal Interface*, WILEY-VCH Verlag GmbH & Co. KGaA, Weinheim, **2013**.

[66] A. Köhler, H. Bässler, *Electronic Processes in Organic Semiconductors: An Introduction*, WILEY-VCH Verlag, Weinheim, **2015**.

[67] J.-L. Brédas, S. R. Marder, Eds. , *The WSPC Reference on Organic Electronics: Organic Semiconductors (in 2 Volumes)*, World Scientific, New Jersey, **2016**.

[68] E. J. Baerends, D. E. Ellis, P. Ros, *Chem. Phys.* **1973**, *2*, 41.

[69] E. Hückel, *Zeitschrift für Phys.* **1931**, *70*, 204.

[70] N. Karl, in *Festkörperprobleme XIV - Adv. Solid State Phys.* (Ed.: H.J. Queisser), Springer, Berlin, Heidelberg, **1974**.

[71] J. Casado, T. M. Pappenfus, L. L. Miller, K. R. Mann, E. Ortí, P. M. Viruela, R. Pou-Amérigo, V. Hernández, J. T. López Navarrete, *J. Am. Chem. Soc.* **2003**, *125*, 2524.

[72] Y. Sakamoto, T. Suzuki, M. Kobayashi, Y. Gao, Y. Fukai, Y. Inoue, F. Sato, S. Tokito, *J. Am. Chem. Soc.* **2004**, *126*, 8138.

[73] J. C. Hummelen, B. W. Knight, F. LePeq, F. Wudl, J. Yao, C. L. Wilkins, *J. Org. Chem.* **1995**, *60*, 532.

[74] Y. Lu, Ed. , *Solitons & Polarons in Conducting Polymers*, World Scientific, Singapore, **1988**.

[75] H. Ishii, K. Sugiyama, E. Ito, K. Seki, *Adv. Mater.* **1999**, *11*, 605.

[76] J.-L. Bredas, *Mater. Horiz.* **2014**, *1*, 17.

[77] A. Kahn, *Mater. Horizons* **2016**, *3*, 7.

[78] G. Man, J. Endres, X. Lin, A. Kahn, in *WSPC Ref. Org. Electron. Org. Semicond. Vol.1* (Eds.: J.-L. Brédas, S.R. Marder), World Scientific, New Jersey, **2016**.

[79] K. Seki, *Mol. Cryst. Liq. Cryst. Inc. Nonlinear Opt.* **1989**, *171*, 255.

[80] N. Sato, K. Seki, H. Inokuchi, *J. Chem. Soc. Faraday Trans. 2* **1981**, *77*, 1621.

[81] J. Hwang, A. Wan, A. Kahn, *Mater. Sci. Eng. R Reports* **2009**, *64*, 1.

[82] S. Olthof, Photoelectron Spectroscopy on Doped Organic Semiconductors and Related Interfaces, Technische Universität Dresden, **2010**.

[83] G. Heimel, I. Salzmann, S. Duhm, N. Koch, *Chem. Mater.* **2011**, *23*, 359.

[84] C. Poelking, M. Tietze, C. Elschner, S. Olthof, D. Hertel, B. Baumeier, F. Würthner, K. Meerholz, K. Leo, D. Andrienko, *Nat. Mater.* **2015**, *14*, 434.

[85] S. Duhm, G. Heimel, I. Salzmann, H. Glowatzki, R. L. Johnson, A. Vollmer, J. P. Rabe, N. Koch, *Nat. Mater.* **2008**, *7*, 326.

[86] I. Salzmann, S. Duhm, G. Heimel, M. Oehzelt, R. Kniprath, R. L. Johnson, J. P. Rabe, N. Koch, *J. Am. Chem. Soc.* **2008**, *130*, 12870.

[87] H. Yoshida, K. Yamada, J. Tsutsumi, N. Sato, *Phys. Rev. B* **2015**, *92*, 075145.

[88] S. Winkler, P. Amsalem, J. Frisch, M. Oehzelt, G. Heimel, N. Koch, *Mater. Horizons* **2015**, *2*, 427.

[89] F. Devreux, F. Genoud, M. Nechtschein, B. Villeret, *Synth. Met.* **1987**, *18*, 89.

[90] C. Enengl, S. Enengl, S. Pluczyk, M. Havlicek, M. Lapkowski, H. Neugebauer, E. Ehrenfreund, *ChemPhysChem* **2016**, *17*, 3830.

[91] F. Moraes, D. Davidov, M. Kobayashi, T. . Chung, J. Chen, A. . Heeger, F. Wudl, *Synth. Met.* **1985**, *10*, 169.

[92] O. Bubnova, Z. U. Khan, H. Wang, S. Braun, D. R. Evans, M. Fabretto, P. Hojati-Talemi, D. Dagnelund, J.-B. Arlin, Y. H. Geerts, S. Desbief, D. W. Breiby, J. W. Andreasen, R. Lazzaroni, W. M. Chen, I. Zozoulenko, M. Fahlman, P. J. Murphy, M. Berggren, X. Crispin, *Nat. Mater.* **2014**, *13*, 190.

[93] D. Fichou, G. Horowitz, B. Xu, F. Garnier, *Synth. Met.* **1990**, *39*, 243.

[94] N. Koch, A. Rajagopal, J. Ghijsen, R. L. Johnson, G. Leising, J.-J. Pireaux, *J. Phys. Chem. B* **2000**, *104*, 1434.

[95] S. Kahmann, M. A. Loi, C. J. Brabec, *J. Mater. Chem. C* **2018**, *6*, 6008.

[96] R. Png, M. C. Y. Ang, M. Teo, K. Choo, C. G. Tang, D. Belaineh, L. Chua, P. K. H. Ho, *Nat. Commun.* **2016**, *7*, 11948.

[97] G. Heimel, *ACS Cent. Sci.* **2016**, *2*, 309.

[98] H. Meier, U. Stalmach, H. Kolshorn, *Acta Polym.* **1997**, *48*, 379.

[99] I. G. Hill, A. Kahn, Z. G. Soos, R. A. Pascal, Jr, *Chem. Phys. Lett.* **2000**, *327*, 181.

[100] S. Krause, M. B. Casu, A. Schöll, E. Umbach, *New J. Phys.* **2008**, *10*, 085001.

[101] L. Sebastian, G. Weiser, G. Peter, H. Bässler, *Chem. Phys.* **1983**, *75*, 103.

[102] O. V. Mikhnenko, P. W. M. Blom, T.-Q. Nguyen, *Energy Environ. Sci.* **2015**, *8*, 1867.

[103] J. A. Jeevarajan, C. C. Wei, A. S. Jeevarajan, L. D. Kispert, *J. Phys. Chem.* **1996**, *100*, 5637.

[104] G. Horowitz, A. Yassar, H. J. von Bardeleben, *Synth. Met.* **1994**, *62*, 245.

[105] J. Cornil, J.-L. Brédas, *Adv. Mater.* **1995**, *7*, 295.

[106] E. Zojer, J. Cornil, G. Leising, J. L. Brédas, *Phys. Rev. B* **1999**, *59*, 7957.

[107] K. Fesser, A. R. Bishop, D. K. Campbell, *Phys. Rev. B* **1983**, *27*, 4804.

[108] Y. Shen, A. R. Hosseini, M. H. Wong, G. G. Malliaras, *ChemPhysChem* **2004**, *5*, 16.

[109] W. Warta, N. Karl, *Phys. Rev. B* **1985**, *32*, 1172.

[110] H. Fukagawa, S. Kera, T. Kataoka, S. Hosoumi, Y. Watanabe, K. Kudo, N. Ueno, *Adv. Mater.* **2007**, *19*, 665.

[111] I. G. Hill, A. Kahn, *J. Appl. Phys.* **1998**, *84*, 5583.

[112] F. J. Zhang, A. Vollmer, J. Zhang, Z. Xu, J. P. Rabe, N. Koch, *Org. Electron.* **2007**, *8*, 606.

[113] M. Grobosch, M. Knupfer, *Adv. Mater.* **2007**, *19*, 754.

[114] A. Kahn, N. Koch, W. Gao, *J. Polym. Sci. B* **2003**, *41*, 2529.

[115] I. G. Hill, D. Milliron, J. Schwartz, A. Kahn, *Appl. Surf. Sci.* **2000**, *166*, 354.

[116] I. Lange, J. C. Blakesley, J. Frisch, A. Vollmer, N. Koch, D. Neher, *Phys. Rev. Lett.* **2011**, *106*, 216402.

[117] M. Oehzelt, N. Koch, G. Heimel, *Nat. Commun.* **2014**, *5*, 4174.

[118] M. Wießner, J. Ziroff, F. Forster, M. Arita, K. Shimada, P. Puschnig, A. Schöll, F. Reinert, *Nat. Commun.* **2013**, *4*, 1514.

[119] H. Vázquez, F. Flores, A. Kahn, *Org. Electron.* **2007**, *8*, 241.

[120] S. Braun, W. R. Salaneck, M. Fahlman, *Adv. Mater.* **2009**, *21*, 1450.

[121] S. Zhong, J. Q. Zhong, H. Y. Mao, J. L. Zhang, J. D. Lin, W. Chen, *Phys. Chem. Chem. Phys.* **2012**, *14*, 14127.

[122] M. Oehzelt, K. Akaike, N. Koch, G. Heimel, *Sci. Adv.* **2015**, *1*, e1501127.

[123] O. V. Molodtsova, M. Grobosch, M. Knupfer, V. Y. Aristov, *Appl. Phys. Lett.* **2007**, *91*, 244103.

[124] H. Vázquez, Y. J. Dappe, J. Ortega, F. Flores, *J. Chem. Phys.* **2007**, *126*, 144703.

[125] S. Winkler, J. Frisch, R. Schlesinger, M. Oehzelt, R. Rieger, J. Räder, J. P. Rabe, K. Müllen, N. Koch, *J. Phys. Chem. C* **2013**, *117*, 22285.

[126] M. T. Greiner, M. G. Helander, W.-M. Tang, Z.-B. Wang, J. Qiu, Z.-H. Lu, *Nat. Mater.* **2012**, *11*, 76.

[127] S. Kirchmeyer, K. Reuter, *J. Mater. Chem.* **2005**, *15*, 2077.

[128] S. A. Paniagua, A. J. Giordano, O. L. Smith, S. Barlow, H. Li, N. R. Armstrong, J. E. Pemberton, J.-L. Brédas, D. Ginger, S. R. Marder, *Chem. Rev.* **2016**, *116*, 7117.

[129] J. C. Love, L. A. Estroff, J. K. Kriebel, R. G. Nuzzo, G. M. Whitesides, *Chem. Rev.* **2005**, *105*, 1103.

[130] Y. Zhou, C. Fuentes-Hernandez, J. Shim, J. Meyer, A. J. Giordano, H. Li, P. Winget, T. Papadopoulos, H. Cheun, J. Kim, M. Fenoll, A. Dindar, W. Haske, E. Najafabadi, T. M. Khan, H. Sojoudi, S. Barlow, S. Graham, J.-L. Bredas, S. R. Marder, A. Kahn, B. Kippelen, *Science* **2012**, *336*, 327.

[131] N. Koch, S. Duhm, J. P. Rabe, A. Vollmer, R. L. Johnson, *Phys. Rev. Lett.* **2005**, *95*, 237601.

[132] K. Akaike, M. V. Nardi, M. Oehzelt, J. Frisch, A. Opitz, C. Christodoulou, G. Ligorio, P. Beyer, M. Timpel, I. Pis, F. Bondino, K. Moudgil, S. Barlow, S. R. Marder, N. Koch, *Adv. Funct. Mater.* **2016**, *26*, 2493.

[133] D. Meyerhofer, *J. Appl. Phys.* **1978**, *49*, 3993.

[134] N. Koch, *ChemPhysChem* **2007**, *8*, 1438.

[135] I. McCulloch, A. Salleo, M. Chabinyc, *Science* **2016**, *352*, 1521.

[136] L.-L. Chua, J. Zaumseil, J.-F. Chang, E. C.-W. Ou, P. K.-H. Ho, H. Sirringhaus, R. H. Friend, *Nature* **2005**, *434*, 194.

[137] L. Lu, T. Zheng, Q. Wu, A. M. Schneider, D. Zhao, L. Yu, *Chem. Rev.* **2015**, *115*, 12666.

[138] M. M. Lee, J. Teuscher, T. Miyasaka, T. N. Murakami, H. J. Snaith, *Science* **2012**, *338*, 643.

[139] H.-S. Kim, C.-R. Lee, J.-H. Im, K.-B. Lee, T. Moehl, A. Marchioro, S.-J. Moon, R. Humphry-Baker, J.-H. Yum, J. E. Moser, M. Grätzel, N.-G. Park, *Sci. Rep.* **2012**, *2*, 591.

[140] M. Pfeiffer, T. Fritz, J. Blochwitz, A. Nollau, B. Plönnigs, A. Beyer, K. Leo, in *Adv. Solid State Phys. 39*, Springer, Berlin, Heidelberg, **1999**.

[141] B. Lüssem, C.-M. Keum, D. Kasemann, B. Naab, Z. Bao, K. Leo, *Chem. Rev.* **2016**, *116*, 13714.

[142] Y. Xu, H. Sun, A. Liu, H.-H. Zhu, W. Li, Y.-F. Lin, Y.-Y. Noh, *Adv. Mater.* **2018**, 1801830.

[143] Z. Bin, Z. Liu, Y. Qiu, L. Duan, *Adv. Opt. Mater.* **2018**, *6*, 1800536.

[144] C. Kittel, *Introduction to Solid State Physics*, John Wiley & Sons, New York, **2005**.

[145] B. Kippelen, in *WSPC Ref. Org. Electron. Org. Semicond. Vol.2* (Eds.: J.-L. Brédas, S.R. Marder), World Scientific, New Jersey, **2016**.

[146] S. M. Sze, K. K. Ng, *Physics of Semiconductor Decices*, John Wiley & Sons, Hoboken, New Jersey, **2006**.

[147] G. Heimel, I. Salzmann, N. Koch, in *AIP Conf. Proc.*, **2012**, p. 148.

[148] C. K. Chan, E.-G. Kim, J.-L. Brédas, A. Kahn, *Adv. Funct. Mater.* **2006**, *16*, 831.

[149] S. Olthof, W. Tress, R. Meerheim, B. Lüssem, K. Leo, *J. Appl. Phys.* **2009**, *106*, 103711.

[150] P. Pingel, D. Neher, *Phys. Rev. B* **2013**, *87*, 115209.

[151] H. Kleemann, C. Schuenemann, A. A. Zakhidov, M. Riede, B. Lüssem, K. Leo, *Org. Electron.* **2012**, *13*, 58.

[152] D. T. Duong, C. Wang, E. Antono, M. F. Toney, A. Salleo, *Org. Electron.* **2013**, *14*, 1330.

[153] K.-H. Yim, G. L. Whiting, C. E. Murphy, J. J. M. Halls, J. H. Burroughes, R. H. Friend, J.-S. Kim, *Adv. Mater.* **2008**, *20*, 3319.

[154] I. E. Jacobs, C. Cendra, T. F. Harrelson, Z. I. Bedolla Valdez, R. Faller, A. Salleo, A. J. Moulé, *Mater. Horizons* **2018**, *5*, 655.

[155] H. Méndez, G. Heimel, A. Opitz, K. Sauer, P. Barkowski, M. Oehzelt, J. Soeda, T. Okamoto, J. Takeya, J.-B. Arlin, J.-Y. Balandier, Y. Geerts, N. Koch, I. Salzmann, *Angew. Chemie Int. Ed.* **2013**, *52*, 7751.

[156] A. Optiz et al., *unpublished data*

[157] E. J. Meijer, C. Detcheverry, P. J. Baesjou, E. van Veenendaal, D. M. de Leeuw, T. M. Klapwijk, *J. Appl. Phys.* **2003**, *93*, 4831.

[158] G. D. Sharma, S. G. Sangodkar, M. S. Roy, *Mater. Sci. Eng. B* **1996**, *41*, 222.

[159] J. B. Torrance, *Acc. Chem. Res.* **1979**, *12*, 79.

[160] D. Jérome, *Chem. Rev.* **2004**, *104*, 5565.

[161] K. Kanai, K. Akaike, K. Koyasu, K. Sakai, T. Nishi, Y. Kamizuru, T. Nishi, Y. Ouchi, K. Seki, *Appl. Phys. A* **2009**, *95*, 309.

[162] B. Maennig, M. Pfeiffer, A. Nollau, X. Zhou, K. Leo, P. Simon, *Phys. Rev. B* **2001**, *64*, 195208.

[163] D. T. Scholes, S. A. Hawks, P. Y. Yee, H. Wu, J. R. Lindemuth, S. H. Tolbert, B. J. Schwartz, *J. Phys. Chem. Lett.* **2015**, *6*, 4786.

[164] R. Meerheim, B. Lüssem, K. Leo, in *Proceedings of the IEEE*, **2009**, p. 1606.

[165] R. Meerheim, S. Olthof, M. Hermenau, S. Scholz, A. Petrich, N. Tessler, O. Solomeshch, B. Lüssem, M. Riede, K. Leo, *J. Appl. Phys.* **2011**, *109*, 103102.

[166] L. Müller, S.-Y. Rhim, V. Sivanesan, D. Wang, S. Hietzschold, P. Reiser, E. Mankel, S. Beck, S. Barlow, S. R. Marder, A. Pucci, W. Kowalsky, R. Lovrincic, *Adv. Mater.* **2017**, *29*, 1701466.

[167] P. Reiser, L. Müller, V. Sivanesan, R. Lovrincic, S. Barlow, S. R. Marder, A. Pucci, W. Jaegermann, E. Mankel, S. Beck, *J. Phys. Chem. C* **2018**, *122*, 14518.

[168] F. Zhang, A. Kahn, *Adv. Funct. Mater.* **2018**, *28*, 1703780.

[169] J. Li, C. W. Rochester, I. E. Jacobs, S. Friedrich, P. Stroeve, M. Riede, A. J. Moulé, *ACS Appl. Mater. Interfaces* **2015**, *7*, 28420.

[170] J. E. Cochran, M. J. N. Junk, A. M. Glaudell, P. L. Miller, J. S. Cowart, M. F. Toney, C. J. Hawker, B. F. Chmelka, M. L. Chabinyc, *Macromolecules* **2014**, *47*, 6836.

[171] Y. Qi, T. Sajoto, S. Barlow, E.-G. Kim, J.-L. Brédas, S. R. Marder, A. Kahn, *J. Am. Chem. Soc.* **2009**, *131*, 12530.

[172] S. A. Paniagua, J. Baltazar, H. Sojoudi, S. K. Mohapatra, S. Zhang, C. L. Henderson, S. Graham, S. Barlow, S. R. Marder, *Mater. Horiz.* **2014**, *1*, 111.

[173] E. Lim, K. A. Peterson, G. M. Su, M. L. Chabinyc, *Chem. Mater.* **2018**, *30*, 998.

[174] D. T. Scholes, P. Y. Yee, J. R. Lindemuth, H. Kang, J. Onorato, R. Ghosh, C. K. Luscombe, F. C. Spano, S. H. Tolbert, B. J. Schwartz, *Adv. Funct. Mater.* **2017**, *27*, 1702654.

[175] D. T. Scholes, S. A. Hawks, P. Y. Yee, H. Wu, J. R. Lindemuth, S. H. Tolbert, B. J. Schwartz, *J. Phys. Chem. Lett.* **2015**, *6*, 4786.

[176] M. Kröger, S. Hamwi, J. Meyer, T. Riedl, W. Kowalsky, A. Kahn, *Org. Electron.* **2009**, *10*, 932.

[177] J.-H. Lee, D.-S. Leem, H.-J. Kim, J.-J. Kim, *Appl. Phys. Lett.* **2009**, *94*, 123306.

[178] T. Matsushima, C. Adachi, *J. Appl. Phys.* **2008**, *103*, 034501.

[179] J. Meyer, S. Hamwi, S. Schmale, T. Winkler, H.-H. Johannes, T. Riedl, W. Kowalsky, *J. Mater. Chem.* **2009**, *19*, 702.

[180] J. Meyer, S. Hamwi, M. Kröger, W. Kowalsky, T. Riedl, A. Kahn, *Adv. Mater.* **2012**, *24*, 5408.

[181] P. Pingel, M. Arvind, L. Kölln, R. Steyrleuthner, F. Kraffert, J. Behrends, S. Janietz, D. Neher, *Adv. Electron. Mater.* **2016**, *2*, 1600204.

[182] A. P. Kulkarni, C. J. Tonzola, A. Babel, S. A. Jenekhe, *Chem. Mater.* **2004**, *16*, 4556.

[183] B. Lüssem, M. Riede, K. Leo, *Phys. Status Solidi A Appl. Mater. Sci.* **2013**, *210*, 9.

[184] R. C. Haddon, A. F. Hebard, M. J. Rosseinsky, D. W. Murphy, S. J. Duclos, K. B. Lyons, B. Miller, J. M. Rosamilia, R. M. Fleming, A. R. Kortan, S. H. Glarum, A. V. Makhija, A. J. Muller, R. H. Eick, S. M. Zahurak, R. Tycko, G. Dabbagh, F. A. Thiel, *Nature* **1991**, *350*, 320.

[185] K. R. Choudhury, J. Yoon, F. So, *Adv. Mater.* **2008**, *20*, 1456.

[186] A. Nollau, M. Pfeiffer, T. Fritz, K. Leo, *J. Appl. Phys.* **2000**, *87*, 4340.

[187] K. Harada, A. G. Werner, M. Pfeiffer, C. J. Bloom, C. M. Elliott, K. Leo, *Phys. Rev. Lett.* **2005**, *94*, 036601.

[188] C. K. Chan, F. Amy, Q. Zhang, S. Barlow, S. Marder, A. Kahn, *Chem. Phys. Lett.* **2006**, *431*, 67.

[189] C. K. Chan, W. Zhao, S. Barlow, S. Marder, A. Kahn, *Org. Electron.* **2008**, *9*, 575.

[190] T. Menke, P. Wei, D. Ray, H. Kleemann, B. D. Naab, Z. Bao, K. Leo, M. Riede, *Org. Electron.* **2012**, *13*, 3319.

[191] A. G. Werner, F. Li, K. Harada, M. Pfeiffer, T. Fritz, K. Leo, *Appl. Phys. Lett.* **2003**, *82*, 4495.

[192] F. Li, A. Werner, M. Pfeiffer, K. Leo, X. Liu, *J. Phys. Chem. B* **2004**, *108*, 17076.

[193] C. K. Chan, E. G. Kim, J.-L. Brédas, A. Kahn, *Adv. Funct. Mater.* **2006**, *16*, 831.

[194] F. Li, M. Pfeiffer, A. Werner, K. Harada, K. Leo, N. Hayashi, K. Seki, X. Liu, X.-D. Dang, *J. Appl. Phys.* **2006**, *100*, 023716.

[195] P. Wei, T. Menke, B. D. Naab, K. Leo, M. Riede, Z. Bao, *J. Am. Chem. Soc.* **2012**, *134*, 3999.

[196] Z. Bin, L. Duan, Y. Qiu, *ACS Appl. Mater. Interfaces* **2015**, *7*, 6444.

[197] P. Wei, J. H. Oh, G. Dong, Z. Bao, *J. Am. Chem. Soc.* **2010**, *132*, 8852.

[198] R. A. Schlitz, F. G. Brunetti, A. M. Glaudell, P. L. Miller, M. A. Brady, C. J. Takacs, C. J. Hawker, M. L. Chabinyc, *Adv. Mater.* **2014**, *26*, 2825.

[199] B. D. Naab, S. Zhang, K. Vandewal, A. Salleo, S. Barlow, S. R. Marder, Z. Bao, *Adv. Mater.* **2014**, *26*, 4268.

[200] S. Rossbauer, C. Müller, T. D. Anthopoulos, *Adv. Funct. Mater.* **2014**, *24*, 7116.

[201] B. D. Naab, S. Guo, S. Olthof, E. G. B. Evans, P. Wei, G. L. Millhauser, A. Kahn, S. Barlow, S. R. Marder, Z. Bao, *J. Am. Chem. Soc.* **2013**, *135*, 15018.

[202] C. D. Weber, C. Bradley, M. C. Lonergan, *J. Mater. Chem. A* **2014**, *2*, 303.

[203] S. K. Mohapatra, A. Fonari, C. Risko, K. Yesudas, K. Moudgil, J. H. Delcamp, T. V. Timofeeva, J.-L. Brédas, S. R. Marder, S. Barlow, *Chem. - A Eur. J.* **2014**, *20*, 15385.

[204] S. Guo, S. K. Mohapatra, A. Romanov, T. V. Timofeeva, K. I. Hardcastle, K. Yesudas, C. Risko, J.-L. Brédas, S. R. Marder, S. Barlow, *Chem. - A Eur. J.* **2012**, *18*, 14760.

[205] S. Guo, S. B. Kim, S. K. Mohapatra, Y. Qi, T. Sajoto, A. Kahn, S. R. Marder, S. Barlow, *Adv. Mater.* **2012**, *24*, 699.

[206] Y. Qi, S. K. Mohapatra, S. Bok Kim, S. Barlow, S. R. Marder, A. Kahn, *Appl. Phys. Lett.* **2012**, *100*, 083305.

[207] S. Olthof, S. Mehraeen, S. K. Mohapatra, S. Barlow, V. Coropceanu, J.-L. Brédas, S. R. Marder, A. Kahn, *Phys. Rev. Lett.* **2012**, *109*, 176601.

[208] A. Higgins, S. K. Mohapatra, S. Barlow, S. R. Marder, A. Kahn, *Appl. Phys. Lett.* **2015**, *106*, 163301.

[209] C. N. N. Berglund, W. E. E. Spicer, *Phys. Rev.* **1964**, *136*, A1030.

[210] W. E. Spicer, C. N. Berglund, *Phys. Rev. Lett.* **1964**, *12*, 9.

[211] D. W. Turner, M. I. Al Jobory, *J. Chem. Phys.* **1962**, *37*, 3007.

[212] K. Siegbahn, C. Nordling, A. Fahlman, H. Hamrin, J. Hedman, G. Johansson, T. Bergmark, S. E. Karlsson, J. Lindgren, B. Lindberg, *Nov. Act. Uppsaliensis* **1967**, *4*.

[213] C. Nordling, E. Sokolowski, K. Siegbahn, *Phys. Rev.* **1957**, *105*, 1676.

[214] F. Reinert, S. Hüfner, *New J. Phys.* **2005**, *7*, 97.

[215] N. Koch, A. C. Dürr, J. Ghijsen, R. L. Johnson, J.-J. Pireaux, J. Schwartz, F. Schreiber, H. Dosch, A. Kahn, *Thin Solid Films* **2003**, *441*, 145.

[216] S. Hüfner, *Photoelectron Spectroscopy: Principles and Applications*, Springer-Verlag, Berlin Heidelberg, **1995**.

[217] J. Braun, *Reports Prog. Phys.* **1996**, *59*, 1267.

[218] D. Cahen, A. Kahn, *Adv. Mater.* **2003**, *15*, 271.

[219] M. L. M. Rocco, M. Haeming, D. R. Batchelor, R. Fink, A. Schöll, E. Umbach, *J. Chem. Phys.* **2008**, *129*, 074702.

[220] B. Sjögren, S. Svensson, A. N. de Brito, N. Correia, M. P. Keane, C. Enkvist, S. Lunell, *J. Chem. Phys.* **1992**, *96*, 6389.

[221] M. P. Seah, W. A. Dench, *Surf. Interface Anal.* **1979**, *1*, 2.

[222] S. Tanuma, C. J. Powell, D. R. Penn, *Surf. Interface Anal.* **2005**, *37*, 1.

[223] P. L. J. Gunter, J. W. Niemantsverdriet, *Appl. Surf. Sci.* **1995**, *89*, 69.

[224] P. J. Cumpson, *Surf. Interface Anal.* **2001**, *31*, 23.

[225] J. Végh, *J. Electron Spectros. Relat. Phenomena* **2006**, *151*, 159.

[226] D. A. Shirley, *Phys. Rev. B* **1972**, *5*, 4709.

[227] S. Tougaard, *Surf. Interface Anal.* **1988**, *11*, 453.

[228] J. F. Moulder, J. Chastain, *Handbook of X Ray Photoelectron Spectroscopy: A Reference Book of Standard Spectra for Identification and Interpretation of XPS Data*, Physical Electronics Division, Perkin-Elmer Corporation, Eden Prairie, **1995**.

[229] N. Ueno, in *Phys. Org. Semicond.* (Eds.: W. Brütting, C. Adachi), WILEY-VCH Verlag GmbH & Co. KGaA, Weinheim, **2012**.

[230] The National Institute of Standards and Technology (NIST), *Handb. Basic At. Spectrosc. Data* **2000**.

[231] A. J. Bard, L. R. Faulkner, *Electrochemical Methods - Fundamentals and Applications*, John Wiley & Sons, New York, **2001**.

[232] N. Elgrishi, K. J. Rountree, B. D. McCarthy, E. S. Rountree, T. T. Eisenhart, J. L. Dempsey, *J. Chem. Educ.* **2018**, *95*, 197.

[233] N. G. Connelly, W. E. Geiger, *Chem. Rev.* **1996**, *96*, 877.

[234] J. Pommerehne, H. Vestweber, W. Guss, R. F. Mahrt, H. Bässler, M. Porsch, J. Daub, *Adv. Mater.* **1995**, *7*, 551.

[235] C. M. Cardona, W. Li, A. E. Kaifer, D. Stockdale, G. C. Bazan, *Adv. Mater.* **2011**, *23*, 2367.

[236] H. Svith, H. Jensen, J. Almstedt, P. Andersson, T. Lundbäck, K. Daasbjerg, M. Jonsson, *J. Phys. Chem. A* **2004**, *108*, 4805.

[237] B. Schumacher, H.-G. Bach, P. Spitzer, J. Obrzut, in *Springer Handbooks Mater. Meas. Methods* (Eds.: H. Czichos, T. Saito, L. Smith), Springer Sience+Business Media, Inc., **2006**.

[238] P. E. DeGarmo, J. T. Black, R. A. Kohser, *Materials and Processes in Manufacturing*, John Wiley & Sons, Hoboken, New Jersey, **2003**.

[239] D. Chercka, Dissertation - Pyrene Derivatives as Donors and Acceptors, Johannes Gutenberg-Universität Mainz, **2014**.

[240] N. J. Jeon, J. Lee, J. H. Noh, M. K. Nazeeruddin, M. Grätzel, S. Il Seok, *J. Am. Chem. Soc.* **2013**, *135*, 19087.

[241] H.-J. Nie, C.-J. Yao, J.-Y. Shao, J. Yao, Y.-W. Zhong, *Chem. - A Eur. J.* **2014**, *20*, 17454.

[242] F. Garnier, A. Yassar, R. Hajlaoui, G. Horowitz, F. Deloffre, B. Servet, S. Ries, P. Alnot, *J. Am. Chem. Soc.* **1993**, *115*, 8716.

[243] A. Dodabalapur, L. Torsi, H. E. Katz, *Science* **1995**, *268*, 270.

[244] M. Halik, H. Klauk, U. Zschieschang, G. Schmid, S. Ponomarenko, S. Kirchmeyer, W. Weber, *Adv. Mater.* **2003**, *15*, 917.

[245] H. Sirringhaus, *Adv. Mater.* **2005**, *17*, 2411.

[246] M. T. Dang, L. Hirsch, G. Wantz, *Adv. Mater.* **2011**, *23*, 3597.

[247] W. Zhang, J. Smith, S. E. Watkins, R. Gysel, M. McGehee, A. Salleo, J. Kirkpatrick, S. Ashraf, T. Anthopoulos, M. Heeney, I. McCulloch, *J. Am. Chem. Soc.* **2010**, *132*, 11437.

[248] H. Bronstein, D. S. Leem, R. Hamilton, P. Woebkenberg, S. King, W. Zhang, R. S. Ashraf, M. Heeney, T. D. Anthopoulos, J. De Mello, I. McCulloch, *Macromolecules* **2011**, *44*, 6649.

[249] D. Venkateshvaran, M. Nikolka, A. Sadhanala, V. Lemaur, M. Zelazny, M. Kepa, M. Hurhangee, A. J. Kronemeijer, V. Pecunia, I. Nasrallah, I. Romanov, K. Broch, I. McCulloch, D. Emin, Y. Olivier, J. Cornil, D. Beljonne, H. Sirringhaus, *Nature* **2014**, *515*, 384.

[250] H. Zollinger, *Color Chemistry: Syntheses, Properties, and Applications of Organic Dyes and Pigments*, Wiley-VCH, Zürich, Weinheim, **2003**.

[251] R. Hudej, G. Bratina, *J. Appl. Phys.* **2003**, *93*, 6090.

[252] Y. Inoue, Y. Sakamoto, T. Suzuki, M. Kobayashi, Y. Gao, S. Tokito, *Jpn. J. Appl. Phys.* **2005**, *44*, 3663.

[253] Y. Shoji, N. Tanaka, K. Mikami, M. Uchiyama, T. Fukushima, *Nat. Chem.* **2014**, *6*, 498.

[254] A. Facchetti, M.-H. Yoon, C. L. Stern, G. R. Hutchison, M. A. Ratner, T. J. Marks, *J. Am. Chem. Soc.* **2004**, *126*, 13480.

[255] Z.-L. Guan, J. Bok Kim, Y.-L. Loo, A. Kahn, *J. Appl. Phys.* **2011**, *110*, 043719.

[256] J. Ivanco, T. Haber, J. R. Krenn, F. P. Netzer, R. Resel, M. G. Ramsey, *Surf. Sci.* **2007**, *601*, 178.

[257] S. Duhm, I. Salzmann, N. Koch, H. Fukagawa, T. Kataoka, S. Hosoumi, K. Nebashi, S. Kera, N. Ueno, *J. Appl. Phys.* **2008**, *104*, 033717.

[258] A. Davison, R. H. Holm, R. E. Benson, W. Mahler, in *Inorg. Synth.*, **2007**, pp. 8–26.

[259] K. Funahashi, N. Tanaka, Y. Shoji, N. Imazu, K. Nakayama, K. Kanahashi, H. Shirae, S. Noda, H. Ohta, T. Fukushima, T. Takenobu, *Appl. Phys. Express* **2017**, *10*, 035101.

[260] H. Matsuoka, K. Kanahashi, N. Tanaka, Y. Shoji, L.-J. Li, J. Pu, H. Ito, H. Ohta, T. Fukushima, T. Takenobu, *Jpn. J. Appl. Phys.* **2018**, *57*, 02CB15.

[261] Y. Shoji, N. Tanaka, D. Hashizume, T. Fukushima, *Chem. Commun.* **2015**, *51*, 13342.

[262] O. V. Gusev, L. I. Denisovich, M. G. Peterleitner, A. Z. Rubezhov, N. A. Ustynyuk, P. M. Maitlis, *J. Organomet. Chem.* **1993**, *452*, 219.

[263] S. van Reenen, S. Kouijzer, R. A. J. Janssen, M. M. Wienk, M. Kemerink, *Adv. Mater. Interfaces* **2014**, *1*, 1400189.

[264] M. Nikolka, M. Hurhangee, A. Sadhanala, H. Chen, I. McCulloch, H. Sirringhaus, *Adv. Electron. Mater.* **2018**, *4*, 1700410.

[265] X. Zhang, H. Bronstein, A. J. Kronemeijer, J. Smith, Y. Kim, R. J. Kline, L. J. Richter, T. D. Anthopoulos, H. Sirringhaus, K. Song, M. Heeney, W. Zhang, I. McCulloch, D. M. DeLongchamp, *Nat. Commun.* **2013**, *4*, 2238.

[266] S. D. Ha, A. Kahn, *Phys. Rev. B* **2009**, *80*, 195410.

[267] P. Pingel, L. Zhu, K. S. Park, J.-O. Vogel, S. Janietz, E.-G. Kim, J. P. Rabe, J.-L. Brédas, N. Koch, *J. Phys. Chem. Lett.* **2010**, *1*, 2037.

[268] J.-H. Lee, H.-M. Kim, K.-B. Kim, R. Kabe, P. Anzenbacher, J.-J. Kim, *Appl. Phys. Lett.* **2011**, *98*, 173303.

[269] G. O. Nikiforov, *Org. Electron.* **2016**, *36*, 120.

[270] J. Sworakowski, *Synth. Met.* **2018**, *235*, 125.

[271] P. I. Djurovich, E. I. Mayo, S. R. Forrest, M. E. Thompson, *Org. Electron.* **2009**, *10*, 515.

[272] C. Arantes, M. Scholz, R. Schmidt, V. Dehm, M. L. M. Rocco, A. Schöll, F. Reinert, F. Würthner, *Appl. Phys. A* **2012**, *108*, 629.

[273] B. W. D'Andrade, S. Datta, S. R. Forrest, P. Djurovich, E. Polikarpov, M. E. Thompson, *Org. Electron.* **2005**, *6*, 11.

[274] J. Sworakowski, K. Janus, *Org. Electron.* **2017**, *48*, 46.

[275] C. K. Song, B. J. Eckstein, T. L. D. Tam, L. Trahey, T. J. Marks, *ACS Appl. Mater. Interfaces* **2014**, *6*, 19347.

[276] T. M. Bockman, H. R. Chang, H. G. Drickamer, J. K. Kochi, *J. Phys. Chem.* **1990**, *94*, 8483.

[277] K. Wang, J. M. McConnachie, E. I. Stiefel, *Inorg. Chem.* **1999**, *38*, 4334.

[278] Y. Sakamoto, S. Komatsu, T. Suzuki, *J. Am. Chem. Soc.* **2001**, *123*, 4643.

[279] H. Tian, J. Wang, J. Shi, D. Yan, L. Wang, Y. Geng, F. Wang, *J. Mater. Chem.* **2005**, *15*, 3026.

[280] Y. Ge, J. E. Whitten, *Chem. Phys. Lett.* **2007**, *448*, 65.

[281] A. Opitz, J. Frisch, R. Schlesinger, A. Wilke, N. Koch, *J. Electron Spectros. Relat. Phenomena* **2013**, *190*, 12.

[282] J. Ivanco, F. P. Netzer, M. G. Ramsey, *J. Appl. Phys.* **2007**, *101*, 103712.

[283] W. Han, H. Yoshida, N. Ueno, S. Kera, *Appl. Phys. Lett.* **2013**, *103*, 123303.

[284] P. Atkins, J. de Paula, *Atkins' Physical Chemistry*, Oxford University Press, Oxford, **2014**.

[285] D. Fichou, J.-M. Nunzi, F. Charra, N. Pfeffer, *Mol. Cryst. Liq. Cryst. Sci. Technol. Sect. A. Mol. Cryst. Liq. Cryst.* **1994**, *255*, 73.

[286] V. Wintgens, P. Valat, F. Garnier, *J. Phys. Chem.* **1994**, *98*, 228.

[287] M. Klessinger, J. Michl, *Excited States and Photochemistry of Organic Molecules*, Wiley-VCH, New York, **1995**.

[288] S. Barlow, *Inorg. Chem.* **2001**, *40*, 7047.

[289] D. Baran, M. S. Vezie, N. Gasparini, F. Deledalle, J. Yao, B. C. Schroeder, H. Bronstein, T. Ameri, T. Kirchartz, I. McCulloch, J. Nelson, C. J. Brabec, *J. Phys. Chem. C* **2015**, *119*, 19668.

[290] R. S. Ashraf, B. C. Schroeder, H. a. Bronstein, Z. Huang, S. Thomas, R. J. Kline, C. J. Brabec, P. Rannou, T. D. Anthopoulos, J. R. Durrant, I. McCulloch, *Adv. Mater.* **2013**, *25*, 2029.

[291] V. Pecunia, M. Nikolka, A. Sou, I. Nasrallah, A. Y. Amin, I. McCulloch, H. Sirringhaus, *Adv. Mater.* **2017**, *29*, 1606938.

[292] S. G. Higgins, B. V. O. Muir, M. Heeney, A. J. Campbell, *MRS Commun.* **2015**, *5*, 599.

[293] E. E. Perry, C.-Y. Chiu, K. Moudgil, R. A. Schlitz, C. J. Takacs, K. A. O'Hara, J. G. Labram, A. M. Glaudell, J. B. Sherman, S. Barlow, C. J. Hawker, S. R. Marder, M. L. Chabinyc, *Chem. Mater.* **2017**, *29*, 9742.

[294] C. Deibel, D. Mack, J. Gorenflot, A. Schöll, S. Krause, F. Reinert, D. Rauh, V. Dyakonov, *Phys. Rev. B* **2010**, *81*, 085202.

[295] S. Alvarado, P. Seidler, D. Lidzey, D. Bradley, *Phys. Rev. Lett.* **1998**, *81*, 1082.

[296] J. Hwang, A. Kahn, *J. Appl. Phys.* **2005**, *97*, 103705.

[297] M. Knupfer, *Appl. Phys. A* **2003**, *77*, 623.

[298] L. S. Liao, M. K. Fung, C. S. Lee, S. T. Lee, M. Inbasekaran, E. P. Woo, W. W. Wu, *Appl. Phys. Lett.* **2000**, *76*, 3582.

[299] M. Nikolka, I. Nasrallah, B. Rose, M. K. Ravva, K. Broch, A. Sadhanala, D. Harkin, J. Charmet, M. Hurhangee, A. Brown, S. Illig, P. Too, J. Jongman, I. McCulloch, J.-L. Bredas, H. Sirringhaus, *Nat. Mater.* **2017**, *16*, 356.

[300] M. Nikolka, G. Schweicher, J. Armitage, I. Nasrallah, C. Jellett, Z. Guo, M. Hurhangee, A. Sadhanala, I. McCulloch, C. B. Nielsen, H. Sirringhaus, *Adv. Mater.* **2018**, *30*, 1801874.

[301] D. M. de Leeuw, M. M. J. Simenon, A. R. Brown, R. E. F. Einerhand, *Synth. Met.* **1997**, *87*, 53.

[302] H. H. Choi, K. Cho, C. D. Frisbie, H. Sirringhaus, V. Podzorov, *Nat. Mater.* **2017**, *17*, 2.

[303] P. J. Brown, D. S. Thomas, A. Köhler, J. S. Wilson, J.-S. Kim, C. M. Ramsdale, H. Sirringhaus, R. H. Friend, *Phys. Rev. B* **2003**, *67*, 064203.

[304] N. Sai, Z. Q. Li, M. C. Martin, D. N. Basov, M. Di Ventra, *Phys. Rev. B* **2007**, *75*, 045307.

[305] I.-W. Hwang, D. Moses, A. J. Heeger, *J. Phys. Chem. C* **2008**, *112*, 4350.

[306] E. L. Ratcliff, J. L. Jenkins, K. Nebesny, N. R. Armstrong, *Chem. Mater.* **2008**, *20*, 5796.

[307] E. L. Ratcliff, P. A. Lee, N. R. Armstrong, *J. Mater. Chem.* **2010**, *20*, 2672.

[308] J. Yamamoto, Y. Furukawa, *J. Phys. Chem. B* **2015**, *119*, 4788.

[309] E. Y.-X. Chen, S. J. Lancaster, in *Compr. Inorg. Chem. II* (Eds.: J. Reedijk, K. Poeppelmeier), Elsevier Ltd., Amsterdam, **2013**.

[310] Y. Hu, Z. D. Rengert, C. McDowell, M. J. Ford, M. Wang, A. Karki, A. T. Lill, G. C. Bazan, T.-Q. Nguyen, *ACS Nano* **2018**, *12*, 3938.

[311] J. Hooz, S. Akiyama, F. J. Cedar, M. J. Bennett, R. M. Tuggle, *J. Am. Chem. Soc.* **1974**, *96*, 274.

[312] C. D. Entwistle, T. B. Marder, P. S. Smith, J. A. K. Howard, M. A. Fox, S. A. Mason, *J. Organomet. Chem.* **2003**, *680*, 165.

[313] A. Pelter, S. Singaram, H. Brown, *Tetrahedron Lett.* **1983**, *24*, 1433.

[314] J. J. Eisch, R. B. King, *Organometallic Syntheses*, New York: Academic Press, New York, **1965**.

[315] A. G. Massey, A. J. Park, *J. Organomet. Chem.* **1964**, *2*, 245.

[316] R. C. Wheland, E. L. Martin, *J. Org. Chem.* **1975**, *40*, 3101.

[317] A. Morherr, S. Witt, A. Chernenkaya, J.-P. Bäcker, G. Schönhense, M. Bolte, C. Krellner, *Phys. B Condens. Matter* **2016**, *496*, 98.

[318] C. Cai, M. Bösch, C. Bosshard, B. Müller, Y. Tao, A. Kündig, J. Weckesser, J. V. Barth, L. Bürgi, O. Jeandupeux, M. Kiy, I. Biaggio, I. Liakatas, K. Kern, P. Günter, in *ACS Symp. Ser.*, **2001**, pp. 34–49.

[319] J. Clark, C. Silva, R. H. Friend, F. C. Spano, *Phys. Rev. Lett.* **2007**, *98*, 206406.

[320] J. Clark, J.-F. Chang, F. C. Spano, R. H. Friend, C. Silva, *Appl. Phys. Lett.* **2009**, *94*, 163306.

[321] Y. Gao, C.-G. Liu, Y.-S. Jiang, *J. Phys. Chem. A* **2002**, *106*, 5380.

[322] J. A. E. H. van Haare, E. E. Havinga, J. L. J. van Dongen, R. A. J. Janssen, J. Cornil, J. L. Brédas, *Chem. - A Eur. J.* **1998**, *4*, 1509.

[323] V. M. Geskin, J.-L. Brédas, *ChemPhysChem* **2003**, *4*, 498.

[324] Y. Furukawa, *J. Phys. Chem.* **1996**, *100*, 15644.

[325] S. Stafström, J. L. Brédas, *Phys. Rev. B* **1988**, *38*, 4180.

[326] J. L. Jenkins, P. A. Lee, K. W. Nebesny, E. L. Ratcliff, *J. Mater. Chem. A* **2014**, *2*, 19221.

[327] M. Sato, S. Tanaka, K. Kaeriyama, *Synth. Met.* **1986**, *14*, 279.

[328] I. Salzmann, G. Heimel, S. Duhm, M. Oehzelt, P. Pingel, B. M. George, A. Schnegg, K. Lips, R.-P. Blum, A. Vollmer, N. Koch, *Phys. Rev. Lett.* **2012**, *108*, 035502.

[329] F. Ghani, A. Opitz, P. Pingel, G. Heimel, I. Salzmann, J. Frisch, D. Neher, A. Tsami, U. Scherf, N. Koch, *J. Polym. Sci. Part B Polym. Phys.* **2015**, *53*, 58.

[330] S. Cho, K. Lee, J. Yuen, G. Wang, D. Moses, A. J. Heeger, M. Surin, R. Lazzaroni, *J. Appl. Phys.* **2006**, *100*, 114503.

[331] L. Ma, *Chinese Phys. Lett.* **2010**, *27*, 128502.

[332] K. Kanai, T. Miyazaki, H. Suzuki, M. Inaba, Y. Ouchi, K. Seki, *Phys. Chem. Chem. Phys.* **2010**, *12*, 273.

[333] E. Verploegen, R. Mondal, C. J. Bettinger, S. Sok, M. F. Toney, Z. Bao, *Adv. Funct. Mater.* **2010**, *20*, 3519.

[334] H. Hase, K. O'Neill, J. Frisch, A. Opitz, N. Koch, I. Salzmann, *J. Phys. Chem. C* **2018**.

[335] J. Frisch, A. Vollmer, J. P. Rabe, N. Koch, *Org. Electron.* **2011**, *12*, 916.

[336] W. R. Salaneck, O. Inganäs, B. Thémans, J. O. Nilsson, B. Sjögren, J. -E. Österholm, J. L. Brédas, S. Svensson, *J. Chem. Phys.* **1988**, *89*, 4613.

[337] A. Dai, Y. Zhou, A. L. Shu, S. K. Mohapatra, H. Wang, C. Fuentes-Hernandez, Y. Zhang, S. Barlow, Y.-L. Loo, S. R. Marder, B. Kippelen, A. Kahn, *Adv. Funct. Mater.* **2014**, *24*, 2197.

[338] B. Lüssem, M. L. Tietze, H. Kleemann, C. Hoßbach, J. W. Bartha, A. Zakhidov, K. Leo, *Nat. Commun.* **2013**, *4*, 2775.

[339] X. Lin, G. E. Purdum, Y. Zhang, S. Barlow, S. R. Marder, Y.-L. Loo, A. Kahn, *Chem. Mater.* **2016**, *28*, 2677.

[340] V. I. Arkhipov, P. Heremans, E. V. Emelianova, H. Bässler, *Phys. Rev. B* **2005**, *71*, 045214.

[341] R. Lazzaroni, M. Lögdlund, S. Stafström, W. R. Salaneck, J. L. Brédas, *J. Chem. Phys.* **1990**, *93*, 4433.

[342] E. F. Aziz, A. Vollmer, S. Eisebitt, W. Eberhardt, P. Pingel, D. Neher, N. Koch, *Adv. Mater.* **2007**, *19*, 3257.

[343] J. Gao, E. T. Niles, J. K. Grey, *J. Phys. Chem. Lett.* **2013**, *4*, 2953.

[344] R. Ghosh, C. M. Pochas, F. C. Spano, *J. Phys. Chem. C* **2016**, *120*, 11394.

[345] R. Ghosh, A. R. Chew, J. Onorato, V. Pakhnyuk, C. K. Luscombe, A. Salleo, F. C. Spano, *J. Phys. Chem. C* **2018**, *122*, 18048.

[346] Y. Jugnet, G. Tourillon, T. M. Duc, *Phys. Rev. Lett.* **1986**, *56*, 1862.

[347] A. Lachkar, A. Selmani, E. Sacher, *Synth. Met.* **1995**, *72*, 73.

[348] D. Beljonne, J. Cornil, H. Sirringhaus, P. J. Brown, M. Shkunov, R. H. Friend, J.-L. Brédas, *Adv. Funct. Mater.* **2001**, *11*, 229.

[349] M. S. A. Abdou, F. P. Orfino, Y. Son, S. Holdcroft, *J. Am. Chem. Soc.* **1997**, *119*, 4518.

[350] M. S. A. Abdou, F. P. Orfino, Z. W. Xie, M. J. Deen, S. Holdcroft, *Adv. Mater.* **1994**, *6*, 838.

[351] H. Hintz, H. Peisert, H.-J. Egelhaaf, T. Chassé, *J. Phys. Chem. C* **2011**, *115*, 13373.

[352] S. Hoshino, M. Yoshida, S. Uemura, T. Kodzasa, N. Takada, T. Kamata, K. Yase, *J. Appl. Phys.* **2004**, *95*, 5088.

[353] E. J. Meijer, A. V. G. Mangnus, B.-H. Huisman, G. W. 't Hooft, D. M. de Leeuw, T. M. Klapwijk, *Synth. Met.* **2004**, *142*, 53.

[354] K. Wojciechowski, I. Ramirez, T. Gorisse, O. Dautel, R. Dasari, N. Sakai, J. M. Hardigree, S. Song, S. Marder, M. Riede, G. Wantz, H. J. Snaith, *ACS Energy Lett.* **2016**, *1*, 648.

[355] J. B. Patel, J. Wong-Leung, S. Van Reenen, N. Sakai, J. T. W. Wang, E. S. Parrott, M. Liu, H. J. Snaith, L. M. Herz, M. B. Johnston, *Adv. Electron. Mater.* **2017**, *3*, 1600470.

[356] J. Huang, Z. Gu, L. Zuo, T. Ye, H. Chen, *Sol. Energy* **2016**, *133*, 331.

[357] H. Zhang, L. Xue, J. Han, Y. Q. Fu, Y. Shen, Z. Zhang, Y. Li, M. Wang, *J. Mater. Chem. A* **2016**, *4*, 8724.

[358] S. S. Kim, S. Bae, W. H. Jo, *RSC Adv.* **2016**, *6*, 19923.

[359] A. J. Giordano, F. Pulvirenti, T. M. Khan, C. Fuentes-Hernandez, K. Moudgil, J. H. Delcamp, B. Kippelen, S. Barlow, S. R. Marder, *ACS Appl. Mater. Interfaces* **2015**, *7*, 4320.

[360] T. Schultz, R. Schlesinger, J. Niederhausen, F. Henneberger, S. Sadofev, S. Blumstengel, A. Vollmer, F. Bussolotti, J.-P. Yang, S. Kera, K. Parvez, N. Ueno, K. Müllen, N. Koch, *Phys. Rev. B* **2016**, *93*, 125309.

[361] C. Padeste, N. W. Cant, D. L. Trimm, *Catal. Letters* **1994**, *28*, 301.

[362] *NIST X-Ray Photoelectron Spectroscopy Database, NIST Standard Reference Database Number 20*, National Institute Of Standards And Technology, Gaithersburg MD, **2000**.

[363] H. Yoshida, *Anal. Bioanal. Chem.* **2014**, *406*, 2231.

[364] I. G. Hill, A. Rajagopal, A. Kahn, Y. Hu, *Appl. Phys. Lett.* **1998**, *73*, 662.

[365] Y. Hirose, W. Chen, E. I. Haskal, S. R. Forrest, A. Kahn, *Appl. Phys. Lett.* **1994**, *64*, 3482.

[366] S. Duhm, A. Gerlach, I. Salzmann, B. Bröker, R. L. Johnson, F. Schreiber, N. Koch, *Org. Electron.* **2008**, *9*, 111.

[367] T. U. Kampen, *Appl. Phys. A* **2006**, *82*, 457.

[368] R. Schlaf, B. A. Parkinson, P. A. Lee, K. W. Nebesny, N. R. Armstrong, *J. Phys. Chem. B* **1999**, *103*, 2984.

[369] I. G. Hill, J. Schwartz, A. Kahn, *Org. Electron.* **2000**, *1*, 5.

[370] L. Zhang, S. S. Roy, N. S. Safron, M. J. Shearer, R. M. Jacobberger, V. Saraswat, R. J. Hamers, M. S. Arnold, T. L. Andrew, *Adv. Mater. Interfaces* **2016**, *3*, 1600621.

[371] Y. Zhu, H. Wang, W. Chen, Y. Wang, D. Yan, *Org. Electron.* **2016**, *35*, 24.

[372] M. L. Tietze, J. Benduhn, P. Pahner, B. Nell, M. Schwarze, H. Kleemann, M. Krammer, K. Zojer, K. Vandewal, K. Leo, *Nat. Commun.* **2018**, *9*, 1182.

[373] E. T. Jaynes, *Probability Theory - The Logic of Science*, Cambridge University Press, Cambridge, **2003**.

[374] S. Mähl, M. Neumann, S. Dieckhoff, V. Schlett, A. Baalmann, *J. Electron Spectros. Relat. Phenomena* **1997**, *85*, 197.

[375] S. Hüfner, G. K. Wertheim, D. N. E. Buchanan, K. W. West, *Phys. Lett. A* **1974**, *46*, 420.

[376] A. M. Glaudell, J. E. Cochran, S. N. Patel, M. L. Chabinyc, *Adv. Energy Mater.* **2015**, *5*, 1401072.

[377] T. Menke, D. Ray, H. Kleemann, M. P. Hein, K. Leo, M. Riede, *Org. Electron.* **2014**, *15*, 365.

[378] M. L. Tietze, B. D. Rose, M. Schwarze, A. Fischer, S. Runge, J. Blochwitz-Nimoth, B. Lüssem, K. Leo, J.-L. Brédas, *Adv. Funct. Mater.* **2016**, *26*, 3730.

[379] K. Sugiyama, D. Yoshimura, E. Ito, T. Miyazaki, Y. Hamatani, I. Kawamoto, Y. Ouchi, K. Seki, H. Ishii, *Mol. Cryst. Liq. Cryst. Sci. Technol. Sect. A. Mol. Cryst. Liq. Cryst.* **1996**, *286*, 239.

[380] T. Mori, H. Fujikawa, S. Tokito, Y. Taga, *Appl. Phys. Lett.* **1998**, *73*, 2763.

[381] N. Koch, A. Kahn, J. Ghijsen, J.-J. Pireaux, J. Schwartz, R. L. Johnson, A. Elschner, *Appl. Phys. Lett.* **2003**, *82*, 70.

[382] L. Zaikowski, P. Kaur, C. Gelfond, E. Selvaggio, S. Asaoka, Q. Wu, H.-C. Chen, N. Takeda, A. R. Cook, A. Yang, J. Rosanelli, J. R. Miller, *J. Am. Chem. Soc.* **2012**, *134*, 10852.

ACKNOWLEDGEMENTS

The work presented in this thesis would not have been possible without the help and great support of many people, whom I want to thank now:

My advisor Prof. Norbert Koch for making this thesis possible in the first place by providing me the opportunity to do my doctorate and for always supporting me whenever necessary. He has been a great mentor throughout the years I spend working in his group and thanks to him, I was able to perform state-of-the-art research in collaboration with many great scientist around the world. Through his guidance I have become the scientist I am today.

My co-advisor PD Andreas Opitz for his great support in all matters regarding my research and dissertation. Our many discussions have greatly expanded my understanding of the physics of organic semiconductors. I also want to thank him for carefully proofreading the final form of this thesis and pointing out some flaws in my argumentation.

Prof. Steffen Duhm for supporting my visit to his labs in Suzhou and for making my stay there very pleasant. With his support, we were able to perform a large number of experiments in a relatively short time. I also want to thank him for our fruitful discussions, which helped me to get a better understanding of the results of our experiments.

Prof. Seth Marder and Dr. Stephen Barlow for our great discussions and their many advices. By always providing the chemists' point of view, they helped me to get a better understanding of the chemistry of organic semiconductors. I also want to thank them for providing the organometallic dimers and the molybdenum based p-dopant.

Prof Klaus Müllen and Dr. Dennis Chercka for providing the pyrene-based donors, Prof. Takanori Fukushima and Dr. Yoshiaki Shoji for providing the organic salt dopant, and Prof. Iain McCulloch and Dr. Christian Nielsen for providing the polymer IDT-BT.

Prof. Jan Behrends and Dr. Claudia Tait for performing the EPR measurements, which ultimately provided clear evidence for our hypothesis of bipolaron formation. I especially want to thank Claudia for spending a lot of time to systematically perform the experiments.

Dr. Lutz Grubert for performing all the CV experiments, although, unfortunately, some of them did not work out as planned. Thanks to our discussions, I got a better understanding of the basic principles of cyclic voltammetry.

Dr. Simon Dalgleish for preparing the OFETs with me and for performing the characterization measurements. Although our experiments have not work out as we planned, maybe they will in the future.

Federico Pulvirenti for our great collaboration. During his stay in Berlin, we were able to conduct a large number of experiments together. The time we spend in the lab together was, although demanding, also a lot of fun. I also want to thank him for thoroughly proof-reading chapter 8 of my thesis.

Tianshu Zhai for greatly supporting my experiments in Suzhou and working a lot of night-shifts with me. His help and company made my stay there very pleasant. Also thanks to him, I got to know a great variety of Chinese cuisine

Naoki Tanaka for bringing the organic salt dopant to Berlin and systematically performing the first sets of experiments with this dopant. Through his patient and diligent work, we discovered the formation of bipolarons in the first place.

Dr. Uwe Vogel, Dr. Ahmed Mansour, Dr. Raphael Schlesinger, Dr. Gabriel Man, Thorsten Schultz, Maryline Ralaiarisoa, and Dominique Lungwitz for carefully proofreading my thesis. Their many helpful comments and grammatically as well as spelling corrections helped me to bring this thesis in its current form.

Henriette Strahl, Timo Florian, Paul Zybarth and Bodo Kranz for their organizational and technical support.

All my colleagues in general for their support on a daily basis. Their help, insights and most of all their company made my doctorate a very joyful time.

Last but not least my family for their support throughout all the years and especially my sister Friederike for carefully proofreading a large portion of this thesis. Finally and most of all, I want to thank my girlfriend Nora for always supporting and believing in me, especially in the last difficult months of writing this thesis.

SELBSTSTÄNDIGKEITSERKLÄRUNG

Ich erkläre, dass ich die Dissertation selbständig und nur unter Verwendung der von mir gemäß § 7 Abs. 3 der Promotionsordnung der Mathematisch-Naturwissenschaftlichen Fakultät, veröffentlicht im Amtlichen Mitteilungsblatt der Humboldt-Universität zu Berlin Nr. 42/2018 am 11. Juli 2018, angegebenen Hilfsmittel angefertigt habe.

Ferner versichere ich, mich nicht anderwärts um einen Doktorgrad in dem Promotionsfach beworben zu haben und keinen entsprechenden Doktorgrad zu besitzen. Die dem Verfahren zu Grunde liegende Promotionsordnung der Mathematisch-Naturwissenschaftlichen Fakultät vom 11. Juli 2018 habe ich zur Kenntnis genommen.

Berthold Wegner
Berlin, 13. November 2018